

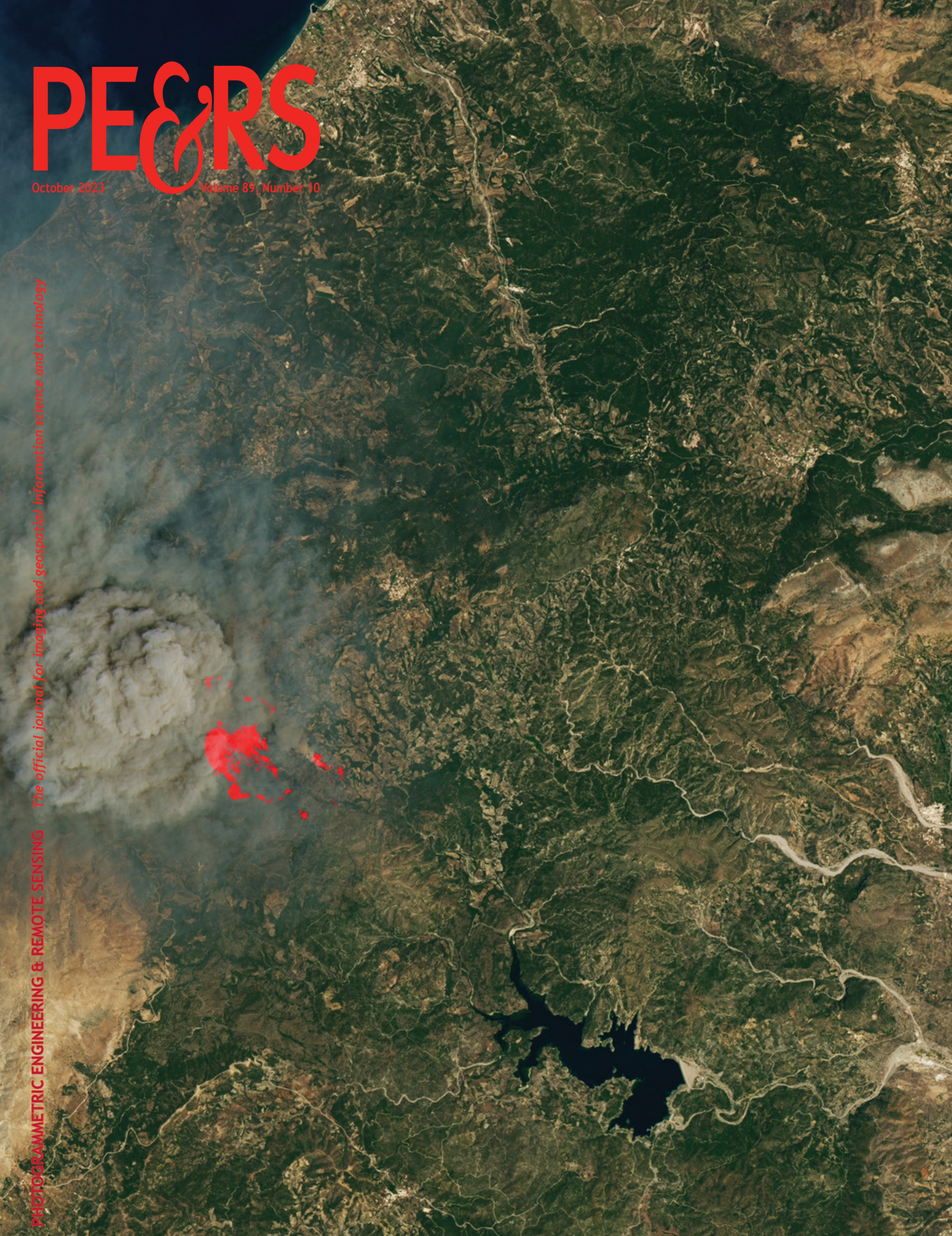
# PE&RS

October 2023

Volume 89, Number 10

*The official journal for imaging and geospatial information science and technology*

**PHOTOGRAMMETRIC ENGINEERING & REMOTE SENSING**





GEO WEEK

geo-week.com



asprs THE IMAGING & GEOSPATIAL INFORMATION SOCIETY

# SAVE THE DATE!

## One conference pass. A world of geospatial education.

FEBRUARY 11-13, 2024 | DENVER, CO

Scan for Attendee Information



The intersection of  
**geospatial**  
the **built world**

### INDUSTRIES SERVED



Architecture, Engineering & Construction



Asset & Facility Management



Disaster & Emergency Response



Earth Observation & Satellite Applications



Energy & Utilities



Infrastructure & Manufacturing



Land & Natural Resource Management



Mining & Aggregates



Surveying & Mapping



Urban Planning & Smart Cities

### EVENT PARTNERS



asprs THE IMAGING & GEOSPATIAL INFORMATION SOCIETY



Information from Imagery



USIBD U.S. Institute of BUILDING DOCUMENTATION



World Geospatial Industry Council

## ANNOUNCEMENTS

TCarta Marine, a global provider of hydrospatial products and services, has been awarded a contract to deliver satellite derived bathymetry (SDB) and seafloor classification data for the coastal zones of 13 regions around the world to the National Geospatial-Intelligence Agency (NGA) under contract to Maxar Technologies.

TCarta will deliver seabed depth and feature maps from high-resolution multispectral Maxar WorldView-2 and WorldView-3 satellite imagery for the 13 regions. SDB measurements are accurate to depths of 20-30 meters depending on water conditions, with two-meter spatial resolution. Feature classification includes coral reefs, large rocks, sandbars, and other navigation hazards.

TCarta has processed thousands of Maxar satellite images for the project, including hundreds of high-resolution scenes for one nation alone. By the time all deliverables have been submitted and approved by NGA, TCarta will have mapped the entire subsurface coastlines of the 13 regions over the 12-month Period of Performance.

“This is the most ambitious SDB mapping program ever conducted in terms of both geographic area and timeline,” said TCarta President Kyle Goodrich. “In particular, one 7,239-square-kilometer coastline by itself is larger than any contiguous SDB project TCarta has undertaken.”

“SDB can be particularly useful for remote or hard-to-access locations and for areas where traditional survey methods are too expensive or time consuming,” said Jennifer Krischer, Maxar’s Vice President and General Manager, Intelligence Programs. “The partnership between Maxar and TCarta offers a valuable service to NGA for accurate and efficient bathymetric data collection, which reflects NGA’s renewed emphasis on collecting data and generating insight ‘from Seabed to Space’.”

A leader in the application of SDB technology worldwide for more than a decade, TCarta has played a key role in enhancing the traditional water depth extraction methodology. With funding from Small Business Innovation Research (SBIR) programs managed by NOAA and the National Science Foundation, the Denver firm has integrated machine learning algorithms into the processing workflow and introduced the use of space-based laser data from the NASA ICESat-2 satellite to validate SDB results.

“A major challenge with this project was the variety of turbid and silty water conditions encountered in different geographic regions, but NGA has been receptive about the results,” said Goodrich. “We have bolstered and refined our existing workflows to deliver products that meet NGA requirements.”



CompassCom Software has released Version 8.2 of the CompassCom GIS-centric hybrid telematics platform that can be deployed on premises or in the cloud for real-time asset

tracking and comprehensive fleet management. The new version offers enhanced ease of use and more robust analytics and reporting functionality for safer, more efficient and secure fleet operations.

Developed on Esri ArcGIS technology and now supporting JavaScript 4.0, the CompassCom telematics software platform is used worldwide to track the real-time locations and status of personnel, vehicles, and other mobile assets. The platform is relied upon by critical infrastructure work forces – including public works and public safety offices – as well as departments of transportation and national government security agencies.

“Building on our 29 years as an Esri Business Partner, we have leveraged the full range of GIS capabilities in Version 8.2 to deliver superior situational awareness related to the safety of personnel and efficient operations of vehicles,” said CompassCom CEO Brant Howard. “Customized alerts and dashboards provide fleet managers with the information they need to make better decisions in real time.”

The flexible CompassCom telematics platform receives location and status data from any GPS-equipped vehicle, handheld device, or high-value asset and serves that information in real-time to a GIS map display or an interactive dashboard. Live alerts give managers instant insight into fleet activities for better decision making, while real-time vehicle performance analytics and reporting enable fine tuning of operational efficiencies.

CompassCom developed the telematics solution to utilize Esri JavaScript API and Esri data formats. The platform also offers data portability to CAD systems, asset management, and other third-party GIS environments. When the client or agency requires hardened secure installations CompassCom offers on premises behind a firewall on the customer’s private network as an option.

“The CompassCom telematics platform is now easier to use and runs exactly the same in the cloud or on premise,” said Howard.

For more information on the CompassCom V8.2 telematics platform or to schedule an online demonstration, visit the CompassCom website at [www.compasscom.com](http://www.compasscom.com).



Bowman Consulting Group Ltd. (the “Company” or “Bowman”) (NASDAQ: BWMN), today announced the acquisition of MTX Surveying, Inc. (“MTX”), a geospatial, land survey and project management company based in Marshall, Texas. Founded by Shane Nafe and Austin Holland in 2016, the firm has grown rapidly to a workforce of over 60 accredited professionals, technicians, and support staff serving clients in Texas, Louisiana, and New Mexico. Today, MTX provides full-service consulting, project management, surveying, mapping, and permitting services for clients working in oil and gas, energy and renewables, utility services, and

land development. The MTX staff will all become Bowman employees in connection with the acquisition.

“Shane and Austin have built an exciting company,” said Gary Bowman, CEO of Bowman. “Their focus on oil and gas, energy, and renewables projects will help to accelerate our goal of increasing the contribution of power and utility-oriented assignments within our revenue mix. Their experience with aerial mapping, data capture, hi-res orthometric imagery, and drone surveying complements other recent acquisitions and investments we have made in geospatial technologies and services.”

“We’re pleased to be joining Bowman and are excited about the opportunities this acquisition provides,” said Shane Nafe, President and Founding Partner of MTX Surveying. “Bowman has an expansive national platform of clients, assignments, and engineering professionals to which we can contribute immediately. We’re ready to get started adding value and growing our collective energy services and geospatial practice.”

For more information on MTX Surveying, their projects, and services, visit <https://www.mtxsurveying.com>.

## EVENTS

GoGeomatics Launches Canada’s Inaugural Geospatial Exposition in Calgary—Canada’s geospatial community is coming together for the first-ever national geospatial exposition in Calgary. The GoGeomatics Expo will take place November 6-8th on the iconic Calgary Stampede grounds.

Co-located with the Expo, the GeoIgnite Career Fair is where Canada’s top organizations will recruit from a diverse pool of professionals, including students and graduates from the Expo’s Education Partners, the University of Calgary Geomatics Engineering Program and the SAIT Geomatics Program.

The GoGeomatics Expo fosters collaboration and will showcase the latest advancements in the geospatial sector. This community-driven event provides an arena for professionals to connect, share ideas and stay updated on the latest developments in research, technologies and services. The event will feature an array of engaging activities, including keynote presentations, panel discussions, workshops and interactive exhibitions.

Highlights of the GoGeomatics Expo include:

- **Speaking Programs:** Renowned experts in the geospatial field will be sharing insights on industry trends, challenges and future opportunities. Thought-provoking panel discussions will bring together experts from various sectors to explore how geospatial technology is shaping industries across Canada. Themes of discussions are: reality capture, earth observation, BIM/

GIS, surveying, leadership, education and public good (government).

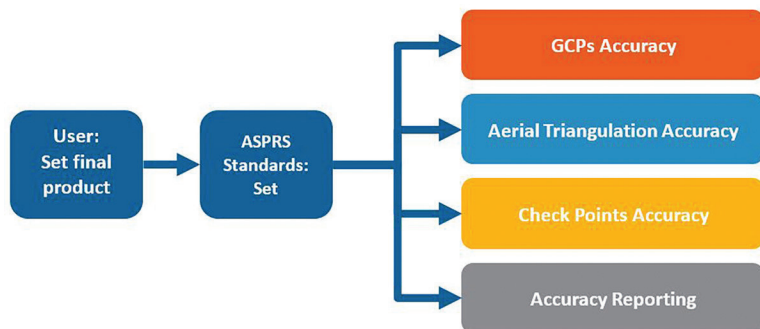
- **Activities:** The trade show will feature cutting-edge geospatial products, solutions and services from engineering firms, product and software developers, navigation specialists, satellite experts and more. Demos and workshops will allow participants to enhance their skills and knowledge in geospatial tools, data analysis and geographic information systems (GIS). The SCAN-Off is a friendly opportunity for companies to participate in a scan-to-scan comparison of their LiDAR mapping platforms.
- **Networking Opportunities:** The GoGeomatics Expo will provide ample opportunities for attendees to network with other professionals, potential employers and industry influencers. From a networking zone on the trade show floor, to the Expo party and the ticketed opening reception and dinner, everyone will have the chance to connect.

“The Expo is about bringing the geospatial and geomatics communities together to learn, network and exchange ideas,” says GoGeomatics founder and Managing Director, Jonathan Murphy. “Everyone is welcomed to this celebration of our sector.”

Registration for the GoGeomatics Expo is now open. For more information about the event please visit the official GoGeomatics Expo website at: [www.gogeomaticsexpo.com](http://www.gogeomaticsexpo.com).

## CALENDAR

- 16-19 October, **GIS-Pro 2023**, Columbus, Ohio; [www.urisa.org/gis-pro](http://www.urisa.org/gis-pro).
- 30 October - 3 November, **ACRS2023**, Taipei, Taiwan; <https://acrs2023.tw>.
- 6-8 November, **GoGeomatics Expo**, Calgary, Alberta, Canada; <https://gogeomaticsexpo.com>.
- 8-10 November, **Smart GEO Expo 2023**, Seoul, South Korea; <https://smartgeoexpo.kr>.
- 27 November - 1 December, **URISA GIS Leadership Academy**, Denver, Colorado; [https://urisa-portal.org/page/URISA\\_GLA](https://urisa-portal.org/page/URISA_GLA).
- 11-13, February 2024, **Geo Week**, Denver, Colorado; <https://www.geo-week.com>.
- 2-4 May, **GISTAM 2024**, Angers, France; <https://gistam.scitevents.org>.
- 13-16 May 2024, **Geospatial World Forum**, Rotterdam, The Netherlands; <https://geospatialworldforum.org>.



## COLUMNS

**595** GIS Tips & Tricks — Making Your Maps more “Mappy Maps”

## ANNOUNCEMENTS

- 588** New ASPRS Members  
Join us in welcoming our newest members to ASPRS.
- 594** ASPRS Certifications
- 599** Headquarters News
- 612** Call for *PE&RS* Special Issue Submissions — Ushering a New Era of Hyperspectral Remote Sensing to Advance Remote Sensing Science in the Twenty-first Century

## DEPARTMENTS

- 577** Industry News
- 578** Calendar
- 600** Ad Index
- 611** In-Press *PE&RS* Articles
- 653** Who’s Who in ASPRS
- 655** ASPRS Sustaining Members

## 581 The ASPRS Positional Accuracy Standards, Edition 2: The Geospatial Mapping Industry Guide to Best Practices

By Qassim Abdullah, Ph.D., PLS, CP, Woolpert Vice President and Chief Scientist

## 589 Highlights from the ASPRS Positional Accuracy Standards for Digital Geospatial Data, Edition 2, Version 1.0

## 591 Table of Contents from the ASPRS Positional Accuracy Standards for Digital Geospatial Data, Edition 2, Version 1.0

### 601 Mapping Lotus Wetland Distribution with the Phenology Normalized Lotus Index Using SAR Time-Series Imagery and the Phenology-Based Method

Sheng Wang, Taixia Wu, and Qiang Shen

Lotus wetland is a type of wetland that can efficiently purify water. Therefore, rapid and accurate remote sensing monitoring of the distribution of lotus wetland has great significance to their conservation and the promotion of a sustainable and healthy development of ecosystems. The phenology-based method has proven effective in mapping some different types of wetlands. However, because of the serious absence of remote sensing data caused by cloud coverage and the differences in the phenological rhythms of lotus wetlands in different areas, achieving high-precision mapping of different regions using a unified approach is a challenge. To address the issue, this article proposes a Phenology Normalized Lotus Index (PNLI) model that combines SAR time-series imagery and the phenology-based method.

### 613 The FABDEM Outperforms the Global DEMs in Representing Bare Terrain Heights

Nahed Osama, Zhenfeng Shao, and Mohamed Freeshah

Many remote sensing and geoscience applications require a high-precision terrain model. In 2022, the Forest And Buildings removed Copernicus digital elevation model (FABDEM) was released, in which trees and buildings were removed at a 30 m resolution. This research aims to perform a qualitative and quantitative analysis of FABDEM in comparison with the commonly used global DEMs.

### 625 Evaluating Surface Mesh Reconstruction Using Real Data

Yanis Marchand, Laurent Caraffa, Raphael Sulzer, Emmanuel Clédat, and Bruno Vallet

Surface reconstruction has been studied thoroughly, but very little work has been done to address its evaluation. In this article, we propose new visibility-based metrics to assess the completeness and accuracy of three-dimensional meshes based on a point cloud of higher accuracy than the one from which the reconstruction has been computed.

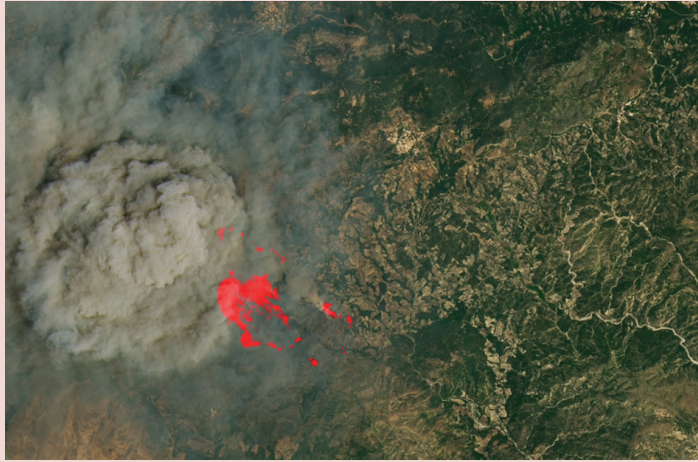
### 639 Different Urbanization Levels Lead to Divergent Responses of Spring Phenology

Chaoya Dang, Zhenfeng Shao, Xiao Huang, Gui Cheng, and Jiaxin Qian

Urban vegetation phenology is important for understanding the relationship between human activities on urban ecosystems and carbon cycle. The relationship between urban and rural vegetation phenology and environmental and meteorological factors were studied across urban-rural gradients. However, the relationship of intra-urban urbanization intensity (UI) gradients on vegetation at the start of season (SOS) is unclear. Here, we used remote sensing data to quantitatively assess the relationship of vegetation SOS to UI gradients at mid-high latitudes in the northern hemisphere.

**See the Cover Description on Page 580**

# COVER DESCRIPTION



Wildfires raging across the Greek island of Rhodes sent tens of thousands of locals and tourists scrambling for safety in late July 2023. A prolonged stretch of extreme heat contributed to high fire risk across much of the country. Blazes also ignited on the mainland and the islands of Corfu and Evia.

The Operational Land Imager (OLI) on Landsat 8 acquired this image of fire activity on Rhodes on July 19. The image is natural color, with the infrared signature from actively burning fires overlaid in red. Thick smoke can be seen drifting westward toward the Aegean Sea.

This image captures the start of what turned into an intense period of wildfire. NASA-affiliated scientists were able to track the fires' spread with the Visible Infrared Imaging Radiometer Suite (VIIRS) sensor on the NASA-NOAA Suomi NPP satellite. Calculating the perimeter of actively burning areas every 12 hours, Eli Orland and Tess McCabe observed how the Rhodes fire spread relatively slowly at first, then picked up rapidly. Between July 21 and July 23, it underwent a six-fold increase in size, from approximately 25 to 150 square kilometers (10 to 60 square miles), according to their analysis. Orland is a research associate at Goddard Space Flight Center and the University of Maryland, Baltimore County, and McCabe is a post-doctoral associate at the University of Maryland, College Park.

An estimated 19,000 people evacuated from areas threatened by the blazes, according to news reports. Many sought refuge in makeshift shelters such as schools, gymnasiums, and docked ships, while some in seaside villages boarded coast guard vessels to move to safety.

As of July 24, there were 82 fires burning across Greece, with 64 of those starting on July 23. In addition to the many people impacted on Rhodes, upwards of 2,500 people on Corfu were evacuated, and residents of villages in southern Evia found themselves in harm's way as high winds fanned the flames.

Fires are not unusual in Greece, but heat-stoked fire weather is projected to become more common as the planet warms. The intense fire season of 2021 came on the heels of extreme heat, and the number of fires and area burned in Greece were far above average. Experts think the current heat wave is set to become Greece's longest on record, with temperatures exceeding 40°C (104°F) for days on end in late July. The area burned by fires is more than double the average for this point in the year.

NASA's Earth Applied Sciences Disasters program area has been activated in support of the fires in Greece, responding to a request from the World Central Kitchen for data and imagery of the fires' location and impacts to inform their humanitarian efforts in setting up kitchens for those affected. As new information becomes available, the team will be posting maps and data products on its open-access mapping portal.

NASA Earth Observatory image by Lauren Dauphin, using Landsat data from the U.S. Geological Survey. Story by Lindsey Doermann. The image images can be viewed online by visiting the Landsat Image Gallery, <https://landsat.gsfc.nasa.gov/>, image id 151628.



## PHOTOGRAMMETRIC ENGINEERING & REMOTE SENSING

JOURNAL STAFF

Publisher ASPRS

Editor-In-Chief Alper Yilmaz

Director of Publications Rae Kelley

Electronic Publications Manager/Graphic Artist

Matthew Austin

*Photogrammetric Engineering & Remote Sensing* is the official journal of the American Society for Photogrammetry and Remote Sensing. It is devoted to the exchange of ideas and information about the applications of photogrammetry, remote sensing, and geographic information systems. The technical activities of the Society are conducted through the following Technical Divisions: Geographic Information Systems, Photogrammetric Applications, Lidar, Primary Data Acquisition, Professional Practice, Remote Sensing Applications, and Unmanned Autonomous Systems. Additional information on the functioning of the Technical Divisions and the Society can be found in the Yearbook issue of *PE&RS*.

All written correspondence should be directed to the American Society for Photogrammetry and Remote Sensing, PO Box 14713, Baton Rouge, LA 70898, including general inquiries, memberships, subscriptions, business and editorial matters, changes in address, manuscripts for publication, advertising, back issues, and publications. The telephone number of the Society Headquarters is 225-408-4747; the fax number is 225-408-4422; web address is [www.asprs.org](http://www.asprs.org).

**PE&RS.** *PE&RS* (ISSN0099-1112) is published monthly by the American Society for Photogrammetry and Remote Sensing, 8550 United Plaza Blvd, Suite 1001, Baton Rouge, Louisiana 70809. Periodicals postage paid at Bethesda, Maryland and at additional mailing offices.

**SUBSCRIPTION.** *PE&RS* is available as an e-Subscription (single-site and multi-site licenses) and an e-Subscription with print add-on (single-site license only). *PE&RS* subscriptions are on a calendar-year, beginning in January and ending in December.

The rate for a single-site e-Subscription for the USA/Non-USA is \$1040 USD, for Canadian\* is \$1092 USD.

The rate for a multi-site e-Subscription for the USA/Non-USA is \$1040 USD plus \$250 USD for each additional license, for Canadian\* is \$1092 USD plus \$263 for each additional license.

The rate for e-Subscription with print add-on for the USA is \$1525 USD, for Canadian\* is \$1612 USD, and for Non-USA is \$1565 USD.

\*Note: Subscription prices for Canada includes 5% of the total amount for Canada's Goods and Services Tax (GST #135123065). **PLEASE NOTE: All Subscription Agencies receive a 20.00 USD discount.**

**POSTMASTER.** Send address changes to *PE&RS*, ASPRS, PO Box 14713, Baton Rouge, LA 70898. CDN CPM # (40020812).

**MEMBERSHIP.** Membership is open to any person actively engaged in the practice of photogrammetry, photointerpretation, remote sensing and geographic information systems; or who by means of education or profession is interested in the application or development of these arts and sciences. Membership is for one year, with renewal based on the anniversary date of the month joined. Membership Dues include a 12-month electronic subscription to *PE&RS*. Annual Individual Membership dues are \$175.00 USD and Student Membership dues are \$50.00 USD. A tax of 5% for Canada's Goods and Service Tax (GST #135123065) is applied to all members residing in Canada.

**COPYRIGHT 2023.** Copyright by the American Society for Photogrammetry and Remote Sensing. Reproduction of this issue or any part thereof (except short quotations for use in preparing technical and scientific papers) may be made only after obtaining the specific approval from ASPRS. The Society is not responsible for any statements made or opinions expressed in technical papers, advertisements, or other portions of this publication. Printed in the United States of America.

**PERMISSION TO PHOTOCOPY.** The copyright owner's consent that copies of the article may be made for personal or internal use or for the personal or internal use of specific clients. This consent is given on the condition, however, that the copier pay the stated per copy fee through the Copyright Clearance Center, Inc., 222 Rosewood Drive, Danvers, Massachusetts 01923, for copying beyond that permitted by Sections 107 or 108 of the U.S. Copyright Law. This consent does not extend to other kinds of copying, such as copying for general distribution, for advertising or promotional purposes, for creating new collective works, or for resale.

# The ASPRS Positional Accuracy Standards, Edition 2: The Geospatial Mapping Industry Guide to Best Practices

**By Qassim Abdullah, Ph.D., PLS, CP, Woolpert Vice President and Chief Scientist**

The geospatial industry is fortunate to have the American Society for Photogrammetry and Remote Sensing to safeguard and advance industry best practices and proper conduct. The ASPRS Positional Accuracy Standards for Digital Geospatial Data of 2014 were the first accuracy standards developed for digital mapping practices and have provided the beacon for this guidance.

The ASPRS Positional Accuracy Standards for Digital Geospatial Data, Edition 2, was approved by the ASPRS Board of Directors on August 23, 2023. This edition was developed through observations and feedback over the last seven years. It became apparent that a new edition of the standards was needed to incorporate recommendations, correct outdated guidelines, and to address quickly evolving sensors, technologies, and industry practices.

This article will highlight the main features of the standards and note the changes introduced in Edition 2. It will also help readers understand the new standards and how they apply to everyday mapping activities.

Edition 2 was developed by community consensus, with specialists from private companies, public agencies, and academia contributing to its development. For the first time, four state departments of transportation contributed to these standards. This paradigm of participation was created to expand the standards to the wider community of mapping, remote sensing, and engineering practices.

---

Photogrammetric Engineering & Remote Sensing  
Vol. 89, No. 10, October 2023, pp. 581-588.  
0099-1112/22/581-588

© 2023 American Society for Photogrammetry  
and Remote Sensing

doi: 10.14358/PERS.89.10.581

## Motivation Behind the New ASPRS Accuracy Standards

- Legacy map accuracy standards, such as the U.S. National Map Accuracy Standards (NMAS) of 1947 and ASPRS 1990 standards, have become outdated.
- Many of the data acquisition and mapping technologies that these standards were based on are no longer used.
- Recent advances in mapping technologies can produce better quality and higher accuracy geospatial products and maps.
- Legacy map accuracy standards were designed with only plotted or drawn maps to represent geospatial data.
- Within the past two decades, as the industry transitioned between hardcopy and softcopy mapping environments, most standard measures for relating ground sample distance (GSD) and map scale to the final mapping accuracy were inherited from photogrammetric practices using scanned film.
- New mapping processes and methodologies have become much more sophisticated with advances in technology and in our knowledge of mapping processes and mathematical modeling.
- Mapping accuracy can no longer be associated with camera geometry and flying altitude alone (focal length,  $x_p$ ,  $y_p$ , B/H ratio, etc.)
- Elevation products from the new technologies and active sensors—such as lidar, UAS, and IFSAR—are not covered in the legacy mapping standards. New accuracy standards are needed to address elevation products derived from these technologies.
- Today's mapping accuracy is influenced by many factors, such as:
  - The quality of camera calibration parameters.
  - Quality and size of a charged coupled device (CCD) used in the digital camera CCD array.
  - Amount of imagery overlap.
  - Quality of parallax determination or photo measurements.
  - Quality of the GPS signal.
  - Quality and density of ground controls.
  - Quality of the aerial triangulation solution.
  - Capability of the processing software to handle GPS drift and shift.
  - Capability of the processing software to handle camera self-calibration.
  - The digital terrain model used to produce orthoimagery.

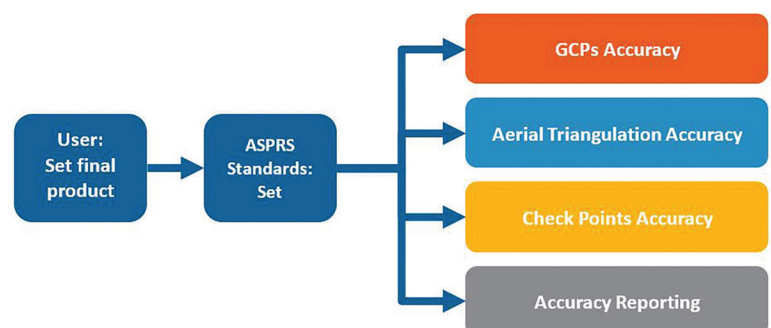
These factors can vary widely from project to project, depending on the sensor used and specific methodology. For these reasons, existing accuracy measures based on map scale, film scale, GSD, c-factor, and scanning resolution no longer apply to current geospatial mapping practices.

## New Standards for a New Era

While old standards guided the initial practices of mapmaking that were based on paper map media and film cameras, new digital sensor technologies like lidar, digital cameras, and geospatial products and practices challenged these standards.

### Highlights of the New Standards Include:

- Sensor agnostic, data driven.
- Designed for today's digital sensors and mapping practices.
- Positional accuracy measure that is based on ground measurement units, not map units.
- Positional accuracy thresholds that are independent of published GSD, map scale or contour interval.
- It is all metric!
- Unlimited horizontal and vertical accuracy classes to support any sensor technology.
- Based on root mean square error (RMSE) alone as an accuracy indicator.
- Provide additional accuracy measures such as:
  - Aerial triangulation accuracy
  - Ground control accuracy
  - Orthoimagery seam lines accuracy
  - Lidar relative swath-to-swath accuracy
  - Independent checkpoint accuracy
- Provide recommended minimum nominal pulse density (NPD) for lidar data.
- Provide a measure for horizontal accuracy for elevation data.
- Provide guidelines on number and spatial distribution of checkpoints based on project area.
- Introduce the new 3D accuracy measure.
- Provide five addenda on guidelines and best practices for various mapping techniques.
- Ease of use and application. Once the user defines the product's accuracy, the standards set the rest of the requirements for the intermediate processes that are involved in producing the final products. An example of that is that users can specify the required product accuracy and the standards will set all requirements for aerial triangulation accuracy, ground control point accuracy, checkpoint accuracy, etc. The figure below illustrates this characteristic of the new standards.





## Introducing Edition 2

In 2022, ASPRS established a formal Positional Accuracy Standards Working Group under the Standards Committee to evaluate user comments and consider technology advancements to implement appropriate changes to the standards. Based on the feedback received from the industry and the advances the industry has witnessed in sensor technologies and best practices, the following important changes were introduced in Edition 2:

### Change #1—Relaxed Accuracy Requirement for Ground Control and Checkpoints

As demand for geospatial products with higher accuracy increases, the accuracy requirements for the surveyed ground control and checkpoints have increased accordingly. According to Edition 1 of the standards, the accuracy of ground controls required for photogrammetric work needs to be four times better than the produced products, and checkpoints need to be three times better than the assessed product.

Advances in today's sensor technologies, processing software and algorithms, and processing methodology are enabling us to produce more accurate products. Therefore, we no longer need the three or four times "safety factor" to ensure the desired accuracy of the delivered products. In addition, imposing such restrictive requirements for the ground control and checkpoint surveys presented a burden on field surveying practices when using Global Navigation Satellite System (GNSS) techniques. Real-time kinematic (RTK)-based surveys also became ineligible to support some high-accuracy products, like the U.S. Geological Survey's Quality Level 0 lidar.

### Change #2—Eliminated References to 95% Confidence Level as Accuracy Measure

The 95% confidence measure of accuracy for geospatial data was introduced in the National Standard for Spatial Data Accuracy (NSSDA), published by the Federal Geographic Data Committee in 1998. This measure was carried forward in the ASPRS Guidelines for Vertical Accuracy Reporting for Lidar Data published in 2004, as well as in Edition 1 of these standards.

Although Edition 1 endorses the use of RMSE as the main accuracy measure, it also references the 95% confidence level throughout. Experience has shown that reporting two quantities that represent the same accuracy at different confidence levels creates confusion for users and data producers alike. Users cannot compute accuracy at a 95% confidence level without computing RMSE first, therefore there is no need for a second accuracy that is derived from the first accuracy. The RMSE is a straightforward accuracy measure that is easy to understand and compute.

### Change #3—Required Inclusion of Survey Checkpoint Accuracy when Computing Accuracy of Final Product

Since checkpoints and control points are no longer needed to meet the three or four times the intended product accuracy and demands for high-accuracy products are on the rise, errors in the surveyed checkpoints used to assess final product accuracy, although small, can no longer be neglected. As product accuracy increases, the impact of error in checkpoints on the computed product accuracy increases. When final products are used for further measurements, calculations, or decision-making, the reliability of these subsequent measurements can be better estimated if the uncertainty associated with the checkpoints or control points is factored in.

### Change #4—Removed Pass/fail Requirement for Vegetated Vertical Accuracy for Lidar Data

Data producers and data users reported that they were challenged in situations where Non-Vegetated Vertical Accuracy (NVA) is well within contract specifications, but Vegetated Vertical Accuracy (VVA) is not. Since VVA is influenced by factors that fall outside the lidar system accuracy, it is fair to all parties involved in a contract to base the data acceptance or rejection decision for the overall project on the quality of the tested NVA.

In most cases, the VVA assessment is compromised and the quality of lidar-derived surface under trees is affected due to the following reasons:

1. Vegetation blocks the lidar pulse from reaching the ground, resulting in less-than-perfect density of the point cloud representing the terrain.
2. The compromised density of lidar points reaching the ground under trees results in poor modeling of the terrain where the checkpoints are located,
3. The performance of algorithms used to separate underground and above-ground points in vegetated areas.
4. The quality of GPS-based surveying techniques in vegetated areas is compromised due to restricted satellite visibility and multipath issues.

Edition 2 calls for the VVA to be evaluated and reported as it is found, but it should not be used as a criterion for rejection or acceptance.

### Change #5—Increased Minimum Number of Checkpoints Required for Product Accuracy Assessment from 20 to 30

In Edition 1, a minimum of 20 checkpoints was required for testing positional accuracy of a final mapping product. This minimum was not based on rigorous science or statistical theory, but was a holdover from NMAS of 1947, published by the U.S. Bureau of the Budget.

In Edition 2, a better scientific approach is introduced based on a well-respected theorem in statistics, the central limit theorem. According to the central limit theorem, regardless of the distribution of the population, if the sample size is

sufficiently large ( $n \geq 30$ ), then the sample mean is approximately normally distributed, and the normal probability model can be used to quantify uncertainty when making inferences about a population based on the sample mean. Therefore, in Edition 2 a product accuracy assessment must have a minimum number of 30 checkpoints to be considered fully compliant.

**Change #6—Limited Maximum Number of Checkpoints for Large Projects to 120**

According to Edition 1 guidelines, large projects require hundreds, sometimes thousands of checkpoints to assess product accuracy. These numbers have proved to be unrealistic for the industry, as they inflate project budgets and, in some cases, hinder project executions—especially for projects in remote or difficult-to-access areas.

Since Edition 2 recognizes the central limit theorem as the basis for statistical testing, there is insufficient evidence to support the need to increase the number of checkpoints indefinitely as the project area increases. The new maximum number of 120 checkpoints is equal to four times the number cited by the central limit theorem, and that should provide a statistically valid sample.

**Change #7—Introduced New Accuracy Term: “Three-dimensional Positional Accuracy.”**

Three-dimensional models and digital twins are gaining acceptance in many engineering and planning applications. Many future geospatial data sets will be in true 3D form. Therefore, a method for assessing positional accuracy of a point or feature within a 3D model is needed to support future innovation and product specifications. 3D models require 3D accuracy, rather than separate horizontal and vertical accuracies. Edition 2 endorses the use of the following three terms:

- Horizontal positional accuracy
- Vertical positional accuracy
- 3D positional accuracy

**Change #8—Added Addenda on Best Practices and Guidelines**

With geospatial mapping practices and technologies evolving quickly, users need guidelines on how to keep up. In response, Edition 2 introduces the following five addenda:

**Addendum I:** General Best Practices and Guidelines

**Addendum II:** Best Practices and Guidelines for Field Surveying of Ground Control and Checkpoints

**Addendum III:** Best Practices and Guidelines for Mapping with Photogrammetry

**Addendum IV:** Best Practices and Guidelines for Mapping with Lidar

**Addendum V:** Best Practices and Guidelines for Mapping with UAS

## Understanding Edition 2 of the ASPRS Positional Accuracy Standards for Digital Geospatial Data

**Horizontal Positional Accuracy Standard for Geospatial Data**

The standards specify horizontal accuracy classes as they relate to digital orthoimagery, digital planimetric data, scaled planimetric maps, and elevation data in terms of  $RMSE_H$ , which is the combined linear error along a horizontal plane in the radial direction.  $RMSE_H$  is derived from  $RMSE_X$  and  $RMSE_Y$  according to the following formula:

$$RMSE_H = \sqrt{RMSE_X^2 + RMSE_Y^2}$$

In the case of digital orthoimagery mosaics, an additional criterion for the allowable mismatch at seamlines of  $\leq 2^*$   $RMSE_H$  is specified in Table 1. The term  $RMSE_H$  should be computed using both  $RMSE_{H_1}$  and  $RMSE_{H_2}$  error components, as will be illustrated in the next sections.

Table 1. Horizontal Positional Accuracy Standard for Geospatial Data.

Horizontal Accuracy Class	Absolute Accuracy	Orthoimagery Mosaic Seamline Mismatch (cm)
	$RMSE_H$ (cm)	
#-cm	$\leq \#$	$\leq 2^*\#$

**Vertical Positional Accuracy Standard for Elevation Data**

Vertical accuracy is to be expressed as  $RMSE_V$  in both vegetated and non-vegetated terrain. Vertical accuracy classes are defined by the associated  $RMSE_V$  specified for the product. The term  $RMSE_V$  should be computed using both  $RMSE_{V_1}$  and  $RMSE_{V_2}$  error components, as will be illustrated in the next sections. While the NVA must meet accuracy thresholds listed in Table 2, the VVA does not and needs only to be tested and reported as found. If the NVA meets user specifications, the VVA should be accepted at the reported accuracy level. Table 2 shows the vertical accuracy class specifications for digital elevation data, including Data Internal Precision requirements where applicable, such as in lidar.

Table 2. Vertical Positional Accuracy Standard for Geospatial Data.

Vertical Accuracy Class	Absolute Accuracy		Data Internal Precision (where applicable)		
	NVA $RMSE_V$ (cm)	VVA $RMSE_V$ (cm)	Within-Swath Smooth Surface Precision Max Diff (cm)	Swath-to-Swath Non-Vegetated $RMS_{Dz}$ (cm)	Swath-to-Swath Non-Vegetated Max Diff (cm)
#-cm	$\leq \#$	As found	$\leq 0.60^*\#$	$\leq 0.80^*\#$	$\leq 1.60^*\#$

### 3D Positional Accuracy Standard for Geospatial Data

3D positional accuracy can be computed for any type of geospatial data, as long as the horizontal and vertical positional accuracy are assessed and reported. It is especially useful in assessing accuracy for colorized point clouds and digital twins. Table 3 defines the 3D accuracy standard for any 3D digital data as a combination of horizontal and vertical radial error.  $RMSE_{3D}$  is derived from the horizontal and vertical components of error according to the following formula:

$$RMSE_{3D} = \sqrt{RMSE_X^2 + RMSE_Y^2 + RMSE_Z^2}$$

or,

$$RMSE_{3D} = \sqrt{RMSE_H^2 + RMSE_V^2}$$

Table 3. 3D Positional Accuracy Standard for Geospatial Data.

3D Accuracy Class	Absolute Accuracy
	$RMSE_{3D}$ (cm)
#-cm	≤ #

### Horizontal Accuracy of Elevation Data

The standards outline horizontal accuracy testing requirements for elevation data created from stereo photogrammetry and lidar. For other technologies, appropriate horizontal accuracies for elevation data should be negotiated between the data producer and the client, with specific accuracy thresholds and methods based on the technology used and the project design. Horizontal accuracy for elevation data is determined using one of the following approaches:

- **Photogrammetric elevation data:** For elevation data derived using stereo photogrammetry, apply the same horizontal accuracy class that would be used for planimetric data or digital orthoimagery produced from the same source, based on the same photogrammetric adjustment.
- **Lidar elevation data:** The standards provide the following equation to estimate the horizontal accuracy for a lidar-derived dataset ( $RMSE_H$ ), based on the main errors introduced by the positional accuracy of the GNSS; roll, pitch, and heading accuracy of the inertial measurement unit (IMU); and the flying height:

$$RMSE_H = \sqrt{(GNSS\ positional\ error)^2 + \left( \frac{\tan(IMU\ roll\ or\ pitch\ error) + \tan(IMU\ heading\ error)}{1.478} * flying\ height \right)^2}$$

Using the above equation, the horizontal accuracy of lidar data acquired from different flying altitude are listed in Table 4.

Table 4. Estimated Horizontal Error ( $RMSE_H$ ) in Lidar Data as a Function of GNSS Error, IMU Error, and Flying Height.

Flying Height (m)	GNSS Error (cm)	IMU Roll/Pitch Error (arc-sec)	IMU Heading Error (arc-sec)	$RMSE_H$ (cm)
500	10	10	15	10.7
1,000	10	10	15	12.9
1,500	10	10	15	15.8
2,000	10	10	15	19.2
2,500	10	10	15	22.8
3,000	10	10	15	26.5
3,500	10	10	15	30.4
4,000	10	10	15	34.3
4,500	10	10	15	38.2
5,000	10	10	15	42.0

### Accuracy Requirements for Aerial Triangulation and IMU-Based Sensor Orientation

The quality and accuracy of the aerial triangulation, if performed, and/or the GNSS/IMU-based direct georeferencing play key roles in determining the final accuracy of imagery-derived mapping products.

- For aerial triangulation designed for digital planimetric data (orthoimagery and/or map) only:

$$RMSE_{H1(AT)} \leq \frac{1}{2} * RMSE_{H(MAP)}$$

$$RMSE_{V1(AT)} \leq RMSE_{H(MAP)}$$

- For aerial triangulation designed for projects that include elevation or 3D products, in addition to digital planimetric data (orthoimagery and/or map):

$$RMSE_{H1(AT)} \leq \frac{1}{2} * RMSE_{H(MAP)}$$

$$RMSE_{V1(AT)} \leq \frac{1}{2} * RMSE_{V(DEM)}$$

**The ASPRS Positional Accuracy Standards for Digital Geospatial Data of 2014 were the first accuracy standards developed for digital mapping practices and have provided the beacon for this guidance**

## Accuracy Requirements for Ground Control Used for Aerial Triangulation

The accuracy of the ground control points should be twice the target accuracy of the final products, according to the following two categories:

- Ground control for aerial triangulation designed for digital planimetric data (orthoimagery and/or map) only:

$$RMSE_{H(GCP)} \leq \frac{1}{2} * RMSE_{H(MAP)}$$

$$RMSE_{V(GCP)} \leq RMSE_{H(MAP)}$$

- Ground control for aerial triangulation designed for projects that include elevation or 3D products, in addition to digital planimetric data (orthoimagery and/or map):

$$RMSE_{H(GCP)} \leq \frac{1}{2} * RMSE_{V(MAP)}$$

$$RMSE_{V(GCP)} \leq \frac{1}{2} * RMSE_{H(DEM)}$$

## Accuracy Requirements for Ground Control Used for Lidar

The accuracy of the ground control points used for lidar calibration and boresighting should be twice the target accuracy of the final products. Similarly, ground checkpoints used to assess lidar data accuracy should be twice the target accuracy of the final products.

$$RMSE_{V(GCP)} \leq \frac{1}{2} * RMSE_{V(DEM)}$$

Similar guidelines can be followed for other digital data acquisition technologies, such as IFSAR.

## Reporting Geospatial Data Accuracy

Knowing the positional accuracy of a geospatial product is important, as it plays a great role in determining the applicability of the data for an intended purpose. Mislabeled or poorly reported positional accuracy can have catastrophic consequences. Therefore, the geospatial data exchanged among users should be accompanied by metadata clearly stating its positional accuracy. To help data users and data producers, Edition 2 provides formal accuracy reporting statements that serve different scenarios.

## Number and Distribution of Checkpoints for Horizontal Accuracy and NVA Assessment

According to Edition 2, a minimum of 30 checkpoints are needed to assess the horizontal and non-vegetated vertical accuracy of a dataset. A large project, or more than 1,000 square kilometers, will need more checkpoints. Table 5 lists the recommended number of checkpoints according to the project size.

Table 5 recommends the use of a minimum of 30 checkpoints for a project area of 1,000 square kilometers or less and a maximum of 120 checkpoints for a project area larger than 10,000 square kilometers. Checkpoints should be evenly distributed across the project area as much as possible.

<sup>1</sup> For very small projects where the use of 30 checkpoints is not feasible, report the accuracy as suggested in section 7.15.

Table 5. Recommended Number of Checkpoints for Horizontal Accuracy and NVA Testing Based on Project Area.

Project Area (Square Kilometers)	Total Number of Checkpoints for NVA
≤1000 <sup>1</sup>	30
1001-2000	40
2001-3000	50
3001-4000	60
4001-5000	70
5001-6000	80
6001-7000	90
7001-8000	100
8001-9000	110
9001-10000	120
>10000	120

Considerations made for challenging circumstances—such as rugged terrain, water bodies, heavy vegetation, and inaccessibility—are acceptable if agreed upon between the data producer and the client. Details on the best locations for these checkpoints are provided in section 7.12 of the standards.

## Testing VVA

If the project requires the VVA to be tested, there should be a minimum of 30 VVA checkpoints regardless of the project area. The data user and data producer may agree to collect a larger number of checkpoints. To avoid situations where errors in checkpoints in the vegetated terrain do not follow a random distribution, no combined statistical terms, such as  $RMSE_V$ , should be used in evaluating the results of the test. In other words, only individual elevation differences (i.e., errors) for each checkpoint shall be used in the evaluation.

## Accuracy of Checkpoints

According to Edition 2, checkpoints used to assess any product accuracy (horizontal, vertical, or 3D) should be twice as accurate as the test products.

## Testing and Reporting of Product Accuracy:

New to the standards is the way accuracy is computed. The following formula represents the updated and accepted method for computing product accuracy:

$$\text{Horizontal Product Accuracy } (RMSE_H) = \sqrt{RMSE_{H_1}^2 + RMSE_{H_2}^2}$$

$$\text{Vertical Product Accuracy } (RMSE_V) = \sqrt{RMSE_{V_1}^2 + RMSE_{V_2}^2}$$

$$RMSE_{3D} = \sqrt{RMSE_H^2 + RMSE_V^2}$$

Where:

$RMSE_H$ ,  $RMSE_V$ , and  $RMSE_{3D}$  are the product's horizontal, vertical, and 3D accuracy, respectively.

$RMSE_{H_1}$  and  $RMSE_{V_1}$  are the components of error derived from product fit to the checkpoints.

$RMSE_{H_2}$  and  $RMSE_{V_2}$  are the components of error associated with checkpoint surveys.

For the purposes of demonstration, suppose you were provided with five checkpoints to verify the final horizontal and vertical accuracy for a dataset (this example uses fewer checkpoints than the minimum 30 for the sake of brevity) according to these standards.

Table 6 provides the map-derived coordinates and the surveyed coordinates for the five points. The table also shows the computed accuracy and other relevant statistics. In this abbreviated example, the data are intended to meet a target horizontal accuracy class of  $RMSE_H = 15\text{cm}$  and a target vertical accuracy class of  $RMSE_V = 10\text{cm}$ .

### Computation of Horizontal, Vertical, and 3D Accuracy

#### 1. Compute the RMSE values:

$$RMSE_x = \sqrt{\frac{1}{n} \sum_{i=1}^n (x_{i(\text{map})} - x_{i(\text{surveyed})})^2}$$

where:

$x_{i(\text{map})}$  is the coordinate in the specified direction of the  $i^{\text{th}}$  checkpoint in the dataset,

$x_{i(\text{surveyed})}$  is the coordinate in the specified direction of the  $i^{\text{th}}$  checkpoint in the independent source of higher accuracy,

$n$  is the number of checkpoints tested, and  $i$  is an integer ranging from 1 to  $n$ .

$$RMSE_x = \sqrt{\frac{(-0.140)^2 + (-0.100)^2 + (0.017)^2 + (-0.070)^2 + (0.130)^2}{5}} = 0.102 \text{ m}$$

$$RMSE_y = \sqrt{\frac{(-0.070)^2 + (-0.100)^2 + (-0.070)^2 + (0.150)^2 + (0.120)^2}{5}} = 0.107 \text{ m}$$

$$RMSE_{H_1} = \sqrt{RMSE_x^2 + RMSE_y^2}$$

$$RMSE_{H_1} = \sqrt{(0.102)^2 + (0.107)^2} = 0.147 \text{ m}$$

$$RMSE_{V_1} = \sqrt{\frac{(-0.071)^2 + (0.010)^2 + (0.102)^2 + (-0.100)^2 + (0.087)^2}{5}} = 0.081 \text{ m}$$

**E**dition 2 was developed through observations and feedback over the last seven years. It became apparent that a new edition of the standards was needed to incorporate recommendations, correct outdated guidelines, and to address quickly evolving sensors, technologies, and industry practices.

#### 2. Compute the final accuracy values:

To complete the accuracy computations, let us assume that the checkpoint report submitted by the surveyor states that the field survey was conducted using an RTK-GPS-based technique to an accuracy of:

$$\text{Horizontal accuracy } RMSE_{H_2} = 1.9\text{cm or } 0.019\text{m}$$

$$\text{Vertical accuracy } RMSE_{V_2} = 2.23\text{cm or } 0.022\text{m}$$

Table 6. Accuracy Statistics for Example Data.

Point ID	Map-derived Values			Surveyed Checkpoints Values			Residuals (Errors)		
	Eastings (E)	Northing (N)	Elevation (Z)	Eastings (E)	Northing (N)	Elevation (Z)	$\Delta E$ (Eastings)	$\Delta N$ (Northing)	$\Delta Z$ (Elevation)
	meter	meter	meter	meter	meter	meter	meter	meter	meter
GCP1	359584.394	5142449.934	477.127	359584.534	5142450.004	477.198	-0.140	-0.070	-0.071
GCP2	359872.190	5147939.180	412.406	359872.290	5147939.280	412.396	-0.100	-0.100	0.010
GCP3	359893.089	5136979.824	487.292	359893.072	5136979.894	487.190	0.017	-0.070	0.102
GCP4	359927.194	5151084.129	393.591	359927.264	5151083.979	393.691	-0.070	0.150	-0.100
GCP5	372737.074	5151675.999	451.305	372736.944	5151675.879	451.218	0.130	0.120	0.087
<b>Number of check points</b>							5	5	5
<b>Mean Error (m)</b>							-0.033	0.006	0.006
<b>Standard Deviation (m)</b>							0.108	0.119	0.091
<b>RMSE (m)</b>							0.102	0.106	0.081
<b>Fit to Checkpoints <math>RMSE_{H_1}</math> (m)</b>							0.147	$RMSE_H = \sqrt{RMSE_E^2 + RMSE_N^2}$	
<b>Fit to Checkpoints <math>RMSE_{V_1}</math> (m)</b>							0.081		

The final horizontal and vertical accuracy should be computed as follows:

$$RMSE_H = \sqrt{RMSE_{H_1}^2 + RMSE_{H_2}^2} = \sqrt{(0.147)^2 + (0.019)^2} = 0.148 \text{ m } (< 15 \text{ cm})$$

$$RMSE_V = \sqrt{RMSE_{V_1}^2 + RMSE_{V_2}^2} = \sqrt{(0.081)^2 + (0.022)^2} = 0.083 \text{ m } (< 10 \text{ cm})$$

Similarly, the 3D positional accuracy can be computed using the following formula:

$$RMSE_{3D} = \sqrt{RMSE_H^2 + RMSE_V^2}$$

Therefore,

$$RMSE_{3D} = \sqrt{0.148^2 + 0.083^2} = 0.170 \text{ m}$$

Based on the computed horizontal and vertical accuracy numbers above, the product is meeting the specified horizontal and vertical accuracies of 15cm and 10cm, respectively.

### Final Notes

The material in this article is intended to shed light on important aspects of the new edition of the ASPRS Positional Accuracy Standards for Digital Geospatial Data. Readers are encouraged to review the standards for full clarity and edification. Edition 2, version 1.0 includes only two of the five addenda. The remaining three Addenda listed in the Table of Contents:

**Addendum III:** Best Practices and Guidelines for Mapping with Photogrammetry

**Addendum IV:** Best Practices and Guidelines for Mapping with Lidar

**Addendum V:** Best Practices and Guidelines for Mapping with UAS

will be available for public comment in the coming weeks and will be added to Edition 2, Version 2.0, which ASPRS anticipates approving in late Fall 2023.

To download Edition 2 document, visit <https://publicdocuments.asprs.org/PositionalAccuracyStd-Ed2-V1>

### Acknowledgment

Dr. Qassim Abdullah would like to extend his gratitude to all individuals who assisted in drafting Edition 2 of the standards, especially members of the ASPRS Positional Accuracy Standards Working Group, Dr. Riadh Munjy of California State University, Fresno; Josh Nimetz of the USGS, Michael Zoltek of GPI Geospatial, Inc.; and Colin Lee of the Minnesota Department of Transportation. Additionally, he would like to recognize the teams who worked on drafting the addenda on best practices and guidelines, led by Jim Gillis of VeriDaaS Corporation; Dr. Sagar Deshpande of Dewberry; Dr. Nora May of Fugro; Jacob Lopez of Towill, Inc.; Dr. Christopher E. Parrish of Oregon State University; Martin Flood of GeoCue Group, Leo Liu of Inertial Labs, Munjy; and Zoltek. He would also like to extend his appreciation to the ASPRS staff under the leadership of Karen Schuckman, who was instrumental in reviewing the draft and providing valuable suggestions and comments. Abdullah said he is grateful to Alan Mikuni of GeoWing Mapping, Inc., who volunteered his time to proofread all drafts. Thank you, Alan, for doing a great job.

This article will be published concurrently in Lidar Magazine.

## NEW ASPRS MEMBERS

**ASPRS would like to welcome the following new members!**

Gabriel Ahoma

David Andes

Gene Bailey

David Buback

DeAnna Clum

Dick Durstein

Mark S. Erickson

Safak Fidan

Hayden Fischer

Felipe Galindo, Sr.

Jason M. Gustafson

Jeffrey Hall

Jacob Heckert

Jared Jacobs

Steve Aury LeBlanc, PLS

Savannah Madden

David Miceli

William Middleton

Angelica M. Otting

Lindsey Rotche

Devlin Rutherford

Zach Saavedra


Claudette Sandoval-Green

Jill Schwarz, PhD

Carlina Wharton-Bucher

Lucas Wilsing

**FOR MORE INFORMATION ON  
ASPRS MEMBERSHIP, VISIT  
[HTTP://WWW.ASPRS.ORG/JOIN-NOW](http://www.asprs.org/join-now)**



# ASPRS Positional Accuracy Standards for Digital Geospatial Data

(EDITION 2, VERSION 1.0 - AUGUST 2023)

## Foreword

Edition 1 of the ASPRS Positional Accuracy Standards for Digital Geospatial Data was published in November 2014. In the years since, users expressed concerns and suggested revisions based on their experience applying the Standards in real-world situations. In addition, technologies have evolved in such a way as to challenge the assumptions upon which Edition 1 was based.

In 2022, ASPRS established a formal Positional Accuracy Standards Working Group under the Standards Committee to evaluate user comments, consider technology advancements, and implement appropriate changes to the Standards. The following individuals were appointed to the Positional Accuracy Standards Working Group:

Chair: Dr. Qassim Abdullah, Vice President and Chief Scientist, Woolpert, Inc.

Members:

- Dr. Riadh Munjy, Professor of Geomatics Engineering, California State University, Fresno
- Josh Nimetz, Senior Elevation Project Lead, U.S. Geological Survey
- Michael Zoltek, National Geospatial Programs Director, GPI Geospatial, Inc.
- Colin Lee, Photogrammetrist, Minnesota Department of Transportation

The ASPRS Positional Accuracy Standards for Digital Geospatial Data are designed to be modular in nature, such that revisions could be made and additional sections added as geospatial technologies and methods evolve. Additionally, the Standards are designed to recommend best practices, methods, and guidelines for the use of emerging technologies to achieve the goals and requirements set forth in the Standards. With support from the ASPRS Technical Divisions, the primary Working Group established subordinate Working Groups to author Addenda for best practices and guidelines for photogrammetry, lidar, UAS, and field surveying. The subordinate Working Group members and contributors are credited in each Addendum, as appropriate.

---

## Summary of Changes in Edition 2

Important changes adopted in Edition 2 of the Standards are as follows:

### 1. Eliminated references to the 95% confidence level as an accuracy measure.

- **Reason for the change:** The 95% confidence measure of accuracy for geospatial data was introduced in the National Standard for Spatial Data Accuracy (NSSDA) published by the Federal Geographic Data Committee in 1998. This measure was carried forward in the ASPRS Guidelines for Vertical Accuracy Reporting for Lidar Data published in 2004, as well as in Edition 1 of the ASPRS Positional Accuracy Standards for Digital Geospatial Data published in 2014. However, RMSE is also a way to express data accuracy, and it is typically reported alongside the 95% confidence level because the two are derived from the same error distribution. As a matter of fact, users need to compute RMSE first in order to obtain the 95% confidence measure. The reporting of two quantities representing the same accuracy at different confidence levels has created confusion for users and data producers alike.

- **Justification for the change:** The RMSE is a reliable statistical term that is sufficient to express product accuracy, and it is well understood by users. Experience has shown that the use of both RMSE and the 95% confidence level leads to confusion and misinterpretation.

### 2. Relaxed the accuracy requirement for ground control and checkpoints.

- **Reason for the change:** Edition 1 called for ground control points of four times the accuracy of the intended final product, and ground checkpoints of three times the accuracy of the intended final product. With goals for final product accuracies approaching a few centimeters in both the horizontal and vertical, it becomes difficult, if not impossible, to use RTK methods for control and checkpoint surveys, introducing a significant burden of cost for many high-accuracy projects.

---

Photogrammetric Engineering & Remote Sensing  
Vol. 89, No. 10, October 2023, pp. 589-592.  
0099-1112/22/589-592

© 2023 American Society for Photogrammetry  
and Remote Sensing  
doi: 10.14358/PERS.89.10.589

- **Justification for the change:** As the demand for higher-accuracy geospatial products grows, accuracy requirements for the surveyed ground control and checkpoints set forth in Edition 1 exceed those that can be achieved in a cost-effective manner, even with high-accuracy GPS. Furthermore, today’s sensors, software, and processing methods have become very precise, diminishing the errors introduced in data acquisition and processing. If best practices are followed, safety factors of three and four times the intended product accuracy are no longer needed.

### 3. Required the inclusion of survey checkpoint accuracy when computing the accuracy of the final product.

- **Reason for the change:** Since checkpoints will no longer need to meet the three-times-intended-product accuracy requirement (see item 2 above), the error in the checkpoints survey may no longer be ignored when reporting the final product accuracy. This is especially important, given the increasing demand for highly accurate products—which, in some cases, approach the same order of magnitude as the survey accuracy of the checkpoints. Therefore, checkpoint error should be factored into the final product accuracy assessment that is used to communicate the reliability of resulting final products.
- **Justification for the change:** Errors in the survey checkpoints used to assess final product accuracy, although small, can no longer be neglected. As product accuracy increases, the impact of error in checkpoints on the computed product accuracy increases. When final products are used for further measurements, calculations, or decision making, the reliability of these subsequent measurements can be better estimated if the uncertainty associated with the checkpoints is factored in.

### 4. Removed the pass/fail requirement for Vegetated Vertical Accuracy (VVA) for lidar data.

- **Reason for the change:** Data producers and data users have reported that they are challenged in situations where Non-Vegetated Vertical Accuracy (NVA) is well within contract specifications, but VVA is not. As explained below, factors affecting VVA are not a function of the lidar system accuracy; therefore, only NVA should be used when making a pass/fail decision for the overall project. VVA should be evaluated and reported, but should not be used as a criterion for acceptance.
- **Justification for the change:** Where lidar can penetrate to bare ground under trees, the accuracy of the points, as a function of system accuracy, should be comparable to lidar points in open areas. However, the accuracy and the quality of lidar-derived surface under trees is affected by:
  1. the type of vegetation where it affects the ability of lidar pulse to reach the ground,

2. the density of lidar points reaching the ground,
3. and the performance of the algorithms used to separate ground and above-ground points in these areas.

Furthermore, the accuracy of the ground checkpoints acquired with GPS surveying techniques in vegetated areas is affected by restricted satellite visibility. As a result, accuracies computed from the lidar-derived surface in vegetated areas are not valid measures of lidar system accuracy.

### 5. Increased the minimum number of checkpoints required for product accuracy assessment from 20 to 30.

- **Reason for the change:** In Edition 1, a minimum of 20 checkpoints are required for testing positional accuracy of the final mapping products. This minimum number is not based on rigorous science or statistical theory; rather, it is a holdover from legacy Standards and can be traced back to the National Map Accuracy Standards published by the U.S. Bureau of the Budget in 1947.
- **Justification for the change:** The Central Limit Theorem calls for at least 30 samples to calculate statistics such as mean, standard deviation, and skew. These statistics are relied upon in positional accuracy assessments. According to The Central Limit Theorem, regardless of the distribution of the population, if the sample size is sufficiently large ( $n \geq 30$ ), then the sample mean is approximately normally distributed, and the normal probability model can be used to quantify uncertainty when making inferences about a population based on the sample mean. Therefore, in Edition 2, a product accuracy assessment must have a minimum number of 30 checkpoints in order to be considered fully compliant.

### 6. Limited the maximum number of checkpoints for large projects to 120.

- **Reason for the change:** Since these Standards recognize the Central Limit Theorem as the basis for statistical testing, there is insufficient evidence for the need to increase the number of checkpoints indefinitely as the project area increases. The new maximum number of checkpoints is equal to four times the number called by the Central Limit Theorem.
- **Justification for the change:** According to the old guidelines, large projects require hundreds, sometimes thousands of checkpoints to assess product accuracy. Such numbers have proven to be unrealistic for the industry, as it inflates project budget and, in some cases, hinders project executions, especially for projects taking place in remote or difficult-to-access areas.

### 7. Introduced a new accuracy term: “three-dimensional positional accuracy.”

- **Reason for the change:** Three-dimensional models require consideration of three-dimensional accuracy,



rather than separate horizontal and vertical accuracies. Edition 2 endorses the use of the following three terms:

- Horizontal positional accuracy
- Vertical positional accuracy
- Three-dimensional (3D) positional accuracy

- **Justification for the change:** Three-dimensional models and digital twins are gaining acceptance in many engineering and planning applications. Many future geospatial data sets will be in true three-dimensional form; therefore, a method for assessing positional accuracy of a point or feature within the 3D model is needed to support future innovation and product specifications.

## 8. Added Best Practices and Guidelines Addenda for:

- General Best Practices and Guidelines
- Field Surveying of Ground Control and Checkpoints
- Mapping with Photogrammetry
- Mapping with Lidar
- Mapping with UAS

This summarizes the most significant changes implemented in Edition 2 of the ASPRS Positional Accuracy Standards for Digital Geospatial Data. Other minor changes will be noted throughout.

# TABLE OF CONTENTS

Foreword	
Summary of Changes in Edition 2	
Foreword to Edition 1 of 2014	
1. Purpose	
1.1 Scope and Applicability	
1.2 Limitations	
1.3 Structure and Format	
2. Conformance	
3. References	
4. Authority	
5. Terms and Definitions	
6. Symbols, Abbreviated Terms, and Notations	
7. Specific Requirements	
7.1 Statistical Assessment of Accuracy	
7.2 Systematic Error and Mean Error Assumptions	
7.3 Horizontal Positional Accuracy Standard for Geospatial Data	
7.4 Vertical Positional Accuracy Standard for Elevation Data	
7.5 Three-Dimensional Positional Accuracy Standard for Geospatial Data	
7.6 Horizontal Accuracy of Elevation Data	
7.7 Low Confidence Areas in Elevation Data	
7.8 Accuracy Requirements for Aerial Triangulation and IMU-Based Sensor Orientation	
7.9 Accuracy Requirements for Ground Control Used for Aerial Triangulation	
7.10 Accuracy Requirements for Ground Control Used for Lidar	
7.11 Positional Accuracy Assessment of Geospatial Data Products	
7.11.1 First Component of Positional Error – Product Fit to Checkpoints	
7.11.2 Second Component of Positional Error – Survey Control and Checkpoint Error	
7.11.3 Horizontal Positional Accuracy	
7.11.4 Vertical Positional Accuracy	
7.11.5 Three-dimensional Positional Accuracy	
7.12 Checkpoint Accuracy and Placement	
7.13 Checkpoint Density and Distribution	
7.14 Data Internal Precision (Relative Accuracy) of Lidar and IFSAR Data	
7.14.1 Within-Swath (Smooth-Surface) Precision	
7.14.2 Swath-to-Swath Precision	
7.15 Accuracy Reporting	
7.15.1 Accuracy Reporting by Data User or Consultant	
7.15.2 Accuracy Reporting by Data Producer	
<b>Appendix A — Background and Justifications (Informative)</b>	
A.1 Legacy Standards and Guidelines	
A.2 A New Standard for a New Era	
A.2.1 Mapping Practices During the Film-based Era	
A.2.2 Mapping Practices During the Softcopy Photogrammetry Era	
A.2.3 Mapping Practices During the Digital Sensors Photogrammetry Era	
<b>Appendix B — Data Accuracy and Quality Examples (Normative)</b>	
B.1 Aerial Triangulation and Ground Control Accuracy Examples	
B.2 Digital Orthoimagery Horizontal Accuracy Classes	
B.3 Digital Planimetric Data Horizontal Accuracy Classes	
B.4 Digital Elevation Data Vertical Accuracy Classes	
B.5 Relating ASPRS Positional Accuracy Standards for Digital Geospatial Data, Edition 2, 2023 Values to Legacy ASPRS 1990 Accuracy Values	
Example 1: Relating the Horizontal Accuracy of a Map or Orthorectified Image calculated with the ASPRS Positional Accuracy Standards for Digital Geospatial Data, Edition 2, 2023 to the Legacy ASPRS Map Standards of 1990	
Example 2: Relating the Vertical Accuracy of an Elevation Data Set calculated with the ASPRS Positional Accuracy Standards for Digital Geospatial Data, Edition 2, 2023 to the Legacy ASPRS Map Standards of 1990	

B.6 Relating ASPRS Positional Accuracy Standards for Digital Geospatial Data, Edition 2, 2023 Values to Legacy NMAS 1947 Accuracy Values

Example 3: Relating the Horizontal Accuracy of a Map or Orthorectified Image calculated with the ASPRS Positional Accuracy Standards for Digital Geospatial Data, Edition 2, 2023 to the Legacy National Map Accuracy Standards of 1947

Example 4: Relating the Vertical Accuracy of an Elevation Data Set calculated with the ASPRS Positional Accuracy Standards for Digital Geospatial Data, Edition 2, 2023 to the Legacy National Map Accuracy Standards of 1947

B.7 Relating ASPRS Positional Accuracy Standards for Digital Geospatial Data, Edition 2, 2023 Values to the FGDC National Standard for Spatial Data Accuracy (NSSDA)

Example 5: Relating the Horizontal Accuracy of a Map or Orthorectified Image calculated with ASPRS Positional Accuracy Standards for Digital Geospatial Data, Edition 2, 2023 to the FGDC National Standard for Spatial Data Accuracy (NSSDA)

Example 6: Relating the Vertical Accuracy of an Elevation Data Set calculated with the ASPRS Positional Accuracy Standards for Digital Geospatial Data, Edition 2, 2023 to the FGDC National Standard for Spatial Data Accuracy (NSSDA)

B.8 Estimating Horizontal Accuracy of Lidar Data

B.9 Elevation Data Accuracy vs. Elevation Data Quality

## Appendix C — Accuracy Testing and Reporting Guidelines (Normative)

- C.1 Checkpoint Requirements
- C.2 Accuracy of Checkpoints
- C.3 Number of Checkpoints
- C.4 Distribution of Vertical Checkpoints Across Land Cover Types
- C.5 Vertical Checkpoints
- C.6 Horizontal Checkpoints for Elevation Data
- C.7 Testing and Reporting of Product Accuracy
  - C.7.1 Testing and Reporting Horizontal Accuracy of Digital Orthophotos and Planimetric Maps
  - C.7.2 Testing and Reporting of Vertical Accuracy of Elevation Data
- C.8 Low Confidence Areas
- C.9 Erroneous Checkpoints
- C.10 Data Internal Precision Assessment
- C.11 Interpolation of Elevation Represented Surface for Checkpoint Comparisons

## Appendix D — Accuracy Statistics and Example (Normative)

- D.1 Reporting Accuracy Statistics
  - D.1.1 Accuracy Computations

### ADDENDUM I: General Best Practices and Guidelines

### ADDENDUM II: Best Practices and Guidelines for Field Surveying of Ground Control and Checkpoints

### ADDENDUM III: Best Practices and Guidelines for Mapping with Photogrammetry

### ADDENDUM IV: Best Practices and Guidelines For Mapping With Lidar

### ADDENDUM V: Best Practices and Guidelines For Mapping With UAS

#### FIGURES

- Figure C.1 Topographic Surface Represented as a TIN
- Figure C.2 Topographic Surface Represented as a DEM

#### TABLES

- Table 7.1 Horizontal Accuracy Classes for Geospatial Data
- Table 7.2 Vertical Accuracy Classes for Digital Elevation Data
- Table 7.3 Three-Dimensional Accuracy Classes for Geospatial Data
- Table 7.4 Computing Vertical Product Accuracy
- Table A.1 Common Photography Scales using Camera with 9" Film Format and 6" Lens
- Table A.2 Relationship Between Film Scale and Derived Map Scale
- Table B.1 Aerial Triangulation and Ground Control Accuracy Requirements- For Orthoimagery and/or Planimetric Data Only
- Table B.2 Aerial Triangulation and Ground Control Accuracy Requirements- For Orthoimagery and/or Planimetric Data and Elevation Data
- Table B.3 Common Horizontal Accuracy Classes According to the New Standard
- Table B.4 Horizontal Accuracy/Quality Examples for High Accuracy Digital Planimetric Data
- Table B.5 Vertical Accuracy/Quality Examples for Digital Elevation Data
- Table B.6 Vertical Accuracy of the ASPRS Positional Accuracy Standards for Digital Geospatial Data, Edition 2, 2023 Compared to Legacy Standards
- Table B.7 Examples of Vertical Accuracy and Recommended Lidar Point Density for Digital Elevation Data according to the ASPRS Positional Accuracy Standards for Digital Geospatial Data, Edition 2, 2023
- Table B.8 Estimated Horizontal Error (RMSEH) as a Function of GNSS Error, IMU Error, and Flying Height
- Table C.1 Recommended Number of Checkpoints for Horizontal Accuracy and NVA Testing Based on Project Area
- Table C. 2 Low Confidence Area Criteria Min NPD: Minimum Nominal Point Density, Max NPS: Maximum Nominal Point Spacing Min NGPD: Minimum Nominal Ground Point Density, Max NGPS: Maximum Nominal Ground Point Spacing
- Table D.1 Accuracy Statistics for Example Data

Dewberry is a leading, market-facing firm with a proven history of providing professional services to public- and private-sector clients. Established in 1956 and headquartered in Fairfax, Virginia, our professionals are dedicated to solving clients' most complex challenges and transforming their communities. The firm harnesses the power of geospatial science to offer complete end-to-end remote sensing and mapping services starting with state-of-the-art airborne lidar sensors to automated processing, surveying, web/mobile GIS, and advanced data analytics. Dewberry creates, analyzes, and builds geospatial data and tools, to help clients integrate, share, and simplify the use of information allowing for more effective and efficient decision making.

Dewberry's geospatial and technology services team includes more than 250 professionals who create, analyze, and build tools to share geospatial data, and help clients integrate these tools into their daily lives. By fusing multiple data sets together for more efficient data mining, Dewberry provides clients with easy-to-use tools that simplify the use of information to allow for more effective and efficient decision making.

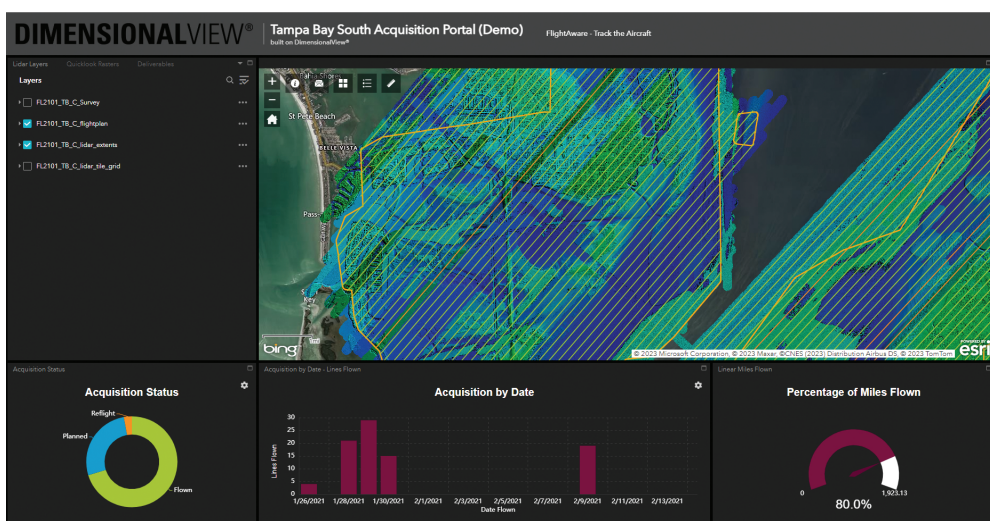
Dewberry recently acquired a new topobathymetric lidar sensor—the RIEGL VQ-880-G II—to add to its growing inventory of lidar sensors. This marks the second topobathymetric sensor acquired by Dewberry, the first being a Teledyne CZML SuperNova, a unique sensor specially made for obtaining deep returns up to ~3.5 Secchi depth. Operating these two sensors provides the firm immense flexibility to map in a wide variety of aquatic environments and conditions.

Dewberry has the ability to tailor its topobathymetric lidar acquisition to fit the strengths of these two systems. Additionally, the firm's RIEGL VQ 1560 IIS topographic lidar sensor adds to its breadth of mapping capabilities by offering high-density lidar collection over land. The firm is excited to empower their clients with access to the most innovative technology to meet their topographic/lidar needs, delivering hi-definition lidar datasets quickly and efficiently.

Dewberry has also implemented two initiatives to facilitate client communication and data processing efficiency. The firm is using Esri-powered, client-facing dashboards combined with quick-look technology, allowing clients to view data acquisition in near real-time and be an active partner in remote sensing activities. The second initiative focuses on improved feature extraction efficiency through automation. Dewberry's IT-team built custom multi-threaded, extended-memory computers dedicated for artificial intelligence (AI)/machine learning (ML) processing. These computers are used for feature extraction and automated classification of lidar data. This AI/ML workflow increases efficiency and decreases delivery time of geospatial products to clients.

Dewberry has received industry-wide recognition winning back-to-back year awards from Esri, the Management Association for Private Photogrammetric Surveyors (MAPPS), and the American Council of Engineering Companies (ACEC) in 2021, 2022, and 2023.

DimensionalView® is a multi-use tool developed in-house that can be used for real-time tracking not only for topobathymetric lidar acquisition, but for acquisition of various data types acquired with a wide variety of sensors and platforms. The platform can be used for topographic lidar, sonar, and aerial imagery to name a few. Another helpful layer that can be included in the portal are ground survey checkpoints, both for planning points and displaying final collected points. The tracker is a powerful project management tool that combines numerous data points into one web-based location and then adds easy-to-use geospatial features allowing the user to access the information they need in the format they need.



DimensionalView® is a multi-use tool developed in-house that can be used for real-time tracking not only for topobathymetric lidar acquisition, but for acquisition of various data types acquired with a wide variety of sensors and platforms.

Dewberry works seamlessly to provide geospatial mapping and technology services (GTS) across various market segments. With nearly 50 years of GTS experience, the firm is dedicated to understanding and applying the latest tools, trends, and technologies. Dewberry employs the latest GIS software and database platforms, including the full suite of ESRI products. The firm's products and services include application, web, and cloud-based development; system integration; database design mapping; data fusion; and mobile solutions. To learn more, visit [www.dewberry.com](http://www.dewberry.com).

Dewberry  
 Amar Nayegandhi  
 1000 North Ashley Drive, Suite 801, Tampa, FL 33602-3718  
 813.421.8642 | [anayegandhi@dewberry.com](mailto:anayegandhi@dewberry.com)  
[www.dewberry.com](http://www.dewberry.com)



# STAND OUT FROM THE REST

## EARN ASPRS CERTIFICATION

ASPRS congratulates these recently Certified and Re-certified individuals:

### RECERTIFIED PHOTOGRAMMETRIST

**Michael Scanlan, Certification #R1531CP**

Effective July 25, 2022, expires July 25, 2027

**Joseph Bartorelli, Certification #R1367CP**

Effective August 7, 2023, expires August 7, 2028

**Christopher Aldridge, Certification #R1163CP**

Effective August 28, 2023, expires August 28, 2028

**Theodore Schall, Certification #R1357CP**

Effective April 7, 2023, expires April 7, 2028

**Craig Sweitzer, Certification #R1633CP**

Effective June 13, 2023, expires June 13, 2028

**Christopher Howell, Certification #R1641CP**

Effective July 10, 2023, expires July 10, 2028

**Sara Reed, Certification #R1634CP**

Effective July 25, 2023, expires July 25, 2028

**Alan Mikuni, Certification #R1127CP**

Effective October 19, 2023, expires October 19, 2028

**Jaime Higgins, Certification #R1635CP**

Effective August 4, 2023, expires August 4, 2028

### RECERTIFIED PHOTOGRAMMETRIST TECHNOLOGIST

**Matthew Peloquin, Certification #R1649PT**

Effective June 19, 2023, expires June 19, 2026

### RECERTIFIED CERTIFIED MAPPING SCIENTIST GIS/LIS

**Luis Ramos, Certification #R202GS**

Effective June 2, 2023, expires June 2, 2028

### RECERTIFIED CERTIFIED MAPPING SCIENTIST LIDAR

**Larry Holtgreive, Certification #R037L**

Effective February 4, 2024, expires February 4, 2029

### RECERTIFIED LIDAR TECHNOLOGIST

**Christian Sovak, Certification #R054LT**

Effective July 17, 2023, expires July 17, 2026

### CERTIFIED LIDAR TECHNOLOGIST

**Travis Gannon, Certification #LT083**

Effective June 17, 2023, expires June 17, 2026

### RECERTIFIED MAPPING SCIENTIST UAS

**Jason Dolf, Certification #R017UAS**

Effective April 19, 2023, expires April 19, 2028

ASPRS Certification validates your professional practice and experience. It differentiates you from others in the profession. For more information on the ASPRS Certification program: contact [certification@asprs.org](mailto:certification@asprs.org), visit <https://www.asprs.org/general/asprs-certification-program.html>.



# GIS Tips & Tricks

By Shira A. Ellenson, YoLani Martin,  
and Al Karlin, Ph.D., CMS-I, GISP

## Making Your Maps more “Mappy Maps”

A cartographer acquaintance of mine once told me that when a map is on a coffee table and no one picks it up to examine, it is just a piece of paper. So, in an effort to help others learn tricks of the trade which draw attention to your map, to follow up on the past two columns on customizing text and colors on your maps, and to continue the theme of “never accepting the defaults”, I asked two experienced map makers/cartographers to share some of the things they use to make their maps more “mappy”. When pushing the art-envelope in cartography, attention to detail can be the difference between a map that sits on the coffee table, a good map, and great one.

### MAP TIP #1—USE DROPSHADOWS TO MAKE POLYGONS POP OUT OF THE PAGE

Take this simple polygon of Gates of the Arctic National Park in northern Alaska (Figure 1). This is the default line symbol and while it does delineate the feature, there is nothing special about the symbology to make a reader pick up the map. By customizing the line symbol, you achieve a look that enhances dimensionality to the area of interest rather than use the default symbology.

To make a more eye-popping boundary:

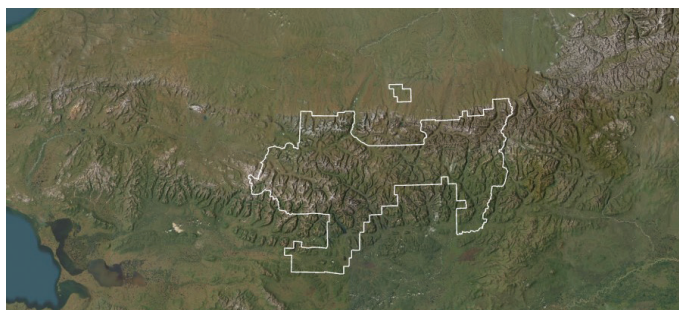


Figure 1. The default boundary polygon symbology for Gates of the Arctic National Park, Alaska.

1. Increase the stroke width and adjust it from “Solid stroke” to “Gradient stroke” (Figure 2)
2. Choose the same two colors as the “start” and “stop” scheme. With the first color selected, under Color Properties, reduce it to 100% transparency
3. Increase the offset to half of the stroke width so it renders on the outside of the polygon

The result is a drop shadow effect (Figure 3) that really makes your area of interest come to life.

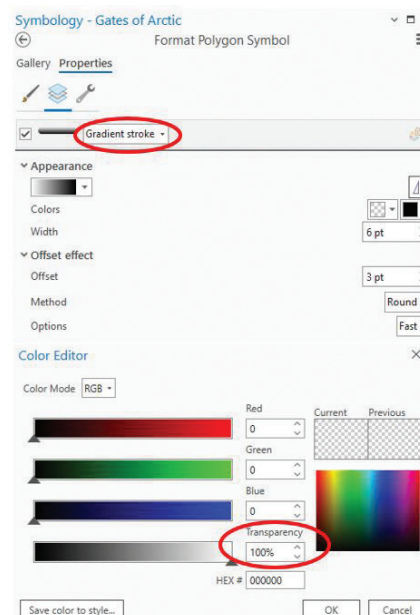


Figure 2. The Format Symbol | Properties dialog box showing the Gradient Fill properties.

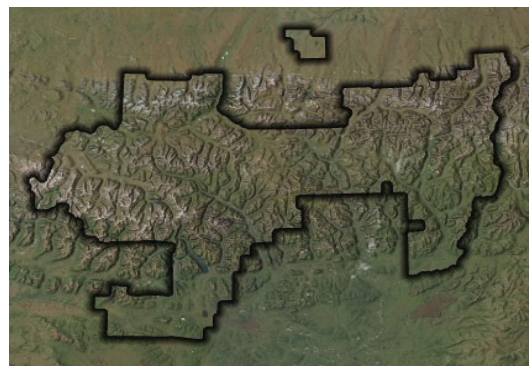


Figure 3. The Gates of the Arctic National Park boundary with customized dropdown shadow effect.

### MAP TIP #2—USE ENHANCED DROP SHADOWS TO MAKE POLYGONS EVEN MORE EFFECTIVE

Take it one step further by using different blend modes! First, adjust the colors of the gradient stroke to go from 100% transparent white to white. Then add a solid fill of 40% gray.

Photogrammetric Engineering & Remote Sensing  
Vol. 89, No. 10, October 2023, pp. 595-597.  
0099-1112/22/595-597

© 2023 American Society for Photogrammetry  
and Remote Sensing  
doi: 10.14358/PERS.89.10.595

With the area of interest selected, under the “Feature Layer” tab on the ribbon (Figure 4), choose “Overlay” as the “Layer Blend”.

This blend mode boost contrasts by taking the lightness and darkness of the underlying layers and blending it with the top layer.

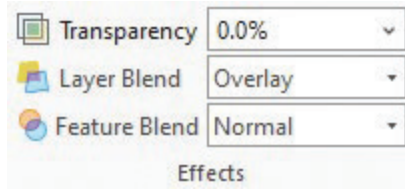


Figure 4. The “Effects” panel on the Feature Layer tab on the ribbon.

The result is a vibrant area of interest with a spotlight effect. The right blend mode is one that you think looks best, ex. Figure 5). Try playing around with different colors, sizes, offsets, and blend modes to achieve different effects!



Figure 5. Modifying the effects with a blend mode gives the area of interest a spotlight.

### MAP TIP #3—MAKE WATER LOOK LIKE WATER

Have you ever wanted to mimic the way light illuminates the surface of a waterbody? By using the same process of customizing symbology with a gradient, you can render basic polygons with an inner glow hack!

1. change your fill from “Solid” to “Gradient” (Figure 6), then
2. choose two colors that

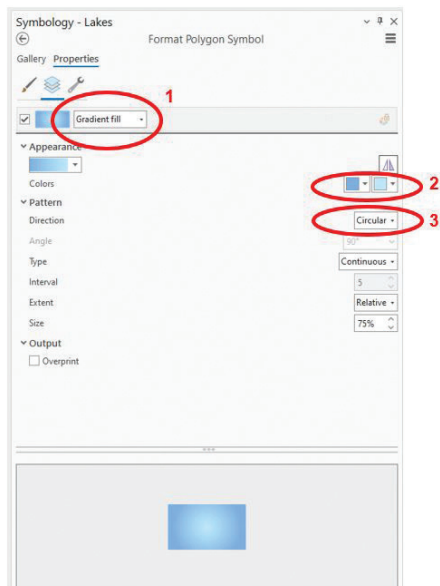


Figure 6. The Format Polygon Symbol | Properties menu showing customizations.

you would like to represent hydrology. I chose “Moorea Blue” (HEX #: 00A9E6) and “Sodalite Blue” (HEX #: BEE8FF) (remember the last month’s color tips).

3. Under “Pattern”, set the Direction to “Circular”, and Type to “Continuous”.

This ensures the gradient radiates in a circular pattern from the center of the polygon, giving the impression of concentric circles of varying colors. A continuous gradient allows for smooth transitions between colors.

The result (Figure 7) is a soft illumination and radiant glow inviting us to jump in!

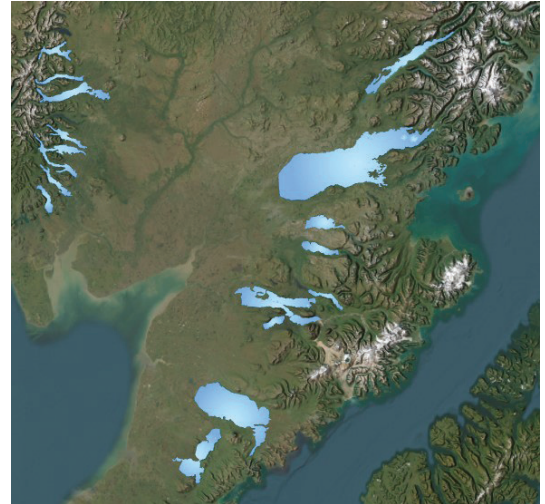


Figure 7. The results of customizing the lake polygon fill symbol with a custom gradient.

### MAP TIP #4—CONTEXT IS EVERYTHING ON A LOCATOR MAP

Shira was recently asked to make a map of Guam. When making the locator map, she realized the area she was working in would not provide much context until the map was really zoomed out to a VERY small scale. Here was an opportunity to use an orthographic projection, where Earth is depicted as a globe.

The only problem is that from this angle (Figure 8), Guam is out of range. To fix this, she had to make a custom coordinate system.

1. under Map Properties, search for “The World from Space” (Figure 9) and
2. set it as the Projected Coordinate System,
3. with the coordinate system selected, right click and select “Copy and Modify”. This will prompt the “Modify Projected Coordinate System” window (Figure 10).
4. adjust the longitude and latitude so the area of interest is repositioned to your liking. Shira chose coordinates that would set Guam to be slightly off-center.



Figure 8. The “default” orthographic project of the earth does not show Guam, the area of interest for the project.

The result is a charming overview globe that gives better reference to the geographic area at large.

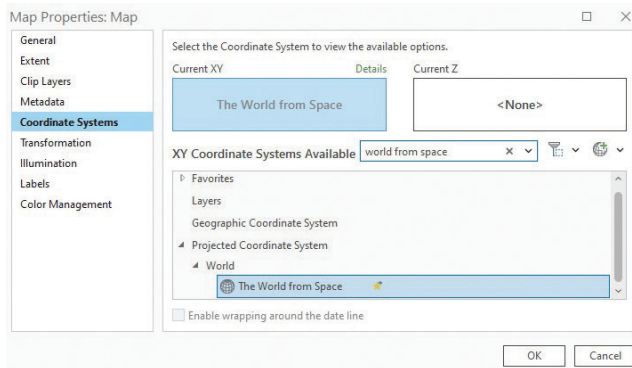


Figure 9. The Map Properties dialog is used to select "The World from Space" as the XY Coordinate System.

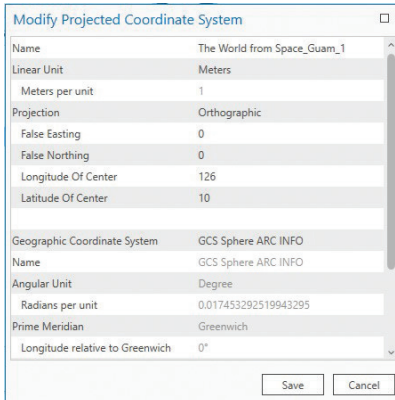


Figure 10. The Modify Project Coordinate System window is used to construct the custom coordinate system.



Figure 11. The custom coordinate system showing the area of interest (Guam) slightly off-center as determined by the cartographer.

### MAP TIP #5—MONOCHROMATIC COLOR THEORY FOR DATA FEATURES

If stumped on what color to select for an individual feature layer's symbology, try using the lighter and darker variations of the feature's base color. This monochromatic approach can provide a variety of color selections and potentially provide more flexibility to a map's overall color scheme.

1. Select the base color that the data will be. In Figure 12 and 14, the base color is Rose Dust (RGB value 215, 158, 158).

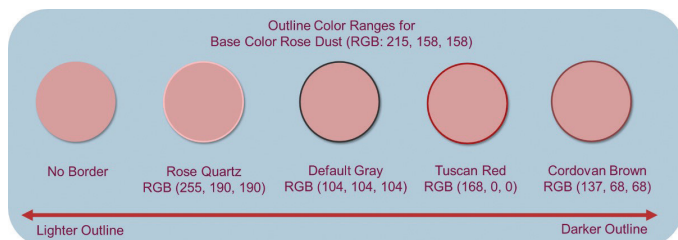


Figure 12. Outline color ranges surrounding the base color of Rose Dust (RGB value 215, 158, 158) where lighter variations of the base color stem to the left and darker variations stem to the right.

Use the color selector tool to find color variations of the base color (this will vary depending on the application being used). If your color selector tool provides default color blocks, focus in on one color range to for shading variations (Figure 13). If your color selector tool provides a color wheel/square (Figure 13), move the selection cursor up and to the left for lighter variations of the base color. Move the selection cursor down and to the right for darker variations of the color.

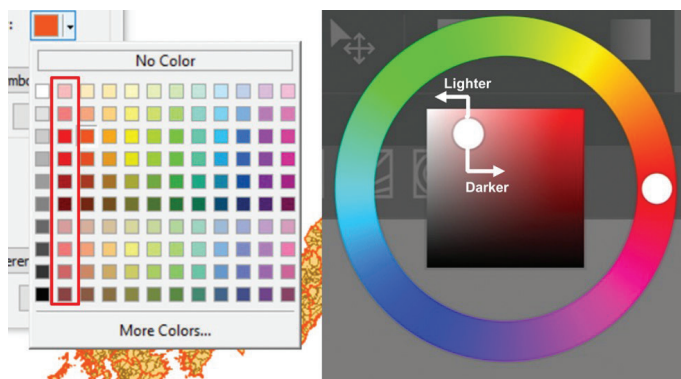


Figure 13. Left image of a color block selection tool from ArcMap Desktop. Right image of a color wheel/square tool from MediBang Paint.

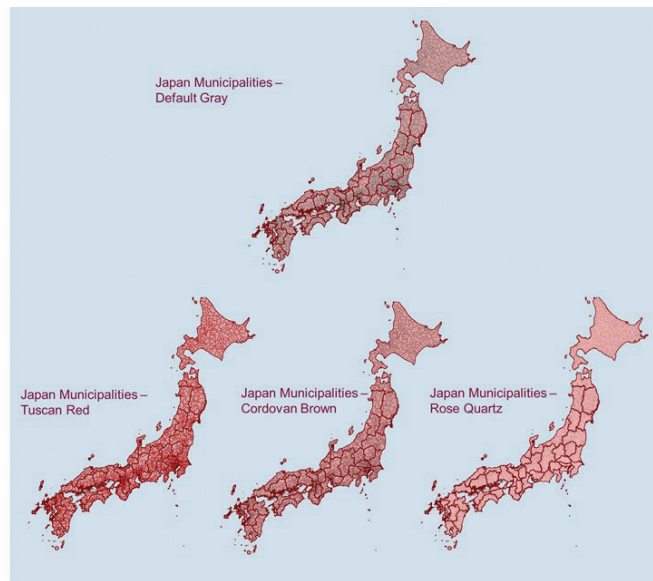


Figure 14. Maps of Japan's municipalities in various outline colors. The top map is in default gray (RGB value 104, 104, 104); bottom left map is in Tuscan Red (RGB value 168, 0, 0); bottom center map is in Cordovan Brown (137, 68, 68); bottom right map is in Rose Quartz (255, 190, 190).

Experiment with the color variations on the data features. In Figure 14, the top map of Japan has a default gray outline surrounding the municipalities feature. Below this, the color variations stemming from the municipalities feature's base color are applied to the outline.

This is a simple trick that can give your data visualizations an extra pop of character or double check if a visualization is accessible for an audience.

Send your questions, comments, and tips to [GISTT@ASPRS.org](mailto:GISTT@ASPRS.org).

*Shira Ellenson is a Senior Geospatial Analyst with Dewberry's Anchorage, AK office. She specializes in remote sensing and cartography. YoLani Martin is a Geospatial Analyst with Dewberry's Fairfax, VA office. She is a resource for open source tools and Python scripting. Al Karlin, Ph.D., CMS-L, GISP is with Dewberry's Geospatial and Technology Services group in Tampa, FL. As a senior geospatial scientist, Al works with all aspects of Lidar, remote sensing, photogrammetry, and GIS-related projects.*

The layman's perspective on technical theory and practical applications of mapping and GIS



# MAPPING MATTERS

YOUR QUESTIONS ANSWERED

by **Qassim Abdullah, Ph.D., PLS, CP**  
Woolpert Vice President and Chief Scientist

- Have you ever wondered about what can and can't be achieved with geospatial technologies and processes?
- Would you like to understand the geospatial industry in layman's terms?
- Have you been intimidated by formulas or equations in scientific journal articles and published reports?
- Do you have a challenging technical question that no one you know can answer?



If you answered “YES” to any of these questions, then you need to read Dr. Qassim Abdullah's column, **Mapping Matters**.

In it, he answers all geospatial questions—no matter how challenging—and offers accessible solutions.

Send your questions to [Mapping\\_Matters@asprs.org](mailto:Mapping_Matters@asprs.org)

To browse previous articles of Mapping Matters, visit <http://www.asprs.org/Mapping-Matters.html>

“Your mapping matters publications have helped us a lot in refining our knowledge on the world of Photogrammetry. I always admire what you are doing to the science of Photogrammetry. Thank You Very much! the world wants more of enthusiast scientists like you.”

“I read through your comments and calculations twice. It is very clear understandable. I am Honored there are experienced professionals like you, willing to help fellow members and promote knowledge in the Geo-Spatial Sciences.”

## YOUR COMPANION TO SUCCESS



## JOURNAL STAFF

### Editor-In-Chief

Alper Yilmaz, Ph.D., PERSeditor@asprs.org

### Associate Editors

Ravishankar Dwivedi, Ph.D., rsdwivedi51@gmail.com

Valérie Gouet-Brunet, Ph.D., valerie.gouet@ign.fr

Petra Helmholz, Ph.D., Petra.Helmholz@curtin.edu.au

Dorota Iwaszczuk, Ph.D., dorota.iwaszczuk@tum.de

Desheng Liu, Ph.D., liu.738@osu.edu

Clement Mallet, Ph.D., clemallet@gmail.com

Sidike Paheding, Ph.D., spahedin@mtu.edu

Norbert Pfeifer, np@ipf.tuwien.ac.at

Rongjun Qin, Ph.D., qin.324@osu.edu

Ribana Roscher, Ph.D., ribana.roscher@uni-bonn.de

Zhenfeng Shao, Ph.D., shaozhenfeng@whu.edu.cn

Filiz Sunar, Ph.D., fsunar@itu.edu.tr

Prasad Thenkabail, Ph.D., pthenkabail@usgs.gov

Dongdong Wang, Ph.D., ddwang@umd.edu

Qunming Wang, Ph.D., wqm11111@126.com

Ruisheng Wang, Ph.D., ruiswang@ucalgary.ca

Jan Dirk Wegner, jan.wegner@geod.baug.ethz.ch

Bo Wu, Ph.D., bo.wu@polyu.edu.hk

Michael Yang, Ph.D., michael.yang@utwente.nl

Hongyan Zhang, zhanghongyan@whu.edu.cn

### Contributing Editors

#### Highlight Editor

Jie Shan, Ph.D., jshan@ecn.purdue.edu

#### Feature Articles

Michael Joos, CP, GISP, featureeditor@asprs.org

#### Grids & Datums Column

Clifford J. Mugnier, C.P., C.M.S., cjmce@lsu.edu

#### Book Reviews

Sagar Deshpande, Ph.D., bookreview@asprs.org

#### Mapping Matters Column

Qassim Abdullah, Ph.D., Mapping\_Matters@asprs.org

#### GIS Tips & Tricks

Alvan Karlin, Ph.D., CMS-L, GISP akarlin@Dewberry.com

#### SectorInsight

Youssef Kaddoura, Ph.D., kaddoura@ufl.edu

Bob Ryerson, Ph.D., FASPRS, bryerson@kimgeomatics.com

Hamdy Elsayed, Hamdy.Elsayed@teledyne.com

### ASPRS Staff

#### Assistant Director — Publications

Rae Kelley, rkelly@asprs.org

#### Electronic Publications Manager/Graphic Artist

Matthew Austin, maustin@asprs.org

#### Advertising Sales Representative

Bill Spilman, bill@innovativemediasolutions.com

## ASPRS APPROVES EDITION 2 OF THE ASPRS POSITIONAL ACCURACY STANDARDS FOR DIGITAL GEOSPATIAL DATA

**The American Society for Photogrammetry and Remote Sensing (ASPRS) is pleased to announce approval of the Positional Accuracy Standards for Geospatial Data, Edition 2, Version 1.0.**

Edition 2, Version 1.0. includes Addendum I: General Best Practices and Guidelines and Addendum II: Best Practices and Guidelines for Field Surveying of Ground Control and Checkpoints. Modifications implemented in Edition 2 respond to evolving technologies and industry needs. The new edition was drafted by ASPRS subject matter experts representing public, private, and academic sectors. Public review was conducted from February 8 – April 30, 2023. Comments were incorporated into the final version adopted on August 23, 2023.

“The new edition of these standards will have a positive impact on our geospatial capabilities and all who benefit from these services here in the United States of America and worldwide for years to come, it is a historical moment that we should all be proud of,” said Dr. Qassim Abdullah, Vice President and Chief Scientist of Woolpert, who led the ASPRS Positional Accuracy Standards Working Group. “We are fortunate to have among our members such talented and willing volunteers who worked hard during the last two years to update this important Standard,” said Lorraine Amenda, ASPRS President.

As the USGS Lidar Base Specifications is well aligned with the ASPRS accuracy standards, users of the 3DEP program will reap the benefits from the modifications introduced in Edition 2. “As our 3DEP Lidar Base Specification is closely aligned with the ASPRS standards, we welcome these updates to the standards introduced in the Second Edition. We hope these updates bring even more clarity to an already well adopted standard on acquiring geospatial data,” said Dr. Michael Tischler, Director, USGS National Geospatial Program.

The most significant changes introduced in this 2nd Edition of the ASPRS Positional Accuracy Standards for Digital Geospatial Data include:

1. Elimination of references to the 95% confidence level as an accuracy measure.
2. Relaxation of the accuracy requirement for ground control and checkpoints.
3. Consideration of survey checkpoint accuracy when computing final product accuracy.
4. Removal of the pass/fail requirement for Vegetated Vertical Accuracy (VVA) for lidar data.
5. Increase the minimum number of checkpoints required for product accuracy assessment from twenty (20) to thirty (30).
6. Limiting the maximum number of checkpoints for accuracy assessment to 120 for large project.

7. Introduction of a new term, “three-dimensional positional accuracy.”
8. Addition of Guidelines and Best Practices Addendums for:
  - a. General Guidelines and Best Practices
  - b. Field Surveying of Ground Control and Checkpoints
  - c. Mapping with Photogrammetry
  - d. Mapping with Lidar
  - e. Mapping with UAS

There are also three additional Addendums listed in the Table of Contents:

- Addendum III: Best Practices and Guidelines for Mapping with Photogrammetry
- Addendum IV: Best Practices and Guidelines for Mapping with Lidar
- Addendum V: Best Practices and Guidelines for Mapping with UAS

These three Addendums will be available for public comment in the coming weeks and will be added to Edition 2, Version 2.0, which ASPRS anticipates approving in late Fall 2023.

The significant changes in Edition 2 are summarized in the Foreword. To download the document, visit <https://publicdocuments.asprs.org/PositionalAccuracyStd-Ed2-V1>.

## CALL FOR PARTICIPATION

### NSRS Modernization Working Group

The Photogrammetric Applications Division of ASPRS is seeking interested community members to engage in the **NSRS Modernization Working Group**.

The National Geodetic Survey is replacing the NAD 83 reference frame and the NAVD 88 datum towards improving the National Spatial Reference System. With these changes, it is essential that the photogrammetry and remote sensing community be prepared to integrate the new reference frames into products and workflows. The NSRS Modernization Working Group seeks to develop and implement plans to support the ASPRS community in this transition.

If you are interested in participating in this working group, please reach out to Dr. Qassim Abdullah Qassim.Abdullah@Woolpert.com or Dr. Ben Wilkinson benew@ufl.edu

### High-Definition Roads Mapping Working Group

The Photogrammetric Applications Division of ASPRS is seeking interested community members to engage in the **HD Roads Mapping Working Group**.

As the development of self-driving cars continues to progress, most automotive manufacturers have recognized the need for highly defined, precise, and accurate geospatial products to support autonomous navigation and steering. These high-definition maps are or can be provided by the ASPRS community and related industry. This working group seeks to engage industry and agencies associated with self-driving cars to identify critical geospatial components, develop national specifications, and to support product generation and standardization.

If you are interested in participating in this working group, please reach out to Dr. Qassim Abdullah Qassim.Abdullah@Woolpert.com or Dr. Ben Wilkinson benew@ufl.edu.

## ASPRS Directory

### Membership/PE&RS Subscription

office@asprs.org

### Conferences

programs@asprs.org

### Certification

applications@asprs.org

### Calendar

calendar@asprs.org

### ASPRS Bookstore

office@asprs.org

### ASPRS Foundation

foundation@asprs.org

### ASPRS Board of Directors

asprsboard@asprs.org

### Student Advisory Council

sac@asprs.org

### Early-Career Professionals Council

ecpc@asprs.org

### Region Officers Council

roc@asprs.org

### Sustaining Members Council

smc@asprs.org

### Technical Division Directors Council

tdcc@asprs.org

PO Box 14713, Baton Rouge, LA 70898 | 225-408-4747, 225-408-4422 (fax), [www.asprs.org](http://www.asprs.org)

## ASPRS Workshop Series

It's not too late to earn Professional Development Hours

Miss one of our Live Online Workshops? You can purchase the workshops now and watch when you are ready!

Check out the workshops offered by visiting <https://asprs.prolearn.io/catalog>

## Ad Index

Dewberry

[www.dewberry.com/](http://www.dewberry.com/)

593

# Mapping Lotus Wetland Distribution with the Phenology Normalized Lotus Index Using SAR Time-Series Imagery and the Phenology-Based Method

Sheng Wang, Taixia Wu, and Qiang Shen

## Abstract

*Lotus wetland is a type of wetland that can efficiently purify water. Therefore, rapid and accurate remote sensing monitoring of the distribution of lotus wetland has great significance to their conservation and the promotion of a sustainable and healthy development of ecosystems. The phenology-based method has proven effective in mapping some different types of wetlands. However, because of the serious absence of remote sensing data caused by cloud coverage and the differences in the phenological rhythms of lotus wetlands in different areas, achieving high-precision mapping of different regions using a unified approach is a challenge. To address the issue, this article proposes a Phenology Normalized Lotus Index (PNLI) model that combines SAR time-series imagery and the phenology-based method. The results of this study demonstrate that the PNL model shows good applicability in different areas and has high mapping accuracy. The model can map the lotus wetland distribution in large areas quickly and simultaneously with high precision.*

## Introduction

An important part of freshwater ecosystems, wetlands have characteristics of both terrestrial and freshwater ecosystems and promote a balance between ecosystems (Colin *et al.* 2018; Seifollahi-Aghmiuni *et al.* 2019). It is renowned for its exceptional purification capabilities, earning it the epithet “the kidney of the earth” (Waltham *et al.* 2019; Kaushalya 2020). Among various types of wetlands, lotus wetland holds particular importance, as it plays a unique role in reducing waterborne pollutants, such as chemical oxygen demand (COD), biochemical oxygen demand (BOD), and ammoniacal nitrogen (Kanabkaew and Puetpaiboon 2004; Jou *et al.* 2008; Abd Rasid *et al.* 2019). Presently, many wetlands in China and other developing countries experience pollution issues, including elevated levels of COD (Chi *et al.* 2020), BOD (Song *et al.* 2006), and ammonia (Teng *et al.* 2017). However, lotus plants in lotus wetlands effectively mitigate these pollutants (Abd Rasid *et al.* 2019). Therefore, obtaining accurate distribution information on lotus wetland vegetation in both time and space holds significant ecological and theoretical significance, as it aids in unraveling the response mechanisms to water environmental factors (Jiang and Xu 2019) while also providing substantial practical value in water pollution control (De Groot *et al.* 2018). Satellite remote sensing, a rapidly evolving technology over the past three decades, has long been extensively employed for mapping vegetation distribution (Skriver 2007; Gholizadeh and Melesse 2017). Consequently, satellite remote sensing technology offers the potential to rapidly and comprehensively

obtain distribution information for lotus wetlands (Fournier *et al.* 2007; Colvin *et al.* 2019).

The phenology-based method offers a valuable approach for mapping the distribution of wetland plants utilizing satellite remote sensing technology. Due to the distinct remote sensing characteristics exhibited by different wetland plant species during phenological stages, this method proves to be feasible for accurately delineating the coverage area of individual wetland vegetation (Wessels *et al.* 2011). By employing multi-temporal optical remote sensing imagery, the phenology-based method generates temporal profiles of remote sensing parameters, enabling the identification of phenological time nodes for each plant species within specific phenological periods. These remote sensing parameters serve as phenological features that, when combined with classification models, facilitate the extraction and mapping of vegetation areas (Dannenberg *et al.* 2020). Notably, previous studies have demonstrated advancements in plant extraction methods based on phenological characteristics, often employing closely related indicators, such as the normalized difference vegetation index (NDVI) or the enhanced vegetation index (EVI), indicative of plant growth conditions (Zhang *et al.* 2022). For example, researchers successfully differentiated between corn, soybean, and tobacco fields in large commercial farms in Africa by utilizing time-series MODIS imagery and NDVI values at phenological time nodes as phenological features (Maguranyanga *et al.* 2015). Another study combined time-series MODIS imagery with ground data to confirm the significant discriminating capability of NDVI-based phenological feature information in distinguishing cotton from corn and sorghum within agricultural landscapes (Sibanda *et al.* 2010). MODIS imagery is a composite observation of Terra and Aqua satellites, providing medium-resolution data. These synthetic satellites enable repeated observations of the entire Earth’s surface within 1–2 days, offering improved temporal resolution accuracy. However, the spatial resolution accuracy of MODIS imagery is limited, with the highest accuracy for plant phenology monitoring being 250 m. Consequently, many scholars opt for high-spatial-resolution remote sensing image data to map plant distributions using phenology-based methods (Xu *et al.* 2018). For example, Chen *et al.* (2014) incorporated the time information of phenological nodes of plants in their study area and employed NDVI and EVI values extracted from *Landsat 8* imagery as phenological features. By combining these features with the maximum likelihood method, they successfully extracted wheat planting areas, demonstrating that EVI combined with the EVI maximum likelihood method (EVI<sub>ML</sub>) outperformed NDVI combined with the maximum likelihood method (NDVI<sub>ML</sub>), achieving mapping accuracy exceeding 85% (Chen *et al.* 2014). Zhang *et al.* (2018) employed the *Landsat 8* time-series curve

Sheng Wang, Taixia Wu, and Qiang Shen are with the School of Earth Sciences and Engineering, Hohai University, Nanjing, China.

Corresponding author: Sheng Wang, wangsh12@hhu.edu.cn

Contributed by Ravi Dwivedi, February 13, 2023 (sent for review May 30, 2023; reviewed by Ajai Ajai, Jai Jai Garg).

Photogrammetric Engineering & Remote Sensing  
Vol. 89, No. 10, October 2023, pp. 601–611.

0099-1112/22/601-611

© 2023 American Society for Photogrammetry  
and Remote Sensing  
doi: 10.14358/PERS.23-00012R2

reconstruction method to capture the unique phenological characteristics of rice. In addition to *Landsat 8*, *Sentinel-2* imagery has also been utilized by scholars to construct time series of normalized vegetation phenology index, enabling the extraction and mapping of mangrove distributions in Zhangjiang Estuary Reserve, Fujian, China (Li *et al.* 2019). Furthermore, researchers such as Immitzer *et al.* (2019) explored the advantages of combining *Sentinel-2* with phenology for multi-type vegetation extraction tasks. By studying five coniferous tree species and seven broad-leaved tree species in central European forests using 18 periods of *Sentinel-2* imagery, they discovered that the average classification accuracy of broad-leaved tree species increased from 72.9% to 85.7% and that the average classification accuracy of coniferous tree species also significantly improved when compared to the best single-temporal classification results.

The current phenology-based methods commonly rely on time-series imagery acquired from optical remote sensing satellites (Faidi *et al.* 2018). However, utilizing these existing methods for mapping lotus wetland distribution presents certain challenges: lotus wetlands are found mainly in regions characterized by monsoon and oceanic climates, which experience frequent cloud cover and rainfall throughout the year. Optical remote sensing satellites are unable to effectively capture ground objects under such cloudy conditions, leading to missing imagery of lotus wetlands during crucial phenological nodes (Ding *et al.* 2020). Consequently, this limitation hampers the accurate determination of phenological time nodes and results in low mapping accuracy. Moreover, lotus wetlands exhibit diverse phenological rhythms across different regions, and employing current phenology-based methods requires precise knowledge of the phenological node dates specific to lotus wetlands in each region. Additionally, mapping accuracy relies on the selection of appropriate remote sensing parameters and classification algorithms, making it challenging to achieve high-precision distribution mapping of lotus wetlands with distinct phenological rhythms in different regions using a unified mapping approach (Ramirez *et al.* 2018). Hence, there is an urgent need for a method capable of accurately mapping lotus wetland distribution with high precision, unaffected by cloudy weather conditions and phenological rhythms.

Co-polarization (VV) and cross-polarization (VH) are widely employed in SAR sensors as common polarization methods. Previous studies have demonstrated that changes in the polarization backscattering coefficients of plants result primarily from variations in canopy structure during plant growth. Given that the key factor for determining phenological time nodes in lotus wetlands is the degree of change in canopy structure and considering that SAR sensor imaging quality remains unaffected by weather conditions (Lee *et al.* 2010) as well as the fact that the imaging time resolution of effective imagery remains unaffected by phenological rhythms, the SAR time-series and the phenology-based method can accurately capture the phenological time nodes of lotus wetlands without losing phenological characteristics. Consequently, the integration of SAR time-series and phenology-based approaches presents a viable solution for mapping the distribution of lotus wetlands.

The goal of this study is to construct a unified method that can overcome the influence of clouds and the phenological rhythms of lotus wetlands in different areas, thus enabling high-precision mapping of the distribution of lotus wetlands in different regions, and this study provides a method for mapping the distribution of lotus wetlands in large regions.

## Study Area

The research area consists of three independent areas (Figure 1): Baiyangdian, Weishan Lake, and Wanmuhetang, China. All of them are in a cloudy monsoon climate area, and the phenological rhythms of lotus wetland in different areas are different:

1. Baiyangdian is located in Hebei Province, China. It is the largest naturally formed freshwater lake with the largest perennial water storage capacity in the North China Plain. The geographical range is 38°43′–39°02′N, 115°38′–116°07′E, with a total area of 366 km<sup>2</sup>. Baiyangdian has an average water depth of 6.5 m and is composed of many lakes and moats of different sizes, including Baiyangzheng Lake, Mapeng Lake, Zaochet Lake, and Shaoche Lake. They are collectively named Baiyangdian (Xie *et al.* 2013). Lotus wetlands in Baiyangdian are the products of the ancient

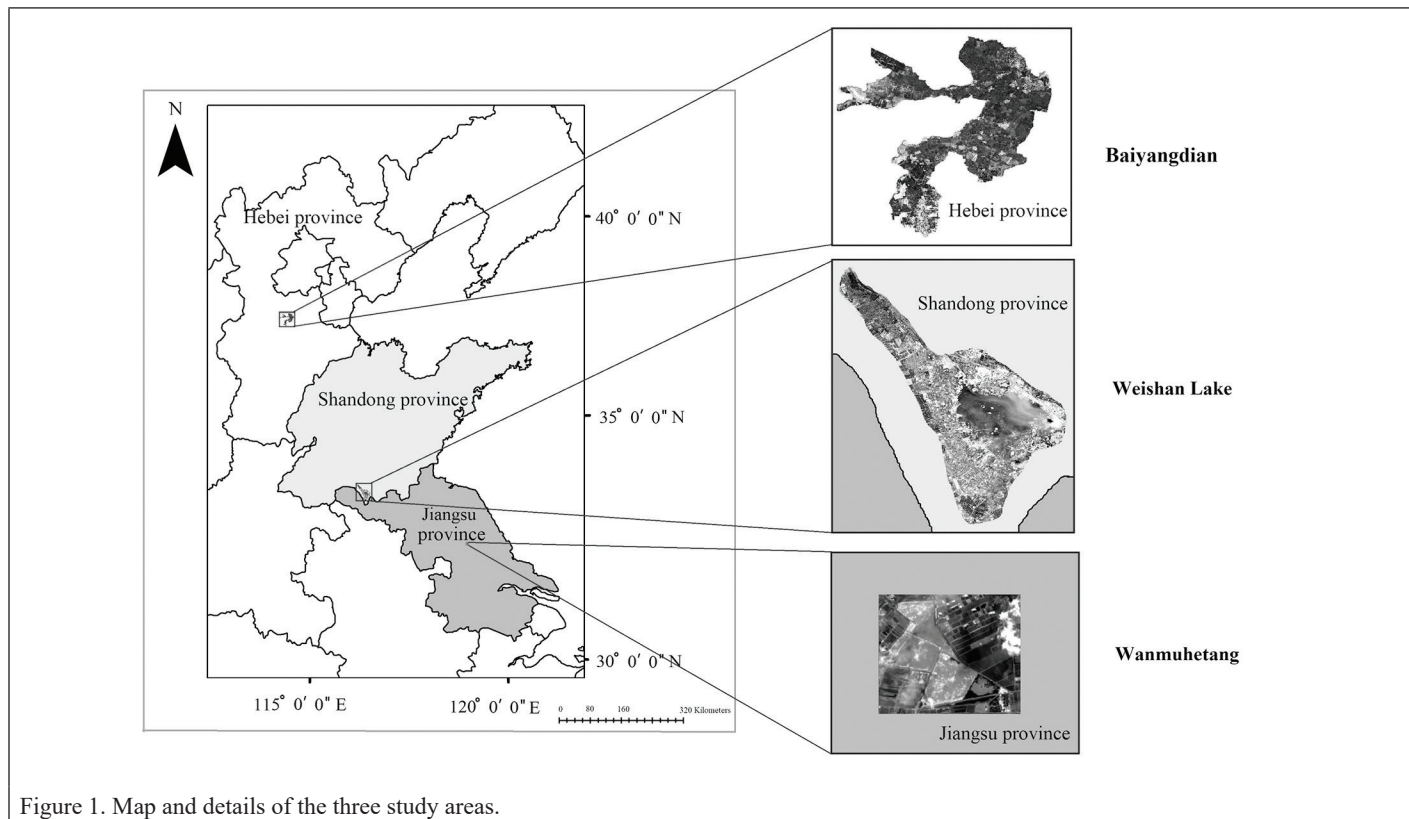


Figure 1. Map and details of the three study areas.

Yellow River flowing through Baiyangdian in the Neolithic Age. It has a long history and tenacious vitality. Lotus wetlands are widely distributed in Baiyangdian.

2. Weishan Lake is located in Shandong Province, in the northwest of Binhu Town, Tengzhou City, China, with a geographical range of 35°2′–35°8′N, 116°49′–116°54′E and a total area of 660 km<sup>2</sup>. The formation of Weishan Lake is the result of the joint action of human activities and crustal movement. The average water depth is 1.5 m, which belongs to shallow-water lakes. Weishan Lake lotus wetland is part of the local freshwater herbaceous swamp wetland ecosystem, distributed mainly in the lake area with a deep water level (Miao and Ju 2020).
3. The Wanmuhetang is located in Xinghua City, Jiangsu Province, China. It is one of the famous natural and artificial lotus wetlands in China. The geographical range is 33°04′–33°06′N, 119°42′–119°44′E, with a total area of 9 km<sup>2</sup>, artificial lotus pond wetlands of 0.8 km<sup>2</sup>, and an average water depth of 2 m. The Wanmuhetang is dominated by lotus wetland land use type, which creates excellent ecological conditions for the growth of lotus leaves. The Wanmuhetang consists of three areas: Wujindang, Xumahuang, and Dazong Lake. Lotus wetlands are distributed in these three areas.

## Data

The data utilized in this study encompassed Sentinel-1A SAR time-series imagery and sample points acquired through field investigations. Specifically, the Sentinel-1A SAR time-series image data were collected for three distinct study areas during 2021, 2020, and 2017, respectively. Notably, the sample points from Baiyangdian were employed for model development and accuracy assessment, while the sample points from the other two research areas were solely utilized for obtaining phenological nodes and conducting accuracy verification of lotus wetland. Consequently, the number of sample points collected from Baiyangdian significantly surpassed those gathered from Weishan Lake and Wanmuhetang.

### Sentinel-1A SAR Data

The Sentinel-1A satellite is an artificial satellite designed by the European Space Agency and Italy's Thales Alenia Space Company for better Earth observation (Guccione *et al.* 2015). It was successfully launched at the French Guiana Cosmodrome in April 2014 and operated in a near-polar sun-synchronous orbit at a height of 693 km, with a design life of 7 years (Carreño and Muñoz 2019). The Sentinel-1A satellite carries a C-band synthetic aperture radar sensor developed by Astrium, as were the European Remote Sensing Satellite and the Environmental Satellite, which have the advantage that imaging is not affected by weather conditions and the repetition period is 12 days (Felegari *et al.* 2021). It has the characteristics of all-day and all-weather imaging and provides a wealth of C-band radar data for land and ocean monitoring (Li *et al.* 2021).

The acquired Sentinel-1A data consist of GRD-type SAR image data, all of which are in the oblique distance projection coordinate system. However, this coordinate system is not optimal for subsequent analysis. Therefore, it is necessary to convert these temporal GRD images into the geographic coordinate system (Zhang *et al.* 2020). Additionally, the pixel values in SAR images do not directly reflect the actual backscattering intensity of ground objects, necessitating preprocessing of the SAR imagery. In this study, software specifically designed for preprocessing Sentinel-1A GRD images was employed to convert the images into backscatter coefficient images in the geographic coordinate system (Giordano *et al.* 2020). The preprocessing procedure involved orbit correction, thermal noise removal, speckle noise filtering, radiometric calibration, terrain correction, and geocoding.

### Sample Point Data

In addition to acquiring SAR backscatter coefficient image data from Sentinel-1A, sample point data were obtained through field surveys in the study area. A portable handheld GPS device was used to record the object types and location information of the sample points in the

three study areas. In the Baiyangdian research area, the sample points served both modeling and verification purposes. A total of 436 sample points were collected for lotus wetlands during the field investigation. Additionally, sample points were collected for non-lotus wetlands, including reeds, rice, buildings, water bodies, and other five types of features, with 206 sample points for each feature type. The sample point data obtained in Weishan Lake and Wanmuhetang were used solely for accuracy verification, resulting in a lower number of sample points collected compared to the Baiyangdian area. In Weishan Lake, 205 sample points were collected for both lotus wetlands and non-lotus wetlands, while in Wanmuhetang, 212 sample points were collected for both lotus wetlands and non-lotus wetlands. All the sample point data were divided into two sets: the training set SET<sub>1</sub> for model building and the test set SET<sub>2</sub> for accuracy verification. The ratio of the training set to the verification set was 1:1 (Kussul *et al.* 2016). Consequently, 218 lotus wetland sample points and 515 non-lotus wetland sample points were randomly selected for building the model and classified into SET<sub>1</sub>. The remaining sample points were used to verify the model's accuracy and classified into SET<sub>2</sub>.

## Methods

In this study, the method flow (Figure 2) used was divided into several steps. First, after preprocessing the SAR image data and collecting the sample point data, the phenology of lotus wetlands from the backscattering time-series characteristics were analyzed, and the SPP time-series fitting method was used to extract the phenological node date from the SAR backscattering coefficient time series. Then, using the Bhattacharyya distance as a parameter, the optimal phenological feature combination and polarization type was selected, and the PNLI model was constructed. Finally, use the PNLI model was used to carry out lotus wetland extraction experiments and verify its mapping accuracy in the three research areas.

### Analysis of Phenological Characteristics of SAR Backscattering Time Series in Lotus Wetlands

The location information of each object type sample point in SET<sub>1</sub> with software was read, and the backscatter coefficient time-series

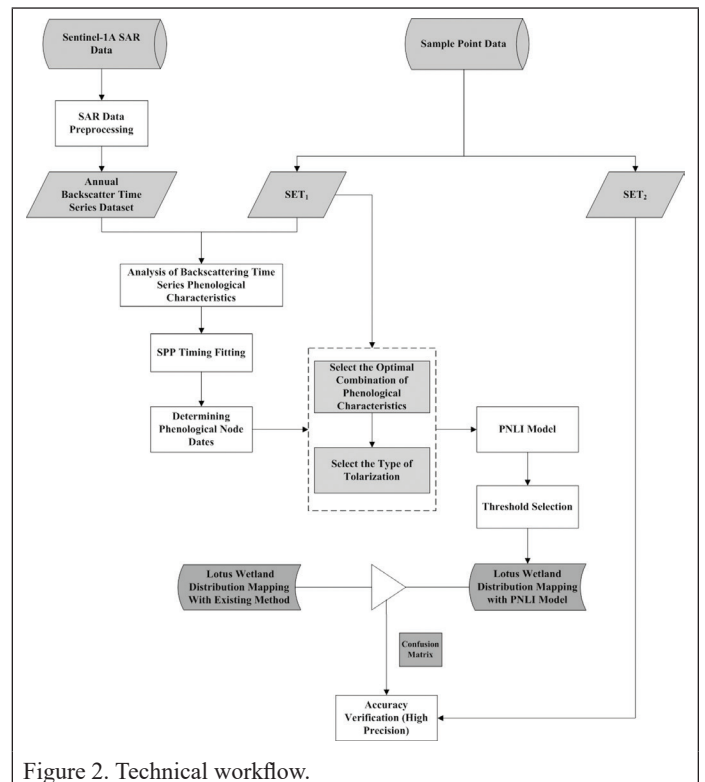


Figure 2. Technical workflow.

data of the VV polarization and VH polarization SAR at the locations were obtained. In these data, 10 sample points of each type of ground feature were randomly selected, and the average backscatter coefficient of the 10 sample points was calculated. Since it is the average value, the influence of random errors can be reduced to compare the time series of different ground features and accurately analyze the time-series backscattering characteristics of lotus wetlands.

After analyzing the data, the phenology of lotus wetlands was divided into five distinct stages: budding stage, leaf spreading stage, mature stage, leaf wilting stage, and dormant stage. The phenological characteristics of the time series were examined, and Table 1 presents the phenological time range of local lotus wetlands in Baiyangdian based on our investigation. Furthermore, Figure 3 showcases the time-series curves of the average backscatter coefficient for 10 sample points in the Baiyangdian area under VV and VH polarizations. The figure also depicts the phenology of lotus wetlands, with VV polarization represented by a solid line and VH polarization by a dotted line.

In Figure 3, the phenological traits of lotus wetlands are clearly evident. During the dormant and budding periods, the backscatter coefficient remains low. This is because, during the dormant period, lotus wetlands do not cover the water surface, leading to a low backscattering signal captured by SAR imagery. In contrast, during the leaf spreading, mature, and leaf wilting stages, unfolded lotus wetlands partially cover the water surface, resulting in a higher backscatter coefficient. Specifically, the backscatter coefficient of lotus wetlands exhibits a noticeable upward trend during the leaf spreading stage, while in the leaf wilting stage, a clear downward trend in backscatter coefficient is observed.

Table 1. Time range of lotus wetland phenology in Baiyangdian.

Lotus Wetland Phenology	Range of Time
Dormancy	November–December
Budding	January–March
Leaf development	April–June
Maturity	July–August
Leaf withering	September–October

### Method for Determining the Dates of Phenological Nodes of Lotus Wetlands

There are multiple time-phase SAR images in each phenological stage of lotus wetlands. It is necessary to determine the node date in each phenological stage. The SAR backscatter coefficient of the date represents the phenology of the corresponding phenological stage feature. In this study, we used the method based on smooth piecewise polynomial (SPP) fitting to determine the phenological node date of lotus wetlands and calculated the important vegetation phenological periods based on the detected maximum, minimum, and inflection points. For important nodes (Rodrigues *et al.* 2012), considering the characteristics of lotus wetland phenology itself, we used the method based on the two-section three-order SPP fitting time-series backscatter coefficient to determine the date of the lotus wetland phenology node. The fitting model is

$$x_1(t_i^{(1)}) = \sum_{j=0}^3 \beta_j^{(1)} \left( \frac{t_i^{(1)}}{t_0} \right)^j, 1 \leq t_i^{(1)} \leq t_0 \quad (1)$$

$$x_2(t_i^{(2)}) = \sum_{j=0}^i \beta_j^{(2)} (t_i^{(2)})^j, t_0 \leq t_i^{(2)} \leq n$$

where  $x_1(t_i^{(1)})$  and  $x_2(t_i^{(2)})$  represent the time points in the first time segment and the second time segment, respectively;  $\beta$  is the fitting parameter;  $t_0$  is the time segment point; and  $n$  is the time end point;  $t_0$  is usually selected as  $3n/4$ . The least squares method is used to solve the fitting parameter  $\beta$  in the fitting model, and it can be derived at  $t_0$  to construct a regression model with constraints

$$\sum_{i=1}^{t_0} (x_1(t_i^{(1)}) - x_i^{(1)})^2 + \sum_{i=t_0}^n (x_2(t_i^{(2)}) - x_i^{(2)})^2 \quad \min \quad (2)$$

s.t.  $x_1(t_0) = x_2(t_0)$   
 $x_1'(t_0) = x_2'(t_0)$

where  $x_i^{(1)}$  and  $x_i^{(2)}$  represent the time points in the first time segment  $t_i^{(1)}$  and the second time segment  $t_i^{(2)}$  backscatter coefficient value, respectively. Then

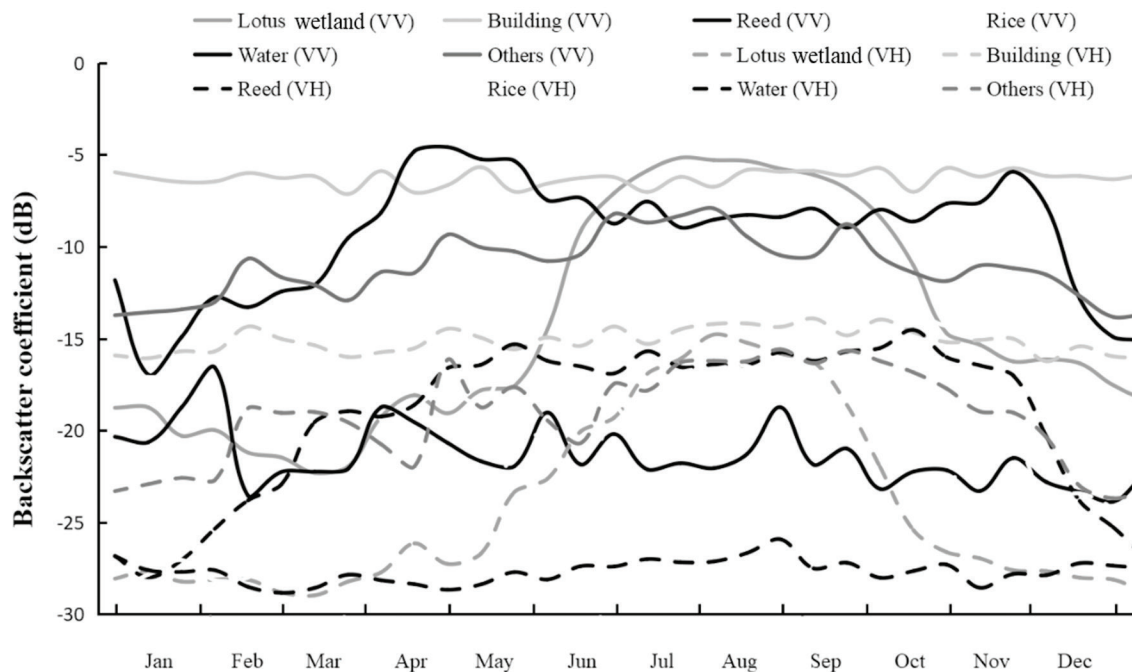


Figure 3. SAR backscattering time series curves.

$$T_k = \begin{pmatrix} (t_1^{(k)})^3 & (t_1^{(k)})^2 & t_1^{(k)} & 1 \\ (t_2^{(k)})^3 & (t_2^{(k)})^2 & t_2^{(k)} & 1 \\ \vdots & \vdots & \vdots & \vdots \\ (t_n^{(k)})^3 & (t_n^{(k)})^2 & t_n^{(k)} & 1 \end{pmatrix}, x_k = \begin{pmatrix} x_1^{(k)} \\ x_2^{(k)} \\ \vdots \\ x_n^{(k)} \end{pmatrix}, \beta_k = \begin{pmatrix} \beta_1^{(k)} \\ \beta_2^{(k)} \\ \beta_3^{(k)} \\ \beta_4^{(k)} \end{pmatrix}, \quad (3)$$

$$z_k = (T_k)', q_k = \left[ (T_k)' \right]', \hat{\beta}_k = (T_k^T T_k)^{-1} T_k^T x_k,$$

where  $k = 1, 2$ . According to the Lagrange multiplier method, the formula for solving the fitting coefficient of SPP is obtained as follows:

$$\begin{aligned} \beta_1 &= \hat{\beta}_1 - (T_1^T T_1)(\lambda z_1 + \mu q_1) \\ \beta_2 &= \hat{\beta}_2 - (T_2^T T_2)(\lambda z_2 + \mu q_2) \end{aligned} \quad (4)$$

where

$$\lambda = \frac{A_2 D_1 - A_1 D_2}{C_2 D_1 - C_1 D_2}, \mu = \frac{C_1 A_2 - C_2 A_1}{C_1 D_2 - C_2 D_1}, \quad (5)$$

$$A_1 = z_1^T \hat{\beta}_1 - z_2^T \hat{\beta}_2, A_2 = q_1^T \hat{\beta}_1 - q_2^T \hat{\beta}_2, B_1 = (T_1^T T_1)^{-1}, B_2 = (T_2^T T_2)^{-1},$$

$$C_1 = z_1^T B_1 z_1 + z_2^T B_2 z_2, C_2 = q_1^T B_1 z_1 + q_2^T B_2 z_2, D_1 = z_1^T B_1 q_1 + z_2^T B_2 q_2,$$

$$D_2 = q_1^T B_1 q_1 + q_2^T B_2 q_2,$$

where  $\beta_1$  is the fitting coefficient of the first time segment and  $\beta_2$  is the fitting coefficient of the second time segment, both of which are four-dimensional vectors. Compared with VH polarization, VV polarization has a lower signal-to-noise ratio (Pang *et al.* 2014), so the time-series backscattering coefficients under VV polarization of lotus wetland sample points are used as the original data to be fitted by SPP, and the time interval between each data point is 12 days (Paek *et al.* 2020). In this study, the phenological node of lotus wetland was determined through the following steps:

Step 1: At the 3n/4 segmentation point, divide the original data into two time segments according to time and use the two-segment third-order SPP method to calculate the fitting coefficients  $\beta_1$  and  $\beta_2$ .

Step 2: Calculate the maximum value point, minimum value point, and inflection point of each fitting polynomial.

Step 3: Determine the each phenological node according to the calculated maximum point, minimum point, and inflection point. The minimum point, inflection point, and maximum point of the fitted polynomials in the first stage were determined to be the nodes of the budding, leaf development, and maturity stages, respectively. The inflection point and the minimum point of the second stage fitting polynomial are determined as the nodes of the wilting stage and the dormant stage, respectively.

Step 4: Select the imaging date of the SAR image closest to each lotus wetland phenological node in terms of imaging time as the phenological node date of the lotus wetland.

### Construction of PNLI Model

The backscatter coefficient value sigma is transformed by the following formula and mapped to the parameter t:

$$t = \ln \left( \frac{\text{Sigma}}{100} + 2 \right) \quad (6)$$

Lotus wetland phenology can be categorized into two types: W type and S type. The W type encompasses the germination period and dormancy period, while the S type includes the leaf spreading period,

mature period, and leaf wilting period. To capture the distinctions in backscatter coefficients across these phenological periods, we have developed a calculation formula for the parameter  $h$  specifically designed for structurally protruding lotus leaf wetland:

$$h = \frac{\ln \left( \frac{\text{Sigma}_s}{100} + 2 \right)}{\ln \left( \frac{\text{Sigma}_w + \text{Sigma}_{\min}}{200} + 2 \right)} \quad (7)$$

The cumulative distribution function transformation of the semilogistic distribution is performed on the parameter  $h$  (Jeon *et al.* 2020):

$$f(h) = \frac{1 - e^{-h}}{1 + e^{-h}} \quad (8)$$

After sorting out, the calculation formula of the PNLI model is obtained:

$$\text{PNLI} = \frac{1 - \left( \frac{\text{Sigma}_s}{100} + 2 \right)^{\ln^{-1} \left( \frac{\text{Sigma}_w + \text{Sigma}_{\min}}{200} + 2 \right)^{-1}}}{1 + \left( \frac{\text{Sigma}_s}{100} + 2 \right)^{\ln^{-1} \left( \frac{\text{Sigma}_w + \text{Sigma}_{\min}}{200} + 2 \right)^{-1}}} \quad (9)$$

Among them,  $\text{Sigma}_w$  is the backscattering coefficient value of the surface object at the W-type phenological node date,  $\text{Sigma}_s$  is the backscattering coefficient value of the surface object at the S-type phenological node date, and  $\text{Sigma}_{\min}$  is the lowest backscattering coefficient value of the surface object in the whole time series. The calculation of phenological node dates is obtained by the above-mentioned method based on SPP fitting. The PNLI model uses the cumulative distribution function of the semilogistic distribution for normalized numerical processing, so the numerical range of the PNLI model is between 0 and 1, which is used to improve the speed and convenience of data processing (Kussul *et al.* 2016).

### Three Polarization PNLI Models

According to the different types of polarization data used, three kinds of polarization PNLI models are set: PNLI models based on VV polarization, VH polarization, and dual polarization, which are represented by  $\text{PNLI}_{\text{VV}}$ ,  $\text{PNLI}_{\text{VH}}$ , and  $\text{PNLI}_{\text{DP}}$ , respectively, according to the following formula:

$$\text{PNLI}_{\text{VV}} = \frac{1 - \left( \frac{\text{Sigma}_{\text{s-VV}}}{100} + 2 \right)^{\ln^{-1} \frac{200}{\text{Sigma}_{\text{w-VV}} + \text{Sigma}_{\text{min-VV}} + 400}}}{1 + \left( \frac{\text{Sigma}_{\text{s-VV}}}{100} + 2 \right)^{\ln^{-1} \frac{200}{\text{Sigma}_{\text{w-VV}} + \text{Sigma}_{\text{min-VV}} + 400}}} \quad (10)$$

$$\text{PNLI}_{\text{VH}} = \frac{1 - \left( \frac{\text{Sigma}_{\text{s-VH}}}{100} + 2 \right)^{\ln^{-1} \frac{200}{\text{Sigma}_{\text{w-VH}} + \text{Sigma}_{\text{min-VH}} + 400}}}{1 + \left( \frac{\text{Sigma}_{\text{s-VH}}}{100} + 2 \right)^{\ln^{-1} \frac{200}{\text{Sigma}_{\text{w-VH}} + \text{Sigma}_{\text{min-VH}} + 400}}} \quad (11)$$

$$\text{PNLI}_{\text{DP}} = \frac{1 - \left( \frac{\text{Sigma}_{\text{s-VV}} + \text{Sigma}_{\text{s-VH}}}{200} + 2 \right)^{\ln^{-1} \frac{400}{\text{Sigma}_{\text{w-VV}} + \text{Sigma}_{\text{w-VH}} + \text{Sigma}_{\text{min-VV}} + \text{Sigma}_{\text{min-VH}} + 800}}}{1 + \left( \frac{\text{Sigma}_{\text{s-VV}} + \text{Sigma}_{\text{s-VH}}}{200} + 2 \right)^{\ln^{-1} \frac{400}{\text{Sigma}_{\text{w-VV}} + \text{Sigma}_{\text{w-VH}} + \text{Sigma}_{\text{min-VV}} + \text{Sigma}_{\text{min-VH}} + 800}}} \quad (12)$$

$\text{Sigma}_{\text{w-VV}}$  and  $\text{Sigma}_{\text{w-VH}}$  are the VV and VH polarization backscatter coefficient values of ground objects at W-type phenological node dates, respectively;  $\text{Sigma}_{\text{s-VV}}$  and  $\text{Sigma}_{\text{s-VH}}$  are the values of ground

objects at S-type phenological node dates VV and VH polarization backscatter coefficient values, respectively; and  $\text{Sigma}_{\text{min-VV}}$  and  $\text{Sigma}_{\text{min-VH}}$  are the minimum backscatter coefficient values of VV and VH polarization of ground objects in the whole time series, respectively.

#### Selection of Optimal PNLI Model

The S-type and W-type periods in the formulas of the three polarization PNLI models encompass multiple phenological periods. To create the phenological feature combination for each polarization PNLI model, it is necessary to select one phenological period from both the S-type and the W-type period. The optimal PNLI model is then determined based on the chosen feature combination and polarization. For each polarized PNLI model, there are six possible combinations of phenological features. To facilitate distinction, superscript numbers 1 to 6 are used to denote different feature combinations. The expressions for the different combinations of phenological characteristics in the three polarized PNLI models ( $\text{PNLI}_{\text{VV}}$ ,  $\text{PNLI}_{\text{VH}}$ , and  $\text{PNLI}_{\text{DP}}$ ) are presented in Table 2.

The criterion for selecting the combination of phenological features is the maximum separability, and the separability is measured by the Bhattacharyya distance between lotus wetlands and another class pair composed of ground features. The calculation formula of Bhattacharyya distance is as follows:

$$B = \frac{1}{8} (\mu_L - \mu_A)^2 \frac{2}{S_L + S_A} + \frac{1}{2} \ln \left( \frac{S_L + S_A}{2\sqrt{S_L S_A}} \right) \quad (13)$$

Among them,  $\mu_L$  and  $\mu_A$  represent the mean value of the PNLI value of lotus wetlands and another type of ground feature, respectively, and  $S_L$  and  $S_A$  represent the variance of the PNLI value of lotus wetlands and another type of ground feature, respectively. These mean and variance parameters are obtained through statistical calculations. Lotus wetlands and the other five types of features constitute five class pairs: lotus wetland—building, lotus wetland—reed, lotus wetland—rice, lotus wetland—water, and lotus wetland—others. For the same class pair, the larger the Bhattacharyya distance  $B$ , the better the separability

Table 2. Expression of different combinations of phenological features for three polarized PNLI models.

PNLI Polarization Type	Combination of Phenological Characteristics		Expression
	S-Type Phenological Period	W-Type Phenological Period	
$\text{PNLI}_{\text{VV}}$	Leaf development	Budding	$\text{PNLI}_{\text{VV}}^1$
	Maturity	Budding	$\text{PNLI}_{\text{VV}}^2$
	Leaf withering	Budding	$\text{PNLI}_{\text{VV}}^3$
	Leaf development	Dormancy	$\text{PNLI}_{\text{VV}}^4$
	Maturity	Dormancy	$\text{PNLI}_{\text{VV}}^5$
	Leaf withering	Dormancy	$\text{PNLI}_{\text{VV}}^6$
$\text{PNLI}_{\text{VH}}$	Leaf development	Budding	$\text{PNLI}_{\text{VH}}^1$
	Maturity	Budding	$\text{PNLI}_{\text{VH}}^2$
	Leaf withering	Budding	$\text{PNLI}_{\text{VH}}^3$
	Leaf development	Dormancy	$\text{PNLI}_{\text{VH}}^4$
	Maturity	Dormancy	$\text{PNLI}_{\text{VH}}^5$
	Leaf withering	Dormancy	$\text{PNLI}_{\text{VH}}^6$
$\text{PNLI}_{\text{DP}}$	Leaf development	Budding	$\text{PNLI}_{\text{DP}}^1$
	Maturity	Budding	$\text{PNLI}_{\text{DP}}^2$
	Leaf withering	Budding	$\text{PNLI}_{\text{DP}}^3$
	Leaf development	Dormancy	$\text{PNLI}_{\text{DP}}^4$
	Maturity	Dormancy	$\text{PNLI}_{\text{DP}}^5$
	Leaf withering	Dormancy	$\text{PNLI}_{\text{DP}}^6$

between the class pairs. For the PNLI with the same polarization but different combinations of phenological characteristics, the greater the number of maximum Bhattacharyya distances between class pairs, the better the discrimination effect on lotus wetlands. Therefore, we made the combination that results in the highest number of maximum Bhattacharyya distances as the optimal combination of phenological features for this kind of polarized PNLI models. After determining the optimal combination of phenological features for each polarized PNLI model, the minimum Bhattacharyya distance values in each polarized PNLI model were compared, and the model with the largest value was selected as the optimal polarized PNLI model.

#### Threshold Selection and Accuracy Verification

Selecting an appropriate mapping threshold is a crucial aspect of the mapping process (Rosin 1998; Rosin and Loannidis 2003). In this study, the extraction method for lotus wetlands in PNLI of the three study areas employs the sliding interquartile range method. This threshold selection method does not rely on the assumption of normal distribution for the sample data of lotus wetlands. The key step in determining the threshold for the sliding interquartile range method is to calculate the median  $M$ , lower quartile ( $Q_1$ ), and upper quartile ( $Q_2$ ) of the PNLI values for lotus wetland. The upper and lower boundaries of the threshold are defined as  $M + 1.5(Q_2 - Q_1)$  and  $M - 1.5(Q_2 - Q_1)$ , respectively. Ground features with PNLI values falling between the upper boundary value and lower than the lower boundary value are identified as lotus wetlands.

To verify the accuracy of the mapping results for the distribution of lotus wetlands, we utilized the  $\text{SET}_2$  sample data as the verification data. A confusion matrix is established based on the mapping outcomes in the three research areas. User accuracy and producer accuracy are computed from the confusion matrix, and the overall accuracy serves as an indicator for accuracy verification. A higher overall accuracy value indicates a better mapping performance for lotus wetland distribution.

## Results

### Select the Optimal Combination of Phenological Characteristics

The optimal combination of phenological periods has been determined for each polarized PNLI model, and the selection methodology for the optimal combination of phenological features was detailed previously. Utilizing  $\text{SET}_1$  as the sample data, we calculated the Bhattacharyya distance between each pair of classes for every different combination of phenological characteristics. By observing the combination of phenological features where the largest Bhattacharyya distance occurred for each class pair, we determined the number of class pairs associated with the largest Bhattacharyya distance in each combination of phenological characteristics. Finally, we identified the phenological period combination corresponding to the highest value among these counts as the optimal selection for the phenological period combination. Tables 3–5 present the Bhattacharyya distances between different class pairs of  $\text{PNLI}_{\text{VV}}$ ,  $\text{PNLI}_{\text{VH}}$ , and  $\text{PNLI}_{\text{DP}}$  under various combinations of phenological periods. These tables highlight the variations in Bhattacharyya distances for different class pairs across the different phenological period combinations.

According to the analysis of Tables 3–5, select the PNLI model with the optimal combination of phenology. For  $\text{PNLI}_{\text{VV}}$ , the maximum Bhattacharyya distance values are 1.681, 2.678, 2.986, 5.552, and 2.303, respectively, and four of them appear in the  $\text{PNLI}_{\text{VV}}^2$  composed of the second phenological period combination. In other words, compared to  $\text{PNLI}_{\text{VV}}^1$ ,  $\text{PNLI}_{\text{VV}}^3$ ,  $\text{PNLI}_{\text{VV}}^4$ ,  $\text{PNLI}_{\text{VV}}^5$ , and  $\text{PNLI}_{\text{VV}}^6$ , the class pair with the largest Bhattacharyya distance value has the largest number; therefore,  $\text{PNLI}_{\text{VV}}^2$  with the second phenological period combination is selected as  $\text{PNLI}_{\text{VV}}$ . For the  $\text{PNLI}_{\text{VH}}$  model, the maximum Bhattacharyya distance values of lotus wetland—reed and lotus wetland—rice appear in  $\text{PNLI}_{\text{VH}}^4$  and  $\text{PNLI}_{\text{VH}}^5$ , respectively, and the maximum Bhattacharyya distance values of the other three class pairs all appear in  $\text{PNLI}_{\text{VH}}^1$ . Therefore, compared with  $\text{PNLI}_{\text{VH}}^1$ ,  $\text{PNLI}_{\text{VH}}^2$ ,  $\text{PNLI}_{\text{VH}}^3$ ,



PNLI<sup>4</sup><sub>VH</sub>, and PNLI<sup>5</sup><sub>VH</sub>, PNLI<sup>5</sup><sub>VH</sub> has the largest number of class pairs with the largest Bhattacharyya distance value; that is, PNLI<sup>5</sup><sub>VH</sub> with the fifth phenological period combination is selected as PNLI<sub>VH</sub>. For PNLI<sub>DP</sub>, the number of class pairs with the largest Bhattacharyya distance value in PNLI<sup>2</sup><sub>DP</sub> reaches four, which is obviously far more than the PNLI<sub>DP</sub> of the other four phenological period combinations. Therefore, PNLI<sup>2</sup><sub>DP</sub> is selected as PNLI<sub>DP</sub>.

### Selecting the Optimal Polarized PNLI Model

Table 6 shows the Bhattacharyya distance values of each class pair in PNLI models with different polarizations. The minimum Bhattacharyya distance values in each PNLI model are shown in bold. It can be seen that compared with PNLI<sub>VV</sub> and PNLI<sub>VH</sub>, PNLI<sub>DP</sub> has the largest minimum Bhattacharyya distance value, so we finally chose the PNLI<sub>DP</sub> as the PNLI model.

### Mapping of Lotus Wetland Distribution Using the PNLI Model

Figure 4 presents the distribution of the PNLI model values of lotus wetlands and different ground features. It is evident that lotus wetlands exhibit the highest median value among all ground features, with minimal overlap between lotus wetlands and the other five features. Moreover, the upper limit of lotus wetlands exceeds the maximum PNLI value of the other five ground features, except for lotus wetland itself. Consequently, when employing the PNLI model for lotus wetland mapping, only the lower boundary of the threshold needs to be determined using the sliding quartile method. Features with PNLI values surpassing this lower boundary are considered lotus wetlands.

In the drawing of lotus wetland distribution in the Baiyangdian research area, the ground features in the whole area are divided into two categories: one is the extracted lotus wetlands, and the other is all the ground features except lotus wetlands (a non-lotus wetlands). Based on the proposed PNLI model, the distribution mapping results of Baiyangdian lotus wetland are shown in Figure 5. The mapping results show that the Baiyangdian lotus wetland is distributed mainly in the west and north of Baiyangdian, which is consistent with the actual situation obtained through field investigations. Consistently, in particular, lotus wetlands located in the west and north of Baiyangdian were completely extracted.

In addition to the Baiyangdian research area, there are two other research areas in this study: Weishan Lake and Wanmuhetang. Due to the different climate types, the phenological rhythms of Weishan Lake and Wanmuhetang are different from those of Baiyangdian, and the phenological rhythms between them are also different. The proposed PNLI model was used to map the distribution of lotus wetlands in Weishan Lake and the Wanmuhetang. Figure 6 shows the distribution of lotus wetlands in the two study areas.

### Accuracy Verification

Using the sample point data from SET<sub>2</sub> obtained through field surveys, the accuracy of the PNLI model in mapping the distribution of lotus wetlands was verified for each of the three study areas. The accuracy verification process involved establishing a confusion matrix, calculating user accuracy and producer accuracy based on the matrix, and subsequently computing the overall accuracy. The overall accuracy served as a measure of the PNLI model's accuracy in mapping lotus wetland distribution. The PNLI mapping accuracy matrices for the three study areas are presented in Tables 7, 10, and 11, respectively. The results indicate that for the distribution mapping of lotus wetland in Baiyangdian, the user accuracy reaches 91.1%, implying a low misclassification rate in the extraction of lotus wetlands using the PNLI model. Furthermore, the overall

Table 3. Bhattacharyya distance between different class pairs of PNLIVV.

Class Pair	PNLI <sup>1</sup> <sub>VV</sub>	PNLI <sup>2</sup> <sub>VV</sub>	PNLI <sup>3</sup> <sub>VV</sub>	PNLI <sup>4</sup> <sub>VV</sub>	PNLI <sup>5</sup> <sub>VV</sub>	PNLI <sup>6</sup> <sub>VV</sub>
Lotus wetland—building	0.605	1.569	1.438	0.046	1.681	1.096
Lotus wetland—reed	0.381	2.678	1.960	1.843	2.102	1.791
Lotus wetland—rice	1.580	2.986	1.838	0.460	1.971	1.095
Lotus wetland—water	1.374	5.552	3.831	0.276	5.038	3.568
Lotus wetland—others	0.836	2.303	1.910	0.215	2.211	1.406

Table 4. Bhattacharyya distance between different class pairs of PNLIVH.

Class Pair	PNLI <sup>1</sup> <sub>VH</sub>	PNLI <sup>2</sup> <sub>VH</sub>	PNLI <sup>3</sup> <sub>VH</sub>	PNLI <sup>4</sup> <sub>VH</sub>	PNLI <sup>5</sup> <sub>VH</sub>	PNLI <sup>6</sup> <sub>VH</sub>
Lotus wetland—building	0.714	2.926	2.109	0.204	2.979	2.373
Lotus wetland—reed	0.861	1.370	0.525	2.494	0.838	0.416
Lotus wetland—rice	0.067	1.192	0.726	0.766	0.737	0.150
Lotus wetland—water	0.946	3.850	3.168	0.366	3.971	3.318
Lotus wetland—others	0.020	1.383	0.920	0.899	1.551	0.531

Table 5. Bhattacharyya distance between different class pairs of PNLIDP.

Class Pair	PNLI <sup>1</sup> <sub>DP</sub>	PNLI <sup>2</sup> <sub>DP</sub>	PNLI <sup>3</sup> <sub>DP</sub>	PNLI <sup>4</sup> <sub>DP</sub>	PNLI <sup>5</sup> <sub>DP</sub>	PNLI <sup>6</sup> <sub>DP</sub>
Lotus wetland—building	1.176	3.308	2.109	0.168	2.682	2.199
Lotus wetland—reed	0.549	2.344	0.525	2.348	1.528	0.210
Lotus wetland—rice	1.037	2.167	0.726	0.095	1.424	0.697
Lotus wetland—water	1.416	5.526	3.168	0.332	4.865	4.005
Lotus wetland—others	0.496	2.184	0.920	0.572	1.988	1.077

Table 6. Bhattacharyya distance value of each class pair in the PNLI model of different polarizations.

Class Pair	PNLI <sub>VV</sub>	PNLI <sub>VH</sub>	PNLI <sub>DP</sub>
Lotus wetland—building	<b>1.569</b>	2.926	3.308
Lotus wetland—reed	2.678	1.370	2.344
Lotus wetland—rice	2.986	<b>1.192</b>	<b>2.167</b>
Lotus wetland—water	5.552	3.850	5.526
Lotus wetland—others	2.303	1.383	2.184

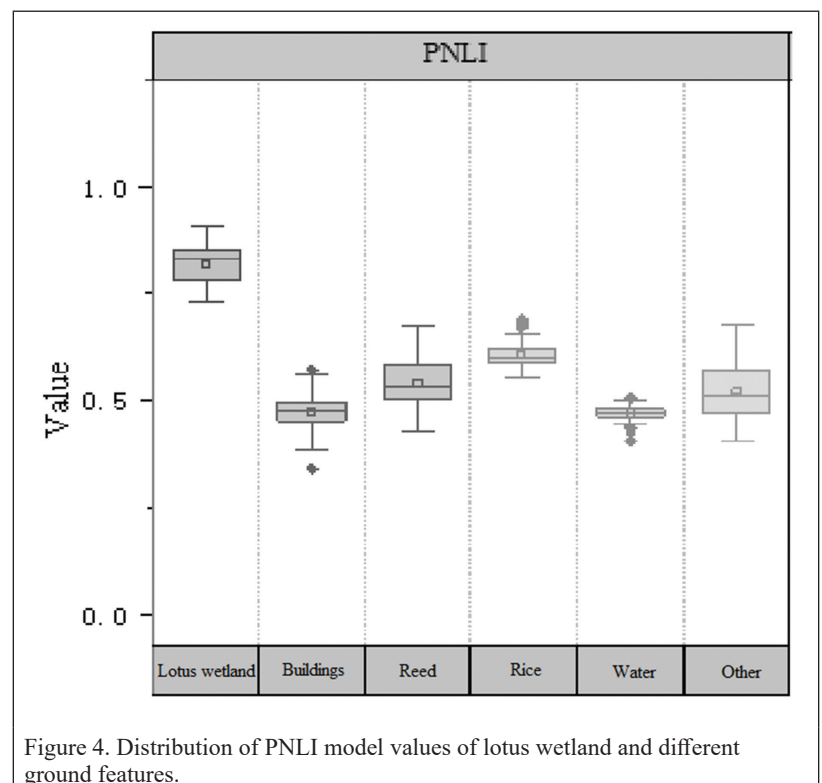


Figure 4. Distribution of PNLI model values of lotus wetland and different ground features.

accuracy for the three research areas is remarkably high, with values of 94.3%, 91.7%, and 92.7%, respectively. These findings confirm the effectiveness of this method in achieving precise mapping of lotus wetland distribution.

Both  $EVI_{ML}$  and  $NDVI_{ML}$  models use optical remote sensing imagery, and key phenological time nodes cannot be obtained in all places in all years. This is reflected in the fact that  $EVI_{ML}$  and  $NDVI_{ML}$  cannot be used for mapping in the Weishan Lake and Wanmuhetang areas. Tables 8 and 9 show the confusion matrix of the traditional phenology-based methods  $EVI_{ML}$  and  $NDVI_{ML}$  for the mapping results of Baiyangdian. The overall accuracy is 87.3% and 73.2%, respectively. Therefore, the proposed PNLI model has a higher overall accuracy of mapping.

## Discussion

### Necessity of the PNLI Model for Mapping Lotus Wetland Distribution

Due to the limitations imposed by cloudy and rainy weather conditions, optical remote sensing imagery is unable to accurately capture information about lotus wetlands. Existing methods for mapping lotus wetland distribution have demonstrated low precision and in some cases fail to provide any mapping at all. In response to these challenges, we have developed the PNLI model, which leverages SAR time-series data. This model overcomes the constraints of weather conditions and enables high-precision mapping of lotus wetlands.

Previous experiments have shown that our proposed PNLI model outperforms traditional phenology-based methods in terms of mapping accuracy. Considering that lotus wetlands grow mainly in the monsoon

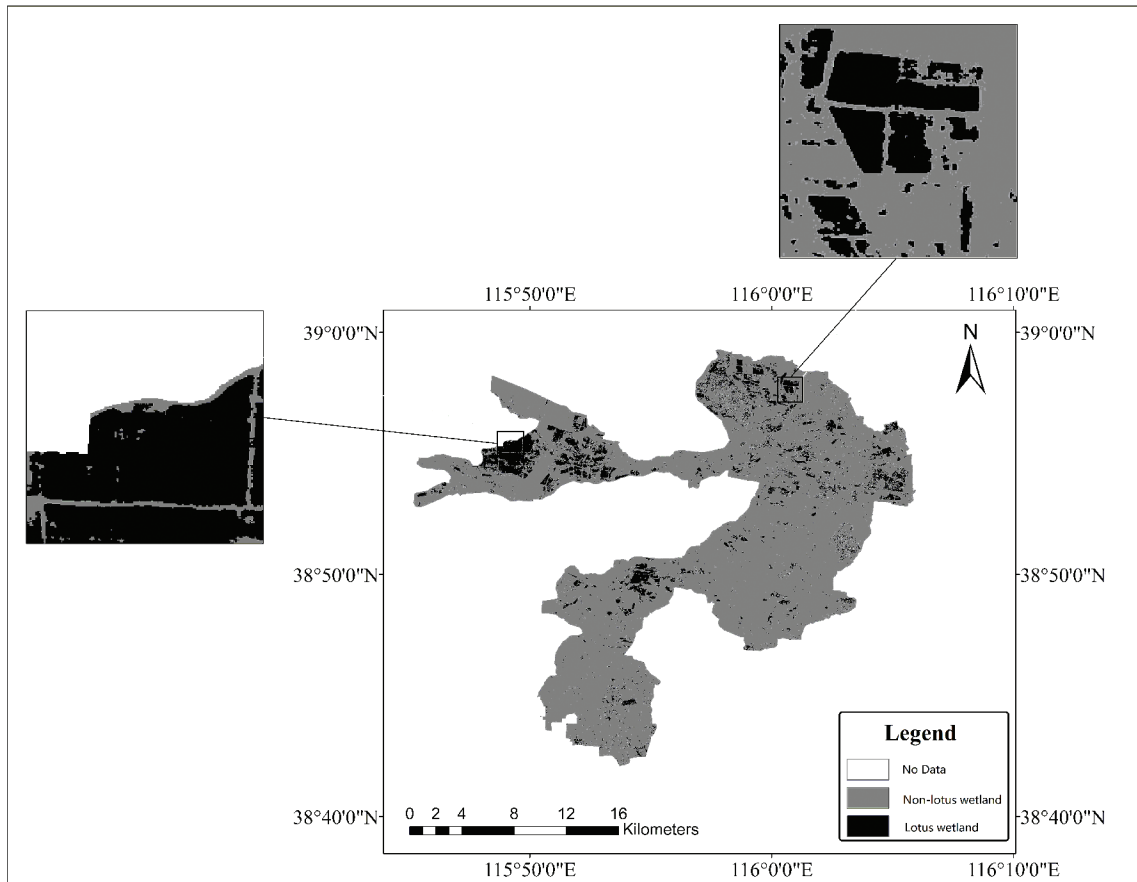


Figure 5. Mapping results of lotus wetland distribution based on PNLI model in Baiyangdian.

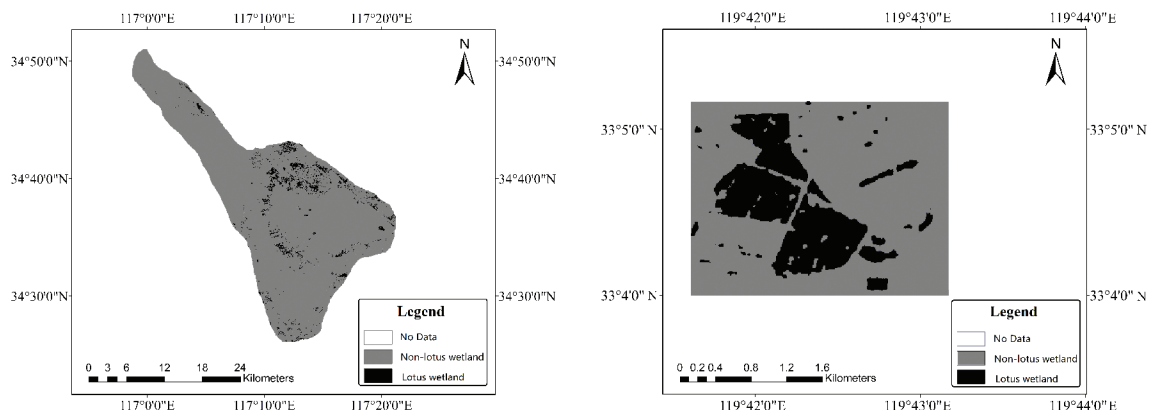


Figure 6. Mapping results of lotus wetland distribution based on PNLI model in Weishan Lake (left) and Wanmuhetang (right).

climate zones of the northern hemisphere, characterized by cloudiness and rainfall during the summer season, it becomes essential to adopt the PNLI model to ensure the high precision mapping of lotus wetland distribution. By employing SAR time-series data, our approach effectively addresses the limitations of optical remote sensing and provides a robust solution for accurate lotus wetland mapping.

### Applicability of the PNLI Model in Regions with Different Phenological Rhythms

The backscattering curves of the three study areas under VV polarization are depicted in Figure 7. It is evident that the time-series curves of lotus wetland backscatter coefficients exhibit a remarkable similarity across the three study areas. Over time, the backscatter coefficient shows an initial increase followed by a subsequent decrease. On comparing the phenological node dates of lotus wetlands in Baiyangdian, Weishan Lake, and Wanmuhetang, as presented in Table 12, it becomes apparent that these three research areas display significantly distinct phenological rhythms. The previous results demonstrate the successful extraction of lotus wetlands in the three study areas using the PNLI model, with overall accuracy surpassing 90%. This outcome underscores the applicability of the proposed PNLI model across diverse phenological rhythms.

### Limitations of the PNLI Model

This study aims to develop a PNLI model using SAR time-series imagery and phenology, enabling the high-precision mapping of lotus wetland distribution across various climate types. However, it is important to acknowledge potential undetected errors arising from the complexity of surface morphology. For example, mountainous regions can obstruct the propagation of microwave signals, particularly in the backscattering direction, leading to the formation of radar shadow areas. These shadow areas can mask the real-time-series backscatter of lotus wetlands, resulting in increased instability and uncertainty in the extraction of lotus wetlands located within radar shadow regions. Thus, it is recommended to avoid using the model in areas affected by radar shadows.

The threshold used in the PNLI model constructed in this study was determined based on dense lotus wetland. However, it is worth noting that different lotus wetland densities can impact mapping accuracy, and the threshold may need to be adjusted accordingly based on local conditions. In future work, as the number of SAR satellites increases and time and spatial resolutions improve, the PNLI model can be further enhanced. One potential improvement is to incorporate adaptive threshold calculation steps that account for lotus wetland density. This enhancement would enable the mapping of lotus wetland distribution on complex surfaces across large areas, thereby reducing the impact of model limitations on the mapping process.

### Conclusion

In this study, we constructed a PNLI model to map the distribution of lotus wetlands by combining SAR time-series images and the phenology-based method. To assess the performance of our model,

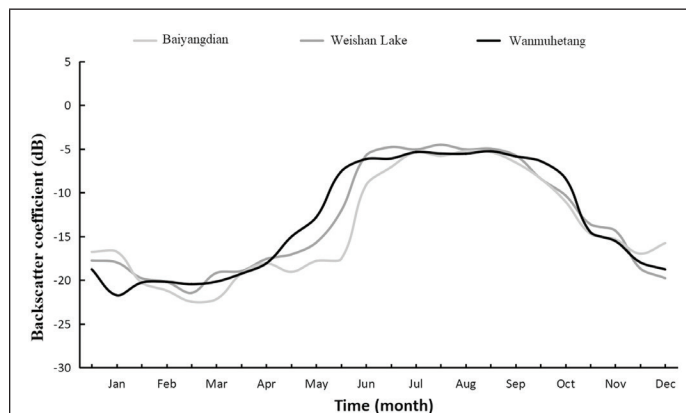


Figure 7. Backscattering curves of the three study areas on VV polarization.

Table 7. Mapping accuracy matrix of lotus wetlands in Baiyangdian using the PNLI model.

Class	Lotus Wetland	Non-Lotus Wetland	Row Total
Lotus wetland	195	23	218
Non-lotus wetland	19	496	515
<b>Column Total</b>	214	519	
<b>User Accuracy (%)</b>	91.1	95.6	
<b>Producer Accuracy (%)</b>	89.5	96.3	
<b>Overall Accuracy (%)</b>	94.3		

Table 8. Mapping accuracy matrix of lotus wetlands in Baiyangdian using the EVIML model.

Class	Lotus Wetland	Non-Lotus Wetland	Row Total
Lotus wetland	163	55	218
Non-lotus wetland	38	477	515
<b>Column Total</b>	201	532	
<b>User Accuracy (%)</b>	81.1	89.7	
<b>Producer Accuracy (%)</b>	74.8	92.6	
<b>Overall Accuracy (%)</b>	87.3		

Table 9. Mapping accuracy matrix of lotus wetlands in Baiyangdian using the NDVIML model.

Class	Lotus Wetland	Non-Lotus Wetland	Row Total
Lotus wetland	206	12	218
Non-lotus wetland	184	331	515
<b>Column Total</b>	390	343	
<b>User Accuracy (%)</b>	52.8	96.5	
<b>Producer Accuracy (%)</b>	94.5	64.3	
<b>Overall Accuracy (%)</b>	73.2		

Table 10. Mapping accuracy matrix of lotus wetlands in Weishan Lake using the PNLI model.

Class	Lotus Wetland	Non-Lotus Wetland	Row Total
Lotus wetland	197	8	205
Non-lotus wetland	22	183	205
<b>Column Total</b>	219	191	
<b>User Accuracy (%)</b>	90.0	95.8	
<b>Producer accuracy (%)</b>	96.1	89.2	
<b>Overall Accuracy (%)</b>	91.7		

Table 11. Mapping accuracy matrix of lotus wetlands in Wanmuhetang using the PNLI model.

Class	Lotus Wetland	Non-Lotus Wetland	Row Total
Lotus wetland	191	21	212
Non-lotus wetland	10	202	212
<b>Column Total</b>	201	223	
<b>User Accuracy (%)</b>	95.0	90.5	
<b>Producer Accuracy (%)</b>	90.2	95.2	
<b>Overall Accuracy (%)</b>	92.7		

Table 12. Phenological rhythms in different study areas.

Lotus Wetland Phenology	Baiyangdian	Weishan Lake	Wanmuhetang
Budding stage	12 March	22 February	8 February 8
Leaf development	23 May	4 May	21 April
Maturity	15 August	27 July	14 July
Leaf withering	14 October	7 October	6 October
Dormancy	25 December	18 December	17 December

we conducted validation experiments at three different locations, each characterized by varying cloud coverage and phenological rhythms. The mapping accuracies achieved were 94.3%, 91.7%, and 92.7% for the respective locations. The PNLI model is more applicable in different regions than existing phenology-based methods, and the model achieves high-precision mapping of lotus wetland distribution in different areas that are cloudy and have different phenological rhythms, which would otherwise not be possible for different regions using a uniform approach. Future research should address the issue of how to fully automate the extraction of lotus wetlands without samples for monitoring changes in the temporal and spatial distribution of lotus wetlands around the world.

## Acknowledgments

We gratefully thank to the research grants from the Specially-Appointed Professor program of Jiangsu Province and the National Natural Science Foundation of China (grant 42141007) and the Remote Sensing Monitoring and Interpretation of Distribution of Aquatic Plants and Algae Project (grant 821107416) for supporting this study.

## References

- Abd Rased, N. S., M. N. Naim, H. C. Man, N. F. Abu Bakar and M. N. Mokhtar. 2019. Evaluation of surface water treated with lotus plant; *Nelumbo nucifera*. *Journal of Environmental Chemical Engineering* 7(3):103048.
- Carreño Conde, F. and M. De Mata Muñoz. 2019. Flood monitoring based on the study of Sentinel-1 SAR imagery: The Ebro River case study. *Water* 11(12):2454.
- Chen, Y., X. Zhang, X. Wang, Q. Luo, Q. Xiong and W. Luo. 2014. Extraction of crop planting structure in seasons prone to waterlogging using Landsat OLI and MODIS data. *Transactions of the Chinese Society of Agricultural Engineering* 30(21):165–173.
- Chi, W., X. Zhang, W. Zhang, X. Bao, Y. Liu, C. Xiong, J. Liu and Y. Zhang. 2020. Impact of tidally induced residual circulations on chemical oxygen demand (COD) distribution in Laizhou Bay, China. *Marine Pollution Bulletin* 151:110811.
- Colin, F., M. Everard, K. Irvine, R. J. McInnes, B. A. Middleton, A. V. Dam and N. Davidson, eds. 2018. *The Wetland Book I: Structure and Function, Management and Methods*. Berlin: Springer-Verlag.
- Colvin, S. A., S.M.P. Sullivan, P. D. Shirey, R. W. Colvin, K. O. Winemiller, R. M. Hughes, K. D. Fausch, D. M. Infante, J. D. Olden, K. R. Bestgen, R. J. Danehy and L. Eby. 2019. Headwater streams and wetland are critical for sustaining fish, fisheries, and ecosystem services. *Fisheries* 44(2):73–91.
- Dannenberg, M., X. Wang, D. Yan and W. Smith. 2020. Phenological characteristics of global ecosystems based on optical, fluorescence, and microwave remote sensing. *Remote Sensing* 12(4):671.
- De Groot, D., L. Brander and C. M. Finlayson. 2018. Wetland ecosystem services. In *The Wetland Book I: Structure and Function, Management and Methods*, edited by F. Colin, M. Everard, K. Irvine, R. J. McInnes, B. A. Middleton, A. V. Dam and N. Davidson, 323–333. Berlin: Springer-Verlag.
- Ding, M., Q. Guan, L. Li, H. Zhang, C. Liu and L. Zhang. 2020. Phenology-based rice paddy mapping using multi-source satellite imagery and a fusion algorithm applied to the Poyang Lake plain, Southern China. *Remote Sensing* 12(6):1022.
- Faidi, M. A., M. G. Hasan and S. A. Shamsuddin. 2018. Mapping of lotus distributions using Sentinel-2 satellite imagery in Tasik Chini. *International Journal of Agriculture, Forestry and Plantation* 6:6.
- Felegari, S., A. Sharifi, K. Moravej, M. Amin, A. Golchin, A. Muzirafuti, A. Tariq and N. Zhao. 2021. Integration of Sentinel 1 and Sentinel 2 satellite imagery for crop mapping. *Applied Sciences* 11(21):10104.
- Fournier, R. A., M. Grenier, A. Lavoie and R. Hélie. 2007. Towards a strategy to implement the Canadian Wetland Inventory using satellite remote sensing. *Canadian Journal of Remote Sensing* 33(suppl. 1):S1–S16.
- Gholizadeh, M. H. and A. M. Melesse. 2017. Study on spatiotemporal variability of water quality parameters in Florida Bay using remote sensing. *Journal of Remote Sensing and GIS* 6(3):1–11.
- Giordano, S., S. Bailly, L. Landrieu and N. Chehata. 2020. Improved crop classification with rotation knowledge using Sentinel-1 and -2 time series. *Photogrammetric Engineering and Remote Sensing* 86(7):431–441.
- Guccione, P., M. Belotti, D. Giudici, A. Monti Guarnieri and I. Navas-Traver. 2015. Sentinel-1A: Analysis of FDBAQ performance on real data. *IEEE Transactions on Geoscience and Remote Sensing* 53(12):6804–6812.
- Immitzer, M., M. Neuwirth, S. Böck, H. Brenner, F. Vuolo and C. Atzberger. 2019. Optimal input features for tree species classification in Central Europe based on multi-temporal Sentinel-2 data. *Remote Sensing* 11(22):2599.
- Jeon, Y. E. and S. B. Kang. 2020. Estimation of the exponentiated half-logistic distribution based on multiply Type-I hybrid censoring. *Communications for Statistical Applications and Methods* 27(1):47–64.
- Jiang, B. and X. Xu. 2019. China needs to incorporate ecosystem services into wetland conservation policies. *Ecosystem Services* 37:100941.
- Jou, C. J., S. W. Chen, C. M. Kao and C. L. Lee. 2008. Assessing the efficiency of a constructed wetland using a first-order biokinetic model. *Wetlands* 28(1):215–219.
- Kanabkaew, T. and U. Puetpaiboon. 2004. Aquatic plants for domestic wastewater treatment: Lotus (*Nelumbo nucifera*) and Hydrilla (*Hydrilla verticillata*) systems. *Songklanakarin Journal of Science and Technology* 26(5):749–756.
- Kaushalya, G. N. 2020. Wetlands becoming wastelands: Factors contributing to the degradation of wetlands in Sri Lanka. *International Journal of Research and Analytical Reviews* 7:713–718.
- Kussul, N., G. Lemoine, F. J. Gallego, S. V. Skakun, M. Lavreniuk and A. Y. Shelestov. 2016. Parcel-based crop classification in Ukraine using Landsat-8 data and Sentinel-1A data. *IEEE Journal of Selected Topics in Applied Earth Observations and Remote Sensing* 9(6):2500–2508.
- Lee, H., H. Chae and S. J. Cho. 2010. Radar backscattering of intertidal mudflats observed by Radarsat-1 SAR imagery and ground-based scatterometer experiments. *IEEE Transactions on Geoscience and Remote Sensing* 49(5):1701–1711.
- Li, H., M. Jia, R. Zhang, Y. Ren and X. Wen. 2019. Incorporating the plant phenological trajectory into mangrove species mapping with dense time series Sentinel-2 imagery and the Google Earth Engine platform. *Remote Sensing* 11(21):2479.
- Li, X., Z. Du, Y. Huang and Z. Tan. 2021. A deep translation (GAN) based change detection network for optical and SAR remote sensing imagery. *ISPRS Journal of Photogrammetry and Remote Sensing* 179:14–34.
- Liu, X., H. Zhai, Y. Shen, B. Lou, C. Jiang, T. Li, S. B. Hussain and G. Shen. 2020. Large-scale crop mapping from multisource remote sensing imagery in Google Earth Engine. *IEEE Journal of Selected Topics in Applied Earth Observations and Remote Sensing* 13:414–427.
- Maguranyanga, C., A. Murwira and M. Sibanda. 2015. Distinguishing maize, soyabean and tobacco fields using temporal MODIS 16 day NDVI imagery in the large scale commercial farming areas of Zimbabwe. *Journal of the Indian Society of Remote Sensing* 43(1):79–87.
- Miao, T. and H. Ju. 2020. Leading small groups in China's inter-city governmental cooperation. *International Journal of Public Leadership* 16(2):249–264.
- Paek, S. W., S. Balasubramanian, S. Kim and O. de Weck. 2020. Small-satellite synthetic aperture radar for continuous global biospheric monitoring: A review. *Remote Sensing* 12(16):2546.
- Pang, J., X. Feng and X. Wang. 2014. Purification and utilization of garlic processing wastewater in lotus pond wetland. *Water Science and Engineering* 7(4):395–402.
- Ramirez, F.J.R., R. M. Navarro-Cerrillo, M. A. Varo-Martínez, J. L. Quero, S. Doerr and R. Hernández-Clemente. 2018. Determination of forest fuels characteristics in mortality-affected Pinus forests using integrated hyperspectral and ALS data. *International Journal of Applied Earth Observation and Geoinformation* 68:157–167.
- Rodrigues, A., A.R.S. Marçal and M. Cunha. 2012. Monitoring vegetation dynamics inferred by satellite data using the PhenoSat tool. *IEEE Transactions on Geoscience and Remote Sensing* 51(4):2096–2104.
- Rosin, P. L. and E. Loannidis. 2003. Evaluation of global image thresholding for change detection. *Pattern Recognition Letters* 24(14):2345–2356.
- Rosin, P. 1998. Thresholding for change detection. *Sixth International Conference on Computer Vision*, held in Bombay, India, 7–7 January 1998. IEEE Cat. No.98CH36271: 274–279.

- Seifollahi-Aghmiuni, S., Z. Kalantari, M. Land and G. Destouni. 2019. Change drivers and impacts in Arctic wetland landscapes—Literature review and gap analysis. *Water* 11(4):722.
- Sibanda, M., A. Murwira and F. Baudron. 2010. *Evaluating the Relative Contribution of Changing Farming Methods to Habitat Loss in the Mid-Zambezi Valley*. Ph.D. dissertation, University of Zimbabwe.
- Skriver, H. 2007. Signatures of polarimetric parameters and their implications on land cover classification. Pages 4195–4198 in *IEEE International Geoscience and Remote Sensing Symposium*, held in Barcelona, Spain, 23–28 July 2007. New York: IEEE.
- Song, Z., Z. Zheng, J. Li, X. Sun, X. Han, W. Wang and M. Xu. 2006. Seasonal and annual performance of a full-scale constructed wetland system for sewage treatment in China. *Ecological Engineering* 26(3):272–282.
- Teng, X., Q. Hu, L. Zhang, J. Qi, J. Shi, H. Xie, H. Gao and X. Yao. 2017. Identification of major sources of atmospheric NH<sub>3</sub> in an urban environment in northern China during wintertime. *Environmental Science and Technology* 51(12):6839–6848.
- Waltham, N. J., D. Burrows, C. Wegscheidl, C. Buelow, M. Ronan, N. Connolly, G. Paul, M. A. Donna, C. Colin and S. Marcus. 2019. Lost floodplain wetland environments and efforts to restore connectivity, habitat, and water quality settings on the Great Barrier Reef. *Frontiers in Marine Science* 6:71.
- Wessels, K., K. Steenkamp, G. Von Maltitz and S. Archibald. 2011. Remotely sensed vegetation phenology for describing and predicting the biomes of South Africa. *Applied Vegetation Science* 14(1):49–66.
- Xie, F., D. Chen, D. J. Meligrana and W. Ren. 2013. Selecting key features for remote sensing classification by using decision-theoretic rough set model. *Photogrammetric Engineering and Remote Sensing* 79(9):787–797.
- Xu, P., Z. Niu and P. Tang. 2018. Comparison and assessment of NDVI time series for seasonal wetland classification. *International Journal of Digital Earth* 11(11):1103–1131.
- Zhang, B., X. Liu, M. Liu and Y. Meng. 2018. Detection of rice phenological variations under heavy metal stress by means of blended Landsat and MODIS image time series. *Remote Sensing* 11(1):13.
- Zhang, H., X. Wang and D. Peng. 2022. Evaluation of urban vegetation phenology using 250 m MODIS vegetation indices. *Photogrammetric Engineering and Remote Sensing* 88(7):461–467.
- Zhang, M., F. Chen, D. Liang, B. Tian and A. Yang. 2020. Use of Sentinel-1 GRD SAR imagery to delineate flood extent in Pakistan. *Sustainability* 12(14):5784.

---

## In-Press Articles

Identification of Critical Urban Clusters for Placating Urban Heat Island Effects over Fast-Growing Tropical City Regions: Estimating the Contribution of Different City Sizes in Escalating UHI Intensity. Kanaya Dutta, Debolina Basu, and Sonam Agrawal.

A Novel Object Detection Method for Solid Waste Incorporating a Weighted Deformable Convolution. Xiong Xu, Tao Cheng, Beibei Zhao, Chao Wang, Xiaohua Tong, Yongjiu Feng, Huan Xie, and Yanmin Jin.

An Integrated Approach for Wildfire Photography Telemetry using WRF Numerical Forecast Products. Ling Tan and Xuelan Ma.

A Powerful Correspondence Selection Method for Point Cloud Registration Based on Machine Learning. Wuyong Tao, Dong Xu, Xijiang Chen, and Ge Tan.

Self-Calibration of the Stereo Vision System on the Chang'E-5 Probe Based on Images and Robot Arm Footprints. Shuo Zhang, Yanhong Zheng, Liping Chen, Youqing Ma, Bo Hu, Zheng Gu, Xiangjin Deng, and Shaochuang Liu.

Combination of Terrestrial Laser Scanning and Unmanned Aerial Vehicle Photogrammetry for Heritage Building Information Modeling: A Case Study of Tarsus St. Paul Church. Şafak Fidan, Ali Ulvi, Abdurahman Yasin Yiğit, Seda Nur Gamze Hamal, and Murat Yakar.

IMU and Bluetooth Data Fusion to Achieve Submeter Position Accuracy in Indoor Positioning. Ugur Acar.

Rice Identification Under Complex Surface Conditions with CNN and Integrated Remote Sensing Spectral-Temporal-Spatial Features. Tianjiao Liu, Jiankui Chen, Li Zhang, and Dong Li.

# Call for *PE&RS* Special Issue Submissions

## Ushering a New Era of Hyperspectral Remote Sensing to Advance Remote Sensing Science in the Twenty-first Century

Great advances are taking place in remote sensing with the advent of new generation of hyperspectral sensors. These include data from, already in orbit sensors such as: 1. Germany's Deutsches Zentrum für Luft- und Raumfahrt (DLR's) Earth Sensing Imaging Spectrometer (DEGIS) sensor onboard the International Space Station (ISS), 2. Italian Space Agency's (ASI's) PRISMA (Hyperspectral Precursor of the Application Mission), and 3. Germany's DLR's Environmental Mapping and Analysis Program (EnMAP). Further, Planet Labs PBC recently announced the launch of two hyperspectral sensors called Tanager in 2023. NASA is planning for the hyperspectral sensor Surface Biology and Geology (SBG) to be launched in the coming years. Further, we already have over 70,000 hyperspectral images of the world acquired from NASA's Earth Observing-1 (EO-1) Hyperion that are freely available to anyone from the U.S. Geological Survey's data archives.

These suites of sensors acquire data in 200 plus hyperspectral narrowbands (HNBs) in 2.55 to 12 nm bandwidth, either in 400-1000 or 400-2500 nm spectral range with SBG also acquiring data in the thermal range. In addition, Landsat-NEXT is planning a constellation of 3 satellites each carrying 26 bands in the 400-12,000 nm wavelength range. HNBS provide data as "spectral signatures" in stark contrast to "a few data points along the spectrum" provided by multispectral broadbands (MBBs) such as the Landsat satellite series.

The goal of this special issue is to seek scientific papers that perform research utilizing data from these new generation hyperspectral narrowband (HNB) sensors for a wide array of science applications and compare them with the performance of the multispectral broadband (MBB) sensors such as Landsat, Sentinels, MODIS, IRS, SPOT, and a host of others.

### Papers on the following topics are of particular interest:

1. Methods and techniques of understanding, processing, and computing hyperspectral data with specific emphasis on machine learning, deep learning, artificial intelligence (ML/DL/AI), and cloud computing.
2. Issues of hyperspectral data volumes, data redundancy, and overcoming Hughes' phenomenon.
3. Building hyperspectral libraries for purposes of creating reference training, testing, and validation data.
4. Utilizing time-series multispectral data and hyperspectral data over many years to build data cubes and apply advanced computational methods of ML/DL/AI methods and approaches on the cloud.
5. Discussions of hyperspectral data analysis techniques like full spectral analysis versus optimal band analysis.
6. Developing hyperspectral vegetation indices (HVIs) for targeted applications to model and map plant biophysical (e.g., Yield, biomass, leaf area index), biochemical (e.g., Nitrogen, anthocyanins, carotenoids), plant health/stress, and plant structural quantities.
7. Classification of complex vegetation and crop types/species using HNBS and HVIs and comparing them with the performance of multispectral broadband data.

All submissions will be peer-reviewed in line with *PE&RS* policy. Because of page limits, not all submissions recommended for acceptance by the review panel may be included in the special issue. Under this circumstance, the guest editors will select the most relevant papers for inclusion in the special issue. Authors must prepare manuscripts according to the *PE&RS* Instructions to Authors, published in each issue of *PE&RS* and also available on the ASPRS website, <https://www.asprs.org/asprs-publications/pers/manuscript-submission>.

### Special Issue Editors

**Dr. Prasad S. Thenkabail**, [pthenkabail@usgs.gov](mailto:pthenkabail@usgs.gov), [thenkabail@gmail.com](mailto:thenkabail@gmail.com)  
Senior Scientist (ST), USGS, Flagstaff, Arizona

**Dr. Itiya Aneece**, [ianeece@usgs.gov](mailto:ianeece@usgs.gov)  
USGS, Flagstaff, Arizona

**Dr. Pardhasaradhi Teluguntla**, [pteluguntla@usgs.gov](mailto:pteluguntla@usgs.gov)  
USGS, Flagstaff, Arizona

### Important Dates

**Manuscripts Due — December 15, 2023**

**Final Papers Due — May 1, 2024**

**Tentative Publication Date — 2024**

**Please submit your manuscript —**  
[www.editorialmanager.com/asprs-pers/](http://www.editorialmanager.com/asprs-pers/)  
select "Hyperspectral Remote Sensing"

# The FABDEM Outperforms the Global DEMs in Representing Bare Terrain Heights

Nahed Osama, Zhenfeng Shao, and Mohamed Freeshah

## Abstract

Many remote sensing and geoscience applications require a high-precision terrain model. In 2022, the Forest And Buildings removed Copernicus digital elevation model (FABDEM) was released, in which trees and buildings were removed at a 30 m resolution. Therefore, it was necessary to make a comprehensive evaluation of this model. This research aims to perform a qualitative and quantitative analysis of FABDEM in comparison with the commonly used global DEMs. We investigated the effect of the terrain slope, aspect, roughness, and land cover types in causing errors in the topographic representation of all DEMs. The FABDEM had the highest overall vertical accuracy of 5.56 m. It was the best DEM in representing the terrain roughness. The FABDEM and Copernicus DEM were equally influenced by the slopes more than the other models and had the worst accuracy of slope representation. In the tree, built, and flooded vegetation areas of the FABDEM, the mean errors in elevation have been reduced by approximately 3.34 m, 1.26 m and 1.55 m, respectively. Based on Welch's *t*-test, there was no significant difference between FABDEM and Copernicus DEM elevations. However, the slight improvements in the FABDEM make it the best filtered DEM to represent the terrain heights over different land cover types.

## Introduction

Digital elevation models (DEMs) are considered the core spatial data set required for a variety of applications such as hydrological research (Chu and Lindenschmidt 2017), terrain analysis (Osama *et al.* 2021), soil science (Park *et al.* 2001), ecology (Amatulli *et al.* 2018; Moore *et al.* 1991), glaciology (Rentsch *et al.* 1990; Wang and Kääh 2015), and volcanology (Grosse *et al.* 2012; Kubanek *et al.* 2021). DEMs have existed at a global or near-global scale with 1 arc second grid spacing based on geo-rectified space data acquired from several sensors such as optical, near-infrared, and radar sensors. In 2000, some satellites have been launched to collect (30 m–90 m) resolution elevation data for the globe such as the Shuttle Radar Topography Mission (SRTM) and the Advanced Spaceborne Thermal Emission and Reflection Radiometer (ASTER) mission (Mukherjee *et al.* 2012). Since then, the DEMs collected by them are freely available for public use in various resolutions. From 2006 to 2011 the Japanese Aerospace Exploration Agency (JAXA) has used the Advanced Land Observing Satellite (ALOS) releases to produce the world three-dimensional (3D) topographic data, the most precise DEM at that time, with a horizontal resolution of 30 meter. In 2020, National Aeronautics and Space Administration (NASA) reprocessed SRTM by an optimized hybrid processing approach based on expanding

Nahed Osama and Zhenfeng Shao are with the State Key Laboratory of Information Engineering in Surveying, Mapping and Remote Sensing, Wuhan University, Wuhan 430079, China.

Zhenfeng Shao is also with Hubei LuoJia Laboratory, Wuhan, China.

Mohamed Freeshah is with the School of Geodesy and Geomatics, Wuhan University, 129 Luyao Road, Wuhan 430079, China and the Department of Geomatics Engineering, Faculty of Engineering at Shoubra, Benha University, Cairo 11629, Egypt.

Corresponding author: Mohamed Freeshah, mohamedfreeshah@whu.edu.cn

Contributed by Prasad S. Thenkabil, April 7, 2023 (sent for review May 8, 2023; reviewed by Fanar M. Abed, Zhaojin Li).

spatial coverage and minimizing data voids. The voids have been filled with a variety of data sets including ASTER, ALOS, United States Geological Survey (USGS) national elevation data set, and Canada and Alaska DEMs. Meanwhile, ground control points and ICESat data were used for vertical and tilt adjustments (NASA JPL 2020). In December 2020, the European Space Agency (ESA) made the 30-meter resolution Copernicus DEM available for free (ESA 2020). Since then, some studies were performed to investigate the Copernicus DEM accuracy and compare its errors with the previous global DEMs errors (Guth and Geoffroy 2021).

DEMs are subjected to several sources of errors during the data processing due to the oldness of data, low density of observation, filtering or interpolation, and resampling errors. In literature, SRTM and Terra Advanced Spaceborne Thermal Emission and Reflection Radiometer (ASTER) DEMs exhibited large vertical errors, especially over complex topography, and they have defects in relatively flat terrain where they cannot deal with microtopographic variations (Chu and Lindenschmidt 2017; Gallien *et al.* 2011). Relative and absolute elevation errors for the SRTM mission were defined as 6 m and 16 m, respectively (Rabus *et al.* 2003). Nevertheless, recent studies have shown that the accuracy of the SRTM DEM is still acceptable in many applications (Liu *et al.* 2020). On this basis, several studies were based on merging different elevation data sets to improve DEMs' accuracy and eliminate biases of vegetation and man-made features, such as buildings and other types of infrastructure (Baugh *et al.* 2013; O'Loughlin *et al.* 2016; Robinson *et al.* 2014; Yamazaki *et al.* 2017; Yue *et al.* 2017). Even so, the derived versions have shown multiple errors in the vertical values much larger than those acceptable for several applications when they have been used widely (Mukherjee *et al.* 2012).

Over the years, the vertical accuracies of the SRTM DEM, ASTER DEM, and the other global DEMs have been investigated by remote sensing community. The SRTM showed a better vertical accuracy than a 1:50 000 topographic maps within the range of 8 m and 20 m (Jarvis *et al.* 2004). The vertical accuracies of ASTER DEM in Spain and Turkey were 4 m and 8 m, respectively (Sefercik 2012). In China, both ASTER DEM and SRTM DEM vertical accuracies have been investigated in two different areas, SRTM DEM showed root-mean-square error (RMSE) values of 2.38 m and 4.43 m, and ASTER DEM showed RMSE values of 6.98 m and 4.83 m (Du *et al.* 2012). ALOS 3D world DEM (AW3D30) accuracy has been tested among seven global DEMs including ASTER and SRTM DEMs. The results showed that ALOS DEM had the greatest vertical accuracy in the selected regions (Liu *et al.* 2019). While in another similar studies AW3D30 DEM was also superior to ASTER DEM and SRTM DEM (González-Moradas and Viveen 2020). Over the five available global one arc second DEMs, (ASTER, SRTM, ALOS, NASA, and Copernicus), evaluated in eight high-relief areas through wide-distributed lidar point clouds and ICESat-2 data. The Copernicus DEM showed superiority in elevation accuracy in slopes (i.e., steep and gentle lands) and in different vegetation regions, over the abovementioned global DEMs (Guth and Geoffroy 2021). Since the DEMs have differences in strategy, models, data collection time, mission, and geographical extent, the

Photogrammetric Engineering & Remote Sensing  
Vol. 89, No. 10, October 2023, pp. 613–624.

0099-1112/22/613-624

© 2023 American Society for Photogrammetry  
and Remote Sensing

doi: 10.14358/PERS.23-00026R2

DEMs' products vary in their accuracies and compatibilities for a range of specific purposes. In 2021, Guth and Geoffroy have concluded that Copernicus GLO-30 resolves the issues accurately and has many advantages, and it should be a standard for the global DEMs (Guth and Geoffroy 2021).

In 2022, Hawker *et al.* chose Copernicus GLO-30 as the basis for producing their new global DEM that was called Forest And Buildings removed Copernicus DEM (FABDEM). They used random forest machine learning techniques to remove the biases of forests and buildings from the most recent Copernicus GLO-30 DEM at a 30 m spatial resolution (Airbus Defence and Space 2020; Hawker *et al.* 2022). They collected data from 12 countries to be used in training the machine learning model created for filtering the FABDEM. The FABDEM showed that the absolute errors were reduced up to half and the median errors were near to zero versus the other DEMs. Hawker *et al.* have concluded that the FABDEM reduced the average vertical error from 1.61 m to 1.12 m, and from 5.15 m to 2.88 m for the urban areas and forests, respectively. In a study evaluating the FABDEM in the Philippines with 17 013 geodetic control points (GCPs), it was found to overestimate the GCPs with an average mean error of 1.74 m and an RMSE of 4.74 m. The vertical accuracy of the FABDEM was better in estimating the heights less than 100 m and the slopes less than two degrees. In some areas, the accuracy of the FABDEM was equal to AW3D30 DEM and it was better than SRTM DEM (Santillan 2023). When the accuracies of the FABDEM, Copernicus DEM, MERIT DEM, and SRTM DEM were evaluated in a steep vegetated mountainous region using unmanned aerial vehicle (UAV) lidar data, the FABDEM was superior to Copernicus DEM elevation RMSE by 24%. It also showed better accuracy and a clearer topographic representation than MERIT DEM (Marsh *et al.* 2023). However, another study in Iran suggested that MERIT DEM has a higher vertical accuracy compared to the FABDEM and other global DEMs where the height RMSE values of the DEMs were reported as SRTM = 5.79 m, ASTER = 6.23 m, FABDEM = 5.01 m, and MERIT = 4.32 m (Saber *et al.* 2023). The FABDEM was used to improve the hydrological models (Xu *et al.* 2022) and quantify the wildfire effect on soil erosion (Stefanidis *et al.* 2022). The hydrological society showed interest in using the FABDEM hoping that the enhancement in it would be of great help to accurately investigate and assess the flood risks. However, there is a lack of research that assesses the model and differentiates between it and the existing global elevation models. In addition, research evaluates DEM accuracy only through elevation accuracy, although many types of geospatial and hydrological research use aspect and slope maps as basic layers for investigation and prediction models.

This work aims to assess the quality of FABDEM in comparison with in situ airborne lidar data and the older global DEMs. Further assessment of FABDEM will determine whether the earlier DEMs such as the 30 m resolution ASTER, SRTM, ALOS, and Copernicus DEMs have acceptable accuracies compared to the FABDEM or not. It will also reveal if the defects can suggest further improvements in the accuracy. This would reveal the impact of the different DEMs upon the accuracy of topographic attributes and terrain representation, particularly in a relatively steeply sloping area. Also, we calculate the errors in terrain elevations, slope, aspect, as well as roughness maps to investigate whether the slope, aspect, and roughness maps accuracies are proportional to the elevation accuracy.

In this paper, the first section contains the introduction and the literature review, we presented the study area and data sources in section two, section three contains a detailed explanation of the evaluation methods and the calculation of errors, and section four presents and analyzes the results compared to previous studies. The last section presents the conclusions of this study.

## Study Area and Data Sets

Haiti is a country in the Caribbean Sea, located in the northern hemisphere at 18.9712° N and 72.2852° W, as latitude and longitude, respectively, as shown in Figure 1. Haiti has rough topography, especially in western and central Hispaniola (Boatner 2021). Due to the vast area of the country, the topographic variations, the variability in the land cover types, and the availability of a high-resolution reference

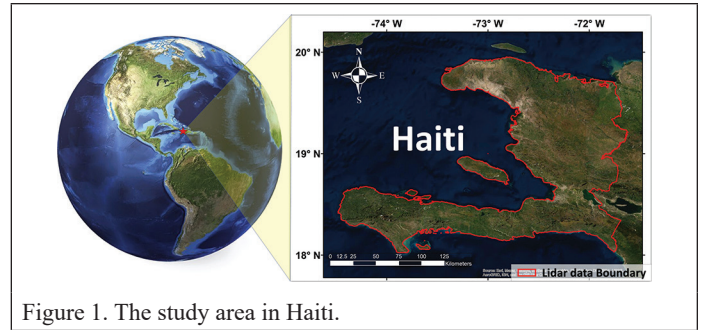


Figure 1. The study area in Haiti.

lidar Digital Terrain Model (DTM) covering all of Haiti, we found that Haiti is the proper location for our study to evaluate the DEMs over the heterogeneous topography.

The Copernicus DEM is a Digital Surface Model (DSM) provided in three different resolutions named EEA-10, GLO-30, and GLO-90 (Cenci *et al.* 2021). The Copernicus DSM represents the surface of the Earth including buildings, infrastructure, and vegetation (ESA 2021). In this study, we used the GLO-30 coverage with 30 m spatial resolution as one of the elevation models. The Forest and Buildings removed Copernicus DEM abbreviated as "FABDEM" is a global elevation map. In December 2021, a research team from the University of Bristol produced the FABDEM by eliminating the trees and buildings' height biases from the Copernicus GLO 30 DEM based on random forest machine learning algorithm. A set of training data from 12 countries were collected to train the correction model. The forest canopy heights were estimated from combining the global forest canopy height 2019 data and Landsat Global Land Analysis and Discovery Analysis Ready Data (GLAD ARD) data together to provide an estimated 30 m resolution forest heights. Since the global forest canopy height 2019 data are based on the Global Ecosystem Dynamics Investigation (GEDI) data and limited by the spatial extend of the GEDI data footprints, the FABDEM spatial resolution is 30 m and the DEM is only available in the spatial extend between 51.6° N and 51.6° S. Multiple buildings data sets were used to predict building heights. The Copernicus/building removed layer and the Copernicus/forest removed layer were combined together and post-processed to create the final product of the FABDEM. (Hawker *et al.* 2022). While the ASTER images were acquired between March 2000 and November 2013 to provide a high-resolution global photogrammetric-based DEM. The newest version of ASTER DEM is version 3.0 which was released in 2019. The ASTER v3.0 DEM provides a 1 arc-second (approximately 30 meters) for DEM grids and extends from 83° North to 83° South (Abrams *et al.* 2020). The SRTM DEM is a high-resolution near-global DEM extending from 60° North to 56° South and covering 80% of the Earth. Several versions of SRTM DEM have been released since 2003 where they were corrected for the noise, data voids, defining coastlines, and removing spikes and wells (Farr and Kobrick 2000; Slater *et al.* 2006). SRTM version 3.0 was released in 2015 at a 30 meters DEM grids. Version 3 is an enhanced version especially, in the steep mountainous regions where many DEM sources were combined together to correct the elevations and fill the voids in those areas (NASA 2015). The ALOS is a Global Digital Surface Model based on the Panchromatic Stereo images of the Advanced Land Observing Satellite operated from 2006 to 2011. The data set has a free-of-charge at 30-meter resolution. The ALOS data set covers the whole globe (Zhang *et al.* 2019). The latest version 3.2 was released in 2022, where the partial anomaly in version 3.1 was corrected for the low-latitude and mid-latitude regions.

The land cover data was provided by Environmental Systems Research Institute (ESRI). The global landcover map was generated from ESA *Sentinel-2* imagery at 10 m resolution by deep learning methods using a very large training data provided by the National Geographic Society. The version used in this research was released in January 2022. The map contains 10 classes of land cover representing water, trees, flooded vegetation, crops, built area, bare ground, snow/ice, and clouds (ESRI 2022). The reference data was provided by the World Bank, which has funded more than 200 flight hrs. to collect aerial imagery and lidar data over the Caribbean to produce an accurate DTM and orthophoto over Haiti (<https://doi.org/10.5069/G9GX48R8>).



The project's purpose was to participate in the reconstruction, and risk and disaster management. The survey covered an area of 29 239 km<sup>2</sup> with a 1.5 m raster resolution, a 0.25 m orthophoto resolution, and a 20 cm altimetric accuracy (IGN FI 2021; The World Bank 2021). The digital terrain model and orthophotos were collected in 2014–2016. The project vertical datum is WGS84 (EGM96 GEOID), and the horizontal coordinates system is UTM Zone 18N WGS84 meters. The boundary of the lidar data is shown in Figure 1. The information of the DEMs' reference datums is listed in Table 1.

Table 1. The reference datums of ASTER DEM, SRTM DEM, ALOS DEM, Copernicus DEM, FABDEM, and the lidar DTM.

DEM	Vertical Datum	Horizontal Datum
ASTER	EGM96 Geoid	WGS84 [EPSG: 4326]
SRTM	EGM96 Geoid	WGS84 [EPSG: 4326]
ALOS	EGM96 Geoid	WGS84 [EPSG: 4326]
Copernicus	EGM2008 [EPSG: 3855]	WGS84 [EPSG: 4326]
FABDEM	EGM2008 [EPSG: 3855]	WGS84 [EPSG: 4326]
Lidar	EGM96 Geoid	UTM Zone 18N WGS84 [EPSG: 32618]

ALOS = Advanced Land Observing Satellite; ASTER = Terra Advanced Spaceborne Thermal Emission and Reflection Radiometer; DEM = digital elevation model; DTM = digital terrain model; FABDEM = Forest And Buildings removed Copernicus DEM; SRTM = Shuttle Radar Topography Mission.

Table 1 shows that the reference lidar data has a projected coordinate system, while ASTER DEM, SRTM DEM, ALOS DEM, Copernicus DEM, and FABDEM have geographic coordinate systems. Therefore, we transformed the lidar observations from projected to geographic datums, then, all the vertical datums were unified to the ellipsoidal datum WGS 84 to compare the DEMs elevations. In order to transform the elevations from the geoid surface to the WGS84 reference ellipsoid, the following equation was used:

$$H = H_0 + N, \quad (1)$$

where  $H$  is the ellipsoidal height,  $H_0$  is the orthometric height, and  $N$  is the geoid undulation.

The transformation of the vertical datums has been performed by the VDatum software provided by the National Oceanic and Atmospheric Administration's National Geodetic Survey (NGS), Office of Coast Survey (OCS), and Center for Operational Oceanographic Products and Services (CO-OPS). Online vertical datums transformation is available through this link: <https://vdatum.noaa.gov/>.

## Evaluation Methods

In order to evaluate the accuracy of the DEMs, we performed a group of qualitative and quantitative analyses. The qualitative analysis aims to map the slopes, aspect, hillshade maps, and Terrain Ruggedness Index (TRI); then, we visually compared the results with the reference lidar maps. The elevations of each DEM were plotted against the elevations of the lidar and the correlation coefficients ( $R^2$ ) between the lidar elevations and each DEM elevations were calculated. The residual errors for all DEMs were plotted against the terrain slopes and roughness length to find out which factor affects the most on the presence of errors in each DEM. The quantitative analysis evaluates the accuracy of the DEMs' elevations, slopes, and roughness by calculating the standard deviations (SDs), the RMSE, and the mean absolute errors (MAE). In addition, the RMSE and the mean errors (ME) values were calculated for each DEM over the different land cover types to quantify the amount of error caused by the land cover. Finally, we performed Welch's t-test to examine if there was a significant enhancement in the FABDEM over the Copernicus DEM or not.

### DEM's Accuracy Assessment

The evaluation of DEMs' elevation, aspect, slope, and roughness values was done based on the SD, RMSE, and MAE, which were calculated according to the following equations:

$$RMSE = \sqrt{\frac{\sum_{i=1}^n (X_{Valid_i} - X_{DEM_i})^2}{n}} \quad (2)$$

$$STD = \sqrt{\frac{\sum_{i=1}^n |X_{DEM_i} - X_{mean}|^2}{n-1}} \quad (3)$$

$$MAE = \frac{1}{n} \sum_{i=1}^n |X_{DEM_i} - X_{Valid}| \quad (4)$$

where  $X_{DEM}$  is the observation value of the DEM,  $n$  is the number of observations,  $X_{mean}$  is the mean value of the DEM observations, and  $X_{Valid}$  is the observation of the validation data.

### Welch's t-test for Comparing Copernicus DEM to FABDEM

The Welch's t-test is one of the statistical hypothesis testing methods used to compare the means of two independent groups of data with the assumption that they have unequal variances. The tested data should have normal distribution; therefore, a Gaussian curve should fit into the data (Ahad and Yahaya 2014). There are two statistical hypotheses: (1) the null hypothesis, which assumes that the means of the two groups are identical ( $\bar{x}_1 = \bar{x}_2$ ), and (2) the alternative hypothesis which assumes that the means of the two groups are different ( $\bar{x}_1 \neq \bar{x}_2$ ). The Welch's t value ( $t$ ) and degree of freedom ( $df$ ) can be calculated from the following formulas:

$$t = \frac{\bar{x}_1 - \bar{x}_2}{\sqrt{\frac{s_1^2}{N_1} + \frac{s_2^2}{N_2}}} \quad (5)$$

$$df = \frac{\left(\frac{s_1^2}{N_1} + \frac{s_2^2}{N_2}\right)^2}{\frac{\left(\frac{s_1^2}{N_1}\right)^2}{N_1 - 1} + \frac{\left(\frac{s_2^2}{N_2}\right)^2}{N_2 - 1}} \quad (6)$$

where  $\bar{x}_1$ ,  $\bar{x}_2$  are the means of group 1 and group 2, respectively.  $s_1^2$ ,  $s_2^2$  are the SD of group 1 and group 2, respectively.  $N_1$ ,  $N_2$  are the size of data of group 1 and group 2, respectively.

To analyze the results, we can reject the null hypothesis and accept the alternative hypothesis if the computed  $t$  value is larger than the critical  $t$  value which can be found in the  $t$ -distribution table or Student's table. Then, we can deduce that the mean values of the two groups are significantly different. Otherwise, we cannot reject the null hypothesis since we don't have sufficient evidence that the two groups are significantly different. This means that there is a significant difference between the tested data sets.

### Terrain Ruggedness Index

The TRI maps were created to define the amount of the difference in elevations between adjacent cells of each DEM. To generate TRI maps for a certain DEM, the focal statistics layers for the raster DEM were calculated (mean focal, min. focal, and max. focal) with the aid of focal statistics function. The focal statistics layers were converted into TRI maps by the raster calculator function in GIS software using the following formula (Mukherjee and Singh 2020).

$$TRI \text{ map} = \frac{\text{Mean focal} - \text{Min focal}}{\text{Max focal} - \text{Min focal}} \quad (7)$$

The TRI values were classified into 3 classes according to the degree of roughness. The three classes are high, medium, and low. The range of each class was defined by the following table suggested by (Riley *et al.* 1999) (Table 2).

Table 2. Classification of terrain ruggedness index.

Roughness Length (m)	Elevation Difference (m)	Riley <i>et al.</i> (1999) Classification	Our Classification
0.005	0–80	Level	Low
0.03	81–116	Nearly level	Low
0.10	117–161	Slightly rough	Medium
0.25	162–239	Intermediately rough	Medium
0.5	240–497	Moderately rough	Medium
1	498–958	Highly rough	High
>1	959–4367	Extremely rough	High

## Results and Discussion

To better understand the nature of the study area, we generated aspect, slope, hillshade, and landcover maps as shown in Figure 2. The landcover map at 10 m resolution in Figure 2a shows the classification and the multiple uses of land. We can observe that most of the area is covered by scrub or shrub lands. The upper right side and the lower left side of the land cover map are covered by trees. The majority of the population exists in Port-au-Prince city, the capital of Haiti, represented by the big red spot in the middle of the area. The rest of the population is distributed randomly throughout the country. The crops most existed around the red spots or very close to them.

The slope and aspect maps in Figures 2b and 2c show the terrain steepness in degrees and the direction of the terrain slope, respectively. In Figure 2c, most of the land slopes towards the south and southeast directions. The sudden changes from south to north directions all over

the areas can reveal the approximate locations of the tops of mountain ranges. The slopes of the terrain were classified into four classes: flat to gentle slopes  $<2^\circ$ , moderate  $2^\circ\text{--}6^\circ$ , steep  $6^\circ\text{--}25^\circ$ , and very steep or mountainous  $>25^\circ$ . In Figure 2b, many spots in the region witness steep slopes exceeding  $25^\circ$ . By matching Figures 2a and 2b, we can notice that the flat areas with slopes ranging from  $0^\circ$  to  $2^\circ$  (the gray colored areas in Figure 2b) are built areas (the red colored areas in Figure 2a) mixed with crops and water (the orange and blue colored areas in Figure 2a), and there is where the population resides. The rest of the area ranges from steep ( $6^\circ$  to  $25^\circ$ ) to mountainous slopes ( $>25^\circ$ ). The hillshade map in Figure 2d provides a clearer picture of the topography by enhancing the 3D appearance of the terrain by simulating the sunlight effect (i.e., shading and illumination) while taking into consideration the slope and aspect of the terrain.

## Elevations Accuracy Assessment

Elevation maps show areas of highs and lows. By comparing the elevation maps for the same area from different data sources, we can reveal the visual differences of each data source in representing the elevations of the terrain in relation to the reference elevation map. The elevation maps of ASTER DEM, SRTM DEM, ALOS DEM, Copernicus DEM, FABDEM, and lidar DTM are shown in Figure 3.

Figure 3 shows that there is no obvious difference in elevations between SRTM DEM, ALOS DEM, Copernicus DEM, FABDEM, and lidar DTM. ASTER DEM in Figure 3a has a problem representing heights in many spots. Unlike other DEMs, it underestimates the heights in the very steep terrain slopes, which leads to the heights being shown to be less than they should be. All the DEMs show that the lower right and the lower left parts of Haiti contain the highest terrain elevations. According to

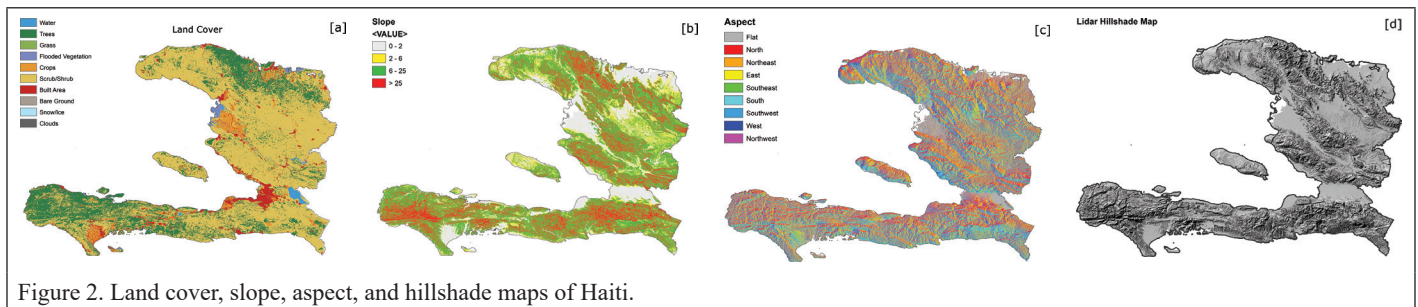


Figure 2. Land cover, slope, aspect, and hillshade maps of Haiti.

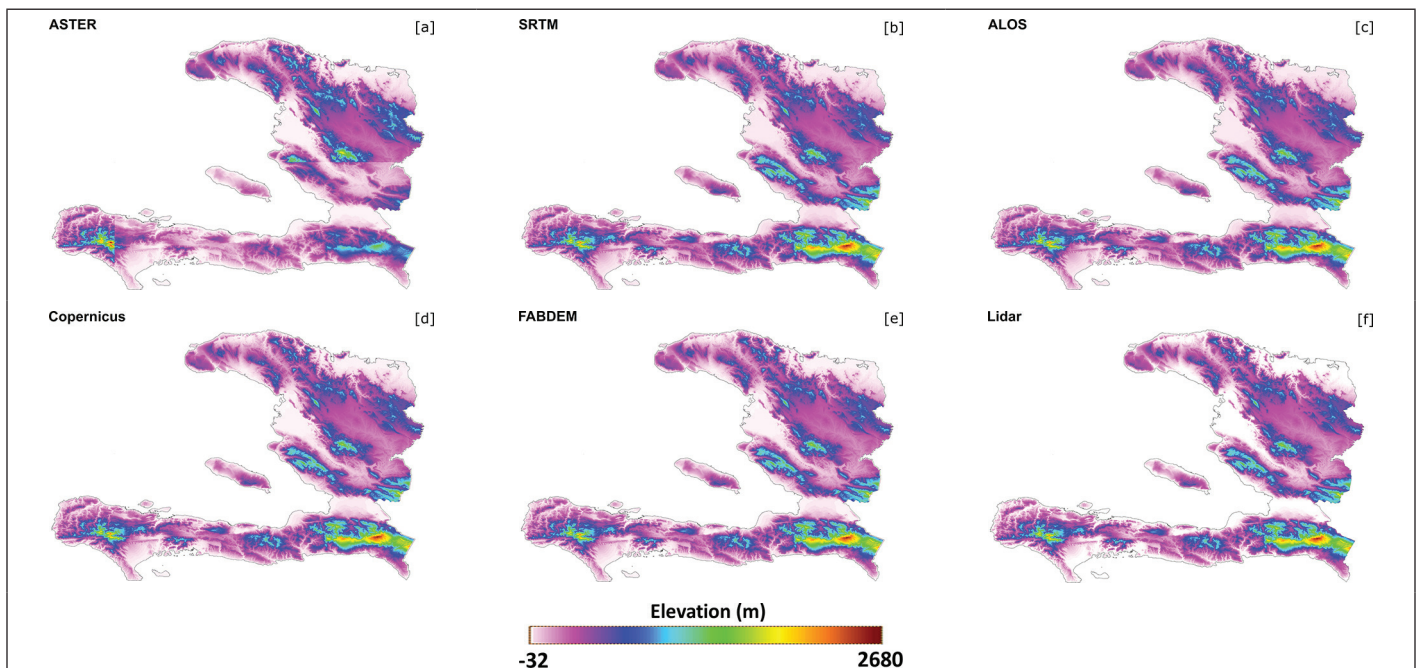


Figure 3. The elevation maps of ASTER DEM, SRTM DEM, ALOS DEM, Copernicus DEM, FABDEM, and lidar DTM in Haiti. ASTER = Terra Advanced Spaceborne Thermal Emission and Reflection Radiometer; DEM = digital elevation model; DTM = digital terrain model; FABDEM = Forest And Buildings removed Copernicus DEM; SRTM = Shuttle Radar Topography Mission.

the reference lidar DTM Figure 3f, the highest terrain lies in the lower right part where the top of Pic La Selle Mountain exists. Compared to the lidar DTM, all the other DEMs slightly overestimate the elevations in flat areas represented by the light gray color. This issue appears clearly when comparing the regions in the upper right part and in the middle of all DEMs. The elevations of ASTER DEM, SRTM DEM, ALOS DEM, Copernicus DEM, and FABDEM were individually compared against the reference lidar elevations in Figure 4 to examine the relationship between them.

Figure 4 shows that SRTM DEM, ALOS DEM, Copernicus DEM, and FABDEM elevations had a very strong positive correlation  $R^2$  to the lidar terrain elevations. The ME and RMSE values of SRTM and ALOS in Figures 4b and 4c are very close to each other within (0.1–0.9 m). However, SRTM showed slightly better results than ALOS. Copernicus and FABDEM

results in Figure 4d and 4e were closer to each other than the other DEMs and provided the best results among all of them. Nevertheless, FABDEM showed better RMSE and ME than Copernicus DEM which makes it has the best correlation and the least errors. ASTER DEM in Figure 4a also showed a strong correlation to the lidar elevations but it is relatively lower than the other DEMs. Despite the strong correlation between ASTER and lidar elevations, the ASTER elevations are unreliable due to the presence of extremely high values of errors (ME = -110.4 m and RMSE = 220.9 m).

### TRI maps

The TRI maps in Figure 5 reveal the morphological features of the terrain. The TRI shows the amount of the difference in elevations between neighboring cells of each DEM. Each map shows three classes of TRI: high, medium, and low roughness.

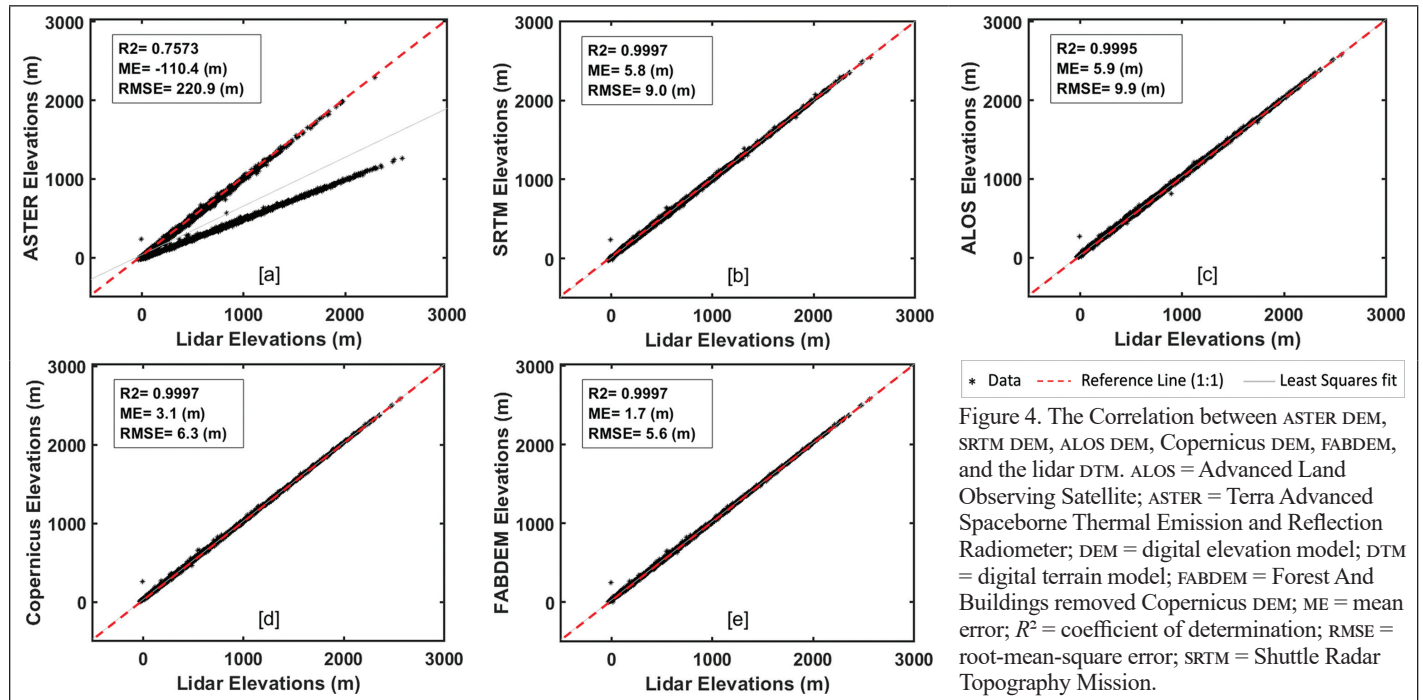


Figure 4. The Correlation between ASTER DEM, SRTM DEM, ALOS DEM, Copernicus DEM, FABDEM, and the lidar DTM. ALOS = Advanced Land Observing Satellite; ASTER = Terra Advanced Spaceborne Thermal Emission and Reflection Radiometer; DEM = digital elevation model; DTM = digital terrain model; FABDEM = Forest And Buildings removed Copernicus DEM; ME = mean error;  $R^2$  = coefficient of determination; RMSE = root-mean-square error; SRTM = Shuttle Radar Topography Mission.

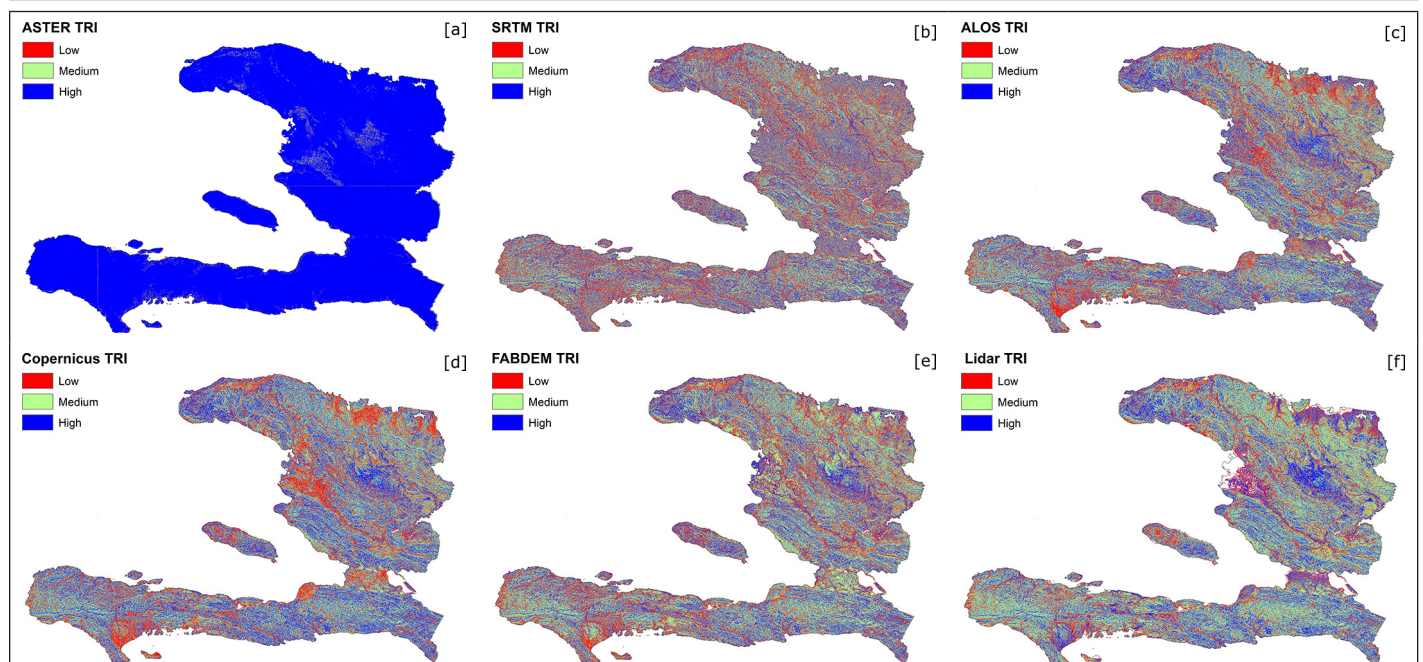


Figure 5. Roughness index maps of ASTER DEM, SRTM DEM, ALOS DEM, Copernicus DEM, FABDEM, and the lidar DTM. ALOS = Advanced Land Observing Satellite; ASTER = Terra Advanced Spaceborne Thermal Emission and Reflection Radiometer; DEM = digital elevation model; DTM = digital terrain model; FABDEM = Forest And Buildings removed Copernicus DEM; SRTM = Shuttle Radar Topography Mission; TRI = Terrain Ruggedness Index.

Since the study area is quite wide, the classes in the subfigures of Figure 5 seem to be intermixed. However, in the reference data in Figure 5f, we can see that most of the area ranges from high to medium roughness. Clear spots of high rough terrain appear in the middle, the upper left, and the upper right parts, presented in blue color. Figures 5c and 5e show that ALOS DEM and FABDEM have the closest morphology to the terrain represented by the reference lidar data. However, unlike FABDEM, ALOS DEM slightly smooths the terrain than it should be. This makes FABDEM the best DEM to visually represent the terrain roughness. ASTER DEM showed the inability to visualize the roughness of the earth accurately, as it displayed all the terrain as very rough, and this is contrary to what the lidar shows because the terrain varies in roughness from one place to another. SRTM DEM in Figure 5b also showed a bad ability to represent the terrain roughness, especially in mountainous areas, where it showed the ground less rough than it is.

### Slope and Aspect Maps

The slope maps in Figure 6 show the degree of steepness of the terrain represented by ASTER DEM, SRTM DEM, ALOS DEM, Copernicus DEM, FABDEM, and lidar DTM. The ability of the DEM to represent accurate slopes is highly related to the DEM resolution. The higher the resolution, the higher the accuracy.

In Figure 6, all of the DEMs severely overestimated the terrain slopes. Since the DEMs have a 30 m resolution which is much lower than the lidar data (1.5 m resolution), the slopes represented by the lidar data are more accurate than the ones represented by the lower resolution DEMs. Also, there is no obvious difference in the generated slope maps of ASTER DEM, SRTM DEM, ALOS DEM, Copernicus DEM, and FABDEM in Figure 6. Since the DEMs failed to calculate the accurate degree of steepness, we investigated their ability to calculate the direction of slopes (aspect) in Figure 7.

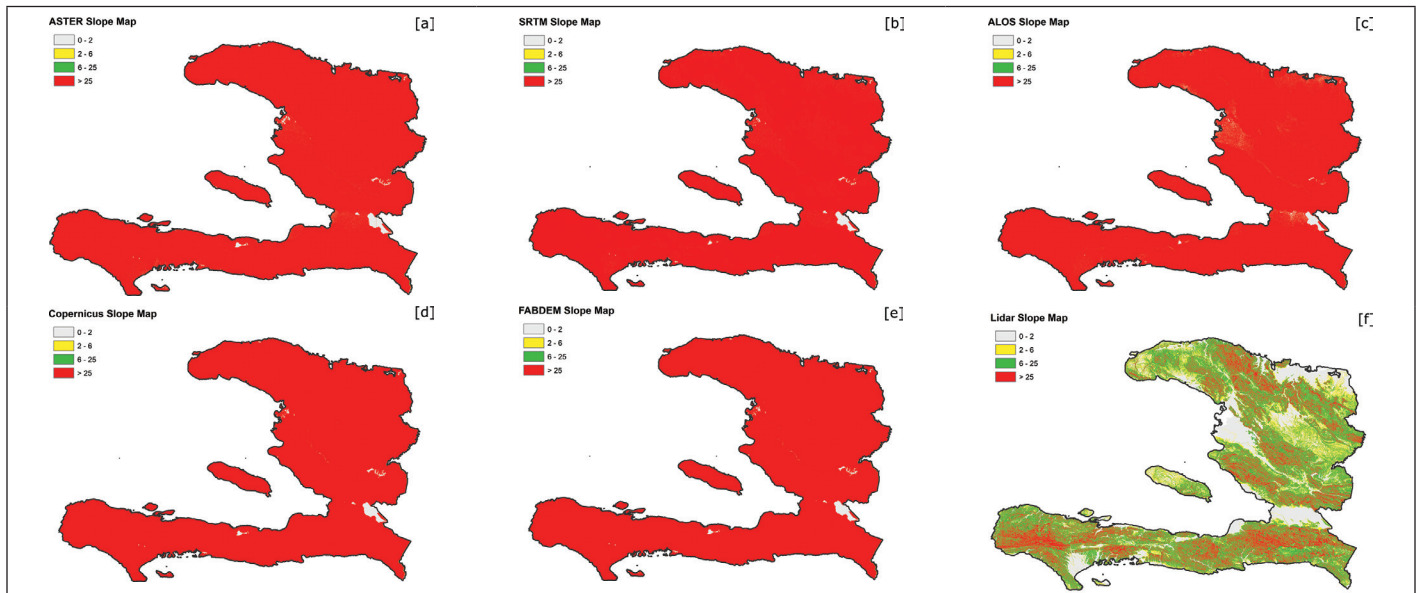


Figure 6. Slope maps of ASTER DEM, SRTM DEM, ALOS DEM, Copernicus DEM, FABDEM, and the lidar DTM. ALOS = Advanced Land Observing Satellite; ASTER = Terra Advanced Spaceborne Thermal Emission and Reflection Radiometer; DEM = digital elevation model; DTM = digital terrain model; FABDEM = Forest And Buildings removed Copernicus DEM; SRTM = Shuttle Radar Topography Mission.

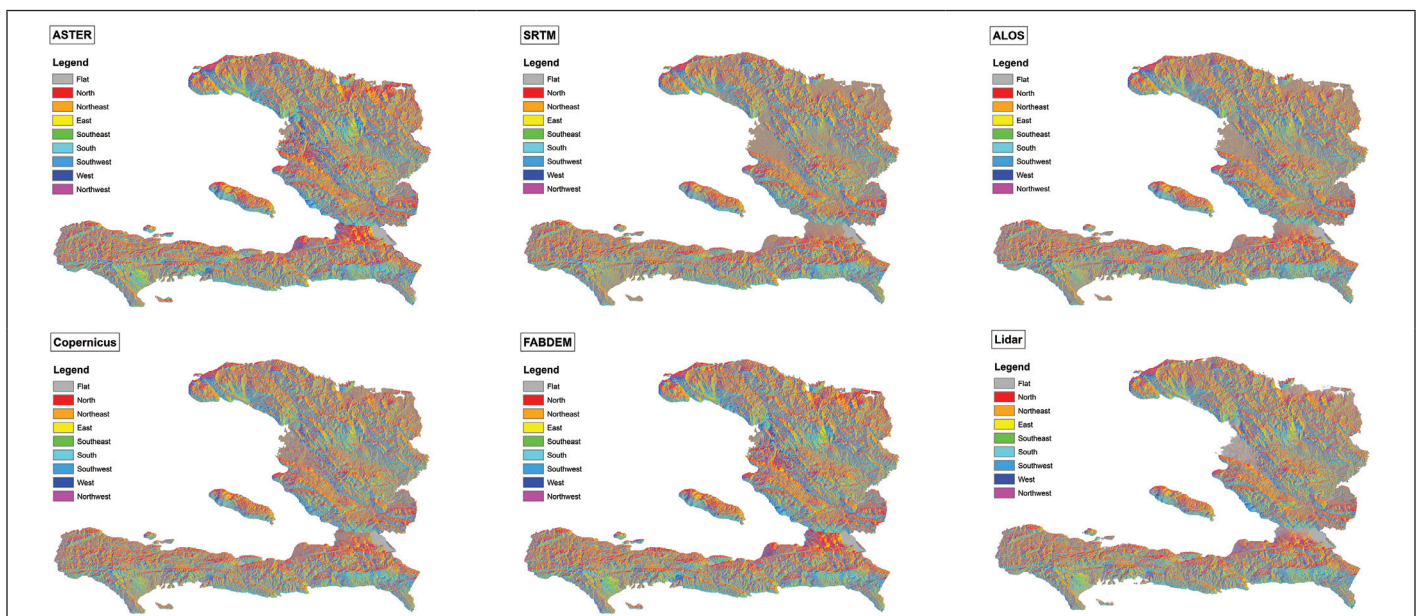


Figure 7. Aspect maps of ASTER DEM, SRTM DEM, ALOS DEM, Copernicus DEM, FABDEM, and the lidar DTM. ALOS = Advanced Land Observing Satellite; ASTER = Terra Advanced Spaceborne Thermal Emission and Reflection Radiometer; DEM = digital elevation model; DTM = digital terrain model; FABDEM = Forest And Buildings removed Copernicus DEM; SRTM = Shuttle Radar Topography Mission.

In Figure 7, the FABDEM, ASTER DEM, and Copernicus DEM aspect maps show obvious differences than the lidar aspect map, especially in the urban areas in the upper left side of the map. These areas were represented by gray color in the lidar aspect map; however, they were represented by different colors in the abovementioned DEMs. The SRTM and ALOS DEMs seem to have a closer representation to the lidar aspect map. Despite that, the SRTM DEM, ALOS DEM, Copernicus DEM, and FABDEM succeeded in displaying a reasonable height, aspect and roughness values close to the lidar DTM, they completely failed to provide accurate terrain slopes. Therefore, we performed error analysis to examine whether the nature of the study area (steepness, roughness, and aspect) caused this significant error in the topographic representation of DEMs.

### Error Analysis

Due to the mountainous nature of the study area, it was necessary to examine the impact of slopes, roughness, and aspect of the terrain on producing errors in the elevation models. Therefore, we plotted the residual errors of each DEM against the slopes as shown in Figure 8, against the terrain roughness (Figure 9), and against the terrain aspect (Figure 10). Also, we calculated the  $R^2$  to measure the degree of correlation between the errors and these factors.

In Figure 8, we can see that the error range of all the DEMs is in the negative direction, which shows that the DEMs overestimated the slopes of the terrain. Figure 8 shows a strong positive correlation between the increase in the terrain slopes and the errors resulting from all DEMs (Hernández 2021). We can also notice that the SRTM is more affected by the slopes than ASTER and ALOS DEM. Therefore, ASTER and ALOS DEM were used to correct and fill in the blanks in SRTM DEM in the steep mountainous areas (JPL 2021; Reuter *et al.* 2007; Yue *et al.* 2017). The FABDEM was not exempt from the slope effect; on the contrary, it was found that FABDEM and Copernicus DEM were the most affected by the slopes, as they showed the strongest correlation values as in Figures 8d and 8e. The correlation coefficients for Copernicus DEM and FABDEM are 0.9691 and 0.9688, respectively. This means that there was no improvement in reducing the influence of slope in FABDEM than it was in Copernicus DEM. ALOS DEM had the lowest value in the correlation coefficient shown by Figure 8c, which indicates that it is the least affected by slopes, yet the influence of slopes on its errors remains very strong. After we examined the effect of slopes on the DEMs error, we examined the effect of the terrain roughness on the DEMs error as shown in Figure 9.

In Figure 9, all the DEMs' errors showed very weak correlations to the increase in the terrain roughness. ASTER DEM in Figure 9a was the

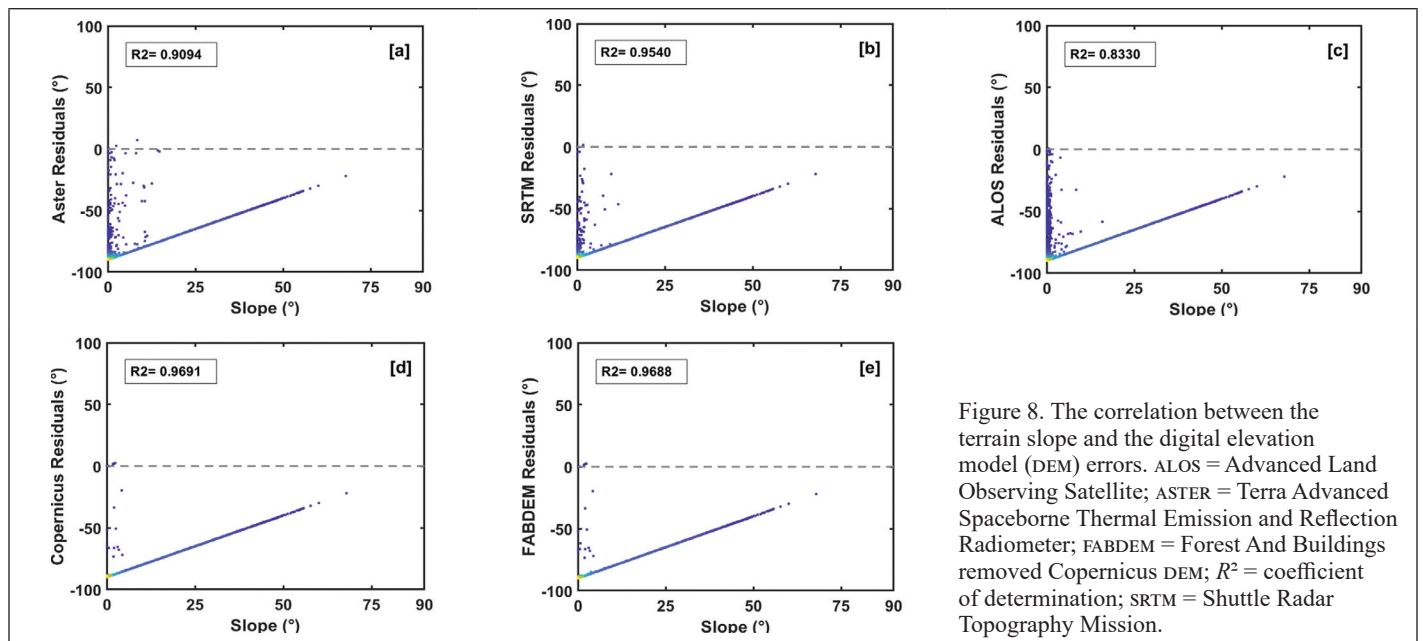


Figure 8. The correlation between the terrain slope and the digital elevation model (DEM) errors. ALOS = Advanced Land Observing Satellite; ASTER = Terra Advanced Spaceborne Thermal Emission and Reflection Radiometer; FABDEM = Forest And Buildings removed Copernicus DEM;  $R^2$  = coefficient of determination; SRTM = Shuttle Radar Topography Mission.

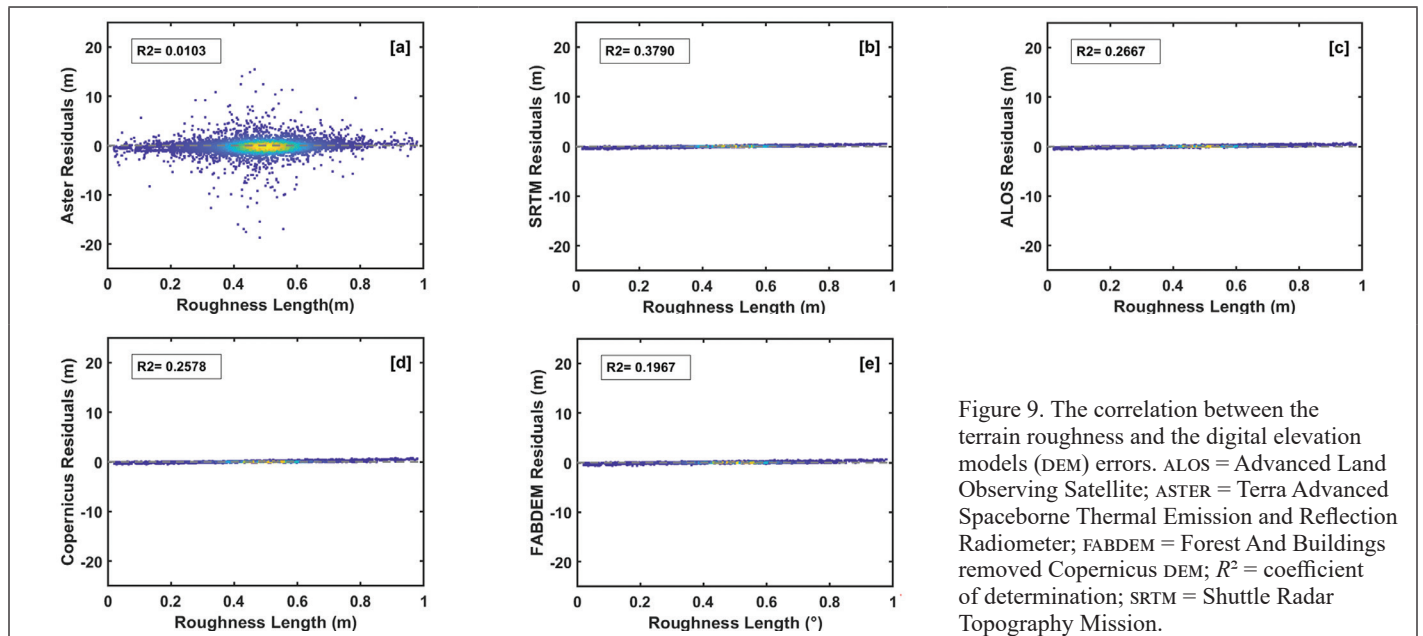


Figure 9. The correlation between the terrain roughness and the digital elevation models (DEM) errors. ALOS = Advanced Land Observing Satellite; ASTER = Terra Advanced Spaceborne Thermal Emission and Reflection Radiometer; FABDEM = Forest And Buildings removed Copernicus DEM;  $R^2$  = coefficient of determination; SRTM = Shuttle Radar Topography Mission.

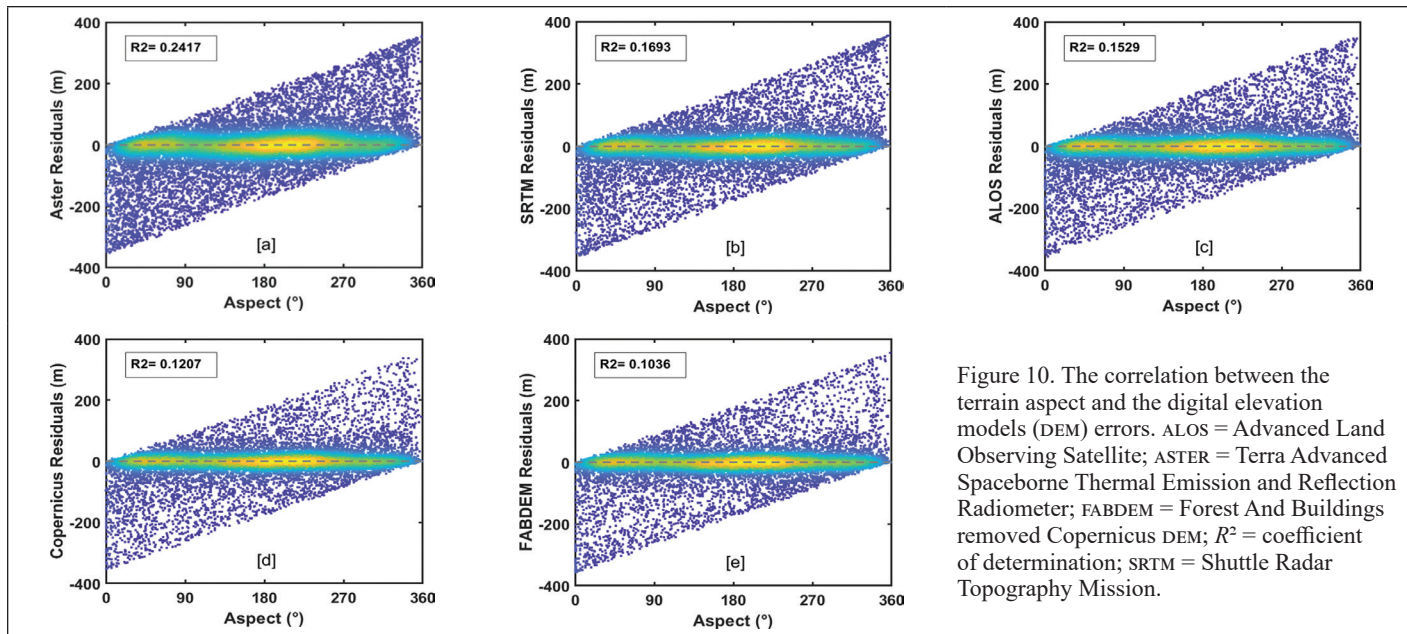


Figure 10. The correlation between the terrain aspect and the digital elevation models (DEM) errors. ALOS = Advanced Land Observing Satellite; ASTER = Terra Advanced Spaceborne Thermal Emission and Reflection Radiometer; FABDEM = Forest And Buildings removed Copernicus DEM;  $R^2$  = coefficient of determination; SRTM = Shuttle Radar Topography Mission.

least affected by this factor as it showed the lowest correlation coefficient. FABDEM in Figure 9e was less affected by the terrain roughness than Copernicus DEM in Figure 9d, where smoothing of the terrain surface was done (Hawker *et al.* 2022), which led to a reduction in the errors caused by the roughness of the surface. The SRTM DEM in Figure 9b was the most affected by the roughness of the terrain (Braun and Fotopoulos 2007). However, the relationship between residual errors and roughness is still very weak.

Similar to the roughness, all the DEMs' errors in Figure 10 showed very weak correlations to the terrain aspect. The FABDEM Figure 10e had a weaker correlation to aspect than Copernicus DEM Figure 10d and the other three DEMs which means it is the least affected by this factor. On the other hand, ASTER DEM Figure 10a showed the strongest correlation to the terrain aspect among the DEMs followed by SRTM DEM Figure 10b and ALOS DEM Figure 10c. Although the DEMs errors in Figure 10 show obvious increasing trends with the terrain aspect, the correlation values prove the weak relationship between the change in the terrain aspect and the residual errors in the DEMs. However, Figure 8 shows that there are very strong correlations between the slope magnitude and the DEMs errors.

### Error Quantification of DEMs

In the previous sections, we visualized the errors in the DEMs and investigated the effect of the terrain slope and terrain roughness in producing these errors. In this section, we are concerned with quantifying the errors in terms of vertical errors, errors in representing the terrain slope, errors in representing the terrain roughness, and the errors caused by the land cover types.

#### DEMs Overall Vertical Errors

We selected 20 000 randomly distributed points covering the whole study area from the lidar DTM and their corresponding locations in DEMs to check the overall vertical accuracy of the ASTER DEM, SRTM DEM, ALOS DEM, Copernicus DEM, and FABDEM. The mean elevations, median elevations, SD, and RMSE were calculated and listed in Table 3.

In Table 3, the FABDEM showed the best vertical accuracy among the other DEMs in terms of RMSE where the vertical accuracy was improved by 0.737 m than Copernicus DEM. The mean elevation of FABDEM was the closest to the mean elevation of the lidar DTM with a difference of about 1.7 m, followed by Copernicus DEM with a difference of about 3 m. The mean elevation values of the other DEMs ranged from about 5.8 m to 110.4 m. The SD measures the amount of variability from the individual elevation values to the mean elevation (Asal 2019; Wu *et al.* 2018). All the DEMs except for ASTER DEM showed very close SD values. The difference between the accuracy of SRTM DEM and ALOS DEM was 0.887 m and the vertical error in both DEMs was less than 10

Table 3. The overall vertical accuracy of ASTER DEM, SRTM DEM, ALOS DEM, Copernicus DEM, and FABDEM.

DEM	Mean (m)	Median (m)	SD (m)	RMSE (m)
ASTER	271.213	211.560	264.187	220.928
SRTM	387.396	297.310	370.221	8.989
ALOS	387.542	296.860	370.057	9.876
Copernicus	384.671	294.500	369.849	6.297
FABDEM	383.309	293.168	369.521	5.560
Lidar	381.596	291.140	370.208	0.20

ALOS = Advanced Land Observing Satellite; ASTER = Terra Advanced Spaceborne Thermal Emission and Reflection Radiometer; DEM = digital elevation model; FABDEM = Forest And Buildings removed Copernicus DEM; RMSE = root-mean-square error; SRTM = Shuttle Radar Topography Mission; SD = standard deviation.

m. Although ASTER DEM showed higher vertical accuracy than SRTM in mountainous areas (Yue *et al.* 2015; Osama *et al.* 2022), the error value in ASTER DEM in our test area was extremely high (RMSE = 220.9 m), which indicates that this DEM is invalid for use in this area. In general, the SRTM DEM is superior to ASTER DEM in the non-void areas, but in the void areas, the vertical accuracy of the SRTM DEM becomes less than the vertical accuracy of the ASTER DEM. This justifies the discrepancy of previous research when comparing the accuracy of both DEMs in mountainous regions (Liu *et al.* 2019; Yue *et al.* 2015).

#### Errors in Representing the Terrain Slopes, Aspect, and Roughness

To quantify the error value of terrain slope, aspect, and roughness for the DEMs, we calculated the mean absolute error (MAE), the RMSE, and the SD for each model. The results are listed in Table 4.

In general, all the models in Table 4 showed an error in calculating the slopes of this area, which led to a significant deterioration of the accuracy. Table 4 also shows that the FABDEM didn't have the best accuracy of slope in terms of RMSE compared to the other DEMs. In addition, there was not a noticeable difference between Copernicus DEM MAE and RMSE, and FABDEM MAE and RMSE which means that they almost have the same accuracy of slope representation. The minimum error values of slope existed in ALOS DEM and the max error value existed in Copernicus DEM.

FABDEM and Copernicus DEM showed the highest MAE values of the terrain aspect, while ALOS DEM showed the lowest MAE value. The Copernicus DEM and FABDEM had the lowest RMSE values, while ASTER DEM and SRTM DEM had the highest RMSE value of aspect. Both MAE and RMSE values of FABDEM and Copernicus DEM show that there is a deterioration in the FABDEM accuracy than Copernicus DEM in calculating the terrain aspect.

Concerning the accuracy of the surface roughness, the FABDEM was slightly better than Copernicus DEM and both were slightly better than other DEMs. ASTER DEM showed the highest value of RMSE than the other DEMs which means it had the worst accuracy of the terrain roughness representation among them.

#### Errors Caused by the Land Cover Types

In order to examine the vertical accuracy of each DEM over the different types of land, we made a classification of the area using the 10 m resolution *Sentinel-2* satellite data. We found that there are eight types of land cover. Therefore, we classified the 20 000 points taken from lidar data into eight classes as follows: water, trees, grass, flooded vegetation, crops, shrub, built area, and bare ground. We made a comparison shown by the bar graphs in Figure 11 between the DEMs RMSE over the different land cover types.

According to Figure 11, we can group the DEMs in terms of accuracy into three groups. FABDEM and Copernicus DEM are in the first group. SRTM DEM and ALOS DEM are in the second group. ASTER DEM is in the last group. Within each group, the DEMs have vertical accuracies close to each other. The FABDEM had the lowest RMSE value and ME among DEMs showing the best accuracy in trees area, grass area, crops, and shrub land. Copernicus DEM had the highest accuracy over water areas in terms of RMSE and ME. It also had the lowest RMSE value over the flooded vegetation. ASTER DEM showed the highest RMSE and ME values among DEMs over all the land cover types. The average difference of the RMSE between Copernicus DEM and FABDEM is approximately 0.43 m.

Figure 11 also shows that in the flooded vegetation, trees, and grass areas, the RMSE values of all DEMs were higher than the values in the other land types. The values of RMSE in those areas ranged between 5.5

m and 12.5 m. The RMSE values for all the DEMs were the lowest over the water areas ranging between 2 m and 4.5 m. In the case of crops, shrubs, built areas, and bare ground areas, the RMSE values ranged between 2.5 m and 9.5 m. The low RMSE values of DEMs in water because the points are located in an area represented by a relatively flat surface (water surface). However, the more complex the surface becomes (heights ranging from crops and trees to high buildings), the higher the RMSE value is expected to be. Especially, with the existence of some unfiltered above-ground features where the top of these features will normally affect the sensor (Athmania and Achour 2014). In order to visualize the variations between the ME of the DEMs over land cover types, we plotted the ME values in Figure 12a. Since we are particularly concerned with FABDEM and how it evolved from Copernicus DEM, we draw the ME of FABDEM and Copernicus DEM in Figure 12b to detect the reduction of error if existed.

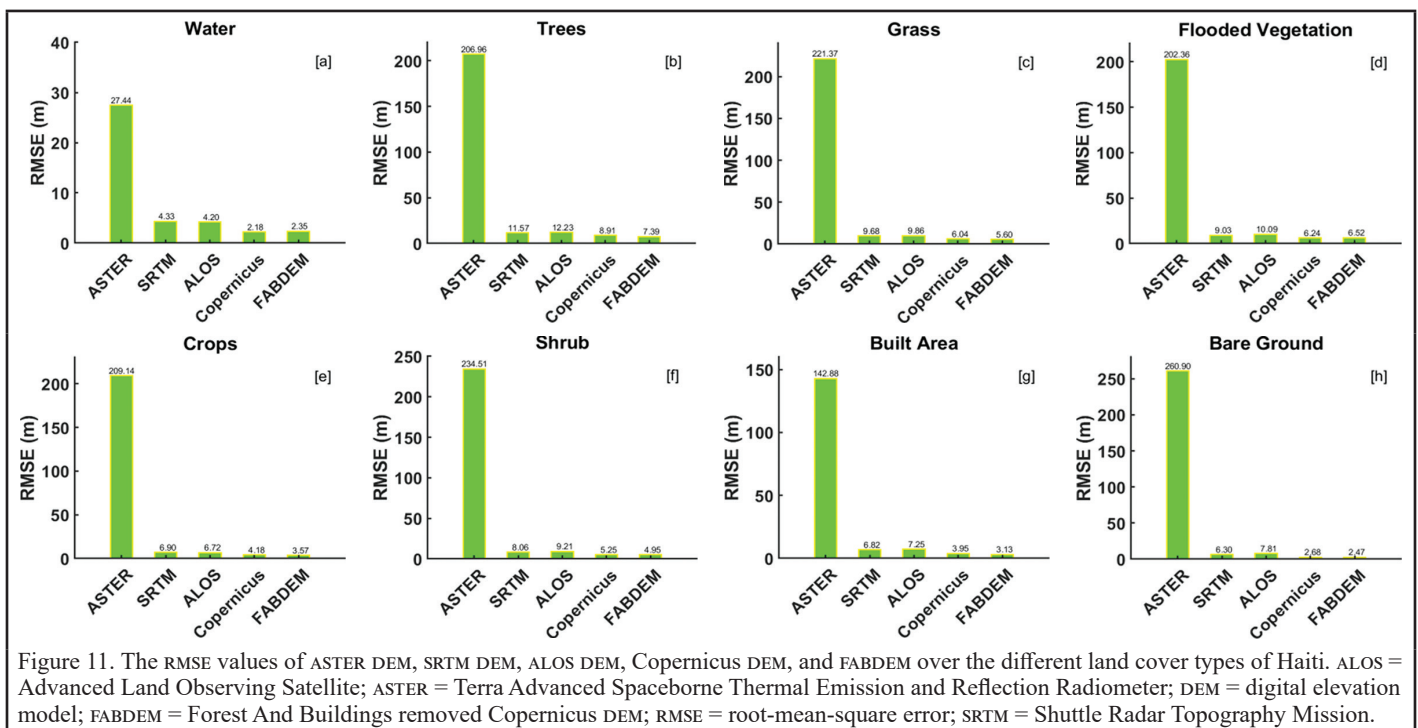
Figure 12a shows a comparison between the ME of the DEMs in the water areas, trees, grass, flooded vegetation, crops, scrub, built area, and bare ground. In general, SRTM DEM, ALOS DEM, Copernicus DEM, and FABDEM have relatively low values of ME in water areas compared to the other land cover types. The error values range between -1.376 m and 0.163 m. Similar to the RMSE values, ASTER DEM has the highest ME among DEMs. The maximum error of ASTER DEM exists in the shrub land and the minimum error exists in the water areas.

Since the FABDEM has been filtered where buildings and trees were removed from it, it is expected that the error rate in modeling the terrain in the tree areas and built areas will be reduced than it was in Copernicus DEM. Looking at Figure 12b, we can see an improvement in the mean error in the tree areas, as shown by the green line. The error has been reduced by approximately 3.34 m. In the built areas and

Table 4. Statistical errors of the terrain slope and roughness length of DEMs.

DEM	Slope			Aspect			Roughness Length		
	MAE (°)	SD (°)	RMSE (°)	MAE (°)	SD (°)	RMSE (°)	MAE (m)	SD (m)	RMSE (m)
ASTER	77.217	2.481	77.95	4.390	93.680	90.36	0.217	1.076	1.100
SRTM	77.205	2.673	77.94	4.197	95.104	77.96	0.006	0.090	0.106
ALOS	76.651	6.090	77.50	3.105	94.159	71.47	0.009	0.101	0.104
Copernicus	77.319	1.724	78.04	6.248	94.348	63.53	0.015	0.101	0.097
FABDEM	77.306	1.717	78.03	6.329	96.805	65.93	0.010	0.107	0.096

ALOS = Advanced Land Observing Satellite; ASTER = Terra Advanced Spaceborne Thermal Emission and Reflection Radiometer; DEM = digital elevation model; FABDEM = Forest And Buildings removed Copernicus DEM; MAE = mean absolute error; RMSE = root-mean-square error; SD = standard deviations; SRTM = Shuttle Radar Topography Mission.



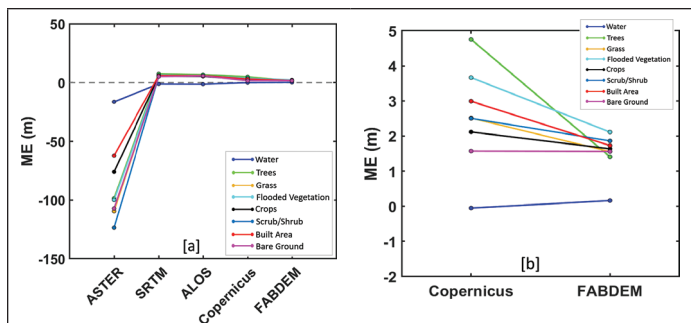


Figure 12. The ME values of ASTER DEM, SRTM DEM, ALOS DEM, Copernicus DEM, and FABDEM over the different land cover types of Haiti. ALOS = Advanced Land Observing Satellite; ASTER = Terra Advanced Spaceborne Thermal Emission and Reflection Radiometer; FABDEM = Forest And Buildings removed Copernicus DEM; ME = mean error; SRTM = Shuttle Radar Topography Mission.

flooded vegetation, the error values were reduced by approximately 1.26 m and 1.55 m, respectively. There is an improvement in the error over the other types of land that does not exceed 1 m. But there is a slight increase in the amount of error in the water areas by about 0.21 m. It is clear from the previous results and analyses that there are many improvements in FABDEM over Copernicus DEM in many aspects, but the question here is, are those improvements significant in order to say that FABDEM is actually different from Copernicus DEM?

To answer this question, we subjected all the DEMs' elevations to the Gaussian fitting to test their normality. Then, we performed a two-tailed Welch's t-test for independent samples. The results are shown in Table 5 and Figure 13.

Table 5. Results of a two-tailed Welch's t-test for the elevations of Copernicus digital elevation model (DEM) and Forest And Buildings removed Copernicus DEM (FABDEM).

Group	N	Mean (m)	SD (m)	t	df	p	Significantly different? (P < 0.05)
Copernicus	19 421	384.7	369.8	0.3627	19420	0.9012	No
FABDEM	19 421	383.3	369.5				

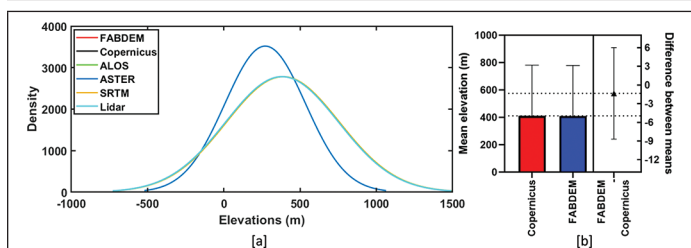


Figure 13. Normal distribution curves and Welch's t-test results for Copernicus DEM and FABDEM. ALOS = Advanced Land Observing Satellite; ASTER = Terra Advanced Spaceborne Thermal Emission and Reflection Radiometer; FABDEM = Forest And Buildings removed Copernicus DEM; SRTM = Shuttle Radar Topography Mission.

Before performing the t-test for Copernicus DEM and FABDEM, we tested the normality of the elevations of both DEMs as well as the other DEMs since the normality is one of the assumptions required for the t-test (Ahad and Yahaya 2014). In Figure 13a, ASTER DEM normal distribution curve is different from the other DEMs. This shows that the SRTM DEM, ALOS DEM, Copernicus DEM, and FABDEM are showing the same trend of terrain surface and they have close values of mean elevations. The statistics of the t-test listed in Table 5 and visualized in Figure 13b show that the mean elevations of two samples of 19 421 elevation values of Copernicus DEM and FABDEM are 384.7 m and 384.3 m, respectively, which are almost similar to each other. In addition, the two samples had very close values of SD of 369.8 m and 369.5

m for Copernicus DEM and FABDEM, respectively. At 95% confidence level, the *p* value was less than 0.05. This proves that the FABDEM is not significantly different from the Copernicus DEM.

## Conclusions

This research performed an evaluation of the 30 m resolution FABDEM, ASTER DEM, SRTM DEM, ALOS DEM, and Copernicus DEM. The following Table 6. summarizes the general characteristics of each DEM as well as the important results obtained from our study.

Table 6 shows that there was about 0.73 m enhancement in the overall vertical accuracy of FABDEM over Copernicus DEM. However, new errors appeared in the FABDEM during data resampling and interpolation process. These errors contributed to the fact that the improvement in the elevations of FABDEM was not significant compared to Copernicus DEM as proven by Welch's t-test. Compared to ASTER, SRTM, and ALOS DEMs, both Copernicus and FABDEM had higher absolute vertical accuracies. Yet, FABDEM was slightly superior to Copernicus DEM. It was found that the terrain slope contributed to most of the errors that existed in all DEMs. Since the majority of the study area has rough terrain with mountainous slopes, all the DEMs failed to provide accurate representations of the slopes. The Copernicus DEM and the FABDEM had the highest correlation to the slope, which means the errors in both DEMs are the most influenced by this factor. The FABDEM and Copernicus DEM showed the highest MAE values of the terrain aspect among DEMs. In addition, there was a deterioration in the FABDEM accuracy (MAE and RMSE) than Copernicus DEM in the terrain aspect representation. There was a false representation of the terrain roughness in urban areas by ASTER DEM, Copernicus DEM, and FABDEM. In addition, the Copernicus DEM appeared smoother than the FABDEM (as previously shown in Figure 5d and 5e), which was not expected since the FABDEM was postprocessed to smooth the surface after the filtration process. However, according to the roughness length RMSE and TRI maps visual analysis, the FABDEM seems to have a better representation of the terrain roughness compared to the reference lidar than Copernicus DEM. Despite that, the buildings and the trees should have been removed from the FABDEM DEM, the RMSE values in the built area and the trees' area were only reduced by 0.82 m and 1.52 m, respectively, and the RMSE of the bare ground was reduced by 0.2 m. Our study highlights that despite the good vertical accuracy of the tested DEMs, they showed low accuracies of slope and aspect representation, which should be noticed when using these DEMs to create aspect and slope maps and not count only on the vertical accuracy of the DEM. In terms of land cover, the Copernicus DEM provided the best vertical accuracy in the water areas and flooded vegetation areas. However, the FABDEM was superior to the other DEMs vertical accuracy in the trees area, grass area, crops, and shrub lands in addition to built area and bare ground. To conclude, regardless of the existing errors in the FABDEM, it is currently the best global DEM to estimate the terrain elevations in the steep mountainous topography.

## Acknowledgments

The FABDEM was downloaded from the University of Bristol via (<https://data.bris.ac.uk/data/dataset/25wfy0f9ukoge2gs7a5mqpq2j7>). ALOS 3D world data was downloaded from the Japan Aerospace Exploration Agency ([https://www.eorc.jaxa.jp/ALOS/en/dataset/aw3d30/aw3d30\\_e.htm](https://www.eorc.jaxa.jp/ALOS/en/dataset/aw3d30/aw3d30_e.htm)). ASTER and SRTM were downloaded from the National Aeronautics and Space Administration (<https://search.earthdata.nasa.gov/search>). Copernicus was downloaded from Open Topography (<https://portal.opentopography.org/raster?opentopoID=O-TSDEM.032021.4326.3>). The land cover data was downloaded from (<https://www.arcgis.com/home/item.html?id=d3da5dd386d140cf93fc9ecbf8da5e31>).

This work was supported in part by the National Natural Science Foundation of China under Grant 42090012, in part by the Guangxi science and technology program (Guangxi key R & D plan, GuiKe 2021AB30019), 03 special research and 5G project of Jiangxi Province in China (20212ABC03A09); Zhuhai industry university research cooperation project of China (ZH22017001210098PWC); Sichuan



Table 6. General characteristics and accuracy of the 30 m resolution FABDEM, ASTER DEM, SRTM DEM, ALOS DEM, and Copernicus DEM.

Characteristic	Copernicus				
	ASTER DEM	SRTM DEM	ALOS DEM	DEM	FABDEM
Resolution (m)	30	30	30	30	30
Spatial coverage	83° N–83° S	60° N–56° S	Global	Global	51.6° N–51.6° S
Mission	the Advanced Spaceborne Thermal Emission and Reflection Radiometer	Shuttle Radar Topography	Advanced Land Observing Satellite	TanDEM-X	TanDEM-X
Collecting instrument type	Optical	Radar	Optical	Radar	Radar
Tested version	V3	V3	V3.2	V1	V1
Released	2019	2015	2022	2021	2022
Institution	METI, NASA	NASA, USGS, NGA	JAXA	ESA	University of Bristol
Average mean error (ME m)	–110.400	5.800	5.900	3.100	1.700
Absolute vertical accuracy (RMSE m)	220.928	8.989	9.876	6.297	5.560
Slope maps error (RMSE °)	77.950	77.940	77.500	78.040	78.030
Aspect maps error (RMSE °)	90.360	77.960	71.470	63.530	65.930
Roughness maps error (RMSE m)	1.100	0.106	0.104	0.097	0.096
Vertical accuracy in water areas (RMSE m)	27.443	4.330	4.201	2.180	2.350
Vertical accuracy in trees areas (RMSE m)	206.960	11.566	12.232	8.907	7.391
Vertical accuracy in grass areas (RMSE m)	221.368	9.676	9.859	6.037	5.603
Vertical accuracy in flooded vegetation areas (RMSE m)	202.362	9.034	10.091	6.237	6.518
Vertical accuracy in crops areas (RMSE m)	209.141	6.897	6.722	4.185	3.566
Vertical accuracy in shrub areas (RMSE m)	234.508	8.06	9.208	5.249	4.952
Vertical accuracy in built areas (RMSE m)	142.884	6.817	7.248	3.95	3.128
Vertical accuracy in bare ground (RMSE m)	260.905	6.296	7.808	2.679	2.474

ALOS = Advanced Land Observing Satellite; ASTER = Terra Advanced Spaceborne Thermal Emission and Reflection Radiometer; DEM = digital elevation model; FABDEM = Forest And Buildings removed Copernicus DEM; ESA = European Space Agency; JAXA = Japanese Aerospace Exploration Agency; ME = mean error; METI = Ministry of Economy, Trade and Industry; NASA = National Aeronautics and Space Administration; NGA = National Geospatial-Intelligence Agency; RMSE = root-mean-square error; SRTM = Shuttle Radar Topography Mission; USGS = United States Geological Survey.

Science and Technology Program (2022YFN0031); Hubei key R & D plan (2022BAA048), and Zhizhuo Research Fund on Spatial-Temporal Artificial Intelligence (Grant No. ZZJJ202202). The authors have no competing interests to declare.

## References

- Abrams, M., R. Crippen and H. Fujisada. 2020. ASTER global digital elevation model (GDEM) and ASTER global water body dataset (ASTWBD). *Remote Sensing* 12:1–12. <https://doi.org/10.3390/rs12071156>.
- Ahad, N. A. and S.S.S. Yahaya. 2014. Sensitivity analysis of Welch's t-test. Pages 888–893 in *Proceedings AIP Conference*. <https://doi.org/10.1063/1.4887707>.
- Airbus Defence and Space. 2020. *Copernicus DEM (Digital Elevation Model) Product Handbook*. <[https://spacedata.copernicus.eu/documents/20126/0/GEO1988-CopernicusDEM-SPE-002\\_ProductHandbook\\_11.00.pdf](https://spacedata.copernicus.eu/documents/20126/0/GEO1988-CopernicusDEM-SPE-002_ProductHandbook_11.00.pdf)> Accessed 30 January 2023
- Amatulli, G., S. Domisch, M. N. Tuanmu, B. Parmentier, A. Ranipeta, J. Malczyk and W. Jetz. 2018. A suite of global, cross-scale topographic variables for environmental and biodiversity modeling. *Science Data* 5:1–15. <https://doi.org/10.1038/sdata.2018.40>.
- Asal, F.F.F. 2019. Creation and analysis of Earth's surface roughness maps from airborne LiDAR measurements in downtown urban landscape. *Journal of Geographic Information Systems* 11:212–238. <https://doi.org/10.4236/jgis.2019.112015>.
- Athmania, D. and H. Achour. 2014. External validation of the ASTER GDEM2, GMTED2010 and CGIAR-CSI-SRTM v4.1 free access digital elevation models (DEMs) in Tunisia and Algeria. *Remote Sensing* 6:4600–4620. <https://doi.org/10.3390/rs6054600>.
- Baugh, C. A., P. D. Bates, G. Schumann and M. A. Trigg. 2013. SRTM vegetation removal and hydrodynamic modeling accuracy. *Water Resources Research* 49:5276–5289. <https://doi.org/10.1002/wrcr.20412>.
- Boatner, K. 2021. Haiti. <<https://kids.nationalgeographic.com/geography/countries/article/haiti>> Accessed 30 October 2022
- Braun, A. and G. Fotopoulos. 2007. Assessment of SRTM, ICESat, and survey control monument elevations in Canada. *Photogrammetric Engineering & Remote Sensing* 73:1333–1342. <https://doi.org/10.14358/PERS.73.12.1333>.
- Carrera-Hernández, J. J. 2021. Not all DEMs are equal: An evaluation of six globally available 30 m resolution DEMs with geodetic benchmarks and LiDAR in Mexico. *Remote Sensing of Environment* 261:112474. <https://doi.org/10.1016/j.rse.2021.112474>. Accessed 15 February 2023
- Cenci, L., M. Galli, G. Palumbo, L. Sapia, C. Santella and C. Albinet. 2021. Describing the quality assessment workflow designed for DEM products distributed via the Copernicus programme. Case study: The absolute vertical accuracy of the copernicus DEM dataset in Spain. Pages 6143–6146 in *Proceedings International Geoscience and Remote Sensing Symposium (IGARSS)*. <https://doi.org/10.1109/IGARSS47720.2021.9554393>.
- Chu, T. and K. E. Lindenschmidt. 2017. Comparison and validation of digital elevation models derived from InSAR for a flat inland delta in the high latitudes of northern Canada. *Canadian Journal of Remote Sensing* 43:109–123. <https://doi.org/10.1080/07038992.2017.1286936>.
- Du, X., H. Guo, X. Fan, J. Zhu, Z. Yan and Q. Zhan. 2012. Vertical accuracy assessment of SRTM and ASTER GDEM over coastal regions of China: A comparative analysis. Pages 1236–1243 in *Proceedings 33<sup>rd</sup> Asian Conference on Remote Sensing 2012 (ACRS 2012)*, held in Pattaya, Thailand, 26–30 November 2012.
- Environmental Systems Research Institute, Inc. (ESRI). 2022. Sentinel-2 10m Land Use/Land Cover Time Series. <<https://www.arcgis.com/home/item.html?id=d3da5dd386d140cf93fc9ecbf8da5e31>> Accessed 30 January 2023
- European Space Agency (ESA). 2020. Copernicus DEM 30 Metre Dataset Now Freely Available. <[https://sentinels.copernicus.eu/web/sentinel/news/-/asset\\_publisher/xR9e/content/copernicus-dem-30-metre-dataset-now-freely-available](https://sentinels.copernicus.eu/web/sentinel/news/-/asset_publisher/xR9e/content/copernicus-dem-30-metre-dataset-now-freely-available)> Accessed 30 December 2022
- ESA. 2021. Copernicus DEM—Global and European Digital Elevation Model (COP-DEM). <https://doi.org/10.5270/ESA-c5d3d65>.
- Farr, T. G. and M. Kobrick. 2000. Shuttle radar topography mission produces a wealth of data. *Eos (Washington, DC)* 81:583–585. <https://doi.org/10.1029/EO081i048p00583>.

- Gallien, T. W., J. E. Schubert and B. F. Sanders. 2011. Predicting tidal flooding of urbanized embayments: A modeling framework and data requirements. *Coastal Engineering* 58:567–577. <https://doi.org/10.1016/j.coastaleng.2011.01.011>.
- del Rosario González-Moradas, M. and W. Viveen. 2020. Evaluation of ASTER GDEM2, SRTMv3.0, ALOS AW3D30 and TanDEM-X DEMs for the Peruvian Andes against highly accurate GNSS ground control points and geomorphological-hydrological metrics. *Remote Sensing of the Environment* 237:111509. <https://doi.org/10.1016/j.rse.2019.111509>.
- Grosse, P., B. van Wyk de Vries, P. A. Euillades, M. Kervyn and I. A. Petrinovic. 2012. Systematic morphometric characterization of volcanic edifices using digital elevation models. *Geomorphology* 136:114–131. <https://doi.org/10.1016/j.geomorph.2011.06.001>.
- Guth, P. L. and T. M. Geoffroy. 2021. LiDAR point cloud and ICESat-2 evaluation of 1 second global digital elevation models: Copernicus wins. *Transactions in GIS* 25:2245–2261. <https://doi.org/10.1111/tgis.12825>.
- Hawker, L., P. Uhe, L. Paulo, J. Sosa, J. Savage, C. Sampson and J. Neal. 2022. A 30 m global map of elevation with forests and buildings removed. *Environmental Research Letters* 17. <https://doi.org/10.1088/1748-9326/ac4d4f>.
- IGN FI. 2021. Aerial Photography, Lidar Acquisition and Derivated Products, Haiti. <<https://www.ignfi.fr/en/portfolio-item/couverture-photographique-aerienne-acquisition-lidar-haiti/>> Accessed 1 November 2022
- Jarvis, A., J. Rubiano, A. Nelson, A. Farrowand and M. Mulligan. 2004. *Practical use of SRTM data in the tropics—Comparisons with digital elevation models (No. 198)*. Cali, Columbia: Centro Internacional de Agricultura Tropical (CIAT), 32p.
- Kubaneck, J., M. P. Poland and J. Biggs. 2021. Applications of bistatic radar to volcano topography—a review of 10 years of TanDEM-X. *IEEE Journal of Selected Topics in Applied Earth Observations and Remote Sensing* 14:3282–3302. <https://doi.org/10.1109/JSTARS.2021.3055653>.
- Jet Propulsion Laboratory (JPL). 2021. Shuttle Radar Topography Mission. <<https://www2.jpl.nasa.gov/srtm/>> Accessed 30 January 2023
- Liu, K., C. Song, L. Ke, L. Jiang, Y. Pan and R. Ma. 2019. Global open-access DEM performances in Earth's most rugged region high mountain Asia: A multi-level assessment. *Geomorphology* 338:16–26. <https://doi.org/10.1016/j.geomorph.2019.04.012>.
- Liu, Z., J. Zhu, H. Fu, C. Zhou and T. Zuo. 2020. Evaluation of the vertical accuracy of open global dems over steep terrain regions using icesat data: A case study over Hunan province, China. *Sensors (Switzerland)* 20:1–16. <https://doi.org/10.3390/s20174865>.
- Marsh, C. B., P. Harder and J. W. Pomeroy. 2023. Validation of FABDEM, a global bare-earth elevation model, against UAV-lidar derived elevation in a complex forested mountain catchment. *Environmental Research Communications* 5(3). <https://doi.org/10.1088/2515-7620/acc56d>.
- Moore, I. D., R. B. Grayson and A. R. Ladson. 1991. Digital terrain modelling: A review of hydrological, geomorphological, and biological applications. *Hydrological Processes* 5:3–30. <https://doi.org/10.1002/hyp.3360050103>.
- Mukherjee, I. and U. K. Singh. 2020. Delineation of groundwater potential zones in a drought-prone semi-arid region of east India using GIS and analytical hierarchical process techniques. *Catena* 194:104681. <https://doi.org/10.1016/j.catena.2020.104681>.
- Mukherjee, S., P. K. Joshi, S. Mukherjee, A. Ghosh, R. D. Garg and A. Mukhopadhyay. 2012. Evaluation of vertical accuracy of open source Digital Elevation Model (DEM). *International Journal of Applied Earth Observation and Geoinformation* 21:205–217. <https://doi.org/10.1016/j.jag.2012.09.004>.
- National Aeronautics and Space Administration (NASA). 2015. The Shuttle Radar Topography Mission (SRTM) Collection User Guide. <[https://lpdaac.usgs.gov/documents/179/SRTM\\_User\\_Guide\\_V3.pdf](https://lpdaac.usgs.gov/documents/179/SRTM_User_Guide_V3.pdf)> Accessed 30 January 2023
- NASA JPL. 2020. NASADEM Merged DEM Global 1 Arc Second V001 [Data Set]. [https://doi.org/10.5067/MEaSURES/NASADEM/NASADEM\\_HGT.001](https://doi.org/10.5067/MEaSURES/NASADEM/NASADEM_HGT.001).
- O'Loughlin, F. E., R.C.D. Paiva, M. Durand, D. E. Alsdorf and P. D. Bates. 2016. A multi-sensor approach towards a global vegetation corrected SRTM DEM product. *Remote Sensing of Environment* 182:49–59. <https://doi.org/10.1016/j.rse.2016.04.018>.
- Osama, N., Z. Shao, Y. Ma, J. Yan, Y. Fan, S. M. Habib and M. Freeshah. 2022. The ATL08 as a height reference for the global digital elevation models. *Geo-spatial Information Science* 1–20. <https://doi.org/10.1080/10095020.2022.2087108>.
- Osama, N., B. Yang, Y. Ma and M. Freeshah. 2021. A digital terrain modeling method in urban areas by the ICESat-2 (generating precise terrain surface profiles from photon-counting technology). *Photogrammetric Engineering & Remote Sensing* 87:237–248. <https://doi.org/10.14358/pers.87.4.237>.
- Park, S. J., K. K. McSweeney and B. B. Lowery. 2001. Identification of the spatial distribution of soils using a process-based terrain characterization. *Geoderma* 103:249–272. [https://doi.org/10.1016/S0016-7061\(01\)00042-8](https://doi.org/10.1016/S0016-7061(01)00042-8).
- Rabus, B., M. Eineder, A. Roth and R. Bamler. 2003. The shuttle radar topography mission—A new class of digital elevation models acquired by spaceborne radar. *ISPRS Journal of Photogrammetry and Remote Sensing* 57:241–262. [https://doi.org/10.1016/S0924-2716\(02\)00124-7](https://doi.org/10.1016/S0924-2716(02)00124-7).
- Rentsch, H., W. Welsch, C. Heipke and M. M. Miller. 1990. Digital terrain models as a tool for glacier studies. *Journal of Glaciology* 36:273–278.
- Reuter, H. I., A. Nelson and A. Jarvis. 2007. An evaluation of void-filling interpolation methods for SRTM data. *International Journal of Geographical Information Science* 983–1008. <https://doi.org/10.1080/13658810601169899>.
- Riley, S. J., S. D. DeGloria and R. Elliot. 1999. A terrain ruggedness index that quantifies topographic heterogeneity. *Intermountain Journal of Sciences* 5:23–27.
- Robinson, N., J. Regetz and R. P. Guralnick. 2014. EarthEnv-DEM90: A nearly-global, void-free, multi-scale smoothed, 90m digital elevation model from fused ASTER and SRTM data. *ISPRS Journal of Photogrammetry and Remote Sensing* 87:57–67. <https://doi.org/10.1016/j.isprsjprs.2013.11.002>.
- Saberi, A., M. Kabolizadeh, K. Rangzan and M. Abrehdary. 2023. Accuracy assessment and improvement of SRTM, ASTER, FABDEM, and MERIT DEMs by polynomial and optimization algorithm: A case study (Khuzestan Province, Iran). *Open Geosciences*. <https://doi.org/10.1515/geo-2022-0455>.
- Santillan, J. R. 2023. Vertical accuracy evaluation of the forest and buildings removed Copernicus DEM (FABDEM) over the Philippines. *The International Archives of the Photogrammetry, Remote Sensing and Spatial Information Sciences* 48:311–318. <https://doi.org/10.5194/isprs-archives-XLVIII-4-W6-2022-311-2023>.
- Sefercic, U. G. 2012. Performance estimation of aster global DEM depending upon the terrain inclination. *Journal of the Indian Society of Remote Sensing* 40:565–576. <https://doi.org/10.1007/s12524-012-0202-y>.
- Slater, J. A., G. Garvey, C. Johnston, J. Haase, B. Heady, G. Kroenung and J. Little. 2006. The SRTM data “finishing” process and products. *Photogrammetric Engineering & Remote Sensing* 72:237–247. <https://doi.org/10.14358/PERS.72.3.237>.
- Stefanidis, S., V. Alexandridis, V. Spalevic and L. Mincato. 2022. Wildfire effects on soil erosion dynamics: The case of 2021 megafires. *Agriculture & Forestry* 68:49–63. <https://doi.org/10.17707/AgricultForest.68.2.04>.
- The World Bank. 2021. *Haiti Digital Terrain Model 2014–2016*. <https://doi.org/10.5069/G9GX48R8>.
- Wang, D. and A. Käab. 2015. Modeling glacier elevation change from DEM time series. *Remote Sensing* 7:10117–10142. <https://doi.org/10.3390/rs70810117>.
- Wu, J., Q. Yang and Y. Li. 2018. Partitioning of terrain features based on roughness. *Remote Sensing* 10:1–21. <https://doi.org/10.3390/rs10121985>.
- Xu, C., H. Fu, J. Yang and L. Wang. 2022. Assessment of the relationship between land use and flood risk based on a coupled hydrological–hydraulic model: A case study of Zhaojue River basin in southwestern China. *Land* 11. <https://doi.org/https://doi.org/10.3390/land11081182>.
- Yamazaki, D., D. Ikeshima, R. Tawatari, T. Yamaguchi, F. O'Loughlin, J. C. Neal, C. C. Sampson, S. Kanae and P. D. Bates. 2017. A high-accuracy map of global terrain elevations. *Geophysical Research Letters* 44:5844–5853. <https://doi.org/10.1002/2017GL072874>.
- Yue, L., H. Shen, L. Zhang, X. Zheng, F. Zhang and Q. Yuan. 2017. High-quality seamless DEM generation blending SRTM-1, ASTER GDEM v2 and ICESat/GLAS observations. *ISPRS Journal of Photogrammetry and Remote Sensing* 123:20–34. <https://doi.org/10.1016/j.isprsjprs.2016.11.002>.
- Yue, L., W. Yu, H. Shen, L. Zhang and Y. He. 2015. Accuracy assessment of SRTM V4.1 and ASTER GDEM V2 in high-altitude mountainous areas: A case study in Yulong Snow Mountain, China. Pages 5011–5014 in *Proceedings IEEE International Geoscience and Remote Sensing Symposium (IGARSS)*. <https://doi.org/10.1109/IGARSS.2015.7326958>.
- Zhang, K., D. Gann, M. Ross, Q. Robertson, J. Sarmiento, S. Santana, J. Rhome and C. Fritz. 2019. Accuracy assessment of ASTER, SRTM, ALOS, and TDX DEMs for Hispaniola and implications for mapping vulnerability to coastal flooding. *Remote Sensing of Environment* 225:290–306. <https://doi.org/10.1016/j.rse.2019.02.028>.

# Evaluating Surface Mesh Reconstruction Using Real Data

Yanis Marchand, Laurent Caraffa, Raphael Sulzer, Emmanuel Clédât, and Bruno Vallet

## Abstract

Surface reconstruction has been studied thoroughly, but very little work has been done to address its evaluation. In this article, we propose new visibility-based metrics to assess the completeness and accuracy of three-dimensional meshes based on a point cloud of higher accuracy than the one from which the reconstruction has been computed. We use the position from which each high-quality point has been acquired to compute the corresponding ray of free space. Based on the intersections between each ray and the reconstructed surface, our metrics allow evaluating both the global coherency of the reconstruction and the accuracy at close range. We validate this evaluation protocol by surveying several open-source algorithms as well as a piece of licensed software on three data sets. The results confirm the relevance of assessing local and global accuracy separately since algorithms sometimes fail at guaranteeing both simultaneously. In addition, algorithms making use of sensor positions perform better than the ones relying only on points and normals, indicating a potentially significant added value of this piece of information. Our implementation is available at <https://github.com/umrlastig/SurfaceReconEval>.

## Introduction

Surface reconstruction is the task of producing a continuous digital representation of a real surface of which discrete information has been acquired. This information may come straight from point clouds produced by a laser scanner. This includes time-of-flight (Lange and Seitz 2001) and structured-light (Geng 2011) devices as well as terrestrial and airborne lidar (Lohani and Ghosh 2017) that allow scanning large environments. Point clouds can also be produced from images using multi-view stereo (Furukawa and Hernández 2015) or structure from motion (Ozyesil *et al.* 2017).

This task has been extensively studied, and a large number of approaches have been proposed. In the section “Related Work,” we provide a description of these state-of-the-art methods. However, very few articles address the evaluation of such a task. In real-case scenarios for which the goal is to produce a digital model of a real object or scene, there is no ground truth other than the real surface itself. It is thus impossible to directly compute the distance or the difference between a digital model and the ideal real surface. The only possible work-around is using synthetic data as in Marchand *et al.* (2021), where a realistic surface is chosen to be the ground truth and then virtually scanned in a way that simulates the defects of a real acquisition; the surface reconstruction algorithms to be evaluated are run on this virtual scan. This makes it more straightforward to compute metrics that assess the difference between the ground-truth model and the reconstructed ones. Another possibility for working with data from real scenes is to sample points from a reconstructed mesh, but this introduces a large bias, as methods producing the same features will be unfairly favored. Our work tackles the real-world case where we do not have access to such a synthetic ground truth. We call *real data* the data acquired in

the physical world with real sensors. This includes lidar scans, images, RGB-D images, and so on. As is usually done to address this issue, we assess the reconstruction of real scenes from real data only based on other real data of significantly higher quality. Even though this idea is quite typical, the main contribution of this article lies in the way that we assess the difference between the reconstructed surface and the high-quality real data as inconsistencies, inspired by recent work on change detection (Xiao *et al.* 2015). The fundamental interest of this work is to propose metrics to assess the quality of reconstructions from low-quality real data based on high-quality data. Although it is possible to assess the quality of models visually, this raises several issues. First, it is a subjective comparison, and one might be tempted to favor their own or preferred method over others. Second, everyone has a different perception of visual quality, and we might not agree even without conflict of interest. Third, while it might sound reasonable to visually evaluate a few different models of a relatively small scene, it is very unlikely that one would be able to carry out a large-scale evaluation involving dozens of models representing large areas. Consequently, we believe that it is essential to find relevant metrics to assess surface reconstruction, and, in our opinion, current metrics are not entirely satisfying. As pointed out by Van Kreveld *et al.* (2013), there is a lack of ground truth and of benchmarks in the field of urban reconstruction. This article aims to tackle this problem. This endeavor is difficult for several reasons.

## Limits in the Quality of the Ground Truth

The specificity of working with real data is the presence of noise in what we consider as the ground truth. In addition, real data are always sparse and incomplete, which means that we do not know the state of space (occupied by the object or empty) everywhere. This raises the question of how to assess pieces of reconstructed surface in unseen, unobserved regions.

Our contributions are twofold:

1. We propose a setting where the high-quality data used to compute metrics are significantly better than the low-quality data on which surface reconstruction is performed in three separate ways:
  - a. Coverage: We use multiple data sources acquired from multiple points of view to ensure that the high-quality data have a significantly better coverage of the surface to reconstruct than the low-quality data.
  - b. Density: We ensure that the density of the points in the high-quality data is significantly better than that of the low-quality data.
  - c. Noise: We ensure that the noise level is lower in the high-quality data than in the low-quality data.
2. We propose metrics that penalize inconsistencies between the surface to be evaluated and the high-quality data: a piece of surface reconstructed within a volume unseen by the high-quality data will simply not be evaluated, as we have no information on it. This does not mean that we do not evaluate the hole-filling capacity of the evaluated methods. As the high-quality data have more coverage, we evaluate hole filling exactly where we have the data to do so.

Yanis Marchand, Laurent Caraffa, Raphael Sulzer, Emmanuel Clédât, and Bruno Vallet are with LASTIG, Univ Gustave Eiffel, IGN-ENSG, F-94160, Saint-Mande, France.

Corresponding author: Yanis Marchand ([yanismarchan@gmail.com](mailto:yanismarchan@gmail.com))

Contributed by Rongjun Qin, January 24, 2023 (sent for review January 29, 2023; reviewed by Shuang Song).

Photogrammetric Engineering & Remote Sensing  
Vol. 89, No. 10, October 2023, pp. 625–638.

0099-1112/22/625-638

© 2023 American Society for Photogrammetry  
and Remote Sensing  
doi: 10.14358/PERS.23-00007R3

## Assumptions and Priors

Algorithms make different assumptions about the type of shape that needs to be reconstructed, and this leads to very different properties. Consequently, depending on the metrics' definitions, these assumptions can dramatically influence the assessment, sometimes in an unjustified manner. An example of such a situation is shown in Figure 1, where the left model would be attributed a bad mark because of the red piece of surface even though the rest of the model is correct. Does this red piece of surface need to be taken into account when assessing the model? We tackle this issue in two complementary ways. First, we use a softer definition of watertightness adapted to the reconstruction of open scenes (see below), and, second, we define metrics that assess hole filling only where relevant high-quality data are available.

A surface is watertight if it has no border. In the case of a triangle mesh, this means that each edge needs to have exactly two incident faces. We will call this property *hard watertightness*. When trying to reconstruct an open scene, for example, it is often more realistic to authorize the reconstructed surface to intersect the boundary of the domain (e.g., a bounding box) as illustrated in Figure 1. We thus define *soft watertightness* as the property that a mesh has when it has no border except on the boundary of the domain. Only triangle edges lying on the domain boundary can have only one incident face. In practice, we ask only for the evaluated methods to be softly watertight, which means that they do not need to randomly fill the very large hole at the boundary of the domain when reconstructing open scenes. In fact, most reconstruction methods have this ability: Poisson reconstruction (Kazhdan and Hoppe 2013) using the Neumann boundary condition (opposite to Dirichlet) allows the reconstructed surface to be open at the domain boundary. For Delaunay-based methods, we can simply add eight points to the input point cloud to correspond to the corners of a bounding box and remove all triangles belonging to this bounding box at surface extraction time (or in postprocessing).

Our proposed metrics are based on the visibility information contained in the high-quality data. We assess the reconstructed surface only where the real one has been observed. For that purpose, we make an extensive use of sensor positions (positions from which points have been acquired). This information is easy to access and provides us with a full ray along which we know that space is free instead of just a single position where we know that the real surface lies. We used these newly defined metrics to assess several open-source surface reconstruction algorithms and a licensed one on different types of scenes. Even though our protocol is intended for real data, one of the data sets that we used is synthetic. This allows to test the algorithms on the same kind of scene they have been trained or tuned with. Having better control on the data also prevents any experimental-related failures of the algorithms. In “Related Work,” we review surface reconstruction and present the algorithms that are evaluated in this article. In the section “Evaluation Protocol,” we define our metrics and discuss their nature. In “Input Data,” we present the three data sets on which we tested our evaluation protocol and present the experimental setup we used to generate the high-quality data. Results are detailed and analyzed in “Results” before we present the conclusions of our work in “Conclusion.”

## Related Work

### Surface Reconstruction

Here we review some existing methods to reconstruct a triangle mesh from a point cloud and classify them by the paradigm they use. See Berger *et al.* (2017) and Khatamian and Arabnia (2016) for an even deeper analysis of them (even though the most recent methods do not appear).

### Indicator Function

Often used to achieve watertight reconstructions, this class of algorithms proceeds by computing a space segmentation. The object itself is defined as the region of space where the labeling equals a certain value. The surface is then computed by finding the changes in the segmentation. Popular approaches in this field include those of Kazhdan (2005), Poisson reconstruction (Kazhdan *et al.* 2006), and the differentiable Poisson solver that has been introduced in Peng *et al.* (2021).

Recently, many learning-based methods have been proposed. While they often outperform non-learning-based ones on simple geometries, especially closed objects, they have not been proven to be able to deal with the complexity of large and open scenes. IM-NET (Chen and Zhang 2019) is a learning framework that predicts whether any point  $(x, y, z)$  is inside or outside the given shape needing to be reconstructed. Occupancy networks (Mescheder *et al.* 2019) present a similar way of computing the so-called occupancy function of the 3D object. Convolutional occupancy networks (Peng *et al.* 2020) introduced a learning-based framework to compute implicit surfaces. Recently, Groueix *et al.* (2018) proposed a general learning framework dubbed AtlasNet to take as input a 3D point cloud or an RGB image. It proceeds by concatenating these data with a sampling of a patch, namely, the unit square, before passing it to multilayer perceptrons with rectified linear unit nonlinearities, producing as output a point cloud of arbitrary resolution. A mesh can be generated either by transferring the connections between vertices of a mesh defined on the patch to their 3D image points or by using Poisson surface reconstruction (Kazhdan *et al.* 2006) on a sufficiently dense point cloud.

### Volumetric Segmentation

This is a subdiscipline of indicator functions, as it consists of giving information about whether a region of space is filled by the object or is empty. The data structure can be as follows:

- the Delaunay triangulation of input samples as in Labatut *et al.* (2009), Lafarge and Alliez (2013), Caraffa *et al.* (2016), and Kolluri *et al.* (2004).
- voxels: Holenstein *et al.* (2011) label them as *free space*, *occupied*, or *unknown*.

To achieve this, point locations combined with sensor positions allow computing the ray corresponding to a beam of free space. An interesting feature is that undesirable moving objects such as humans can be erased in the final surface thanks to scans of the same area from different sensor positions.

Robust and efficient surface reconstruction (RESR) (Labatut *et al.* 2009) labels as *inside* or *outside* each tetrahedron of the Delaunay triangulation of the point samples. The triangles separating an empty-labeled tetrahedron from an occupied-labeled one are extracted thanks

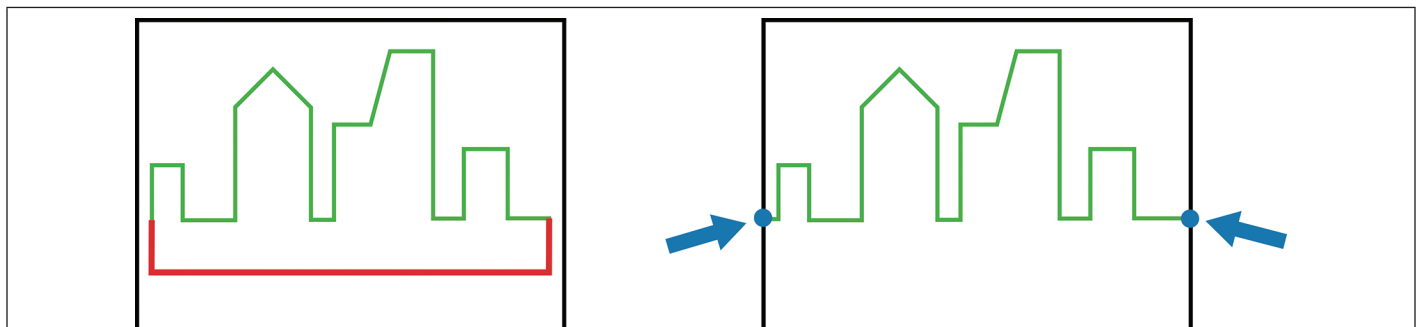


Figure 1. Two-dimensional comparison between hard watertightness (left) and soft watertightness (right). The soft watertight surface has a border (materialized by the blue dots) but only on the boundary of the domain. When trying to model urban environments, the red piece of surface from the hard watertight surface does not have any significant meaning. This illustrates why soft watertightness is better suited to open scenes.

to a graph-cut optimization of an energy function defined thanks to the lines of sight (emanating from the vertex and pointing at the laser scanner) and the shape of the triangles:

$$I_T = \arg \min_{I_T \in L^T} (E_{data}(I_T) + \lambda E_{prior}(I_T)) \quad (1)$$

Delaunay-graph neural networks (DGNNs) (Sulzer *et al.* 2021) also use this paradigm (Equation 1), but they estimate the occupancy of the tetrahedra thanks to a graph neural network.

### Signed-Distance Function

Another way of generating a watertight surface is to compute the signed-distance function  $f$  to the surface and to extract its zero-level set. This is the approach chosen in multi-level partition of unity (MPU) (Ohtake *et al.* 2003) and smooth signed distance (SSD) (Calakli and Taubin 2011). Recently, DeepSDF (Park *et al.* 2019) has shown how to learn the surface distance field.

### Primitive Based

In this field, PolyFit (Nan and Wonka 2017) uses RANSAC (Schnabel *et al.* 2007) to detect planar segments and refine them. The surface is extracted by combining the optimization of an objective function that favors data fitting, point coverage and model complexity, and the enforcement of watertightness and manifoldness.

Point set structuring (PSS) (Lafarge and Alliez 2013) relies on the Delaunay triangulation of input points and the labeling of its tetrahedrons as empty or occupied, but their specificity resides in the extraction of primitives as a preprocessing step, a resampling of the resulting structures, and the combination of points from planar regions and unstructured ones in the reconstruction step.

### Moving Least Squares Based

Moving least squares (MLS) was first introduced by Lancaster (1979), based on the work conducted by, among others, Shepard (1968). Since then, a tremendous number of extensions have been added, as pointed out by a survey conducted in 2008 in Cheng *et al.* (2008). For example, Levin (2000, 2003) and Alexa *et al.* (2001) significantly contributed to the advances in MLS-based algorithms. As explained in Cheng *et al.* (2008), MLS-based algorithms can be roughly classified into two main categories: implicit MLS surfaces require the computation of a level set function of which the zero isosurface can be extracted, and projection MLS surfaces consist of first computing a projection operator that maps any point of the space to a point on the surface. The surface is then made of the set of stationary points.

### Evaluation of Surface Reconstruction

In order to assess the quality of a reconstruction, there is need for a ground truth, an input point cloud, and a means of calculating the difference between a given output surface and the so-called ground truth. Let us present the various possibilities that have so far been considered for these three aspects.

#### Ground Truth

Ground truth could potentially take any surface form, that is, implicit field, triangle mesh, volumetric segmentation, point set, deformed model, skeleton curve, or primitives. However, only two have so far been considered: triangle mesh (Kazhdan 2005; Ter Haar *et al.* 2005; Marchand *et al.* 2021) and implicit field (Berger *et al.* 2013).

#### Input Point Cloud

Producing point samples from a surface can be carried out in several ways:

- Real scanning: Based on a physical object (or scene), laser-based scanning generates a point cloud directly. Such technologies include time-of-flight (Lange and Seitz 2001) and structured-light (Geng 2011) devices. In addition, terrestrial or airborne lidar (Lohani and Ghosh 2017) offers the possibility of dealing with large areas.
- Image based: Multi-view stereo (Furukawa and Hernández 2015) and structure from motion (Ozyesil *et al.* 2017) allow creating a 3D model from images that can be the starting point for surface reconstruction.
- Model sampling: Based on a continuous digital input model, synthetic sampling has the advantage of making it possible to

fully control the data. In particular, one can generate more realistic data by adding noise, outliers, misalignment, and occlusions and by setting the density. In this field, several procedures have been considered: random or uniform sampling (Kazhdan 2005; Manson *et al.* 2008; Süßmuth *et al.* 2010), synthetic raytracing (Hoppe *et al.* 1996; Berger *et al.* 2013; Marchand *et al.* 2021), or z-buffering (Ter Haar *et al.* 2005). Of particular interest is the recent work presented in Winiwarter *et al.* (2022), Marchand *et al.* (2021), and (Manivasagam *et al.* (2020). Helios++ (Winiwarter *et al.* 2022) is an open-source tool for the simulation of airborne, UAV-based, and terrestrial static and mobile laser scanning implemented in C++. Marchand *et al.* (2021) provided an airborne lidar simulator, and Manivasagam *et al.* (2020) developed LiDARsim, which is a virtual terrestrial lidar platform generating realistic point clouds based on a high-quality mesh, free of moving objects.

### Comparison

With regard to comparing an output reconstruction, three main possibilities have been explored:

- Visually: Most of the time, surface reconstruction aims at producing a digital representation as visually similar as possible to a real object. Hence, Poisson (Kazhdan *et al.* 2006), MPU (Ohtake *et al.* 2003), and SSD (Calakli and Taubin 2011) have simply compared models on a visual basis. This obviously raises the issues of being sensitive to the observer's perception, conflict of interest, and the lack of quantitative information.
- Point-to-mesh distance computation: When the only ground truth that is available comes in the form of a point cloud, it is relatively straightforward to compute the distance from each of those points to the reconstructed model. Kazhdan and Hoppe (2013) have evaluated their method by randomly partitioning their point cloud into two equal-sized subsets: points serving as input for the reconstruction algorithms and validation points from which distances to the output meshes are computed.
- Mesh-to-mesh distance computation: This method comes with the advantage of providing a quantitative quality assessment that is independent of any human bias. Ter Haar *et al.* (2005) and Kazhdan and Hoppe (2013) use the Metro tool (Cignoni *et al.* 1998), which works as follows. Given two meshes (a sampled one  $\mathcal{M}_s$  and a target one  $\mathcal{M}_t$ ), Metro samples  $\mathcal{M}_s$  and measures the shortest distance from each sample to  $\mathcal{M}_t$ . Metro then computes the mean distance, the max, and the root mean square (RMS) over all samples. Marchand *et al.* (2021) have used such a distance on the reconstructed and the ground-truth meshes. Their specificity was to filter out triangles further than the input point cloud used for reconstruction. They thus produce a curve of distances for the different threshold values of this filtering procedure.
- Mesh-to-implicit distance computation: Berger *et al.* (2013) chose to use an implicit field that we will call  $\Omega$  as ground truth, and consequently they adapted the Metro methodology in order to compute the distance from a nearly uniform sampling of  $\Omega$  to the evaluated mesh and vice versa. The evaluation process answers the question, how well does the reconstructed mesh fit to the implicit surface computed by the MPU (Ohtake *et al.* 2003) algorithm? To address this issue, several measures are proposed by the benchmark (Berger *et al.* 2013): Hausdorff distance (Equation 4), mean distance (Equation 5), max (Equation 6), and mean angle deviation (Equation 7). The former two allow us to know how close the two surfaces are to each other, while the latter two give an insight into how similar the local orientation is.

In order to compute these, defining point correspondences between the two surfaces are needed. Let us denote by  $M$  the implicit surface and by  $\bar{M}$  the output triangle mesh. As defined in Hildebrandt *et al.* (2006), the mapping  $\Phi: M \rightarrow \bar{M}$  attributes to one point  $p \in M$  the intersection of the normal line through  $p$  and the mesh  $\bar{M}$ . The inverse mapping  $\Phi^{-1}: \bar{M} \rightarrow M$  attributes to  $\Phi(p)$  its closest neighbor on the implicit surface  $M$ . This definition, associated with a sampling  $P_M$  of  $M$ , produces a set of nearest neighbor correspondences that we call  $C_M$ :

$$C_M = \{(x,p) | p \in P_M, x = \Phi(p)\} \quad (2)$$

By defining the corresponding operator  $\Psi: \bar{M} \rightarrow M$  and a sampling  $P_{\bar{M}}$  of the reconstructed mesh  $\bar{M}$ , we get  $C_{\bar{M}}$ :

$$C_{\bar{M}} = \{(p,x) | x \in P_{\bar{M}}, p = \Psi(x)\} \quad (3)$$

Denoting  $|S| = |C_M| + |C_{\bar{M}}|$  and with  $\gamma(p,x)$  the angle between the normals  $N_m(p)$  and  $N_{\bar{M}}(x)$ , error measures are the following:

$$H(M, \bar{M}) = \max \left\{ \max_{(x,p) \in C_M} |x-p|, \max_{(p,x) \in C_{\bar{M}}} |p-x| \right\} \quad (4)$$

$$\mu(M, \bar{M}) = \frac{1}{|S|} \left( \sum_{(x,p) \in C_M} |x-p| + \sum_{(p,x) \in C_{\bar{M}}} |p-x| \right) \quad (5)$$

$$H_N(M, \bar{M}) = \max \left\{ \max_{(x,p) \in C_M} \gamma(p,x), \max_{(p,x) \in C_{\bar{M}}} \gamma(p,x) \right\} \quad (6)$$

$$\mu_N(M, \bar{M}) = \frac{1}{|S|} \left( \sum_{(x,p) \in C_M} \gamma(p,x) + \sum_{(p,x) \in C_{\bar{M}}} \gamma(p,x) \right) \quad (7)$$

## Evaluation Protocol

### Intuition

Let us give some examples of situations where current metrics are not adequate to evaluate surface reconstruction and what we suggest would be an improvement. This is going to help understand our metrics' definitions in "Metrics Definitions."

First, as presented in "Evaluation of Surface Reconstruction," comparing a reconstructed mesh with a ground-truth point cloud can be done by computing the distances from those points to the mesh model. While this seems like a good starting point to assess how well holes have been filled around those points, it is inadequate to evaluate the overall accuracy of the surface. Figure 2 shows an example of such a situation where a surface would be evaluated as almost perfect even though large portions are clearly incompatible with the ground truth if we take into account the positions from which points have been acquired.

Second, it is possible to measure accuracy solely with ground-truth points by sampling the reconstructed surface and measuring the distance from these samples to the ground-truth points. Nevertheless, large pieces of the reconstructed surface might be judged as being of poor quality (if lying far from the nearest ground-truth point) despite being correct just because of a low ground-truth density. We want to assess both accuracy and completeness only in regions where ground-truth information is available, and this is possible using sensor positions as shown in Figure 2.

Third, as surface reconstruction has often been evaluated visually, we wanted to find metrics that would imitate this human intuition-based assessment. We believe that visibility-based metrics are more appropriate for assessing how the reconstructed surface matches the real one everywhere where we can see and compare them. Figure 3 shows four situations for which the piece of reconstructed surface would be marked similarly by a point-to-mesh distance. The distance from the high-quality point to the nearest piece of reconstructed surface is indeed the same in all four situations. However, we are certain that they should correspond to three completely different outcomes, and we want our metrics to be able to differentiate between them:

- In (a), the reconstructed surface lies slightly behind the high-quality point. We consider it as correct at the threshold defined by our tolerance zone.
- In (b), the reconstructed surface lies slightly in front of the high-quality point. As in (a), we consider it as correct even though we can measure a slight error.

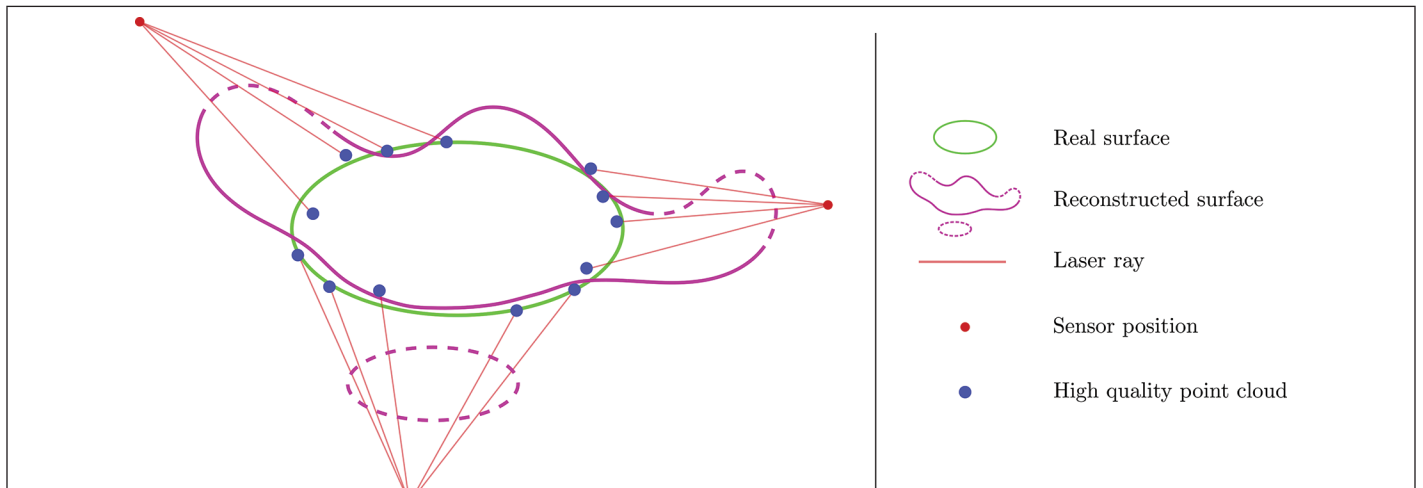


Figure 2. The importance of sensor positions: The dashed part of the reconstructed surface can be identified as wrong by making use of sensor positions when the high-quality point cloud does not provide enough information.

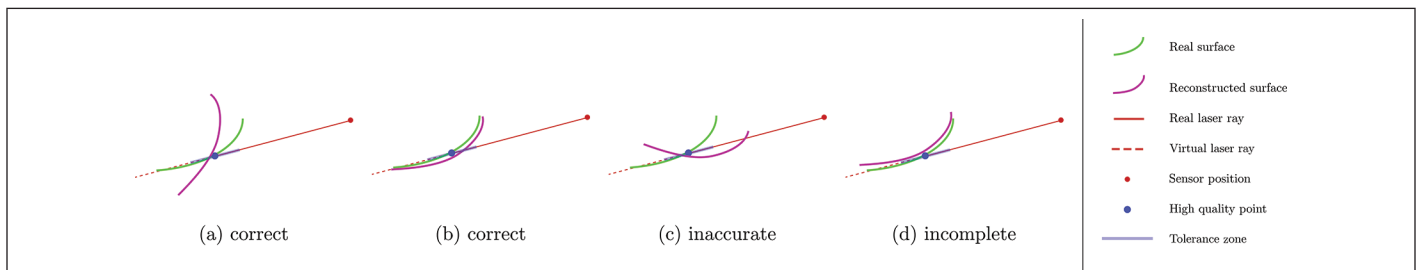


Figure 3. These four cases would be evaluated in the same way by a basic point-to-mesh distance. However, they are very different in terms of what a human being would be able to see from the sensor position.

- In (c), while the piece of real surface corresponding the high-quality point has been recovered just like in (a), the reconstructed surface hides the nearest intersection by crossing the laser ray, resulting in an obvious inaccuracy. What one would see by looking in the direction of the laser ray is not the right piece of reconstructed surface but rather something else far in front of it.
- Situation (d) might look similar to (a), but there is actually no intersection between the reconstructed surface and the laser ray. Consequently, what one would see by looking in the direction of the laser ray is not the right piece of reconstructed surface but something else in the background. We thus consider that the surface has not been recovered at all here.

The ETH3D benchmark (Schops *et al.* 2017) proposed metrics to evaluate how well a two- or multi-view stereo point cloud matches a lidar-based one using sensor positions. While surface reconstruction is a different task from MVS (in particular in terms of the expected output properties), Schops *et al.* (2017) still evaluate the matching between two three-dimensional structures, and we were inspired by their use of sensor positions. However, we chose different paradigms that are more adapted to surfaces, so our evaluation protocol is considerably different.

The ETH3D benchmark (Schops *et al.* 2017) defines completeness as the proportion of ground-truth points for which the distance to its closest reconstructed point is below a given threshold. We could keep this definition and find the point from the reconstructed surface that minimizes the distance to each point of the high-quality point cloud. Nonetheless, given that we know in what direction this point is supposed to be encountered thanks to the sensor position, we find it more relevant to compute the distance between the high-quality point and the nearest intersection between the corresponding laser ray and the mesh model. In other words, while the most natural adaptation of this point-to-point distance would be a point-to-mesh distance, we believe that for each ray that hit the real surface, there should be a piece of reconstructed surface close by and along the ray.

However, we also leverage the information given by each laser ray: the space between each sensor position and its associated high-quality point should be empty. We soften this property by defining a tolerance zone: a piece of reconstructed surface will be considered as correct if its distance along the ray from the high-quality point is smaller than a given threshold  $d_{max}$ . Every piece of surface farther than  $d_{max}$  and situated in front of the high-quality point will affect the accuracy of the model.

Contrary to the ETH3D benchmark (Schops *et al.* 2017), we do not model the shape of a laser beam as a truncated cone. The first reason for this is that we do not need to since the model we are trying to

evaluate (a surface) is continuous instead of discrete (a point cloud). Hence, we are not at risk of missing any part of it. In addition, it makes it simpler to get a point as the intersection between a ray and a piece of surface. This way, every couple (ray and piece of surface) gives the same amount of information.

Schops *et al.* (2017) use voxels to prevent a “cheating” strategy from achieving both high accuracy and completeness despite raising other issues. For example, regions of low ground-truth density contribute as much as high-density ones while encapsulating less information. A cheating strategy for surface reconstruction would be to add several parallel layers of surface in regions of high confidence. We do not need to discretize space as in (Schops *et al.* 2017) since for each ray, we propose to keep only the closest intersection as a potential correct one and penalize all the ones situated in front of it. Note that even layers situated behind the closest intersection might be obstacles to rays pointing at another object in the background.

If the nearest intersection is found behind the high-quality point at a greater distance than  $d_{max}$  or if no intersection is found at all, then we consider that this piece of surface has not been recovered. This therefore affects the completeness of the model.

### Definitions and Notations

In this article, we want to evaluate the quality of surface reconstructions from low-quality data  $\mathcal{P}_{LQ}$ , having access only to high-quality data  $\mathcal{P}_{HQ}$  of the same scene and without having access to the perfect ground-truth surface that the algorithms are supposed to produce:

- $\mathcal{P}_{LQ}$ : the low-quality point cloud that will be fed to the evaluated surface reconstruction methods to produce the output surface meshes to be evaluated.
- $\mathcal{P}_{HQ}$ : the high-quality (ground-truth) point cloud with better coverage, higher density, and less noise than  $\mathcal{P}_{LQ}$  and for which we know the sensor positions, defining one ray per point.
- $\mathcal{M}_E$ : the reconstructed mesh to evaluate, produced by an algorithm from  $\mathcal{P}_{LQ}$ .
- $d_{max}$ : the maximum distance at which we evaluate the reconstruction. It is a parameter that influences the different metrics as we use it to separate noise (distance  $< d_{max}$ ) from outliers (distance  $> d_{max}$ ).

### Metric Definitions

Similar to Marchand *et al.* (2021), we would like to assess both the precision of each part of the reconstructed surface (each part of the surface should lie near some part of the real surface) and the completeness of the model (there should be as few missing parts of the real surface as possible). As we do not have access to a digital model of the real surface, we cannot compute the actual precision and recall as in Marchand *et al.* (2021). Our knowledge of the ground truth is limited

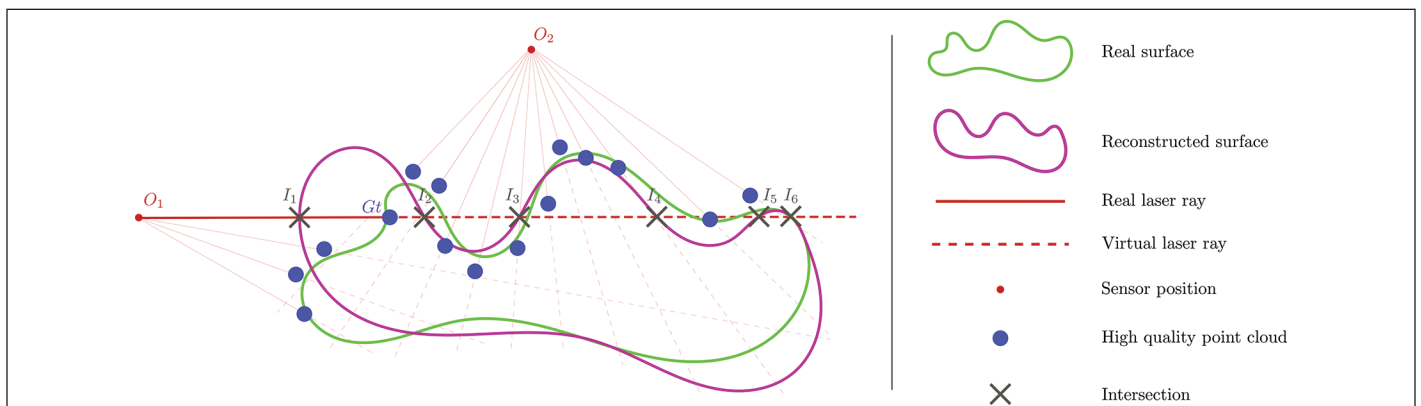


Figure 4. Toy example to visualize the definitions of the metrics. The real surface has been scanned from two positions:  $O_1$  and  $O_2$ . A given real laser ray (the thick one) was cast from  $O_1$  and hit the real surface at  $Gt$ . Note that the position of the intersection might be noisy, hence the shift between the real surface and the high-quality point cloud. We compute all intersections between the associated virtual ray (i.e., the extension of the real laser ray and the reconstructed surface). In this case, it results in six intersections:  $I_1, \dots, I_6$ . The closest intersection to  $Gt$  happens to be  $I_2$ , so the ray distance metric for that particular ray is the distance  $(Gt, I_2)$ . We found one intersection  $I_1$  on the way to the closest intersection  $I_2$ , which is counted as a false positive. In addition, if  $(Gt, I_2) < d_{max}$ ,  $Gt$  is to be counted as a true positive; otherwise, it will not be taken into account in the evaluation since it is situated after  $Gt$ . Note that this piece of surface might still be evaluated thanks to another ray (e.g., as one emanating from  $O_2$ ).

to the high-quality data  $\mathcal{P}_{\text{HQ}}$ . However, we also know where the surface is not supposed to lie since we know the sensor position from which every point of  $\mathcal{P}_{\text{HQ}}$  has been acquired, thus defining a ray of free space. Therefore, we define a precision metric that penalizes inconsistencies between the reconstructed surface and the visibility information contained in  $\mathcal{P}_{\text{HQ}}$ . We propose an equivalent of the recall metric: for each  $[OP]$  ray from  $\mathcal{P}_{\text{HQ}}$ , we compute the distance from the  $P$  to the closest intersection between the  $[OP]$  half line and the reconstructed surface. Here is the formalization of these metrics in more detail:

- **Ray distance:** For each point/ray  $(p, r) \in \mathcal{P}_{\text{HQ}}$ , we compute the distance from  $p$  to the closest intersection (which we will denote as  $c$ ) between  $r$  and  $\mathcal{M}_E$  (among all potential intersections, we choose the one with the smallest distance with respect to  $p$ ). If this distance is  $< d_{\text{max}}$ , then the piece of reconstructed surface is considered as being correct, and we add this distance to an array of distances.
- **Precision:** For each point or ray  $(p, r) \in \mathcal{P}_{\text{HQ}}$ , if the ray distance (between  $p$  and  $c$ ) is  $< d_{\text{max}}$ , then we count  $c$  as a true positive (TP) (since there is a piece of surface, and it is correct). Otherwise, if the intersected point  $c$  lies at a distance greater than  $d_{\text{max}}$  and it is *before* the corresponding high-quality point  $p$ , we consider it as being false and we count it as a false positive (FP) (since there is a piece of surface, and it is false). We consider that we cannot say anything about the closest point  $c$  if it lies at a greater distance than  $d_{\text{max}}$ , and it is situated *after* the corresponding high-quality point  $p$  (neither can we say anything for all intersected points lying after it), so we just ignore them. All intersected points lying *before* this closest intersection  $c$  are also counted as FP, as they are inconsistent with the corresponding ray of free space  $(p, r)$ . This is enough to define the precision ratio (Equation 8).
- **Recall:** This is defined as the ratio between the number of TP and the number of cast rays (Equation 9). Every high-quality point  $p \in \mathcal{P}_{\text{HQ}}$  is either mapped to its corresponding TP (in which case the piece of real surface has actually been recovered by the algorithm) or not (meaning a lack of exhaustiveness of the reconstruction and corresponding to a false negative [FN]). The number of rays thus equals the sum of the TP and the FN.
- **Cumulative distances:** The cumulative histogram of the ray distances where the x-axis corresponds to the distance, and on the y-axis, we plot the number of points for which the ray distance is below the x-distance divided by the total number of rays cast. It contains the information of both recall (the rightmost value) and mean ray distance. Figure 5b shows an example of this histogram.

$$\text{Precision} = \frac{\text{TP}}{\text{TP} + \text{FP}} \quad (8)$$

$$\text{Recall} = \frac{\text{TP}}{\text{TP} + \text{FN}} = \frac{\text{TP}}{\text{Number of rays}} \quad (9)$$

$$\text{F-score} = 2 \cdot \frac{\text{precision} \cdot \text{recall}}{\text{precision} + \text{recall}} \quad (10)$$

As we define precision and recall as ratios, the harmonic mean (F-score; see Equation 10) allows ranking the methods by taking into account both metrics.

### Tuning and Training

Either the algorithms we evaluate in this article are tunable for the most part or learn parameters in order to reconstruct surfaces. For example, DGNN (Sulzer *et al.* 2021) needs a training data set in order to learn the parameters of its model, and Poisson (Kazhdan *et al.* 2006) can be run at different resolutions by changing the depth of the octree that is used. In order to be as fair as possible, we used the same data set to tune or train the algorithms. We therefore ran the non-learning-based methods with different values for their parameters and carried out an evaluation. A first interesting result is that for some methods, it can be hard to obtain a good performance regarding the precision and the recall metrics at the same time. For PSS, the higher the value of the trade-off parameter  $\lambda$  (therefore, the more importance given to the prior term; see Equation 1), the higher the precision (up to a certain value) but the lower the recall. Maximizing the score of one metric (by varying  $\lambda$ ) results in minimizing the score of the other one (we explain why in “Results”). Thus, we selected the two  $\lambda$  values that maximize each of these metrics individually.

The tuning and training data set that we decided to use is composed of three scenes from STRAS. The reason behind this choice is the availability of ground-truth meshes, which are absolutely necessary for the training phase of DGNN. We then also used these three scenes to find the best parameters (in terms of ray distance, precision, and recall) for the non-learning-based algorithms.

### Input Data

We aim to evaluate the algorithms in very different scenarios, as the methods’ priors might influence the quality of the reconstruction, depending on the type of scene or the type of data involved. We therefore compute the metrics introduced above on three significantly varying data sets.

### STRAS: Strasbourg Data Set and Lidar Simulator

In order to control the data, we started by using a synthetic data set<sup>1</sup> taking the form of a high-quality mesh representing a large area covering the Métropole de Strasbourg. Figure 6 shows a  $250 \times \mathcal{P}_{\text{HQ}} 250$  m tile of this mesh. In order to generate the ground truth and the input point

1. The data set is available at 3d.strasbourg.eu. It was produced by Ville et Eurométropole de Strasbourg with financial support from the European Union as part of a Fonds Européen de Développement Régional.

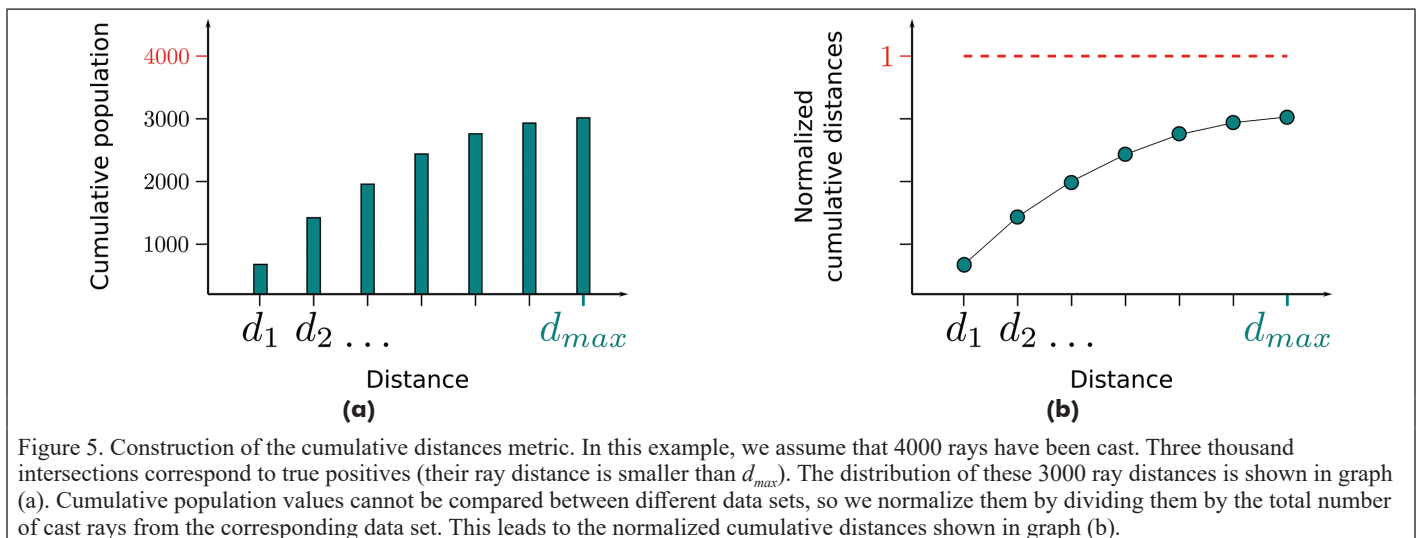


Figure 5. Construction of the cumulative distances metric. In this example, we assume that 4000 rays have been cast. Three thousand intersections correspond to true positives (their ray distance is smaller than  $d_{\text{max}}$ ). The distribution of these 3000 ray distances is shown in graph (a). Cumulative population values cannot be compared between different data sets, so we normalize them by dividing them by the total number of cast rays from the corresponding data set. This leads to the normalized cumulative distances shown in graph (b).



clouds  $\mathcal{P}_{LO}$  and PLQ, we used the aerial lidar simulator from Marchand *et al.* (2021). This is because such a large urban environment is typically scanned using an airborne lidar system. Their code offers the possibility to simulate a plane flying above the scene with the laser ray of a lidar system following a parallel line pattern. Realistic noise can be added as a postprocessing step to imitate typical devices from the market. The problem with the parallel line pattern is that facades that are perpendicular to the direction of the plane are not reachable by the laser ray and thus are absent from the resulting point cloud. In order to overcome this issue, we implemented the elliptical scanning pattern. It is indeed better suited to urban environments, for the laser ray will be able to point at far more facades than with the parallel line pattern, resulting in better coverage.

#### Elliptical Aerial Lidar Simulator

We use  $(O, \vec{e}_x, \vec{e}_y, \vec{e}_z)$  as the global coordinate frame, in which mesh vertices coordinates are expressed as shown in Figure 7. We model the acquisition by a linear trajectory of the lidar optical center  $M$  moving straight from  $A (X_A, Y_A, Z_A)$  to  $B (X_B, Y_B, Z_B)$  at constant speed  $v_0$ . We define a local coordinate frame  $(M, \vec{i}, \vec{j}, \vec{k})$  associated to  $M$  defined as

$$\vec{k} = \frac{\overrightarrow{AB}}{\|\overrightarrow{AB}\|}; \quad \vec{j} = \frac{\vec{e}_z \wedge \vec{k}}{\|\vec{e}_z \wedge \vec{k}\|}; \quad \vec{i} = \vec{j} \wedge \vec{k} \quad (11)$$

Denoting  $\vec{r}$  as the direction of the laser ray and using  $(M, \vec{u}, \vec{v}, \vec{w})$  as the canonical spherical coordinate frame,  $\vec{r}$  is rotating around  $\vec{w}$  at

constant angular speed  $\omega = \dot{\phi}$  with  $\phi$  as the azimuthal angle of  $\vec{r}$ . The polar angle  $\theta$  is constant. In accordance with Marchand *et al.* (2021), the noise that is added to the point positions follows a normal distribution that we can split between a planimetric  $\Delta X, \Delta y$ , and altimetric  $\Delta z$  component:

$$\Delta x, \Delta y \sim \mathcal{N}(\mu_{xy}, \sigma_{xy}^2); \quad \Delta z \sim \mathcal{N}(\mu_z, \sigma_z^2) \quad (12)$$

The values of all the parameters we used can be found in Table 1. We chose these values based on the default values of a real aerial lidar system (Leica TerrainMapper). In the future, we intend on fine-tuning this simulator to maximize point coverage.

Table 1. Values of experimental parameters used.

Symbol	Value	Unit	Description
$h$	1000	m	Flying altitude
$v_0$	60	m·s <sup>-1</sup>	Flying speed
$\omega$	150	Hz	Angular speed
$\theta_0$	160	(°)	Polar angle
$f_p$	400 000	Hz	Pulse frequency
$\sigma_{xy}$	0.13	m	Planimetric error
$\sigma_z$	0.05	m	Altimetric error

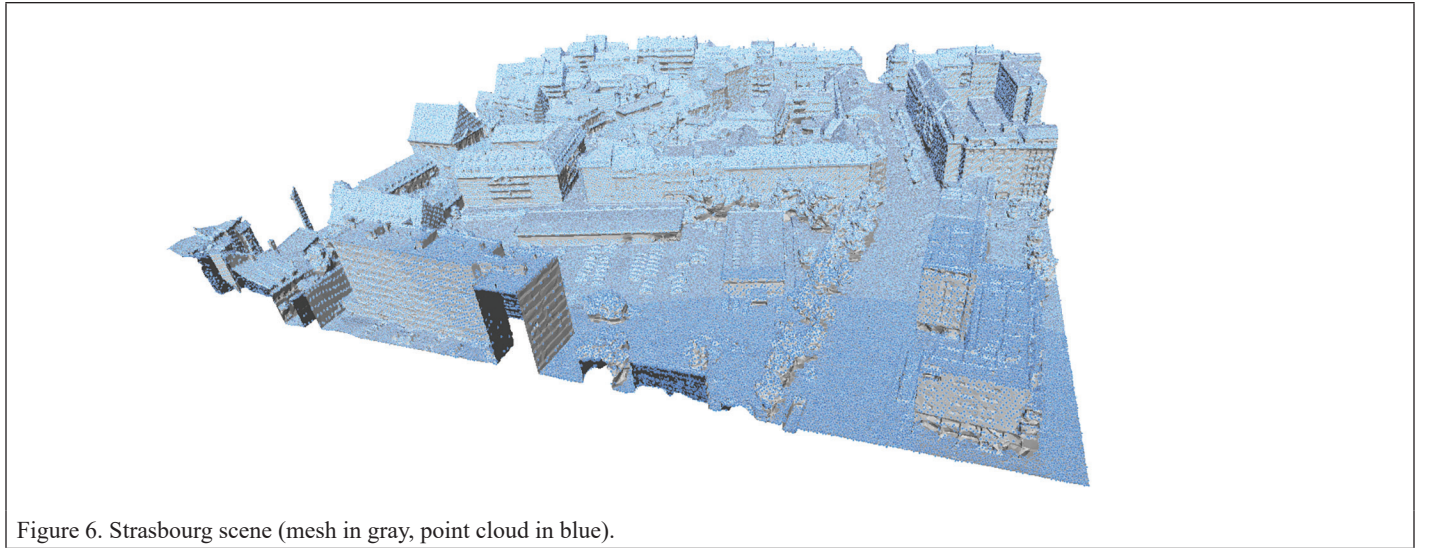


Figure 6. Strasbourg scene (mesh in gray, point cloud in blue).

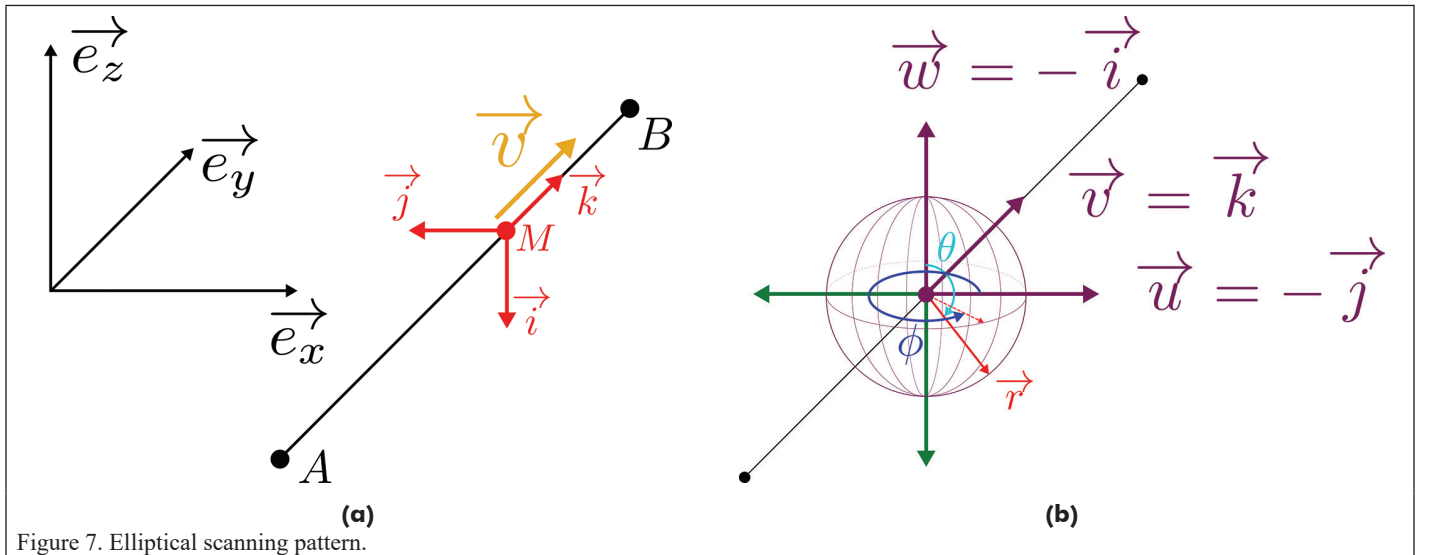


Figure 7. Elliptical scanning pattern.

### Experimental Setup

We aim to produce two point clouds  $\mathcal{P}_{\text{HQ}}$  and  $\mathcal{P}_{\text{LQ}}$  in such a way that  $\mathcal{P}_{\text{HQ}}$  should have fewer occlusions and be denser than  $\mathcal{P}_{\text{LQ}}$ . The scenes are all  $250 \times 250$  m tiles of an urban environment for which positions are expressed in a global coordinate frame  $(O, \vec{e}_x, \vec{e}_y, \vec{e}_z)$  such that  $\vec{e}_z$  represents the ascending vertical direction. In our setup, a trajectory of the lidar system for each scene is a single straight pass of the plane

along axis  $\vec{e}_y$  for  $x = \alpha_x (x_{\text{max}} - x_{\text{min}})$ ,  $\alpha_x \in [0, 1]$ . We generate  $\mathcal{P}_{\text{LQ}}$  thanks to one pass of the plane with  $\alpha_x = 0.5$  and  $\mathcal{P}_{\text{HQ}}$  thanks to three passes with  $\alpha_x \in \{0.25, 0.5, 0.75\}$ . We denote  $\mathcal{P}_{\alpha_x}$  as the point cloud resulting from the flight  $x = \alpha_x (x_{\text{max}} - x_{\text{min}})$ . We then have  $\mathcal{P}_{\text{LQ}} \mathcal{P}_{\text{LQ}} = \mathcal{P}_{0.5}$  and  $\mathcal{P}_{\text{HQ}} = \mathcal{P}_{0.25} \cup \mathcal{P}_{0.5} \cup \mathcal{P}_{0.75}$ . This way, forms part of  $\mathcal{P}_{\text{HQ}}$  and contains a lot more occlusions, in particular on facades parallel to the direction of the plane. Figure 8 gives an example of such a situation.

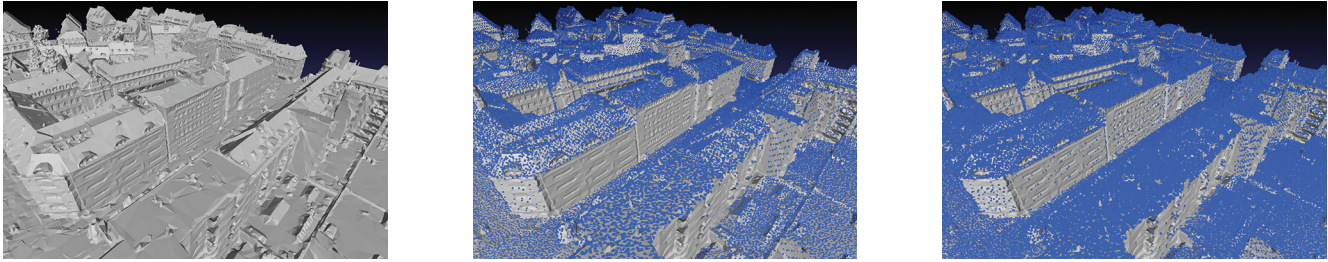


Figure 8. Left: mesh. Center:  $\mathcal{P}_{\text{LQ}}$ . Right:  $\mathcal{P}_{\text{HQ}}$ . The facades parallel to the direction of the plane are a lot more occluded in  $\mathcal{P}_{\text{LQ}}$ .

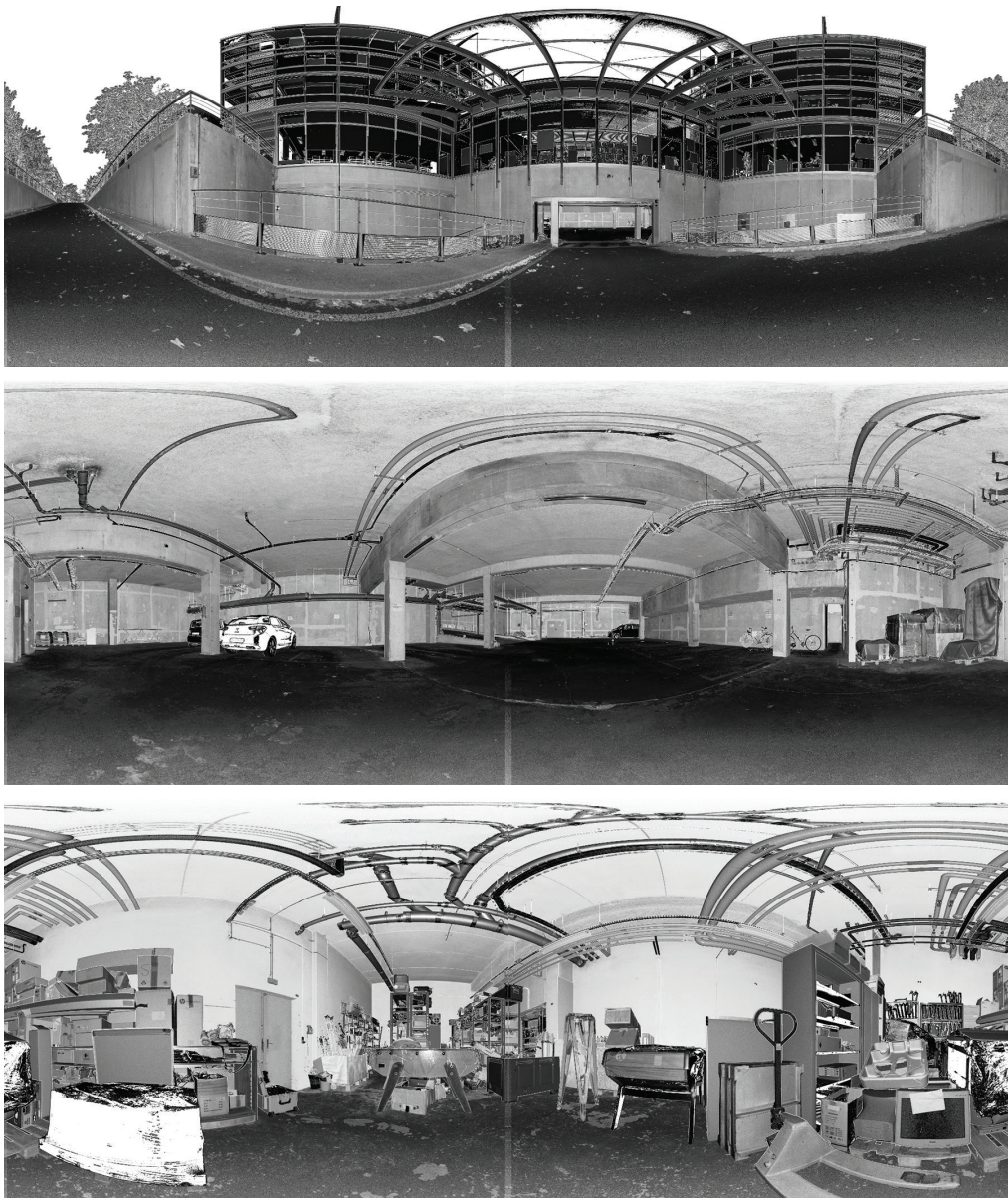


Figure 9. Equirectangular projection of the lidar points. Top: outdoor scene (Building) from  $O_3$ . Middle: indoor scene (Parking Lot) from  $O_2$ . Bottom: indoor scene (Clutter) from  $O_1$ . Building and Parking Lot share some space thanks to what can be seen through the open door in the middle of both images.

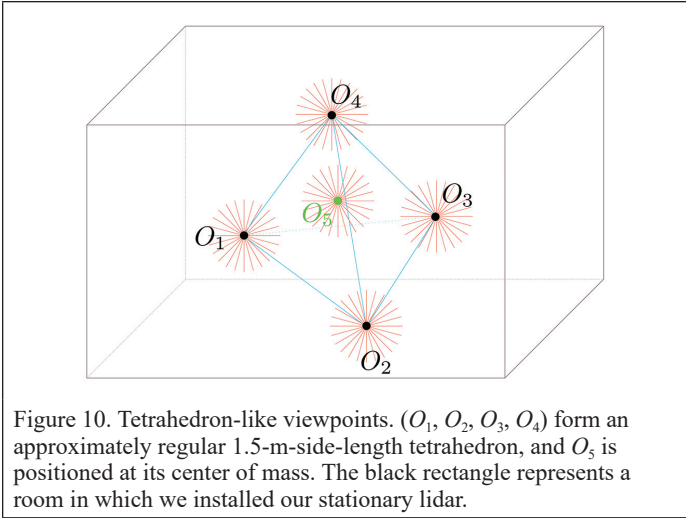


Figure 10. Tetrahedron-like viewpoints. ( $O_1, O_2, O_3, O_4$ ) form an approximately regular 1.5-m-side-length tetrahedron, and  $O_5$  is positioned at its center of mass. The black rectangle represents a room in which we installed our stationary lidar.

**ENSG Data Set: Indoor and Outdoor Terrestrial Lidar Scan**

As the original goal of our study was to propose an evaluation protocol suited for real data, this data set is based only on real data that we acquired ourselves. The resulting point cloud intensity channel can be visualized in Figure 9.

**Stationary Lidar Station**

We used the stationary lidar station Leica ScanStation P40, for which we will give a brief introduction. Once the station is settled, rays are cast  $360^\circ$  horizontally around its origin and  $290^\circ$  vertically (the ground area immediately underneath the station remains unobserved during the acquisition). It can acquire up to 1,000,000 points per second from 0.4 to 270 m  $\mathcal{P}_{HQ}$  with a 3D position accuracy of 3 mm at 50 m. In order to satisfy the condition of being of higher quality than  $\mathcal{P}_{LQ}$ , we decided to acquire points from more viewpoints to generate  $\mathcal{P}_{HQ}$ , using the same

lidar station. We thus scanned each environment from five positions: the four vertices of an approximately regular 1.5 m side length tetrahedron ( $O_1, O_2, O_3, O_4$ ) and its center of mass  $O_5$  as shown in Figure 10. In order to evaluate surface reconstruction algorithms in several different scenarios, we repeated this procedure for three scenes:

- Building: an outdoor scene made of a building, a sloped road, trees, and an opening to another scene called Parking Lot.
- Parking Lot: an indoor scene with pipes, partially occluded cars, and open doors, including one communicating with the outdoor scene Building.
- Clutter: a closed indoor scene with a lot of occlusions due to a high density of objects.

**Matrix Format and Subsampling**

Following the definition of our protocol (see “Evaluation Protocol”), we need to generate poorer-quality point clouds to run reconstructions. Our lidar system has a spherical geometry. The horizontal resolution and vertical resolution of the scanner define a fixed number  $w$  of values for  $\phi$  and a fixed number  $h$  of values for  $\theta$ , respectively. Laser rays are thus cast in the directions given by every pair of angles  $(\phi, \theta)$ . We can thus represent the points as a matrix of height  $h$  and width  $w$  and then index all points by their  $(i, j) \in [1, h] \times [1, w]$  coordinates. Figure 9 shows the intensity of the returns in this matrix-like format. Each raw acquired point cloud did not fit into the memory of our machine, so we down-sampled them by keeping odd-indexed points. Starting from the raw point clouds with origins centered on  $O_1, O_2, O_3, O_4$ , and  $O_5$ , respectively, we down-sampled them all (roughly four times) following this matrix-based scheme, and  $\mathcal{P}_{HQ}$  is the union of these five four-time down-sampled point clouds. We repeated this matrix-based down-sampling scheme on the point cloud centered on  $O_5$  to generate  $\mathcal{P}_{LQ}$ .

**ETH3D Data Set**

Schops *et al.* (2017) present a two- and multi-view stereo benchmark. Their data set contains several scenes with the following:

- input images at 24 MP resolution on several scenes
- ground-truth 3D laser scan point clouds

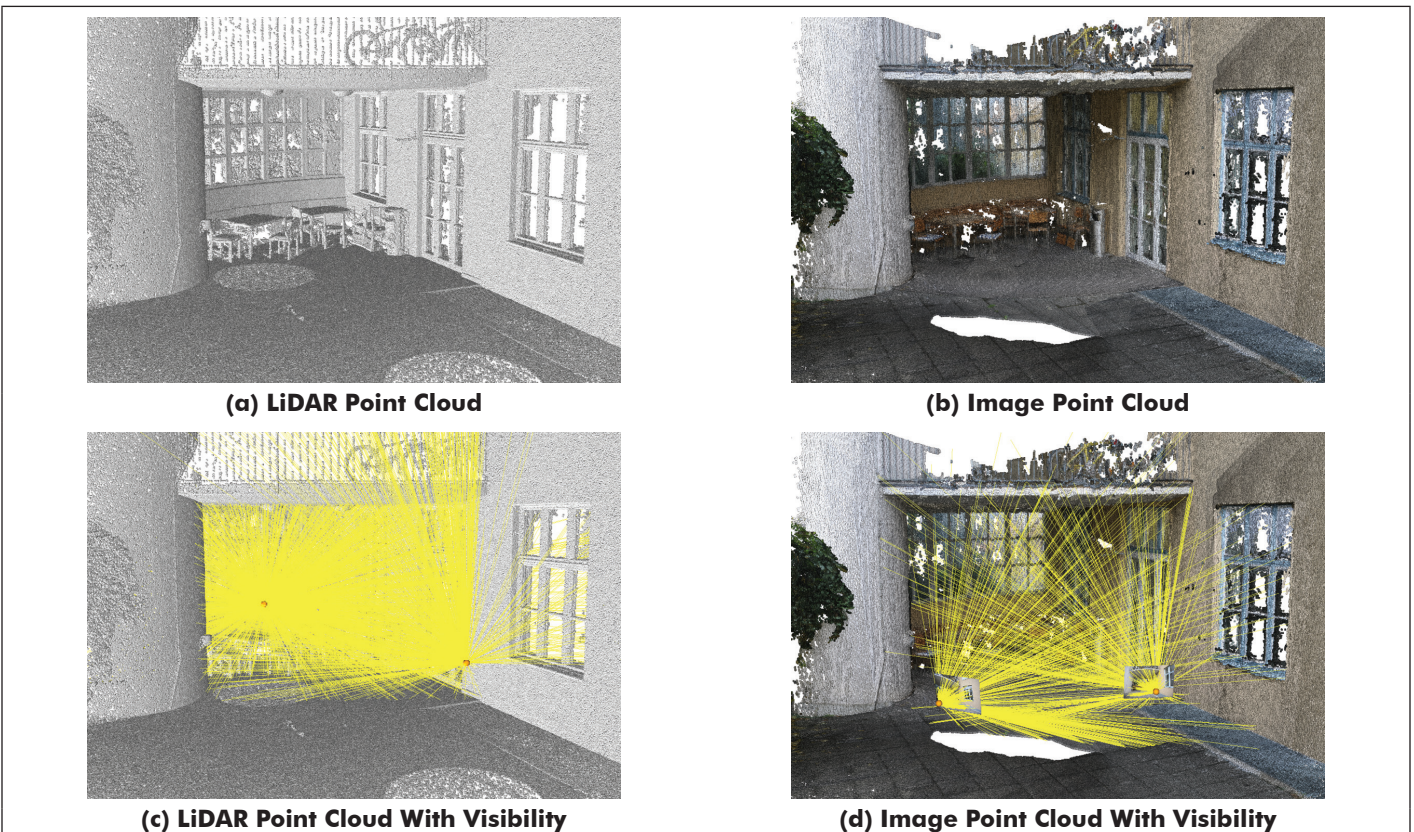


Figure 11. Point clouds with visibility information: terrestrial point clouds (a, b) from the Terrace scene of ETH3D (Schops *et al.* 2017). We visualize some of the sensor positions (●) and lines of sight (c, d).

### Generating the Point Clouds: Multi-View Stereo and Real Lidar

In order to generate the low-quality data, we used the OpenMVS (Cernea 2020) library to generate dense point clouds from images using the provided camera poses of three scenes (Terrace, Courtyard, and Pipes) of the ETH3D train data set. We used the DensifyPointCloud tool of OpenMVS with the standard settings, except for the following parameters: number-views-fuse = 2; optimize = 0; and resolution-level = 4. We used the provided lidar point clouds as our high-quality data. A typical MVS pipeline generates a much sparser and more noisy point cloud than what a laser scan provides. It also contains more outliers. For all these reasons, we consider it relevant to carry out an evaluation on a set of MVS-based point clouds. We thus used three scenes from the ETH3D data set (Schops *et al.* 2017), which can be seen in Figures 11 and 12.



Figure 12. Images of the three scenes from the ETH3D data set we used. Top: Outdoor scene (Courtyard). Middle: indoor scene (Pipes). Bottom: Outdoor Scene (Terrace).

## Results

In this survey, we assessed the following:

- RESR (Labatut *et al.* 2009).
- SSD (Calakli and Taubin 2011) with two combinations of the octree depth and the B-spline degree parameters: (depth = 8; degree = 2) and (depth = 12; degree = 3).
- Poisson (Kazhdan and Hoppe 2013) with two values for the octree depth parameter: 8 and 11. The B-spline degree will always be 2.
- DGNN (Sulzer *et al.* 2021).
- PSS (Lafarge and Alliez 2013) with two values for the trade-off parameter: 0.1 and 0.6.
- Agisoft Metashape version 1.6.4 (2020year) with extrapolated mode and ultra-high resolution. Only the meshing tool has been used on the point cloud data.

For the ETH3D data set only, we assess two other surface reconstruction algorithms, as they are part of the OpenMVS (Cernea 2020) pipeline. Mesh reconstruction is initiated using exploiting visibility information in surface reconstruction to preserve weakly supported surfaces (WSS) (Jancosek and Pajdla 2014). A refinement step is then carried out using high accuracy and visibility-consistent dense multi-view stereo (DMS) (Vu *et al.* 2011). We thus computed the metrics on the resulting meshes from both these methods. According to the definitions provided in “Metric Definitions,” Tables 2–5 give the mean ray distance (for those smaller than  $d_{max}$ ), the precision and recall ratios, as well as the F-score.

### STRAS Data Set

Table 2 shows the results for one single mesh from the STRAS data set, and Table 3 shows the average of those results for the three meshes of

Table 2. Raw numerical results from STRAS PC3E44\_3 for  $d_{max} = 50$  cm.

Method	TP	FP	TP + FN	MD (cm)	P (%)	R (%)	F1 (%)
RESR	1 278 734	57 089	1 365 120	6.58	95.73	93.67	94.69
DGNN	1 246 228	72 899	1 365 120	6.79	94.47	91.29	92.85
Poisson 11/2	1 267 301	128 888	1 365 120	8.91	90.77	92.83	91.79
PSS 0.6	1 217 138	81 549	1 365 120	7.39	93.72	89.16	91.38
SSD 12/3	1 271 969	172 285	1 365 120	9.56	88.07	93.18	90.55
SSD 8/2	1 203 150	167 204	1 365 120	13.04	87.80	88.14	87.97
Poisson 8/2	1 174 069	151 134	1 365 120	12.77	88.60	86.00	87.28
Metashape	1 033 179	195 725	1 365 120	19.41	84.07	75.68	79.66
PSS 0.1	1 280 230	686 825	1 365 120	7.47	65.08	93.78	76.84

DGNN = Delaunay-graph neural network; F1 = F-score; MD = mean ray distance; P = precision; PSS = point set structuring; R = recall; RESR = robust and efficient surface reconstruction; SSD = smooth signed distance.

Table 3. Average numerical results on the three scenes from the STRAS data set sorted by decreasing the F-score for  $d_{max} = 50$  cm.

Method	Mean Distance (cm)	Precision (%)	Recall (%)	F-score (%)
RESR	5.98	96.68	94.88	95.77
DGNN	6.13	96.08	92.56	94.29
Poisson 11/2	7.99	93.19	94.31	93.75
PSS 0.6	6.67	95.08	91.35	93.17
SSD 12/3	8.53	90.72	94.63	92.63
SSD 8/2	11.57	90.11	90.48	90.30
Poisson 8/2	11.49	91.11	88.39	89.73
Metashape	16.21	87.92	80.63	84.11
PSS 0.1	6.76	72.72	95.00	82.28
Mean methods	9.04	90.40	91.36	90.67

DGNN = Delaunay-graph neural network; PSS = point set structuring; RESR = robust and efficient surface reconstruction; SSD = smooth signed distance.

the STRAS data set. In accordance with the survey conducted and published in Marchand *et al.* (2021) on the same data set but with different assumptions and metrics, Table 3 shows that RESR achieves the best performance again on the urban environment from STRAS regarding

Table 4. Average numerical results on the three scenes from the ENSG data set sorted by decreasing the F-score for  $d_{max} = 20$  cm.

Method	Mean Distance (cm)	Precision (%)	Recall (%)	F-score (%)
RESR	0.45	93.10	95.99	94.51
Poisson 11/2	0.90	78.38	96.96	86.22
Poisson 8/2	2.72	78.66	88.16	83.05
SSD 12/3	1.27	72.41	96.04	82.23
Metashape	1.63	79.00	83.95	81.37
SSD 8/2	3.04	71.95	87.77	78.96
DGNN	0.49	52.99	96.22	68.28
PSS 0.6	0.54	28.44	97.92	43.94
PSS 0.1	0.54	22.30	98.19	36.18
Mean methods	1.29	64.14	93.47	72.75

DGNN = Delaunay-graph neural network; PSS = point set structuring; RESR = robust and efficient surface reconstruction; SSD = smooth signed distance.

Table 5. Average numerical results on the three scenes from the ETH3D data set sorted by decreasing the F-score for  $d_{max} = 20$  cm.

Method	Mean Distance (cm)	Precision (%)	Recall (%)	F-score (%)
DMS	2.04	95.33	93.72	94.47
Poisson 11/2	2.56	93.91	94.04	93.96
RESR	2.62	94.12	92.65	93.29
Metashape	2.57	95.09	91.18	93.00
WSS	2.66	91.31	93.79	92.51
SSD 12/3	2.66	90.65	94.44	92.48
SSD 8/2	4.21	93.38	89.03	91.13
Poisson 8/2	3.99	94.66	86.94	90.59
DGNN	2.61	79.47	93.63	85.95
PSS 0.6	2.52	67.41	94.63	78.52
PSS 0.1	2.56	53.79	95.16	66.99
Mean methods	2.82	86.28	92.66	88.44

DGNN = Delaunay-graph neural network; DMS = dense multiview stereo; PSS = point set structuring; RESR = robust and efficient surface reconstruction; SSD = smooth signed distance; weakly supported surfaces.

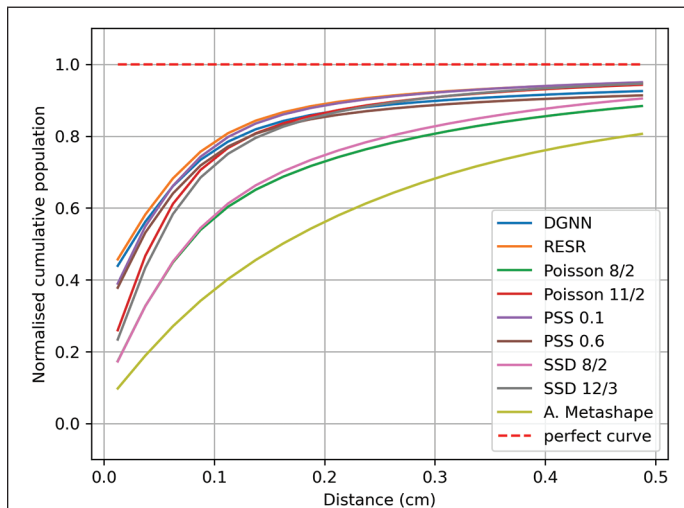


Figure 13. Cumulative distances over the three scenes from the STRAS data set for  $d_{max} = 50$  cm.

both precision and recall. As evaluating surface reconstruction from only real data is harder than using synthetic data (we do not have an exhaustive ground truth), it is a very sound validation that the metrics that we defined without access to the ground-truth surface show similar tendencies to the metrics that are based on ground-truth surfaces.

We also carried out a more detailed evaluation by testing several values for the main parameters of selected methods. We found that the trade-off of PSS (Lafarge and Alliez 2013) has a big effect on the metrics. More precisely, the lower we set it (i.e., the more confidence we give to the data), the lower the precision but the higher the recall (and vice versa). A high confidence in the data results in a lot more interfaces between occupied tetrahedra and empty ones. Conversely, a higher trade-off  $\lambda$  gives more power to the regularization term, resulting in fewer couples of adjacent tetrahedra being labeled differently and thus fewer triangles in the output mesh. When more confidence is given to the data, there are a lot more undesired triangles “floating” in regions of free space, which dramatically affects the precision. However, small structures might be erased from the mesh if less confidence is given to the data term, resulting in a poorer recall.

Both Poisson (Kazhdan *et al.* 2006) and SSD (Calakli and Taubin 2011) are influenced positively by an increase in the octree depth. This was expected since more points are used to reconstruct the mesh, which results in an increase in the computation time and memory footprint.

DGNN performs a lot better on the STRAS data set than on the two others, which highlights a problem in its capacity to generalize to scenes that differ from the ones in the training set. However, its poorer F-score performance on ETH3D and ENSG is due mostly to the precision metric. DGNN often succeeds in recovering the scene features but adds too many undesired triangles in the scene.

While precision, recall, and ray distance provide complete information on the quality of the reconstruction, one might find it more intuitive to start by having a look at the cumulative distances shown in Figure 13. The precision at small range can be estimated as the area under the curve. The closer the curve is to the top left-hand corner, the better it is since this means that all the TPs are actually very close to it. Besides, the highest value of each curve is the recall of the corresponding method, so the gap between the cumulative population in the last category and the line  $y = 1$  should be as small as possible.

### ENSG Data Set

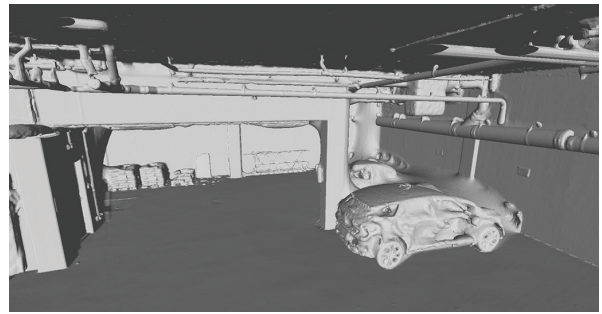
The ENSG data set, having been generated using a stationary lidar system, is the one containing the least amount of noise, hence the overall good performance of all of the methods. In particular, we can see that the mean distance is generally a lot smaller than with other data sets even though the scenes themselves have much more complicated geometries and more occlusions.

Figure 14 shows the meshes reconstructed by every assessed algorithm on the Parking Lot scene (part of the ENSG data set). One can fairly easily interpret the performance achieved by these methods by analyzing the type of mistake they made on the corresponding scene. RESR succeeds at reconstructing most of the visible parts, and very few undesired triangles lie in free space (most of them are connecting the pipes to the wall and the ceiling).

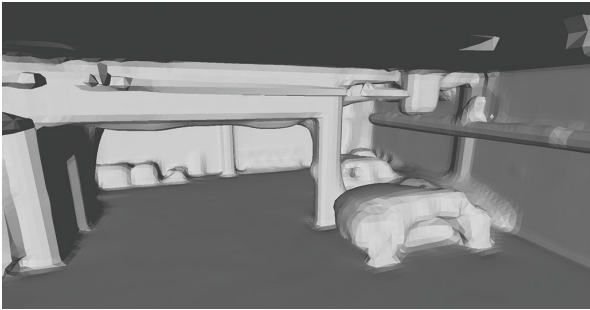
At first glance, Poisson 11/2 reconstruction seems to be a lot more accurate than Poisson 8/2, so it might not be obvious why they have the same precision. This situation actually shows the interest of the mean distance metric. While the two reconstructed models are structurally the same, the difference between them is visible at close range: under the threshold  $d_{max}$ . Consequently, Poisson 8/2 has a much higher mean distance than Poisson 11/2 but achieves a similar precision. The same kind of argument holds for explaining the relatively poor performance of SSD 12/3 and Metashape: while being locally more accurate than Poisson 8/2, the meshes are structurally not in accordance with the visibility information provided by the high-quality point cloud. The precision metric is dramatically affected by large portions of surface lying in free space. DGNN and PSS have the same problem: while having a high recall, denoting their capacity to recover most of the existing pieces of surface (and very accurately given the very low mean



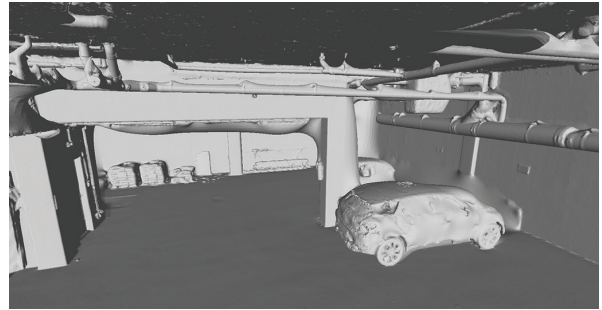
**(a) RESR**



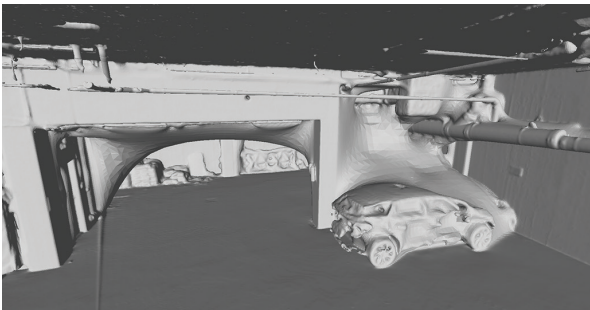
**(b) Poisson 11/2**



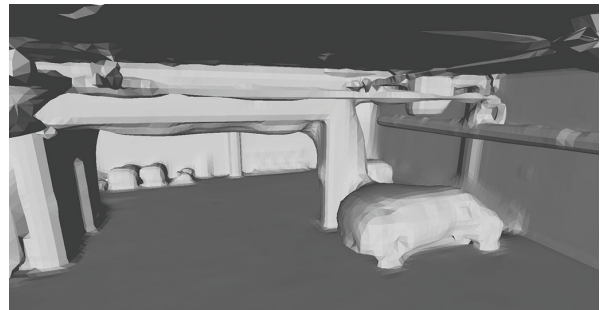
**(c) Poisson 8/2**



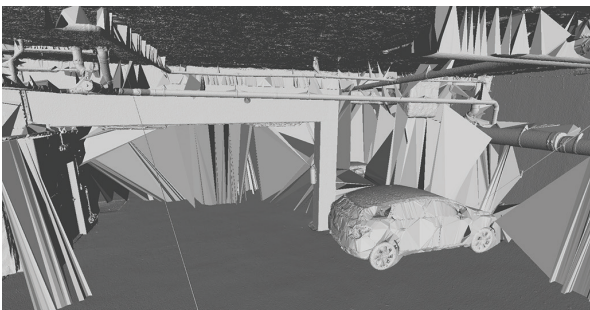
**(d) SSD 12/3**



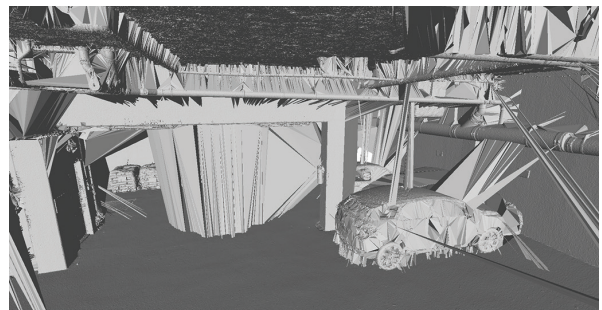
**(e) A. Metashape**



**(f) SSD 8/2**



**(g) DGNN**



**(h) PSS 0.6**



**(i) PSS 0.1**

Figure 14. Reconstructed meshes from the ENSG Parking Lot scene.

distance metric), they connect too many regions of space with triangles lying in empty space, thus affecting their precision.

The accordance between all of these visual observations and the corresponding quantitative results given by our metrics prove their relevance.

### ETH3D Data Set

MVS-based point clouds are known to be noisy and contain a lot of outliers. This seems to have an effect on the performance of the different methods. The ones performing best on ENSG and STRAS seem to struggle more, and, surprisingly, Poisson 8 (Kazhdan *et al.* 2006) achieves a fairly high precision on this data set. We believe that this is because it is more capable of filtering out the noise with an 8-depth than with an 11-depth octree. That would explain why SSD 8/2 also has a better precision than SSD 12/3. However, their poorer recall indicates that more pieces of real surface have not been recovered.

The method that performs best, however, is DMS, which is not very surprising considering the fact that it is the best version of a real MVS pipeline, fed with images and not with an image-derived point cloud.

The relatively good performance of Agisoft Metashape on ETH3D compared to the other data sets might suggest that it copes pretty well with outliers. More generally, considering that it is a licensed solution, we might have expected a better overall performance on at least one of our data sets.

### General Remarks

Overall, RESR is the method that performs best almost everywhere. DGNN shows that learning how to reconstruct large, complex and open scenes is indeed possible, but it faced generalization problems since the metrics on the ENSG and ETH3D data sets are significantly lower than those on STRAS (from which its training set was extracted). However, with RESR and DGNN being the only methods from this survey making use of sensor positions, we believe that this is an important reason behind their good results. Sensor positions give an important piece of information that neither the points themselves nor the associated normals provide.

Poisson generally performs structurally better than SSD. Small-scale differences are noticeable when changing the octree depth used by both these algorithms.

PSS often reconstructs meshes very close to the real surface but also connects pieces of surface in regions of space that should remain empty. We can assume that we failed to find the right parameter settings because it was definitely the hardest algorithm to tune, but this is the best performance we managed to get.

### Conclusion

Surface reconstruction is hard to evaluate since it is impossible to directly compute the difference between the real surface and a reconstructed one. It has often been assessed visually because it seems fairly intuitive to know whether a piece of surface has been accurately recovered. However, human perception can be unfair, and a purely visual evaluation lacks quantitative information. In this article, we proposed new metrics to assess surface reconstruction. We have leveraged the visual information obtained by combining the acquired points and the associated sensor positions in order to define what we believe are more relevant metrics than the ones currently used. They imitate the process of a human being looking at and comparing the two surfaces (the real one and the reconstructed one). This goal has been achieved since our survey validates behaviors that a human can interpret by just looking at the meshes. In “Results,” we drew parallels between the specific visual observations and the quantitative evidence provided by our metrics that confirms them.

Our metrics enable the assessment of the completeness of the reconstructions as well as their precision both locally and globally. One can thus analyze the results from different points of view. As a relevant outcome, our survey also confirms that sensor positions are very relevant when trying to separate occupied from empty space.

As well as all these advantages that make surface reconstruction evaluation more objective, the fact that we use only raw data acquired with basic sensors makes it easy to set up a new experiment. Having access to expensive data is not a requirement. We provide a tool to make surface reconstruction evaluation easier and wish to see it used widely.

### References

- Agisoft LLC, 2020. *Metashape* version 1.6.4. Platform, Agisoft LLC. URL: [https://www.agisoft.com/pdf/metashape-pro\\_1\\_6\\_en.pdf](https://www.agisoft.com/pdf/metashape-pro_1_6_en.pdf).
- Alexa, M., J. Behr, D. Cohen-Or, S. Fleishman, D. Levin and C. T. Silva. 2001. Point set surfaces. Pages 21-28 in *Proceedings of the Conference on Visualization '01*, held in San Diego, CA, USA, October 24-26, 2001. Washington, DC, USA: IEEE Computer Society.
- Berger, M., J. A. Levine, L. G. Nonato, G. Taubin and C. T. Silva. 2013. A benchmark for surface reconstruction. *ACM Transactions on Graphics* 32(2):1–17.
- Berger, M., A. Tagliasacchi, L. M. Seversky, P. Alliez, G. Guennebaud, J. A. Levine, A. Sharf and C. T. Silva. 2017. A survey of surface reconstruction from point clouds. *Computer Graphics Forum* 36(1):301–329.
- Calakli, F. and G. Taubin. 2011. SSD: Smooth signed distance surface reconstruction. *Computer Graphics Forum* 30(7):1993–2002.
- Caraffa, L., M. Brédif and B. Vallet. 2016. 3D watertight mesh generation with uncertainties from ubiquitous data. In *Computer Vision—ACCV 2016*, edited by S.-H. Lei, V. Lepetit, K. Nishino and Y. Sato, 377–391. Lecture Notes in Computer Science. Cham, Switzerland: Springer International Publishing.
- Cernea, D. 2020. OpenMVS: Multi-View Stereo Reconstruction Library.
- Chen, Z. and Zhang, H. 2019. Learning implicit fields for generative shape modeling. Pages 5939–5948 in *Proceedings of the IEEE Conference on Computer Vision and Pattern Recognition*, held in Long Beach, California, United States, June 16-20 2019. Edited by Lisa O’Conner. Washington, DC, USA: IEEE Computer Society.
- Cheng, Z.-Q., Y.-Z. Wang, B. Li, K. Xu, G. Dang and S.-Y. Jin. 2008. A survey of methods for moving least squares surfaces. Pages 9–23 in *Proceedings of the Fifth Eurographics/IEEE VGTC Conference on Point-Based Graphics, SPBG’08*, held in Los Angeles, CA, USA, August 10-11 2008. Edited by Hans-Christian Hege, David Laidlaw, Renato Pajarola, Oliver Staadt. Los Angeles: Eurographics Association.
- Cignoni, P., C. Rocchini and R. Scopigno. 1998. Metro: Measuring error on simplified surfaces. *Computer Graphics Forum* 17(2):167–174.
- Furukawa, Y. and C. Hernández. 2015. Multi-view stereo: A tutorial. *Foundations and Trends in Computer Graphics and Vision* 9(1–2):1–148.
- Geng, J. 2011. Structured-light 3D surface imaging: A tutorial. *Advances in Optics and Photonics* 3(2):128–160.
- Groueix, T., M. Fisher, V. G. Kim, B. C. Russell and M. Aubry. 2018. A Papier-Mâché Approach to Learning 3D Surface Generation. Pages 216–224 in *IEEE Conference on Computer Vision and Pattern Recognition (CVPR)*, held in Salt Lake City, Utah, USA, June 18-22 2018. Edited by Lisa O’Conner. Washington, DC, USA: IEEE Computer Society.
- Hildebrandt, K., K. Polthier and M. Wardetzky. 2006. On the convergence of metric and geometric properties of polyhedral surfaces. *Geometriae Dedicata* 123(1):89–112.
- Holenstein, C., R. Zlot and M. Bosse. 2011. Watertight surface reconstruction of caves from 3D laser data. Pages 3830–3837 in *2011 IEEE/RSJ International Conference on Intelligent Robots and Systems*, held in San Francisco, USA, September 25-30 2011. Edited by Nancy M. Amato. New York: IEEE.
- Hoppe, H., T. Derose, T. Duchamp, J. McDonald and W. Stuetzle. 1996. Surface reconstruction from unorganized points. *SIGGRAPH Computer Graphics* 26(2):71–78.
- Jancosek, M. and T. Pajdla. 2014. Exploiting visibility information in surface reconstruction to preserve weakly supported surfaces. *International Scholarly Research Notices* 2014(XX):1–20.
- Kazhdan, M. 2005. Reconstruction of solid models from oriented point sets. Pages 73 in *Proceedings of the Third Eurographics Symposium on Geometry Processing*, held in Vienna, Austria, July 04-06 2005. Edited by Mathieu Desbrun and Helmut Pottmann. Los Angeles: Eurographics Association.

- Kazhdan, M., M. Bolitho and H. Hoppe. 2006. Poisson surface reconstruction. Pages 61–70 in *Proceedings of the Fourth Eurographics Symposium on Geometry Processing*, held in Cagliari Sardinia, Italy, June 26-28 2006. Edited by Alla Sheffer and Konrad Polthier. Los Angeles: Eurographics Association.
- Kazhdan, M. and H. Hoppe. 2013. Screened Poisson surface reconstruction. *ACM Transactions on Graphics* 32(3):1–13.
- Khatamian, A. and H. Arabnia. 2016. Survey on 3D surface reconstruction. *Journal of Information Processing Systems* 12:338–357.
- Kolluri, R., J. R. Shewchuk and J. F. O'Brien. 2004. Spectral surface reconstruction from noisy point clouds. Pages 11–21 in *Proceedings of the 2004 Eurographics/ACM SIGGRAPH Symposium on Geometry Processing, SGP '04*, held in Nice, France, July 08-10 2004. Edited by R. Scopigno and D. Zorin. New York: Association for Computing Machinery.
- Labatut, P., J.-P. Pons and R. Keriven. 2009. Robust and efficient surface reconstruction from range data. *Computer Graphics Forum* 28(8): 2275–2290.
- Lafarge, F. and P. Alliez. 2013. Surface reconstruction through point set structuring. *Computer Graphics Forum*, 32(2): 225-234
- Lancaster, P. 1979. Moving weighted least-squares methods. In *Polynomial and Spline Approximation: Theory and Applications*, edited by B. N. Sahney, 103–120. NATO Advanced Study Institutes Series. Dordrecht: Springer Netherlands.
- Lange, R. and P. Seitz. 2001. Solid-state time-of-flight range camera. *IEEE Journal of Quantum Electronics* 37(3):390–397.
- Levin, D. 1998. The approximation power of moving least-squares. *Mathematics of Computation* 67:1517–1531.
- Levin, D. 2003. Mesh-independent surface interpolation. *Geometric Modeling for Scientific Visualization* 3:37–49.
- Lohani, B. and S. Ghosh. 2017. Airborne LiDAR technology: A review of data collection and processing systems. *Proceedings of the National Academy of Sciences, India Section A: Physical Sciences* 87(4):567–579.
- Manivasagam, S., S. Wang, K. Wong, W. Zeng, M. Sazanovich, S. Tan, B. Yang, W.-C. Ma and R. Urtasun. 2020. LiDARsim: Realistic LiDAR simulation by leveraging the real world. Pages 11167–11176 in *Proceedings of the IEEE/CVF Conference on Computer Vision and Pattern Recognition (CVPR)*, held online, June 14-19 2020. Edited by Lisa O'Conner. Washington, DC, USA: IEEE Computer Society.
- Manson, J., G. Petrova and S. Schaefer. 2008. Streaming surface reconstruction using wavelets. Pages 1411–1420 in *Proceedings of the Symposium on Geometry Processing, SGP '08*, held in Copenhagen, Denmark, July 02-04 2008. Edited by Pierre Alliez and Szymon Rusinkiewicz. Los Angeles: Eurographics Association.
- Marchand, Y., B. Vallet and L. Caraffa. 2021. Evaluating surface mesh reconstruction of open scenes. *International Archives of the Photogrammetry, Remote Sensing and Spatial Information Sciences* 43:369–376.
- Mescheder, L., M. Oechsle, M. Niemeyer, S. Nowozin and A. Geiger. 2019. Occupancy networks: Learning 3d reconstruction in function space. Pages 4460–4470 in *Proceedings of the IEEE Conference on Computer Vision and Pattern Recognition*, held in Long Beach, California, United States, June 16-20 2019. Edited by Lisa O'Conner. Washington, DC, USA: IEEE Computer Society.
- Nan, L. and P. Wonka. 2017. Polyfit: Polygonal surface reconstruction from point clouds. Pages 2353–2361 in *Proceedings of the IEEE International Conference on Computer Vision*, held in Venice, Italy, October 22-29 2017. Edited by Lisa O'Conner. Washington, DC, USA: IEEE Computer Society.
- Ohtake, Y., A. Belyaev, M. Alexa, G. Turk and H.-P. Seidel. 2003. Multi-level partition of unity implicits. *ACM Transactions on Graphics* 22(3):463–470.
- Ozyesil, O., V. Voroninski, R. Basri and A. Singer. 2017. A survey of structure from motion. Preprint, arXiv:1701.08493.
- Park, J. J., P. Florence, J. Straub, R. Newcombe and S. Lovegrove. 2019. DeepSDF: Learning continuous signed distance functions for shape representation. Pages 165–174 in *Proceedings of the IEEE Conference on Computer Vision and Pattern Recognition*, held in Long Beach, California, USA, June 16-20 2019. Edited by Lisa O'Conner. Washington, DC, USA: IEEE Computer Society.
- Peng, S., C. M. Jiang, Y. Liao, M. Niemeyer, M. Pollefeys and A. Geiger. 2021. Shape as points: A differentiable Poisson solver. Pages 13032–13044 in *35th Conference on Neural Information Processing Systems (NeurIPS 2021)*, held online, December 06-14 2021. Edited by M. Ranzato and A. Beygelzimer and Y. Dauphin and P.S. Liang and J. Wortman Vaughan. La Jolla, CA, USA: Neural Information Processing Systems Foundation, Inc. (NeurIPS).
- Peng, S., M. Niemeyer, L. Mescheder, M. Pollefeys and A. Geiger. 2020. Convolutional occupancy networks. Pages 523–540 in *Computer Vision—ECCV 2020: 16th European Conference*, held in Glasgow, UK, 23–28 August 2020. Edited by Andrea Vedaldi, Horst Bischof, Thomas Brox and Jan-Michael Frahm. New York: Springer.
- Schnabel, R., R. Wahl and R. Klein. 2007. Efficient RANSAC for point-cloud shape detection. *Computer Graphics Forum* 26(2):214–226.
- Schops, T., J. L. Schonberger, S. Galliani, T. Sattler, K. Schindler, M. Pollefeys and A. Geiger. 2017. A multi-view stereo benchmark with high-resolution images and multi-camera videos. Pages 2538–2547 in *Proceedings of the IEEE Conference on Computer Vision and Pattern Recognition (CVPR)*, held in Honolulu, HI, USA, July 21-26 2017. Edited by Lisa O'Conner. Washington, DC, USA: IEEE Computer Society.
- Shepard, D. 1968. A two-dimensional interpolation function for irregularly-spaced data. Pages 517–524 in *Proceedings of the 1968 23rd ACM National Conference, ACM '68*, held in USA, August 27-29 1968. Edited by Richard B. Blue Sr. and Arthur M. Rosenberg. New York: Association for Computing Machinery.
- Sulzer, R., L. Landrieu, R. Marlet and B. Vallet. 2021. Scalable surface reconstruction with Delaunay-graph neural networks. *Computer Graphics Forum* 40(5):157–167.
- Süßmuth, J., Q. Meyer and G. Greiner. 2010. Surface reconstruction based on hierarchical floating radial basis functions. *Computer Graphics Forum* 29(6):1854–1864.
- Ter Haar, F., P. Cignoni, P. Min and R. Veltkamp. 2005. A comparison of systems and tools for 3D scanning. In *3D Digital Imaging and Modeling: Applications of Heritage, Industry, Medicine and Land..*
- Van Kreveland, M., T. Van Lankveld and R. C. Veltkamp. 2013. Watertight scenes from urban lidar and planar surfaces. *Computer Graphics Forum* 32(5):217–228.
- Vu, H.-H., P. Labatut, J.-P. Pons and R. Keriven. 2011. High accuracy and visibility-consistent dense multiview stereo. *IEEE Transactions on Pattern Analysis and Machine Intelligence* 34(5):889–901.
- Winiwarter, L., A.M.E. Pena, H. Weiser, K. Anders, J. M. Sánchez, M. Searle and B. Höfle. 2022. Virtual laser scanning with HELIOS++: A novel take on ray tracing-based simulation of topographic full-waveform 3D laser scanning. *Remote Sensing of Environment* 269:112772.
- Xiao, W., B. Vallet, M. Brédif, and N. Paparoditis. 2015. Street environment change detection from mobile laser scanning point clouds. *ISPRS Journal of Photogrammetry and Remote Sensing* 107:38–49.



# Different Urbanization Levels Lead to Divergent Responses of Spring Phenology

Chaoya Dang, Zhenfeng Shao, Xiao Huang, Gui Cheng, and Jiaxin Qian

## Abstract

Urban vegetation phenology is important for understanding the relationship between human activities on urban ecosystems and carbon cycle. The relationship between urban and rural vegetation phenology and environmental and meteorological factors were studied across urban-rural gradients. However, the relationship of intra-urban urbanization intensity (UI) gradients on vegetation at the start of season (SOS) is unclear. Here, we used remote sensing data to quantitatively assess the relationship of vegetation SOS to UI gradients at mid-high latitudes in the northern hemisphere. The results showed that urban area vegetation SOS widely presented earlier than for rural area vegetation. Across the cities we investigated the extent UI gradient was prevalent as a threshold ( $33.2\% \pm 2.3\%$ ) of surface temperature to SOS advance enhancement and offset. At low urbanization enhanced surface temperature on SOS advances, while at high urbanization offset surface temperature on SOS advances. Overall, UI demonstrated a nonlinear relationship with SOS. The results of this study suggest that there may be thresholds of impact on vegetation SOS in future global climate and environment change processes, where opposite effects can occur below and above thresholds.

## Introduction

Vegetation phenology serves as a significant indicator of vegetation dynamics (Shen *et al.* 2018) and is highly sensitive to the impacts of climate change (Zhou *et al.* 2016; Dang *et al.* 2023a). Global warming has the potential to advance the timing of spring phenology (Körner and Basler 2010; Fu *et al.* 2015). Changes in vegetation phenology have implications for the exchange of carbon, water, and energy between the terrestrial biosphere and the atmosphere (Keenan *et al.* 2014; Richardson *et al.* 2013; Piao *et al.* 2008). Because of the association of urbanization with increasing temperature (Zhang *et al.* 2009) and CO<sub>2</sub> concentration, urban climate conditions are considered to be similar to those under future global warming, making urban environments a natural laboratory for simulating the effects of future climate change on phenology (Wang *et al.* 2019; Yuan *et al.* 2020). Therefore, in-depth studies of urban vegetation phenology changes provide insight into future global climate change, carbon cycle, water cycle, energy cycle, and biodiversity.

Previous studies have often compared urban-rural factors affecting phenology (Zhou *et al.* 2016; Jia *et al.* 2021; Li *et al.* 2016; Meng *et al.* 2020), suggesting that urban-rural phenology differences correlate with urban-rural surface temperatures (Yuan *et al.* 2020; Zhang *et al.* 2004; Shao *et al.* 2021). Studies have investigated the different responses of vegetation phenology to urbanization-induced factors such as surface temperature, CO<sub>2</sub> concentration, precipitation, and urban size (Li *et al.*

2016; Qiu *et al.* 2020; Wang *et al.* 2019; Zhang *et al.* 2022b). However, the pattern of spring vegetation phenology response to urbanization gradients has not been assessed regionally. In addition, urbanization does not only increase surface temperature, but also leads to significant changes in other environmental factors (e.g., CO<sub>2</sub>, population density, and nighttime lighting). Studies have shown that both temperature and CO<sub>2</sub> concentration are major factors in the advancement of photosynthetic phenology in spring (Wang *et al.* 2019). Moreover, urbanization and climate change jointly shift land surface phenology in large cities (Qiu *et al.* 2020). Therefore, the impact of urbanization on vegetation phenology is the result of a joint action of multiple factors. It is very important to separate the direct and indirect impacts of urbanization on urban vegetation phenology.

Badgley *et al.* (2017) proposed a new vegetation index, the near-infrared reflectance of vegetation (NIR<sub>v</sub>), which was the product of the near-infrared band reflectance (NIR) and the normalized difference vegetation index (NDVI) (i.e.,  $NIR_v = NDVI \times NIR$ ). NIR<sub>v</sub> has a good theoretical basis, eliminates most of the mixed image element problems, and is insensitive to background contamination (Badgley *et al.* 2017). Meanwhile, studies have shown that NIR<sub>v</sub> is better than NDVI and enhance vegetation index (EVI) in estimating phenological metrics and in revealing the effects of vegetation phenology on the carbon cycle (Zhang *et al.* 2022a). However, NIR<sub>v</sub> has not been used to explore the response of vegetation phenology to urbanization.

To quantitatively assess the impact of urbanization on vegetation phenology, we modified the conceptual framework of the impact of urbanization on vegetation productivity (Zhao *et al.* 2016; Zhuang *et al.* 2022). We propose the following theoretical framework (Figure 2) and give several necessary definitions. Numerous efforts that use the greenness vegetation indices and NIR<sub>v</sub> have shown that SOS was advanced in urban areas (Wang *et al.* 2019; Li *et al.* 2016; Meng *et al.* 2020). The total actual impact of urbanization on SOS is the change in SOS after urbanization, including indirect impact and direct impact. Cities such as the cities in Minnesota (Yuan and Bauer 2007), Indianapolis (Lu and Weng 2006), Beijing (Xiao *et al.* 2007) and Shanghai (Li *et al.* 2011) have shown a linear positive correlation between surface temperature and impervious surface cover. Moreover, the negative correlation between start of season (SOS) and temperature is linear. Ideally, a negative correlation between SOS and urbanization intensity (UI) should be linear. Therefore, the direct effect refers to the advancement of SOS due to changes in surface temperature caused by the UI. Post-urbanization environments can alter vegetation phenology (e.g., germination and defoliation), and this effect is indirect. Indirect effects refer to the changes in SOS caused by environmental factors (e.g., CO<sub>2</sub> concentration, population density, and nighttime lighting) as a result of urbanization.

In this study, we used NIR<sub>v</sub> extraction of SOS and Moderate Resolution Imaging Spectroradiometer (MODIS) phenology products to explore patterns of SOS relationship to UI in the Northern Hemisphere. The SOS of NIR<sub>v</sub> was extracted using two widely used inflection point detection and threshold methods. Meanwhile, the developed conceptual framework was used to quantify the direct and

Chaoya Dang, Zhenfeng Shao, Gui Cheng, and Jiaxin Qian are with the State Key Laboratory Information Engineering Survey Mapping and Remote Sensing, Wuhan University, Wuhan 430079, China (shaozhenfeng@whu.edu.cn).

Xiao Huang is with the Department of Geosciences, University of Arkansas, Fayetteville, Arkansas 72701.

Corresponding author: Zhenfeng Shao (shaozhenfeng@whu.edu.cn)

Contributed by John Rogan, February 3, 2023 (sent for review June 6, 2023; reviewed by Dexter Locke, Alper Yilmaz).

Photogrammetric Engineering & Remote Sensing  
Vol. 89, No. 10, October 2023, pp. 639–651.

0099-1112/22/639-651

© 2023 American Society for Photogrammetry  
and Remote Sensing

doi: 10.14358/PERS.23-00008R2

indirect relationships of UI gradients on SOS. This study explored the following issues: 1) SOS in urban areas prevalent earlier onset than SOS in rural areas; 2) the changing relationship between SOS and UI; and 3) the magnitude of direct and indirect effects of UI on SOS.

## Materials and Methods

### Study Area

We calculated the UI using 2020 Global 30m Fine Land Cover Product (GLC\_FCS30-2020) (Zhong *et al.* 2021) and the urban extent map based on the impervious surface. The product made use of multi-source auxiliary data sets and expert a priori knowledge sets to improve a small number of misclassification and omission problems, and targeted processing and optimization for a small number of spatial transition discontinuities problems that existed. Consistent with the spatial resolution of MODIS data, UI is defined as the percentage of pixels falling into the urban or land impervious surface within a 1 km window in the land cover map (Zhao *et al.* 2016). Then, urban boundaries in the Northern Hemisphere greater than 25° N are extracted (Figure 1), where the vegetation is highly seasonal and climate-sensitive (Liu *et al.* 2016; Jeong *et al.* 2011). The threshold value of the urban area was determined using the Otsu (Otsu, 1979) method, depending on the threshold extracted urban area. Cities with urban areas larger than 500 km<sup>2</sup> were selected in this study (Meng *et al.* 2020; Zipper *et al.* 2016). When the proportion of pixel crop coverage was less than 5% of the pixel, these were chosen to study the relationship between UI and SOS.

### MODIS Products

We used eight-day synthetic surface reflectance data from MODIS MOD09A1 from 2019 to 2020 with a spatial resolution of 500 m to calculate the near-infrared reflectance of terrestrial vegetation (NIR<sub>v</sub>) index for SOS extraction. Also, we used the MODIS MOD11A2 eight-day average surface temperature data from 2019 to 2020 under clear weather with a spatial resolution of 1000 m to obtain pre-season temperatures for SOS. The SOS was also derived from the MODIS Land Cover Dynamics (MCD12Q2) product (Ganguly *et al.* 2010) in 2019, which has a spatial resolution of 500 m. MODIS data were retrieved from the National Aeronautics and Space Administration (NASA) from <https://search.earthdata.nasa.gov/>. For consistency, we resampled all data to a spatial resolution of 1 km.

### Vegetation Phenology Extraction Method

In this study, single logistic (SL) (Ganguly *et al.* 2010; Zhang *et al.* 2003; Verger *et al.* 2016) and dynamic thresholding (DT) (White *et al.* 1997; Cong *et al.* 2012) methods were used to define the spring phenology of NIR<sub>v</sub> time series. In addition, the spring phenology of MODIS phenology products was also applied. We used three SOS to explore the relationship between UI and SOS to increase the credibility of the results.

#### Single Logistic Method

We applied a logistic function to fit the eight-day NIR<sub>v</sub> observations. To further eliminate the effect of outliers, the data were smoothed using Savitzky-Golay filtering (Chen *et al.* 2004). The remote sensing indices were reconstructed into a time series for vegetation phenology extraction. We opted for the single logistic method for the following reasons: firstly, we focused solely on extracting the spring phenology of urban vegetation. Secondly, the logistic function fitting method offers advantages in estimating phenology from noisy data (Hird and

McDermid 2009). In the urban complex context, noise levels tend to be relatively high. The fitting equation used was (Ganguly *et al.* 2010; Zhang *et al.* 2003; Verger *et al.* 2016):

$$y(t) = \frac{c}{1 + e^{-a(t-b)}} + d \quad (1)$$

where  $t$  is time in days,  $y(t)$  is the NIR<sub>v</sub> value at time  $t$ , and  $a$  and  $b$  are fitting parameters associated with the NIR<sub>v</sub>, respectively. The  $c$  represents the value at the spring and early summer plateau. The  $d$  is the NIR<sub>v</sub> value in the winter dormant period. SOS was determined with  $b-1.317/a$  (Wang *et al.* 2019; Zhang *et al.* 2020).

#### Dynamic Thresholding Method

In this study, we used dynamic thresholding (DT) method (White *et al.* 1997; Cong *et al.* 2012) to extract SOS of urban vegetation from NIR<sub>v</sub> data. The equation of DT follows:

$$\text{NIR}_{v\text{ratio}}(i, j, t) = \frac{\text{NIR}_v(i, j, t) - \text{NIR}_{v\text{min}}(i, j)}{\text{NIR}_{v\text{max}}(i, j) - \text{NIR}_{v\text{min}}(i, j)} \times 100\% \quad (2)$$

where NIR<sub>v</sub>( $i, j, t$ ) denotes the NIR<sub>v</sub> value of pixel ( $i, j$ ) at time  $t$ ; NIR<sub>vmin</sub>( $i, j$ ) and NIR<sub>vmax</sub>( $i, j$ ) denote the minimum and maximum values of NIR<sub>v</sub> at pixel ( $i, j$ ) during the investigated year; and NIR<sub>vratio</sub>( $i, j, t$ ) denotes when pixel ( $i, j$ ) reaches 20% at time  $t$  to represent SOS (Shang *et al.* 2017), respectively.

## A Conceptual Framework for Analyzing Impacts of Urbanization on SOS

There is a positive linear correlation between surface temperature and UI, and there is a negative linear correlation between SOS and temperature. Therefore, there should be a negative linear correlation between UI and SOS ideally, indicating a linear between SOS and surface temperature impact line, i.e., SOS<sub>u</sub>. Indirect impacts can be measured by the difference between SOS and the surface temperature-impact line SOS<sub>ti</sub> (i.e., SOS<sub>obs</sub> - SOS<sub>ti</sub>). In addition, the direct impact can be evaluated as the difference between SOS<sub>rural</sub> and SOS<sub>ti</sub> (i.e., SOS<sub>rural</sub> - SOS<sub>ti</sub>). Conceptually, vegetation phenology in urban areas is directly and indirectly affected by urbanization.

$$\text{SOS}_{\text{obs}} = (1 + \beta)(100 - \text{UI}) \times \text{SOS}_{\text{rural}} + \text{UI} \times \text{SOS}_{\text{urban}} \quad (3)$$

where UI is the urbanization intensity, expressed as the coverage percentage of impervious surface in the pixel; SOS<sub>obs</sub> is the observed SOS value;  $\beta$  is the relationship of UI on SOS. SOS<sub>rural</sub> is the pre-urbanization SOS or rural SOS. SOS<sub>urban</sub> is the SOS in urban areas. In fact, the SOS is nonfactual for any disturbed pixels. However, SOS<sub>rural</sub> can be approximated by the median SOS values in rural areas around urban areas (UI < 10%). In addition, we approximated the built-up area SOS<sub>urban</sub> of cities by taking the median of UI > 90%, where pixels with NIR<sub>v</sub> less than 0.05 were excluded given the low vegetation activity. The measures of SOS impact described in the conceptual framework were calculated for all UI binning (1% interval) with SOS data greater than 50% in the study area.

The surface temperature-impact line defined by the two characteristic SOS values corresponding to vegetation unaffected by urbanization

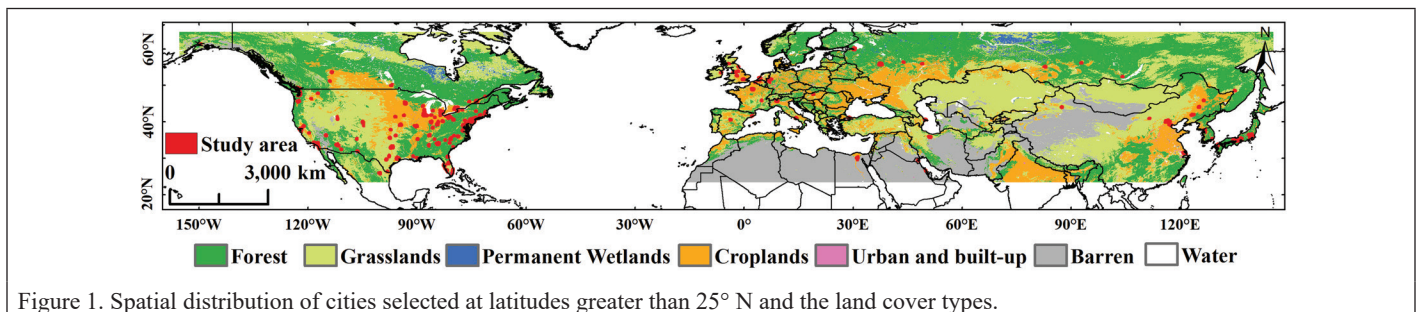


Figure 1. Spatial distribution of cities selected at latitudes greater than 25° N and the land cover types.

(i.e., vegetation in rural areas,  $UI = 0$ ,  $SOS = SOS_{rural}$ ) and fully urbanized (i.e., vegetation in urban area,  $UI > 90$ ,  $SOS = SOS_{urban}$ ) pixels indicates that urbanization does not have indirect impact conditions (i.e.,  $\beta = 0$  in Equation 2).

$$SOS_{ti} = (100 - UI) \times SOS_{rural} + UI \times SOS_{urban} \quad (4)$$

Any point below the surface temperature-impact line indicates that indirect effects of urbanization enhance SOS advance, while any point above the surface temperature-impact line indicates that indirect effects of urbanization offsets SOS advance. With this conceptual framework, we are able to quantitatively assess the direct, indirect, and total impacts of urbanization on SOS.

The direct impact of urbanization refers to the advancement of SOS after partial of vegetated ground surface is covered by impermeable surface resulting in temperature increase, excluding the indirect impact of urbanization. This is because studies have shown that urban-rural differences in phenology are significantly correlated with urban-rural surface temperatures (Yuan *et al.* 2020; Zhang *et al.* 2004). It is calculated as:

$$SOS_{DI} = \frac{SOS_{ti} - SOS_{rural}}{SOS_{rural}} \times 100\% \quad (5)$$

where  $SOS_{DI}$  indicates the direct impact of urbanization on SOS. In the conceptual model,  $SOS_{ti}$  is smaller than  $SOS_{rural}$ , leading to negative  $SOS_{DI}$  (Figure 2). That is to say, the  $SOS_{DI}$  of urbanization always advances vegetation SOS.

Indirect and direct impacts can be compared using the concept of advance offset coefficient  $\eta$ .

$$\eta = \frac{SOS_{obs} - SOS_{ti}}{SOS_{rural} - SOS_{ti}} \times 100\% \quad (6)$$

where a positive  $\eta$  indicates that urbanization offset the surface temperature to SOS advance while a negative one indicates that urbanization enhanced surface temperature to SOS advance.  $H$  is to show the enhanced ( $\eta < 0$ ) or offsetting ( $\eta > 0$ ) impact of urbanization on the SOS advance of the remaining vegetation.

## Results and Discussion

### The Differences in Urban SOS Across UI

The SOS showed notable differences in urban SOS along UI in the Northern Hemisphere greater than  $25^\circ N$ , presenting an earlier SOS in the urban areas than in the rural areas between 1.9 and 5.7 days (Figure 1 and Figure S1, *see Appendix section for all supplemental images*). It can be seen that SOS at high and low UI level are highly consistent ( $R > 0.84$ ,  $P < 0.001$ ), but high-UI vegetation SOS is markedly earlier than low-UI vegetation SOS (the slope is reduced by between 4% and 26%), which has been supported by many existing efforts (Wang *et al.* 2019; Li *et al.* 2016; Meng *et al.* 2020). The slope between high-UI and low-UI areas for  $SOS_{SL}$  and  $SOS_{DT}$  ranges from 0.74 to 0.91, with 77.39% to 86% of high-UI vegetation SOS earlier than

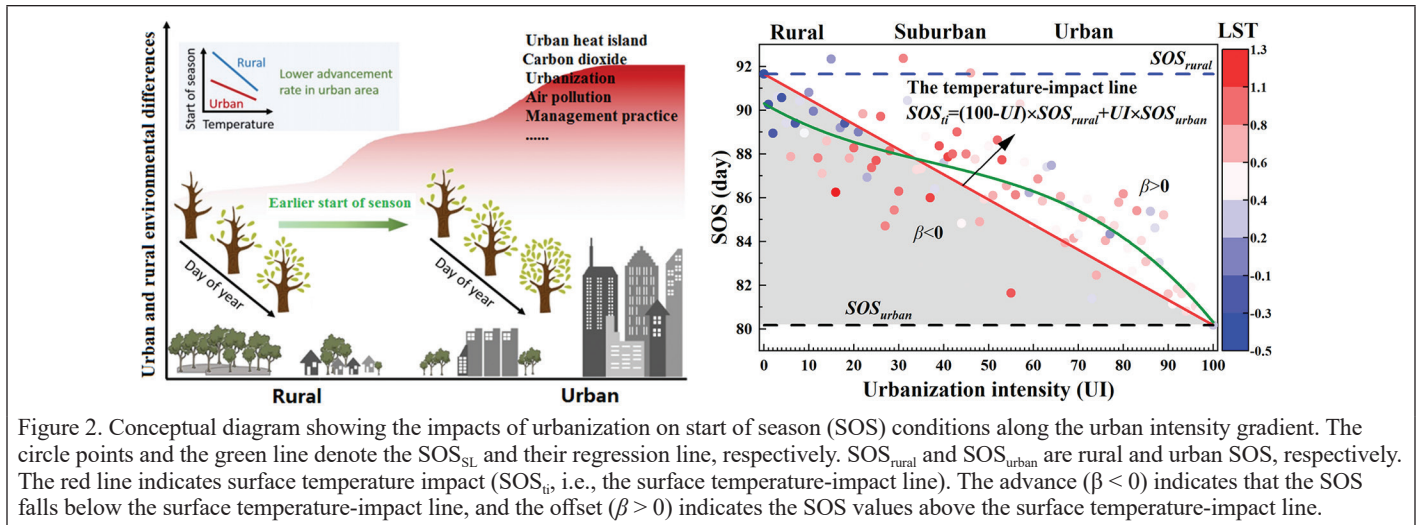


Figure 2. Conceptual diagram showing the impacts of urbanization on start of season (SOS) conditions along the urban intensity gradient. The circle points and the green line denote the  $SOS_{SL}$  and their regression line, respectively.  $SOS_{rural}$  and  $SOS_{urban}$  are rural and urban SOS, respectively. The red line indicates surface temperature impact ( $SOS_{ti}$ , i.e., the surface temperature-impact line). The advance ( $\beta < 0$ ) indicates that the SOS falls below the surface temperature-impact line, and the offset ( $\beta > 0$ ) indicates the SOS values above the surface temperature-impact line.

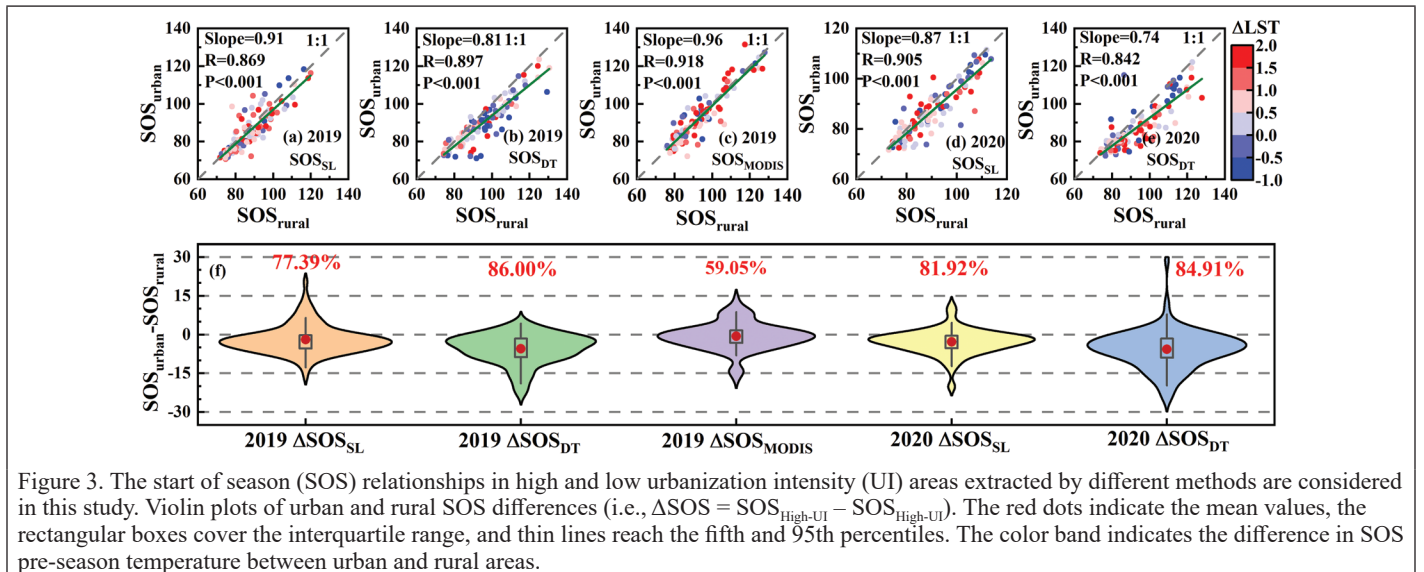


Figure 3. The start of season (SOS) relationships in high and low urbanization intensity (UI) areas extracted by different methods are considered in this study. Violin plots of urban and rural SOS differences (i.e.,  $\Delta SOS = SOS_{High-UI} - SOS_{Low-UI}$ ). The red dots indicate the mean values, the rectangular boxes cover the interquartile range, and thin lines reach the fifth and 95th percentiles. The color band indicates the difference in SOS pre-season temperature between urban and rural areas.

low-UI vegetation SOS (Figure 3a, 3b, 3d–f). Compared with  $SOS_{SL}$  and  $SOS_{DT}$  in high-low UI differences, the  $SOS_{MODIS}$  presents trivial high-low UI differences (Slope = 0.96), as only 59.05% of high-UI vegetation SOS is earlier than low-UI vegetation SOS (Figure 3c, 3f). One important reason is that  $SOS_{MODIS}$  extracts vegetation phenology using EVI, which has no value in pixels with high UI. Thus, it fails to include the vegetation SOS with high-UI.

In addition, the spatial pattern and SOS of urban clusters describe the impact of urbanization on vegetation SOS, and the number of days of difference between high and low UI vegetation phenology in different cities is clearly presented (Figure S1). Our study suggests that high-UI vegetation SOS is generally ahead of low-UI vegetation SOS in 0 to 10 days (Figure 3f and Figure S1), which is consistent with the results of previous studies (Zhou *et al.* 2016; Wang *et al.* 2019; Li *et al.* 2016; Meng *et al.* 2020). However, a few of the existing efforts present opposite patterns, presumably due to their unique local conditions that include vegetation types and climatic conditions (Higgins *et al.* 2011).

The disparities in spring phenology between urban and rural areas can be attributed to variations in temperature. Studies have emphasized the role of temperature as a crucial driver of spring phenology (Meng *et al.* 2020; Piao *et al.* 2019). In fact, the variations between areas with high and low UI are determined by the complex interplay of multiple factors, including the urban heat island effect (Zhou *et al.* 2016; Zhong *et al.* 2021; Huang *et al.* 2021; Li *et al.* 2022; Zhao *et al.* 2023), CO<sub>2</sub> concentration, urban location, urban scale, and climatic context (Wang *et al.* 2019; Reyes-Fox *et al.* 2014). The relationship of SOS to temperature is influenced by vegetation type and climatic zone (Li *et al.* 2016). Furthermore, irrigation and precipitation practices in urban areas can also alter vegetation phenology, particularly in arid regions (Buyantuyev and Wu 2012). Some regions exhibit an advanced SOS due to these factors, while others experience delayed SOS. Consequently, there are select cities where the onset of high UI areas spring phenology occurs later than that in low UI areas in Figure 3.

Studies have shown that advanced spring vegetation phenology increases the carbon sink capacity of vegetation (Keenan *et al.* 2014; Dang *et al.* 2023b). This study and previous studies suggest that urbanization generally advances spring vegetation phenology (Wang *et al.* 2019; Meng *et al.* 2019; Zhou *et al.* 2016). Advance spring phenology prolong vegetation photosynthesis and can increase vegetation carbon sink capacity (Gonsamo *et al.* 2018). Therefore, urban vegetation phenology changes have a great impact on the urban carbon cycle. In addition, UI can change urban temperature, which in turn has an impact on vegetation productivity (Dang *et al.* 2022).

### The Relationship Between SOS and UI Across Cities

Figure 4 shows the typical city-level relationship between SOS and UI in 2020. We notice that SOS shows an advancing trend along with the UI gradient. Certain cities present larger advancing patterns of SOS.

This study found that the cubic fit was better by learning from previous experience (Zhao *et al.* 2016; Zhang *et al.* 2022b) and after several experiments. The cubic regression curve between SOS and UI reaches statistical significance ( $P < 0.05$ ). We also observe that the y-intercept of the SOS and UI regression equation presents a large difference across cities, and its intercept can well represent the maximum vegetation SOS determined by the regional background climate.

In general, the SOS is observed to lie below the SOS surface temperature-impact line at lower UI but lie above the SOS surface temperature-impact line at high UI in all cities (Figure 4). Thus, SOS is advanced at low UI and is offset at high UI. Such a phenomenon is supported by other phenology extraction methods along the UI gradient (Figures S2–S6). In 2019, 68.42%, 77.34%, and 58.59% of all investigated cities respectively in  $SOS_{SL}$ ,  $SOS_{DT}$ , and  $SOS_{MODIS}$  showed advancement along the UI gradient. Regression equations of  $SOS_{SL}$ ,  $SOS_{DT}$ , and  $SOS_{MODIS}$  in all investigated cities reach statistical significance with 81.95%, 84.38%, and 63.28%, respectively ( $p < 0.05$ ). In 2020, the  $SOS_{SL}$  and  $SOS_{DT}$  showed advancement along the UI gradient with 62.60% and 79.69% of all investigated cities, respectively. 71.76% and 87.50% of the total urban regression equations reach statistical significance ( $p < 0.05$ ), respectively. Their y-intercept standard deviations range from 10.32 to 13.41 (Table 1). In general, the relationships between SOS and UI for different vegetation indices extracted by different phenology methods present highly similar patterns, which indicate that low-level urbanization advances surface

Table 1. Summary of the ratios of start of season (SOS) reduced along the urbanization intensity (UI) gradient, regression equations reaching statistical  $P < 0.05$  significance and standard deviation of y-intercept.

Method	Year	Slope < 0 (%)	Regression equation P < 0.05 (%)	y-Intercept Standard Deviation
SL	2019	68.42	81.95	10.32
	2020	62.60	71.76	11.62
DT	2019	77.34	84.38	13.41
	2020	79.69	87.50	13.41
MODIS	2019	58.59	63.28	11.87

DT = dynamic thresholding; MODIS = Moderate Resolution Imaging Spectroradiometer; SL = single logistic.

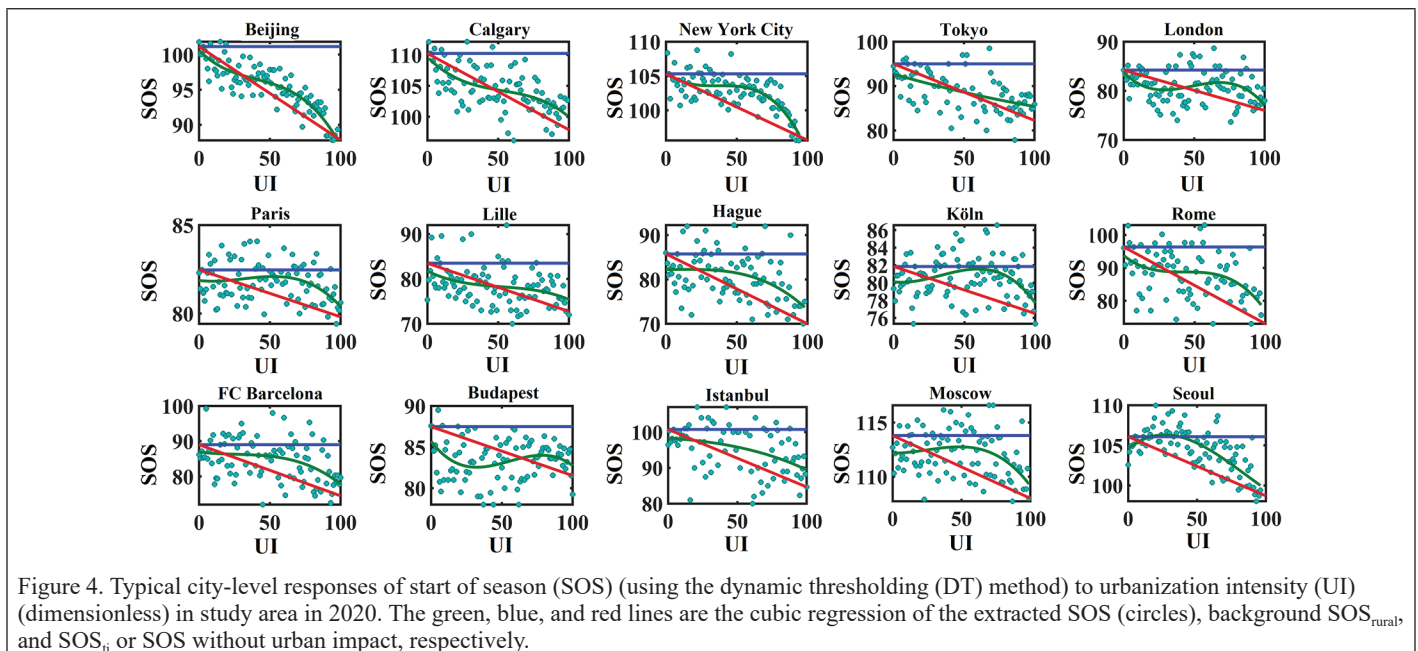


Figure 4. Typical city-level responses of start of season (SOS) (using the dynamic thresholding (DT) method) to urbanization intensity (UI) (dimensionless) in study area in 2020. The green, blue, and red lines are the cubic regression of the extracted SOS (circles), background  $SOS_{rural}$ , and  $SOS_i$  or SOS without urban impact, respectively.

temperature to SOS advance while high-level urbanization SOS is partially offset surface temperature to SOS advance. However, there exist a small number of cities where the relationship between SOS and UI deviates from the general pattern described above, which can be explained by the fact that vegetation phenology can be driven by a combination of regionally specific environmental factors (Zhang *et al.* 2022a; Reyes-Fox *et al.* 2014; Menzel *et al.* 2006).

### The Direct and Indirect Impact of UI on SOS

We analyzed SOS responses to UI in all cities and revealed diverse urbanization impacts (Figure 5). The aforementioned pattern still remains, i.e., low UI enhances surface temperature to SOS advance while high UI offsets surface temperature to SOS advance. We further quantitatively assessed the magnitude of the impact of UI on SOS. The direct impact of urbanization on urban vegetation SOS is linearly advanced with increasing UI (Figure S7), and uncertainty increases, with a maximum SOS advance of  $-11.56\%$  of PS. Urban vegetation SOS enhances surface temperature to SOS advance at low UI up to  $138.08\%$ . However, high UI offsets surface temperature to SOS advances, with a maximum offset of  $80.03\%$  of SOS advance (Figure 5). Importantly, the pattern of UI on SOS advance enhancement and offset is universal regardless of the use of SOS extraction methods. We notice that the threshold for the indirect effect of UI on surface temperature on SOS advance enhancement and offset is about  $31\%$  to  $36\%$ . (Figure 5), so the average value of  $33.2\% \pm 2.3\%$  is taken as the threshold value of UI. When the UI is less than the threshold value, more than half of the pixels in  $75.86\%$  to  $90\%$  of the urban SOS extracted by different methods enhance surface temperature on SOS advance (Figure 5f). However, when UI is greater than the threshold, more than half of the pixels in  $95.38\%$  to  $100\%$  of the urban SOS extracted by different methods offset surface temperature on SOS advance (Figure 5f). Our study shows that there is a threshold for the indirect impact of UI on SOS, showing opposite impacts below and above the threshold. Such a finding provides essential knowledge for the natural vegetation phenology response to future climate change in enhancing or offsetting SOS advances.

The nonlinear relationship between SOS and UI gradients can be attributed to various factors within urban ecosystems, as demonstrated in natural environments (Fu *et al.* 2015) as well as urban ecosystems (Meng *et al.* 2020). These factors include temperature,  $\text{CO}_2$  concentration, vegetation type, urban scale, nitrogen deposition, and nighttime lighting, which influence the relationship of vegetation phenology to urbanization (Zhou *et al.* 2016; Wang *et al.* 2019; Li *et al.* 2016; Meng *et al.* 2020). There are many factors coupled with each other in urban areas, including positive (e.g., heat island,  $\text{CO}_2$  concentration, nitrogen deposition) and negative (e.g., ozone) drivers. Studies have indicated that photoperiod and temperature were the primary factors influencing phenology (Lim and Jung 2007), with nighttime lighting in cities also

affecting vegetation phenology (Zhao *et al.* 2019; Zheng *et al.* 2021). The aforementioned factors that influence phenology have a close relationship with UI. Consequently, the combined influence of multiple factors leads to a nonlinear response of SOS to the UI gradient, where thresholds exist that enhance or offset the surface temperature-driven SOS advancement along the UI gradient.

This study hypothesized that urbanization was the only factor and that the other drivers were caused by urbanization. Vegetation phenology in urban environments is subject to many drivers (e.g., temperature,  $\text{CO}_2$ , vegetation type, urban size, nitrogen deposition, aerosols, and nighttime lighting), as well as making this study complex and challenging. Therefore, it needs good experimental design to properly do attribution analysis. For example, the heat island impact in urban areas is known to prolong the season length of vegetation growth (Zhou *et al.* 2016). In addition, a photoperiod can also affect vegetation phenology. While aerosols and  $\text{NO}_2$  reduce the photosynthetically active radiation of vegetation (Su *et al.* 2021), nighttime lights increase the light hours of vegetation. Therefore, it is necessary to further decouple the magnitude of the contribution of each factor to urban vegetation phenology. In addition, this study did not consider the effects of vegetation and water bodies and elevation on the relationship between urbanization and SOS. The influence on the relationship between UI and SOS was not considered using fundamental natural geography principles related to weather and climate as guidelines. In future studies, we will further develop experimental exploration to address the research shortcomings and better understand the quantitative relationship between vegetation phenology and urbanization dynamics.

### Conclusion

We used different phenology extraction methods to derive SOS in urban area vegetation. Furthermore, we developed a conceptual framework to quantify the relationship between UI and SOS in cities at mid-high latitudes ( $>25^\circ \text{N}$ ) in the Northern Hemisphere. We summarized the patterns of the overall relationship of urbanization on SOS. Our study revealed that SOS in high-UI areas started earlier than in low-UI areas. The number of days of SOS advancement increases linearly with increasing UI, as long as UI remained below a specific threshold. Under low-UI conditions, the indirect effects of urbanization contribute to surface temperature-driven SOS advancement. Conversely, under high-UI conditions, the indirect effects of urbanization offset the surface temperature-driven SOS advancement. As climate change is now widely believed to advance vegetation SOS, the UI gradient can be used to simulate present-to-future climate change to provide a priori information on the SOS changes of natural vegetation under the context of global climate change.

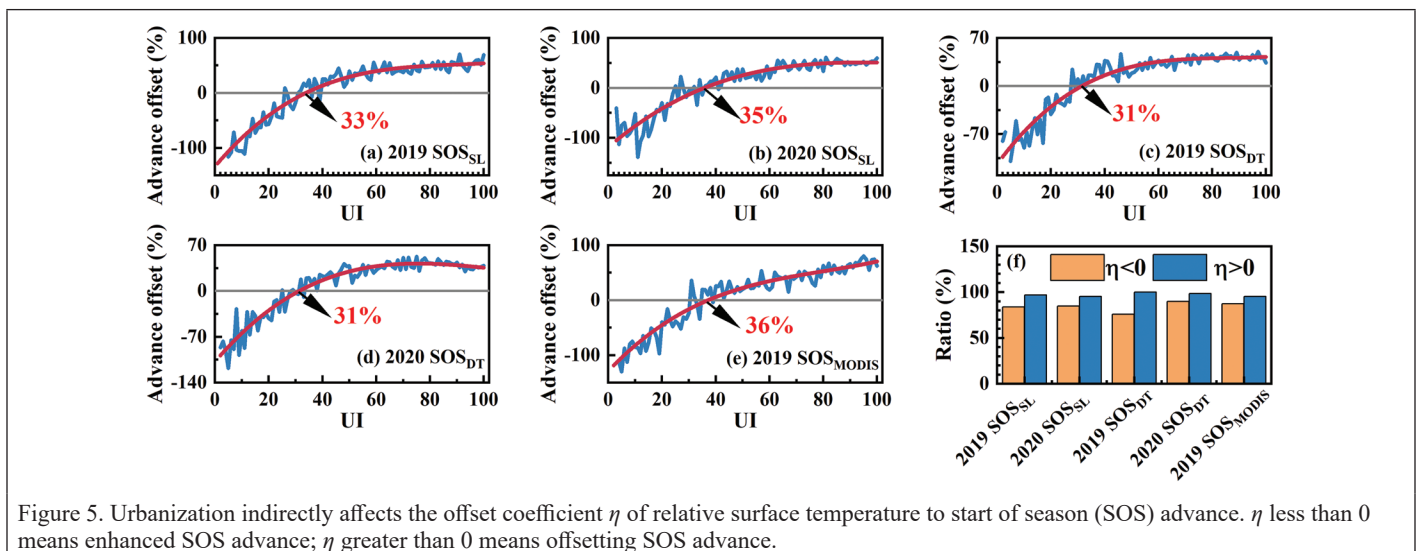


Figure 5. Urbanization indirectly affects the offset coefficient  $\eta$  of relative surface temperature to start of season (SOS) advance.  $\eta$  less than 0 means enhanced SOS advance;  $\eta$  greater than 0 means offsetting SOS advance.

## Acknowledgments

This work was supported in part by the National Natural Science Foundation of China under Grants 42090012; in part by the Guangxi science and technology program under Grants 2021AB30019; 03 special research and 5G project of Jiangxi Province in China under Grants 20212ABC03A09; Zhuhai industry university research cooperation project of China under Grants ZH22017001210098PWC; Sichuan Science and Technology Program under Grants 2022YFN0031, 2023YFS0381, and 2023YFN0022; Hubei key R & D plan under Grants 2022BAA048; Shanxi Province Science and Technology Major Special Project under Grants 202201150401020, Guangxi Key Laboratory of Spatial Information and Mapping Fund Project under Grants 21-238-21-01 and 21-238-21-07; and Open Research Project of The Hubei Key Laboratory of Intelligent Geo-Information Processing under Grants KLIIGIP-2022-A05.

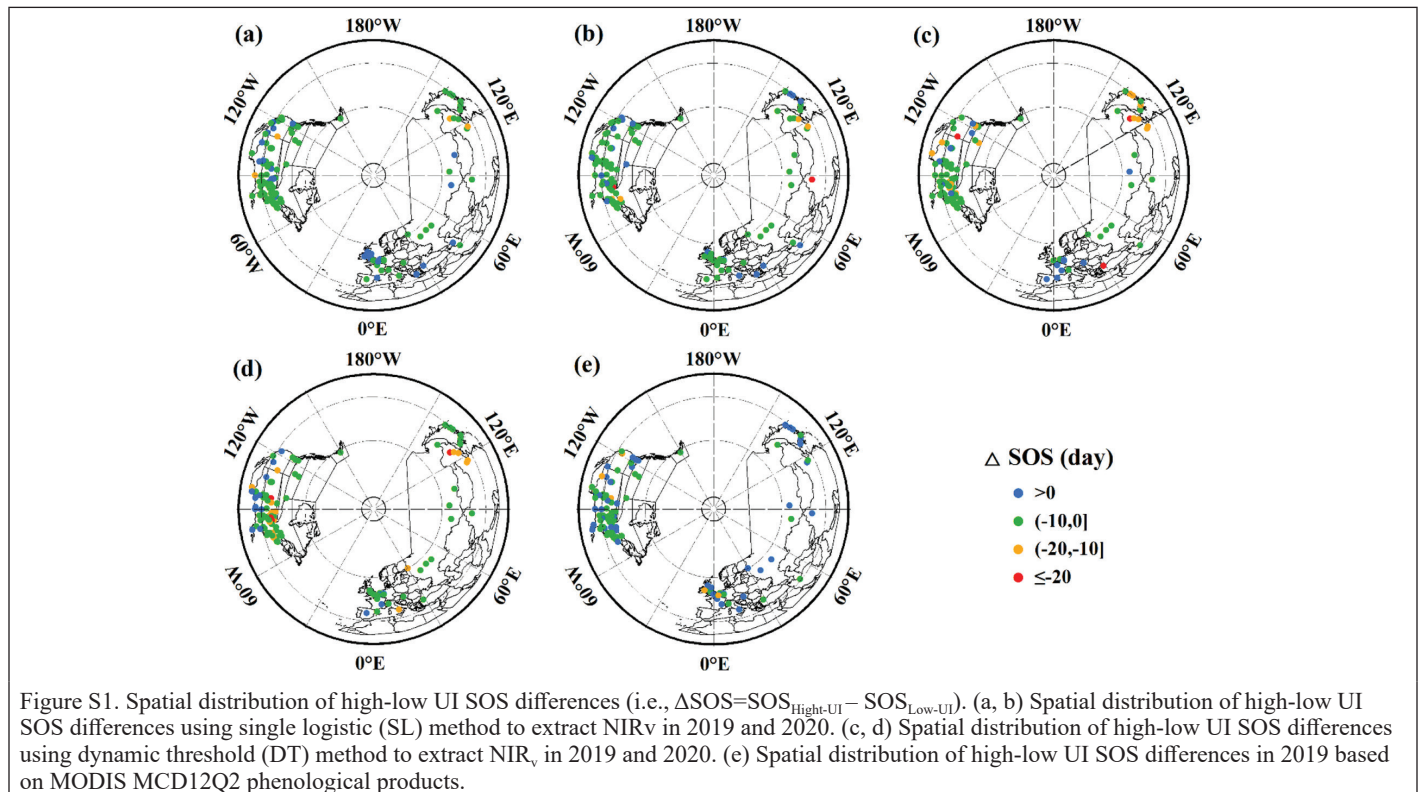
The authors sincerely thank the National Aeronautics and Space Administration (NASA) for providing MODIS product data. In addition, the authors are sincerely grateful to the scientists of the Global 30 m Fine Land Cover Product for 2020 (GLC\_FCS30-2020). Please see the appendix for supplementary materials. The authors declare no competing interests.

## References

- Badgley, G., C. B. Field and J. A. Berry. 2017. Canopy near-infrared reflectance and terrestrial photosynthesis. *Science Advances* 3(3):e1602244.
- Buyantuyev, A. and J. Wu. 2012. Urbanization diversifies land surface phenology in arid environments: Interactions among vegetation, climatic variation, and land use pattern in the Phoenix metropolitan region, USA. *Landscape and Urban Planning* 105(1–2):149–159.
- Chen J., P. Jönsson, M. Tamura, Z. H. Gu, B. Matsushita and L. Eklundh. 2004. A simple method for reconstructing a high-quality NDVI time-series data set based on the Savitzky–Golay filter. *Remote Sensing of Environment* 91(3–4):332–344.
- Cong N., S. L. Piao, A. P. Chen, X. H. Wang, X. Lin, S. P. Chen, S. J. Han, G. S. Zhou and X. P. Zhang. 2012. Spring vegetation green-up date in China inferred from SPOT NDVI data: A multiple model analysis. *Agricultural and Forest Meteorology* 165:104–113.
- Dang, C., Z. Shao, X. Huang, J. Qian, G. Cheng, Q. Ding and Y. Fan. 2022. Assessment of the importance of increasing temperature and decreasing soil moisture on global ecosystem productivity using solar-induced chlorophyll fluorescence. *Global Change Biology* 28(6):2066–2080.
- Dang, C., Z. Shao, X. Huang, Q. Zhuang, G. Cheng and J. Qian. 2023a. Vegetation greenness and photosynthetic phenology in response to climatic determinants. *Frontiers in Forests and Global Change* 6:1172220.
- Dang, C., Z. Shao, X. Huang, Q. Zhuang, G. Cheng and J. Qian. 2023b. Climate warming-induced phenology changes dominate vegetation productivity in Northern Hemisphere ecosystems. *Ecological Indicators* 151:110326.
- Fu, Y. H., H. Zhao, S. Piao, M. Peaucelle, S. Peng, G. Zhou and I. A. Janssens. 2015. Declining global warming effects on the phenology of spring leaf unfolding. *Nature* 526(7571):104–107.
- Ganguly, S., M. A. Friedl, B. Tan, X. Zhang and M. Verma. 2010. Land surface phenology from MODIS: Characterization of the Collection 5 global land cover dynamics product. *Remote Sensing of Environment* 114(8):1805–1816.
- Gonsamo, A., J. M. Chen and Y. W. Ooi. 2018. Peak season plant activity shift towards spring is reflected by increasing carbon uptake by extratropical ecosystems. *Global Change Biology* 24(5):2117–2128.
- Higgins, S. I., M. D. Delgado-Cartay, E. C. February and H. J. Combrink. 2011. Is there a temporal niche separation in the leaf phenology of savanna trees and grasses? *Journal of Biogeography* 38(11):2165–2175.
- Hird J. N. and G. J. Mederimid. 2009. Noise reduction of NDVI time series: An empirical comparison of selected techniques. *Remote Sensing of Environment* 113(1):248–258.
- Huang, X., A. Liu and J. Li. 2021. Mapping and analyzing the local climate zones in China's 32 major cities using Landsat imagery based on a novel convolutional neural network. *Geo-spatial Information Science* 24(4):528–557.
- Jeong, S. J., C. H. Ho, H. J. Gim and M. E. Brown. 2011. Phenology shifts at start vs. end of growing season in temperate vegetation over the Northern Hemisphere for the period 1982–2008. *Global Change Biology* 17(7):2385–2399.
- Jia, W., S. Zhao, X. Zhang, S. Liu, G. M. Henebry and L. Liu. 2021. Urbanization imprint on land surface phenology: The urban–rural gradient analysis for Chinese cities. *Global Change Biology* 27(12):2895–2904.
- Keenan T. F., J. Gray, M. A. Friedl, M. Toomey, G. Bohrer, D. Y. Hollinger, J. W. Munger, J. O'Keefe, H. P. Schmid and I. S. Wing. 2014. Net carbon uptake has increased through warming-induced changes in temperate forest phenology. *Nature Climate Change* 4(7):598–604.
- Körner, C. and D. Basler. 2010. Phenology under global warming. *Science* 327:1461–1462.
- Li, B., Y. Liu, H. Xing, Y. Meng, G. Yang, W. Liu and Y. Zhao. 2022. Integrating urban morphology and land surface temperature characteristics for urban functional area classification. *Geo-spatial Information Science* 25(2):337–352.
- Li, J., C. Song, L. Cao, F. Zhu, X. Meng and J. Wu. 2011. Impacts of landscape structure on surface urban heat islands: A case study of Shanghai, China. *Remote Sensing of Environment* 115(12):3249–3263.
- Li, X., Y. Zhou, G. R. Asrar, J. Mao, X. Li and W. Li. 2016. Response of vegetation phenology to urbanization in the conterminous United States. *Global Change Biology* 23(7):2818–2830.
- Lim, P. and H. Jung. 2007. Leaf senescence. *Annual Review of Plant Physiology* 58:115–136.
- Liu, Q., Y. H. Fu, Z. Zhu, Y. Liu, Z. Liu, M. Huang and S. Piao. 2016. Delayed autumn phenology in the Northern Hemisphere is related to change in both climate and spring phenology. *Global Change Biology* 22(11):3702–3711.
- Lu, D. and Q. Weng. 2006. Spectral mixture analysis of ASTER images for examining the relationship between urban thermal features and biophysical descriptors in Indianapolis, Indiana, USA. *Remote Sensing of Environment* 104(2):157–167.
- Meng, L., J. Mao, Y. Zhou, A. D. Richardson, X. Lee, P. E. Thornton and G. Jia. 2020. Urban warming advances spring phenology but reduces the response of phenology to temperature in the conterminous United States. *Proceedings of the National Academy of Sciences* 117(8):4228–4233.
- Meng, L., Y. Zhou, X. Li, G. R. Asrar and Y. Wang. 2019. Divergent responses of spring phenology to daytime and nighttime warming. *Agricultural and Forest Meteorology* 281:107832.
- Menzel, A., T. H. Sparks, N. Estrella, E. Koch, A. Aasa, R. Ahas and A.N.A. Zust. 2006. European phenological response to climate change matches the warming pattern. *Global Change Biology* 12(10):1969–1976.
- Otsu, N. 1979. A threshold selection method from gray-level histograms. *IEEE Transactions on Systems, Man, and Cybernetics* 9(1):62–66.
- Piao, S., P. Ciais, P. Friedlingstein, P. Peylin, M. Reichstein, S. Luysaert and T. Vesala. 2008. Net carbon dioxide losses of northern ecosystems in response to autumn warming. *Nature* 451(7174):49–52.
- Piao, S., Q. Liu, A. Chen, I. A. Janssens, Y. Fu, J. Dai and X. Zhu. 2019. Plant phenology and global climate change: Current progresses and challenges. *Global Change Biology* 25:1922–1940.
- Qiu, T., C. Song, Y. Zhang, H. Liu and J. M. Vose. 2020. Urbanization and climate change jointly shift land surface phenology in the northern mid-latitude large cities. *Remote Sensing of Environment* 236:111477.
- Reyes-Fox, M., H. Steltzer, M. J. Trlica, G. S. McMaster, A. A. Andales, D. R. LeCain and J. A. Morgan. 2014. Elevated CO<sub>2</sub> further lengthens growing season under warming conditions. *Nature* 510(7504):259–262.
- Richardson, A. D., T. F. Keenan, M. Migliavacca, Y. Ryu, O. Sonnentag and M. Toomey. 2013. Climate change, phenology, and phenological control of vegetation feedbacks to the climate system. *Agricultural and Forest Meteorology* 169:156–173.
- Shang, R., R. Liu, M. Xu, Y. Liu, L. Zuo and Q. Ge. 2017. The relationship between threshold-based and inflexion-based approaches for extraction of land surface phenology. *Remote Sensing of Environment* 199:167–170.
- Shao, Z., W. Wu and D. Li. 2021. Spatio-temporal-spectral observation model for urban remote sensing. *Geo-spatial Information Science* 24(3):372–386.
- Shen, X., B. Liu, M. Henderson, L. Wang, Z. Wu and W. Wu. 2018. Asymmetric effects of daytime and nighttime warming on spring phenology in the temperate grasslands of China. *Agricultural and Forest Meteorology* 259:240–249.

- Su, F., D. Fu, F. Yan, H. Xiao, T. Pan, Y. Xiao and G. Liu. 2021. Rapid greening response of China's 2020 spring vegetation to COVID-19 restrictions: Implications for climate change. *Science Advances* 7(35):eabe8044.
- Verger, A., I. Filella, F. Baret and J. Peñuelas. 2016. Vegetation baseline phenology from kilometric global LAI satellite products. *Remote Sensing of Environment* 178:1–14.
- Wang, S., W. Ju, J. Peñuelas, A. Cescatti, Y. Zhou, Y. Fu and Y. Zhang. 2019. Urban–rural gradients reveal joint control of elevated CO<sub>2</sub> and temperature on extended photosynthetic seasons. *Nature Ecology & Evolution* 3(7):1076–1085.
- White, M. A., P. E. Thornton and S. W. Running. 1997. A continental phenology model for monitoring vegetation responses to interannual climatic variability. *Global Biogeochemical Cycles* 11(2):217–234.
- Xiao, R., Z. Ouyang, H. Zheng, W. Li, E. W. Schienke and X. Wang. 2007. Spatial pattern of impervious surfaces and their impacts on land surface temperature in Beijing, China. *Journal of Environmental Sciences* 19(2):250–256.
- Yuan, F. and M. E. Bauer. 2007. Comparison of impervious surface area and normalized difference vegetation index as indicators of surface urban heat island effects in Landsat imagery. *Remote Sensing of Environment* 106(3):375–386.
- Yuan, M., L. Wang, A. Lin, Z. Liu, Q. Li and S. Qu. 2020. Vegetation green up under the influence of daily minimum temperature and urbanization in the Yellow River Basin, China. *Ecological Indicators* 108:105760.
- Zhang, D. L., Y. X. Shou and R. R. Dickerson. 2009. Upstream urbanization exacerbates urban heat island effects. *Geophysical Research Letters* 36(24).
- Zhang, J., J. Xiao, X. Tong, J. Zhang, P. Meng, J. Li, P. Liu and P. Yu. 2022a. NIR<sub>v</sub> and SIF better estimate phenology than NDVI and EVI: Effects of spring and autumn phenology on ecosystem production of planted forests. *Agricultural and Forest Meteorology* 315:108819.
- Zhang, X. and L. Liu. 2021. GLC\_FCS30: Global land-cover product with fine classification system at 30 m using time-series Landsat imagery. *Earth System Science Data* 13:2753–2776.
- Zhang, X., M. A. Friedl, C. B. Schaaf, A. H. Strahler and A. Schneider. 2004. The footprint of urban climates on vegetation phenology. *Geophysical Research Letters* 31(12):179–206.
- Zhang, X., M. A. Friedl, C. B. Schaaf, A. H. Strahler, J. C. Hodges, F. Gao and A. Huete. 2003. Monitoring vegetation phenology using MODIS. *Remote Sensing of Environment* 84(3):471–475.
- Zhang, Y., P. Yin, X. Li, Q. Niu, Y. Wang, W. Cao, J. Huang, H. Chen, X. Yao and B. Li. 2022b. The divergent response of vegetation phenology to urbanization: A case study of Beijing city, China. *Science of the Total Environment* 803:150079.
- Zhang, Y., R. Commane, S. Zhou, A. P. Williams and P. Gentile. 2020. Light limitation regulates the response of autumn terrestrial carbon uptake to warming. *Nature Climate Change* 10(8):739–743.
- Zhao, F., Z. Peng, J. Qian, C. Chu, Z. Zhao, J. Chao and S. Xu. 2023. Detection of geothermal potential based on land surface temperature derived from remotely sensed and in-situ data. *Geo-spatial Information Science* 1–17. <https://doi.org/10.1080/10095020.2023.2178335>.
- Zhao, M., Y. Zhou, X. Li, W. Cao and C. Zhou. 2019. Applications of satellite remote sensing of nighttime light observations: advances, challenges, and perspectives. *Remote Sensing* 11(17):1971.
- Zhao, S. Q., S. G. Liu and D. C. Zhou. 2016. Prevalent vegetation growth enhancement in urban environment. *Proceedings of the National Academy of Sciences* 113(22):6313–6318.
- Zheng, Q., H. C. Teo and L. P. Koh. 2021. Artificial light at night advances spring phenology in the United States. *Remote Sensing* 13(3):399.
- Zhong, Y., X. Wang, S. Wang and L. Zhang. 2021. Advances in spaceborne hyperspectral remote sensing in China. *Geo-spatial Information Science* 24(1):95–120.
- Zhou, D., S. Zhao, L. Zhang and S. Liu. 2016. Remotely sensed assessment of urbanization effects on vegetation phenology in China's 32 major cities. *Remote Sensing of Environment* 176:272–281.
- Zhuang, Q., Z. Shao, D. Li, X. Huang, O. Altan, S. Wu and Y. Li. 2022. Isolating the direct and indirect impacts of urbanization on vegetation carbon sequestration capacity in a large oasis city: Evidence from Urumqi, China. *Geo-spatial Information Science* 1–13.
- Zipper, S. C., J. Schatz, A. Singh, C. J. Kucharik, P. A. Townsend and S. P. Loheide. 2016. Urban heat island impacts on plant phenology: intra-urban variability and response to land cover. *Environmental Research Letters* 11(5):054023.

## Appendix



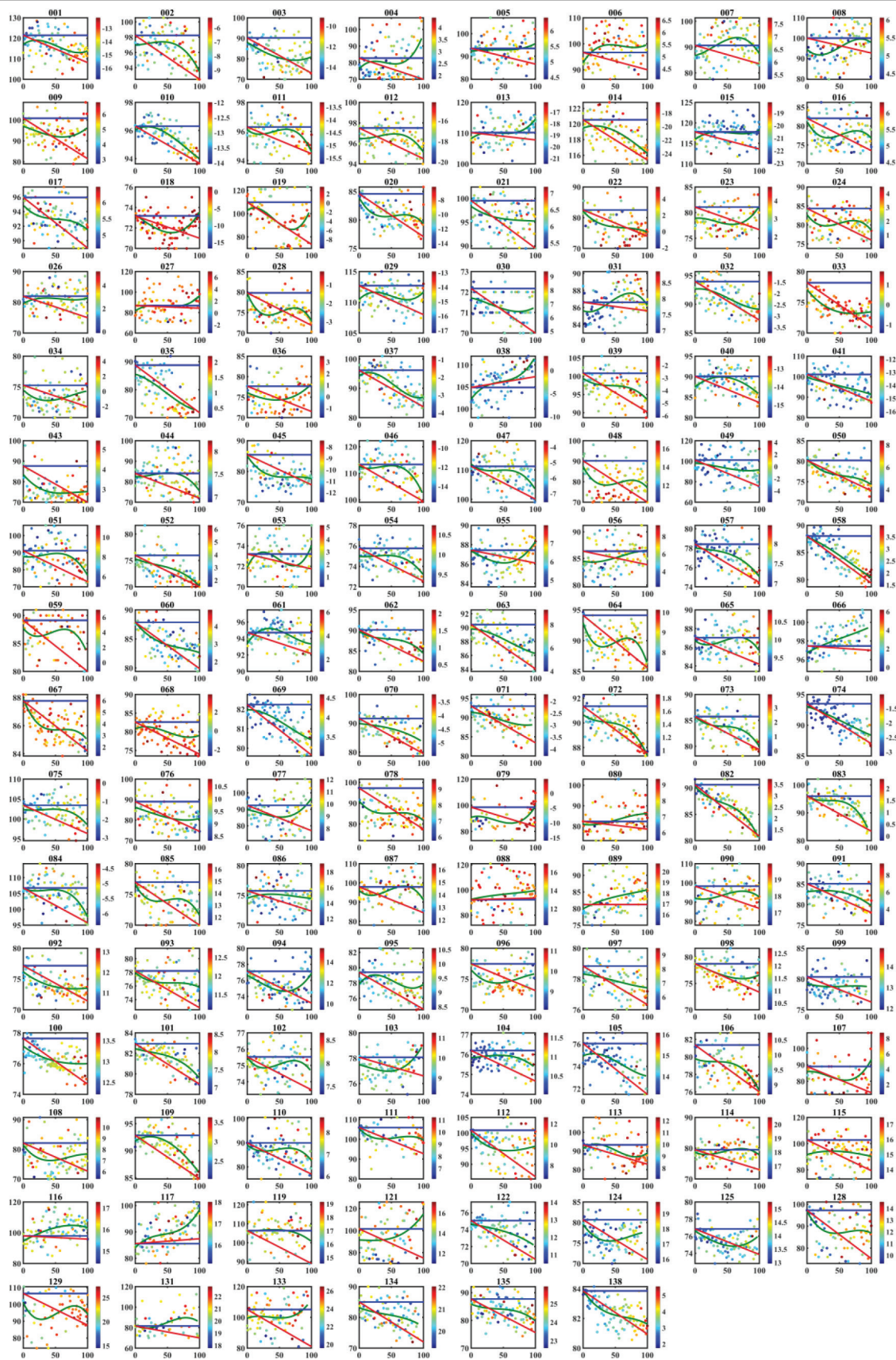


Figure S2. City-level responses of SOS (using the SL method) to UI (dimensionless) in 2019. The  $x$ -axis denotes SOS, while the  $y$ -axis denotes dimensionless UI. The green, blue, and red lines are the cubic regression of the extracted SOS (circles), background  $SOS_{\text{rural}}$  (i.e., the rural SOS), and  $SOS_{\text{ii}}$  or SOS without urban impact, respectively. The colored bands indicate the average temperature from January to April. 81.95% regression reached  $P < 0.05$  significance. The number represents the order of investigated cities.



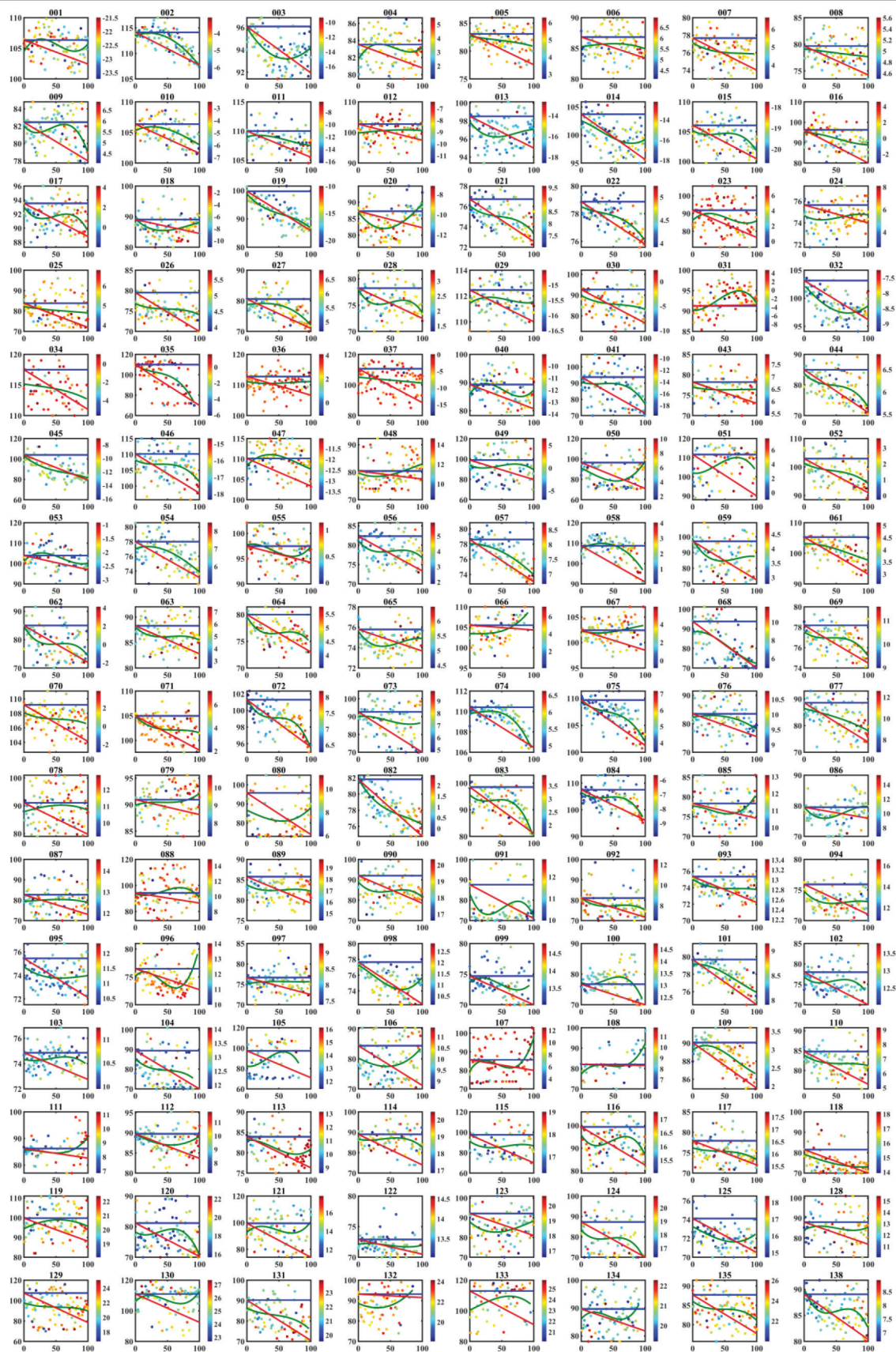


Figure S3. City-level responses of SOS (using the SL method) to UI (dimensionless) in 2020. The x-axis denotes SOS, while the y-axis denotes dimensionless UI. The green, blue, and red lines are the cubic regression of the extracted SOS (circles), background SOS<sub>rural</sub>, and SOS<sub>ti</sub> or SOS without urban impact, respectively. The colored bands indicate the average temperature from January to April. 71.76% regression reached P<0.05 significance. The number represents the order of investigated cities.

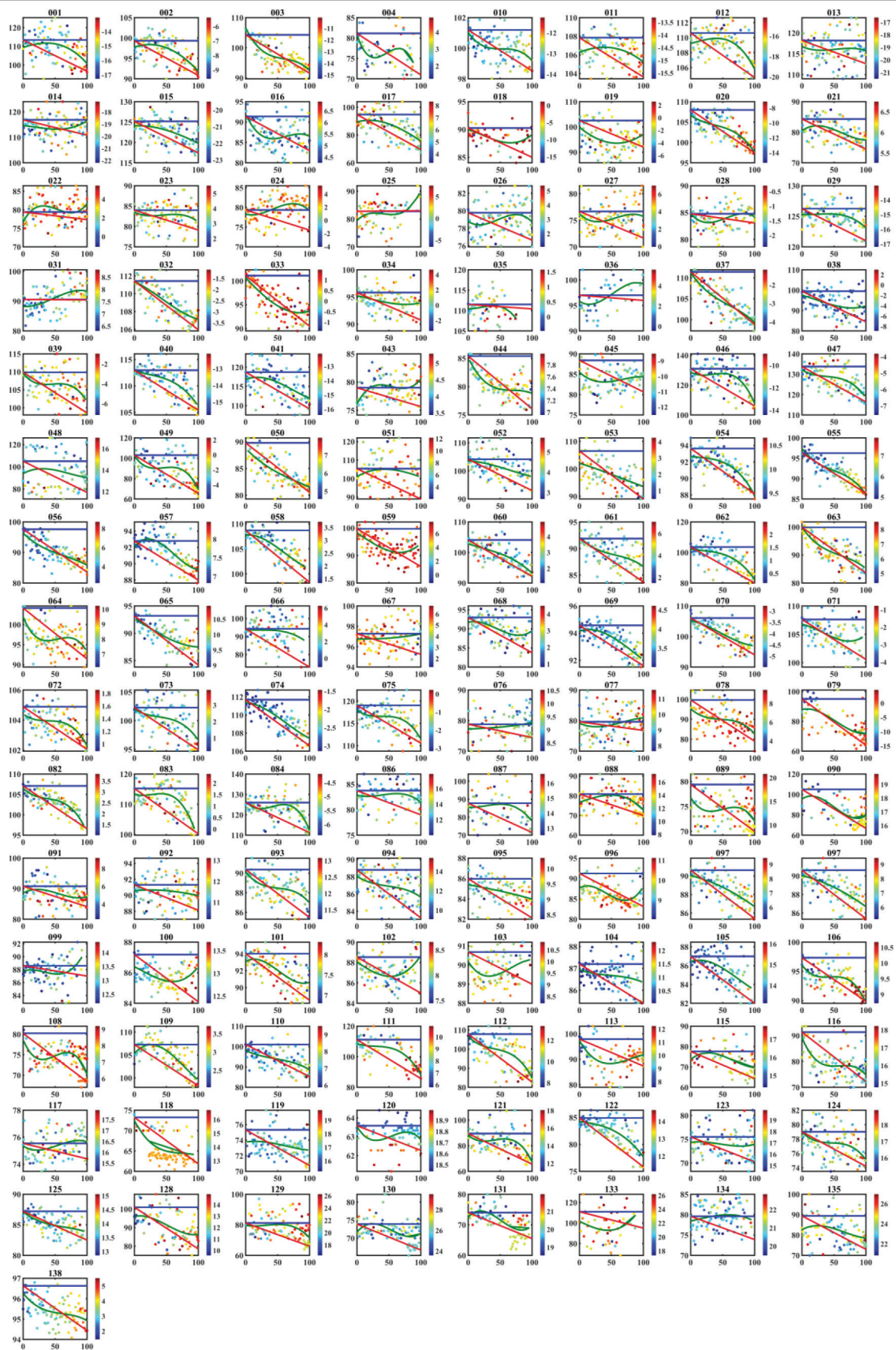


Figure S4. City-level responses of SOS (using the DT method) to UI (dimensionless) in 2019. The x-axis denotes SOS, while the y-axis denotes dimensionless UI. The green, blue, and red lines are the cubic regression of the extracted SOS (circles), background  $SOS_{\text{urban}}$  and  $V_{\text{ii}}$  or SOS without urban impact, respectively. The colored bands indicate the average temperature from January to April. 84.38% regression reached  $P < 0.05$  significance. The number represents the order of investigated cities.

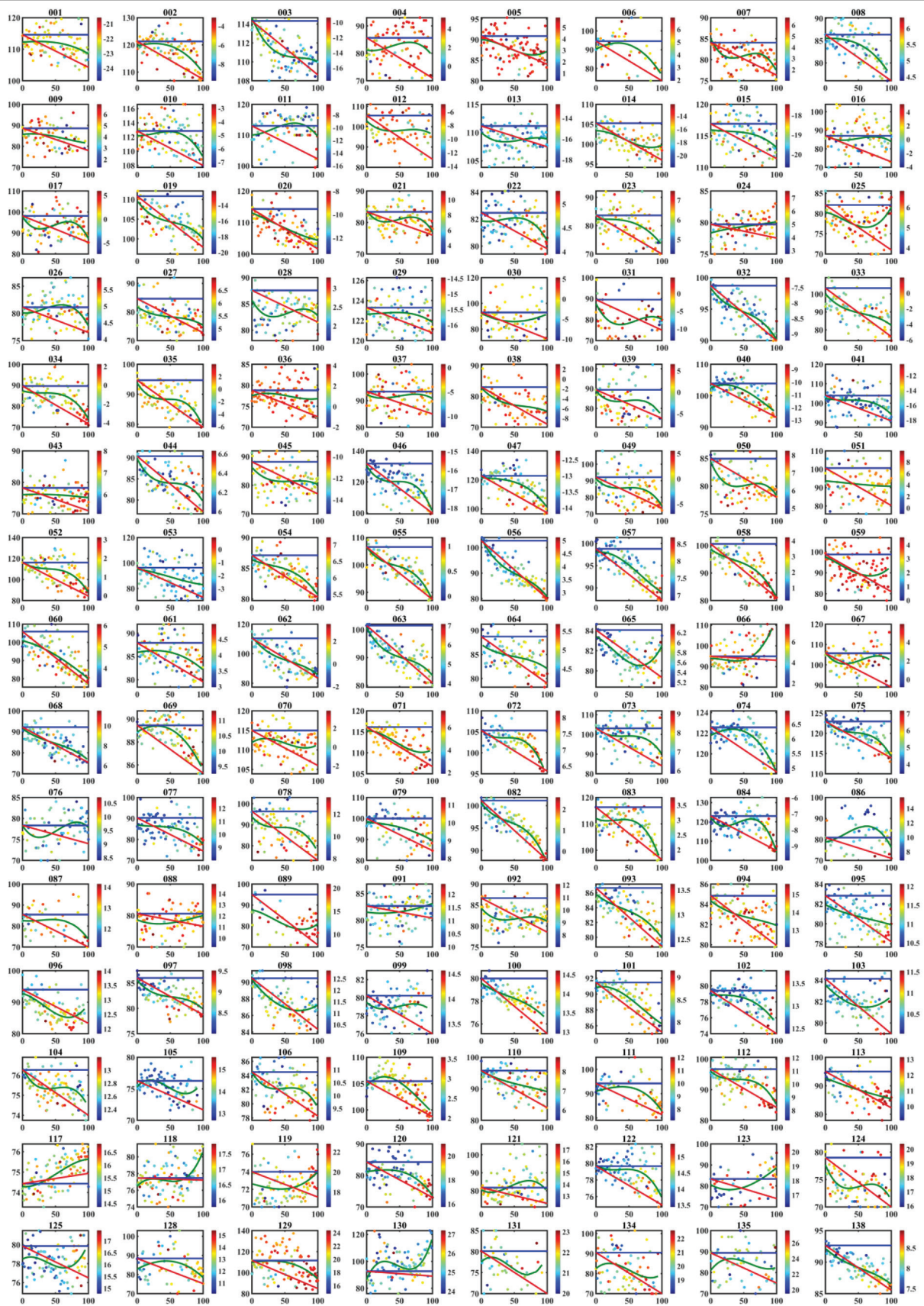


Fig. S5. City-level responses of SOS (using the DT method) to UI (dimensionless) in 2020. The x-axis denotes SOS, while the y-axis denotes dimensionless UI. The green, blue, and red lines are the cubic regression of the extracted SOS (circles), background SOS<sub>rural</sub>, and SOS<sub>ti</sub> or SOS without urban impact, respectively. The colored bands indicate the average temperature from January to April. 87.50% regression reached P<0.05 significance. The number represents the order of investigated cities.

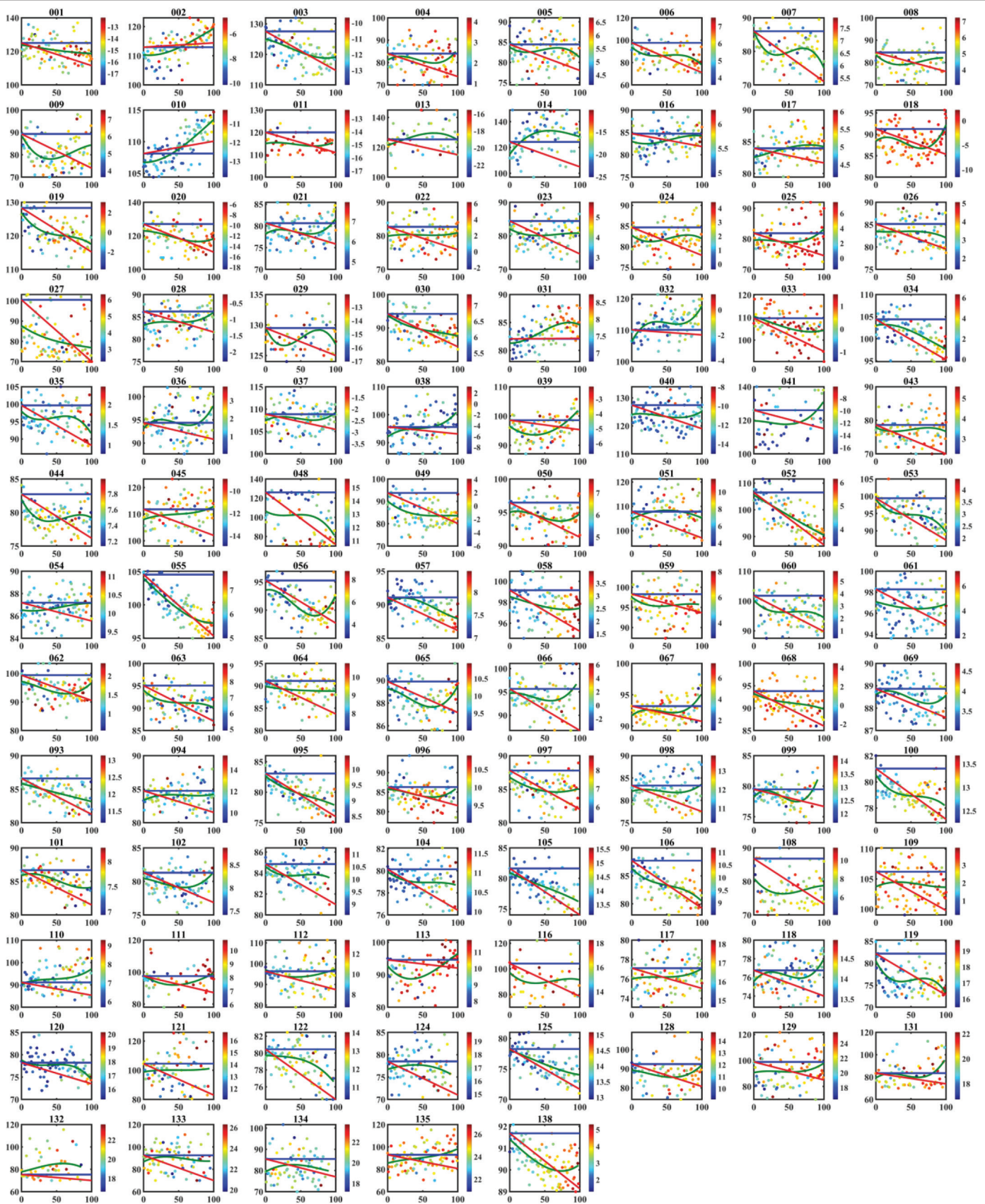


Figure S6. City-level responses of SOS (the MODIS MCD12Q2 phenological product SOS) to UI (dimensionless) in 2019. The  $x$ -axis denotes SOS, while the  $y$ -axis denotes dimensionless UI. The green, blue, and red lines are the cubic regression of the extracted SOS (circles), background  $SOS_{\text{rural}}$ , and  $SOS_{\text{ti}}$  or SOS without urban impact, respectively. The colored bands indicate the average temperature from January to April. 63.28% regression reached  $P < 0.05$  significance. The number represents the order of investigated cities.

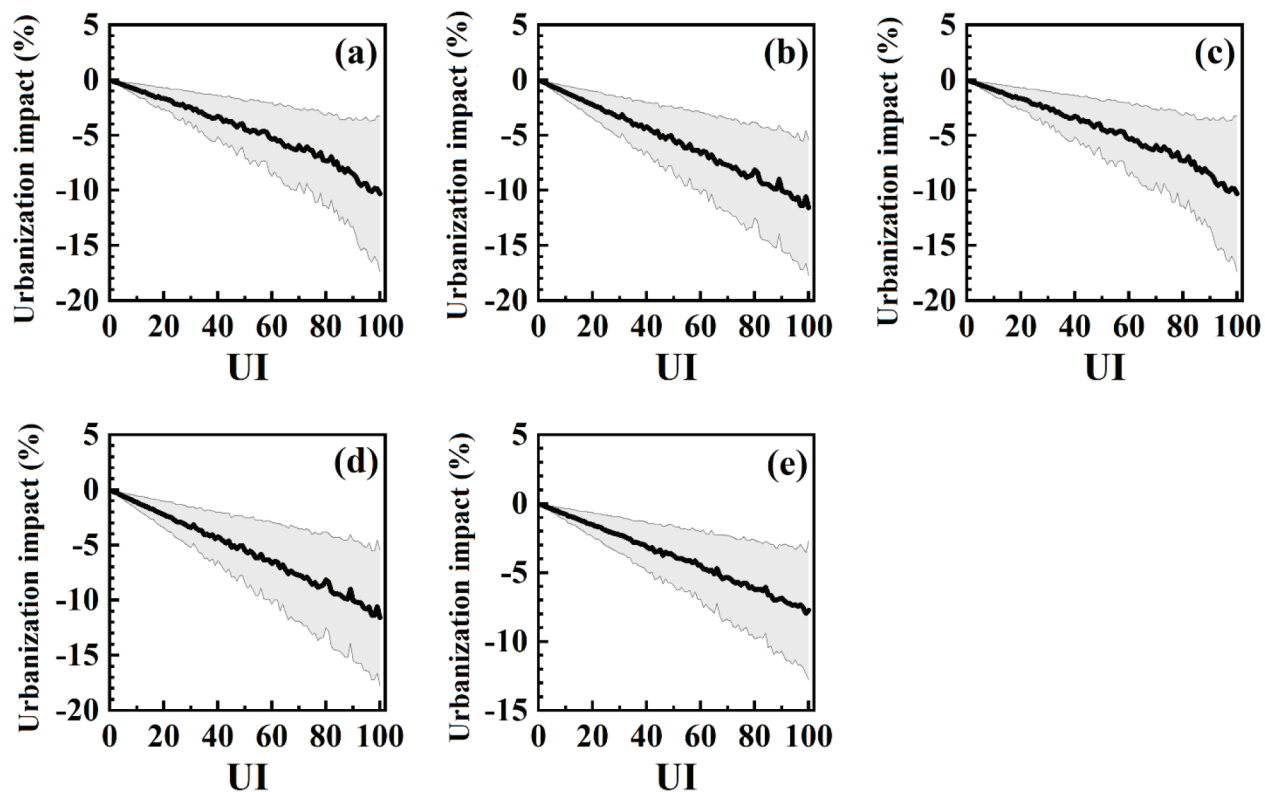


Figure S7. Urbanization intensity (UI) relative impacts on SOS magnitude. (a, b) SL extracted SOS of NIR<sub>v</sub> data in 2019 and 2020, respectively. (c, d) DT extracted SOS of NIR<sub>v</sub> data in 2019 and 2020, respectively. (e) MODIS MCD12Q2 phenological product SOS in 2019. The gray shading indicates standard deviation.

*Gain a professional advantage with*  
**ASPRS CERTIFICATION**



A growing number of scientific and technical disciplines depend on photogrammetry and the mapping sciences for reliable measurements and information.



It is in the interest of those who provide photogrammetric and mapping sciences services, as well as the user of these services, that such information and data be accurate and dependable.



The ASPRS Certification Program has as its purpose the establishment and maintenance of high standards of ethical conduct and professional practice among photogrammetrists, mapping scientists, technologists, and interns.



ASPRS offers certification in the following areas

**Photogrammetry**

**Remote Sensing**

**GIS/LIS**

**Lidar**

**UAS**

Each area has 2 levels of certification

✓ **Mapping Scientist**

✓ **Technologist**

All exams offered via computer based testing through Prometric.com

[asprs.org/certification](https://asprs.org/certification)

# WHO'S WHO IN ASPRS

Founded in 1934, the American Society for Photogrammetry and Remote Sensing (ASPRS) is a scientific association serving thousands of professional members around the world. Our mission is to advance knowledge and improve understanding of mapping sciences to promote the responsible applications of photogrammetry, remote sensing, geographic information systems (GIS) and supporting technologies.

## BOARD OF DIRECTORS

### BOARD OFFICERS

**President**

Lorraine B. Amenda, PLS, CP  
Towill, Inc

**Vice President**

Amr Abd-Elrahman  
University of Florida

**Treasurer**

John McCombs  
NOAA

**President-Elect**

Bandana Kar  
Oak Ridge National Lab

**Past President**

Christopher Parrish, Ph.D  
Oregon State University

**Secretary**

Harold Rempel  
ESP Associates, Inc.

---

## COUNCIL OFFICERS

ASPRS has six councils. To learn more, visit <https://www.asprs.org/Councils.html>.

**Sustaining Members Council**

Chair: Ryan Bowe  
Deputy Chair: Melissa Martin

**Early-Career Professionals Council**

Chair: Youssef Kaddoura  
Deputy Chair: : Greg Stamnes

**Student Advisory Council**

Chair: Oscar Duran  
Deputy Chair: Ali Alruzuq

**Technical Division Directors Council**

Chair: Hope Morgan  
Deputy Chair: Tao Liu

**Region Officers Council**

Chair: Demetrio Zourarakis  
Deputy Chair: Cody Condon

---

## TECHNICAL DIVISION OFFICERS

ASPRS has seven professional divisions. To learn more, visit <https://www.asprs.org/Divisions.html>.

**Geographic Information Systems Division**

Director: Denise Theunissen  
Assistant Director: Jin Lee

**Photogrammetric Applications Division**

Director: Ben Wilkinson  
Assistant Director: Hank Theiss

**Remote Sensing Applications Division**

Director: Tao Liu  
Assistant Director: Indu Jeyachandran

**Lidar Division**

Director: Ajit Sampath  
Assistant Director: Mat Bethel

**Primary Data Acquisition Division**

Director: Sridhar Dharmapuri  
Assistant Director: Ravi Soneja

**Unmanned Autonomous Systems (UAS)**

Director: Jacob Lopez  
Assistant Director: Bahram Salehi

**Professional Practice Division**

Director: Hope Morgan  
Assistant Director: Christian Stallings

---

## REGION PRESIDENTS

ASPRS has 13 regions to serve the United States. To learn more, visit <https://www.asprs.org/regions.html>.

**Alaska Region**

Dave Parret

**Gulf South**

Stuart Babin

**Pacific Southwest Region**

Omar Mora

**Cascadia Region**

Jimmy Schulz

**Heartland Region**

Whit Lynn

**Potomac Region**

Jason Brown

**Eastern Great Lakes Region**

Craig Fry

**Mid-South Region**

David Hughes

**Rocky Mountain Region**

Melissa Martin

**Florida Region**

Matt LaLuzerne

**North Atlantic Region**

Kurt Lutz

**Western Great Lakes Region**

Adam Smith

**Northeast Region**

# PUBLISHING OPEN-ACCESS IN *PE&RS* IS NOW EASIER!

ASPRS is changing the subscription model of our monthly journal, *PE&RS*. ASPRS is waiving open-access fees for primary authors from subscribing institutions. Additionally, primary authors who are Individual Members of ASPRS will be able to publish one open-access article per year at no cost and will receive a 50% discount on open-access fees for additional articles.



- **Open Access matters!** By providing unrestricted access to research we can advance the geospatial industry and provide research that is available to everyone.
- **Institutions and authors receive more recognition!** Giving permission to everyone to read, share, reuse the research without asking for permission, as long as the author is credited.
- **Reputation matters!** Known for its high standards, *PE&RS* is the industry leading peer-review journal. Adding open access increases authors' visibility and reputation for quality research.
- **Fostering the geospatial industry!** Open access allows for sharing without restriction. Research is freely available to everyone without an embargo period.

*Under the previous subscription model, authors and institutions paid \$1500 or more in open-access fees per article. This will represent a significant cost savings. Open-access publications benefit authors through greater visibility of their work and conformance with open science mandates of funding agencies.*

**Subscriptions** [asprs.org/subscribe](https://asprs.org/subscribe)  
**Membership** [asprs.org/membership](https://asprs.org/membership)





# SUSTAINING MEMBERS

## ACI USA Inc.

Weston, Florida  
<https://acicorporation.com/>  
 Member Since: 2/2018

## Aerial Services, Inc.

Cedar Falls, Iowa  
[www.AerialServicesInc.com](http://www.AerialServicesInc.com)  
 Member Since: 5/2001

## Airworks Solutions Inc.

Boston, Massachusetts  
 Member Since: 5/2022

## Applanix

Richmond Hill, Ontario, Canada  
<http://www.applanix.com>  
 Member Since: 7/1997

## Ayres Associates

Madison, Wisconsin  
[www.AyresAssociates.com](http://www.AyresAssociates.com)  
 Member Since: 1/1953

## Cardinal Systems, LLC

Flagler Beach, Florida  
[www.cardinalsystems.net](http://www.cardinalsystems.net)  
 Member Since: 1/2001

## Dewberry

Fairfax, Virginia  
[www.dewberry.com](http://www.dewberry.com)  
 Member Since: 1/1985

## Esri

Redlands, California  
[www.esri.com](http://www.esri.com)  
 Member Since: 1/1987

## GeoCue Group

Madison, Alabama  
<http://www.geocue.com>  
 Member Since: 10/2003

## Geographic Imperatives LLC

Centennial, Colorado  
 Member Since: 12/2020

## GPI Geospatial Inc.

Orlando, Florida  
[www.aca-net.com](http://www.aca-net.com)  
 Member Since: 1/1994

## Half Associates, Inc.

Richardson, Texas  
[www.half.com](http://www.half.com)  
 Member Since: 8/2021

## Keystone Aerial Surveys, Inc.

Philadelphia, Pennsylvania  
[www.kasurveys.com](http://www.kasurveys.com)  
 Member Since: 1/1985

## Kucera International

Willoughby, Ohio  
[www.kucerainternational.com](http://www.kucerainternational.com)  
 Member Since: 1/1992

## L3Harris Technologies

Broomfield, Colorado  
[www.l3harris.com](http://www.l3harris.com)  
 Member Since: 6/2008

## Merrick & Company

Greenwood Village, Colorado  
[www.merrick.com](http://www.merrick.com)  
 Member Since: 4/1995

## Miller Creek Associates

SeaTac Washington  
[www.mcamaps.com](http://www.mcamaps.com)  
 Member Since: 12/2014

## Nearmap

South Jordan, Utah  
[www.nearmap.com](http://www.nearmap.com)  
 Member Since: 6/2023

## NV5 Geospatial

Sheboygan Falls, Wisconsin  
[www.quantumspatial.com](http://www.quantumspatial.com)  
 Member Since: 1/1974

## Pickett and Associates, Inc.

Bartow, Florida  
[www.pickettusa.com](http://www.pickettusa.com)  
 Member Since: 4/2007

## PixElement

Belmont, Michigan  
<https://pixelement.com>  
 Member Since: 2/2017

## Riegl USA, Inc.

Orlando, Florida  
[www.rieglusa.com](http://www.rieglusa.com)  
 Member Since: 11/2004

## Sanborn Map Company

Colorado Springs, Colorado  
[www.sanborn.com](http://www.sanborn.com)  
 Member Since: 10/1984

## Surdex Corporation

Chesterfield, Missouri  
[www.surdex.com](http://www.surdex.com)  
 Member Since: 12/2011

## Surveying And Mapping, LLC (SAM)

Austin, Texas  
[www.sam.biz](http://www.sam.biz)  
 Member Since: 12/2005

## T3 Global Strategies, Inc.

Bridgeville, Pennsylvania  
<https://t3gs.com/>  
 Member Since: 6/2020

## Towill, Inc.

San Francisco, California  
[www.towill.com](http://www.towill.com)  
 Member Since: 1/1952

## Woolpert LLP

Dayton, Ohio  
[www.woolpert.com](http://www.woolpert.com)  
 Member Since: 1/1985

# SUSTAINING MEMBER BENEFITS

## Membership

- ✓ Provides a means for dissemination of new information
- ✓ Encourages an exchange of ideas and communication
- ✓ Offers prime exposure for companies

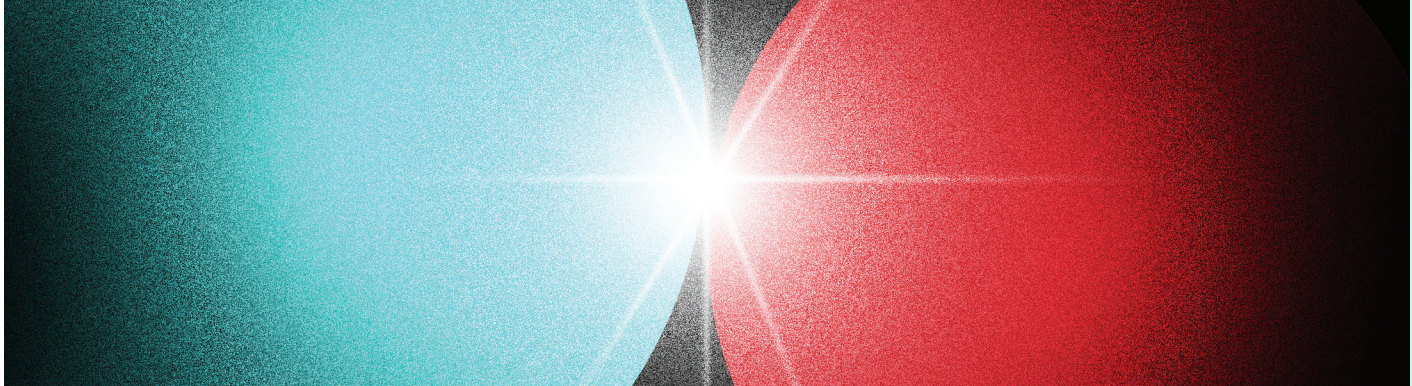
## Benefits of an ASPRS Membership

- Complimentary and discounted Employee Membership\*
- E-mail blast to full ASPRS membership\*
- Professional Certification Application fee discount for any employee
- Member price for ASPRS publications
- Discount on group registration to ASPRS virtual conferences
- Sustaining Member company listing in ASPRS directory/website
- Hot link to company website from Sustaining Member company listing page on ASPRS website
- Press Release Priority Listing in PE&RS Industry News
- Priority publishing of Highlight Articles in PE&RS plus, 20% discount off cover fee
- Discount on PE&RS advertising
- Exhibit discounts at ASPRS sponsored conferences (exception ASPRS/ILMF)
- Free training webinar registrations per year\*
- Discount on additional training webinar registrations for employees
- Discount for each new SMC member brought on board (Discount for first year only)

\*quantity depends on membership level

CONNECT WITH YOUR AUDIENCE, CONNECT WITH YOUR CUSTOMERS!

# ADVERTISE IN *PE&RS*



Nearly 60% of *PE&RS* readers select, authorize, or approve the purchase of products and services

*PE&RS* regularly ranks in the **Top 20** out of over 11,000 journals for full-text downloads with Ingenta Connect.

## FRONT COVER SPONSORSHIP

A *PE&RS* cover sponsorship is a unique opportunity to capture the undivided attention of your target market through three premium points of contact.

### ***PE&RS* FRONT COVER**

(Only twelve available, first-come, first-served)  
*PE&RS* is world-renowned for the outstanding imagery displayed monthly on its front cover—and readers have told us they eagerly anticipate every issue. This is a premium opportunity for any company, government agency, university or non-profit organization to provide a strong image that demonstrates their expertise in the geospatial information industry

### **FREE ACCOMPANYING “HIGHLIGHT” ARTICLE**

A detailed article to enhance your cover image is welcome but not a condition of placing an image. Many readers have asked for more information about the covers and your article is a highly visible way to tell your story in more depth for an audience keenly interested in your products and services.\*

### **FREE TABLE OF CONTENTS COVER DESCRIPTION**

Use this highly visible position to showcase your organization by featuring highlights of the technology used in capturing the front cover imagery.\*

## OTHER ADVERTISING OPPORTUNITIES

### ***PE&RS***

- Covers 2–4
- Full Page
- Classified Ad
- 2/3 Page\*\*
- 1/2 Page\*\*
- 1/3 Page\*\*
- 1/4 Page\*\*
- 1/8 Page\*\*

\*\*horizontal or vertical format supported

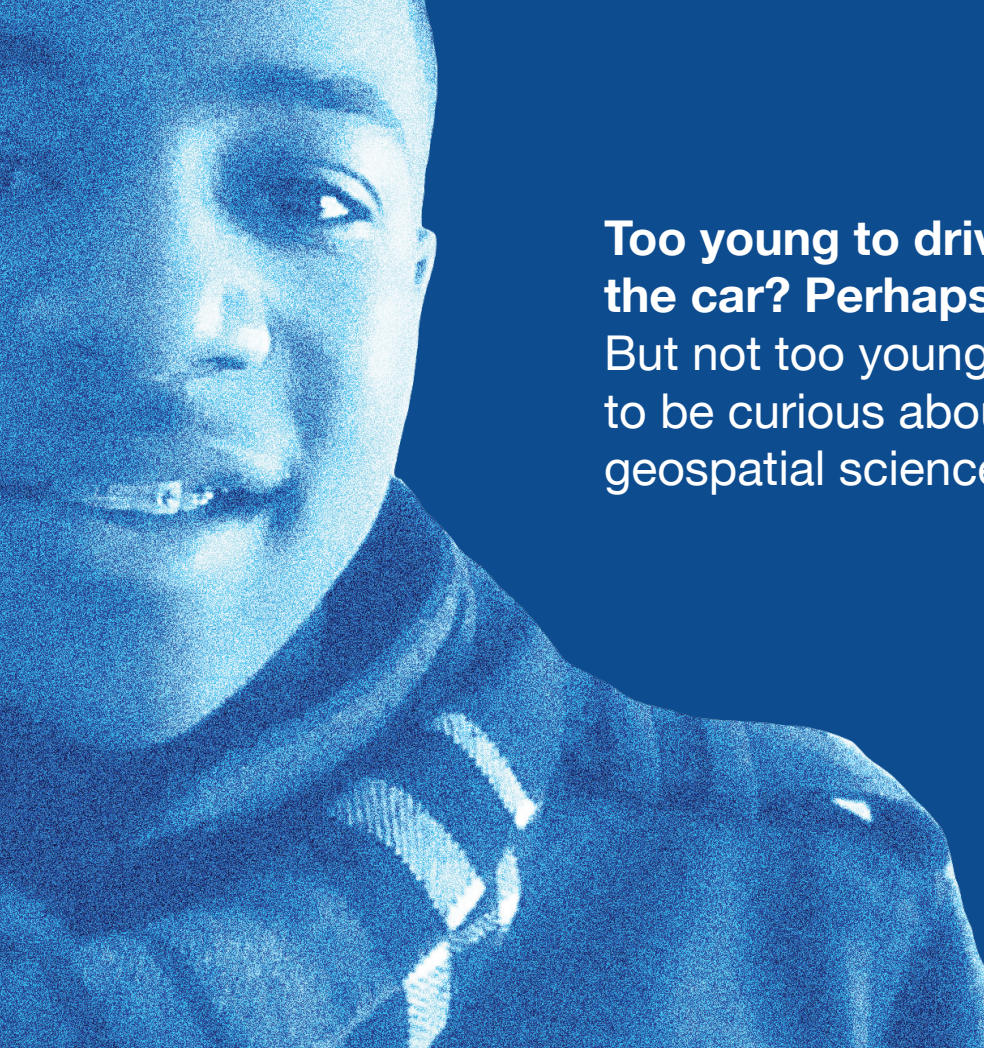
### ***Digital Ads***

Employment Promotion  
Email Blast  
Newsletter Display Ads

## CONTACT

Bill Spilman  
*ASPRS Advertising, Exhibit Sales & Sponsorships*  
320 W. Chestnut St.  
P.O. Box 399  
Oneida, IL 61467  
(877) 878-3260 toll-free  
(309) 483-6467 direct  
(309) 483-2371 fax  
bill@innovativemediasolutions.com

\*Limitations apply. Contact Bill Spilman for full details



**Too young to drive  
the car? Perhaps!**  
But not too young  
to be curious about  
geospatial sciences.



**The ASPRS Foundation  
was established to advance  
the understanding and  
use of spatial data for the  
betterment of humankind.**

*The Foundation provides grants,  
scholarships, loans and other forms of aid  
to individuals or organizations pursuing  
knowledge of imaging and geospatial  
information science and technology, and  
their applications across the scientific,  
governmental, and commercial sectors.*

**Support the foundation, so when  
they are ready, we are too.**

**[asprsfoundation.org/donate](http://asprsfoundation.org/donate)**



# JOIN ASPRS TODAY!



**asprs** THE IMAGING & GEOSPATIAL  
INFORMATION SOCIETY

## ***ACCELERATE YOUR CAREER!***

*PHOTOGRAMMETRY · REMOTE SENSING · GIS · LIDAR · UAS ...and more!*

### **LEARN**

- Read our journal, *PE&RS*
- Attend professional development workshops, GeoBytes, and online courses through the ASPRS ProLearn platform
- Earn professional development hours (PDH)
- Attend our national & regional meetings and conferences

### **DO**

- Write for *PE&RS*
- Innovate to create new geospatial technologies
- Present at our national & regional meetings and conferences
- Engage & network

### **GIVE**

- Participate in the development of standards & best practices
- Influence state licensure through our NCEES affiliation
- Mentor colleagues & support students
- Educate others about geospatial science & technology

### **BELONG**

- Establish yourself as a geospatial expert
- Grow business relationships
- Brand yourself and your company as geospatial leaders
- Connect to the world via our affiliation with ISPRS

---

Don't delay, join today at **asprs.org**